Design of Sustainable Materials by the Transformation of Biorefinery Derived Waste Biomass into Biobased Polymeric Resins: Synthesis, Characterization, Applications

by

Archana Shivaji Bansode

A dissertation submitted to the Graduate Faculty of
Auburn University
in partial fulfillment of the
requirements for the Degree of
Doctor of Philosophy

Auburn, Alabama
December 10, 2022

Keywords: Lignocellulosic Biomass, Structural Characterization,
Biobased Polymeric Resins, Wood Adhesives, Curing Kinetics, Controlled Release Fertilizer

Approved by

Maria L. Auad, Chair, Director of Center and Polymers and Advanced Composites and Professor of Chemical Engineering, Auburn University, Auburn, AL
Sushil Adhikari, Director of Center of Bioenergy and Bioproducts and Professor of Biosystems Engineering, Auburn University, Auburn, AL
Brian K. Via, Director of Forest Product Development Center and Regions and Professor of School of Forestry and Wildlife Sciences, Auburn University, Auburn, AL
Xinyu Zhang, Professor of Chemical Engineering, Auburn University, Auburn, AL
Iris Beatriz Vega Erramuspe, Graduate Research Fellow III of School of Forestry and Wildlife Sciences, Auburn University, Auburn, AL

Abstract

Polymeric resins (PRs) are one of the most versatile materials, with a wide range of application fields. However, the synthesis of these polymeric resins predominantly relies on the precursor derived from the petroleum refinery that utilizes crude oil as feedstock, posing environmental, economic, and human health concerns at various points of its life cycle. Biorefinery offers the potential to replace fossil fuel-based products by converting renewable biomass into multiple products, hence maximizing biomass's value. Lignocellulosic biomass derived from plant resources and municipal solid waste has been proven as the most abundant one among the diverse biomass resources. The present research aimed to develop biobased polymeric resins by replacing or substituting conventional monomers/chemicals with biorefinery-derived biomass for applications such as wood adhesives, 3D printing of structural materials, and functional coating for controlled release of fertilizers.

In Chapter 2, lignin recovered from kraft biorefinery (L-KB) and two bio-oils, prepared from laboratory scale solvent liquefaction of lignin (BO-SL/L) and fast pyrolysis of pinewood (BO-FP/PW), respectively, have been used to substitute 50% (w/w) of phenol in novolac phenol-formaldehyde (NPF) resin system. The adhesive derived from lignin showed the highest tensile strength (3.46 ± 0.55 MPa). This indicates that the lignin derived from kraft biorefinery is a potential substitute for phenol in NPF resin systems for wood adhesive applications.

In Chapter 3, biobased novolac phenol-formaldehyde (BNPF) resin was developed by partially replacing petroleum-based phenol and formaldehyde with lignin derived from kraft biorefinery- and modified kraft biorefinery-derived lignin, respectively. The chemical modification of lignin

was performed through a periodate oxidation process using sodium periodate ($NaIO_4$) as an oxidizing agent. The bonding performance tests indicated that BNPF resin adhesives have high adhesion strengths (>0.7 MPa). The outcome of this research provides a new way to utilize bio feedstock such as lignin for synthesizing biobased wood adhesives.

In Chapter 4, bio-oils produced from hydrothermal liquefaction (HTL) of municipal sewage sludge (MSS) at different processing conditions have been utilized as a natural filler for pMDI wood adhesive formulation. For each MSS bio-oils, three different loading levels (MSS Bio-oil/pMDI weight ratio: 0.18, 0.33, and 0.54) were selected as a treatment to understand better the chemical interaction of the MSS-Bio-oil/pMDI adhesive formulation with the wood substrate. Overall, the bio-oil produced under a nitrogen atmosphere demonstrated significant potential to reduce the usage of petroleum-derived pMDI while maintaining good bonding performance.

In Chapter 5, a biobased novolac phenol-formaldehyde (BNPF) resin was successfully developed by partially substituting phenol with a bio-oil obtained by fast pyrolysis of pinewood biomass. The curing kinetics of BNPF resin cured with hexamethylenetetramine (HMTA) was studied using the differential scanning calorimetry (DSC) method. The thermal curing kinetics were studied through model-fitting approaches. The Kamal model is employed and proved a best-fitting model in describing the curing behavior of the BNPF/HMTA resin.

In the final chapter, biobased polyurethane (BPU) was synthesized out of lignin derived from kraft biorefinery. Then, BPU coatings were utilized to coat urea fertilizer to achieve a controlled release of nutrients. The nutrient-release behavior of developed coated fertilizers was systematically studied in water and soil environments. The experimental results indicated that the coating

material derived from all lignin was beneficial for slowing down the nutrient release. This study highlights the potential of lignin in developing controlled-release fertilizers for sustainable agriculture.

Keywords: Kraft Lignin, Solvent Liquefaction, Fast Pyrolysis, Bio-oil, Structural Characterization, Polymerization, Curing, Adhesion Strength, Periodate Oxidation, Oxidized Lignin, Municipal Sewage Sludge, Hydrothermal Liquefaction, Biobased Novolac Phenol-formaldehyde Resin, Differential Scanning Calorimetry, Curing Reaction Kinetics, Polymeric methylene diphenyl diisocyanate (pMDI), Wood Adhesives, Controlled-release Fertilizer, Biobased Polyurethane, Nutrient Release

Acknowledgments

First of all, I would like to thank our sponsors – US Department of Agriculture-National Institute of Food and Agriculture (USDA-NIFA-2015-67021-22842), National Science Foundation - Center of Excellence in Nano-Bio Materials derived from Biorenewable and Waste Resources (NSF-CREST), NSF-CREST Center for Sustainable Lightweight Materials (C-SLAM) award #1735971, PrinTimber NSF EPSCoR RII Track-2 project, Travel Grant by 100,000 Strong in the Americas Innovation Foundation (to travel and work on the research project with the University of Mar del Plata, Argentina, 2019) for providing financial support throughout almost last five years for research, personnel and travel.

I would take this opportunity to express my gratitude to the Ph.D. committee members: Dr. Maria L. Auad, Dr. Brian Via, Dr. Sushil Adhikari, Dr. Xinyu Zhang, and Dr. Iris Beatriz Vega Erramuspe for their time, technical expertise, and feedback throughout my research at Auburn University. Also, other contributors and collaborators, Dr. Elizabeth Guertal, Dr. Ramsis Farag, Dr. Allan David, Dr. Thomas Elder, Dr. Andrew J. Adamczyk, and Dr. Maria Alejandra Marino (School of Agricultural Sciences, National University of Mar del Plata, Balcarce, Argentina) for their support and expertise in terms of instruments, some specific techniques, and general scientific guidance. I am thankful to Dr. Mario Eden (Department Chair and Professor of Chemical Engineering), Dr. Alvaro Herrera (Director NMR Center at Auburn University), and Dr. Michael Miller (Director of the Research Instrumentation Facility) for providing the research facilities. I would like to thank Emmanuel Winful (Health and Safety Manager), Christian Brodbeck, Elaine Manning, Naomi Gehling, Emma Goodlett, and Kristy Rinker for providing administrative support.

My colleagues from Dr. Auad's lab: Dr. Mehul Barde, Dr. Nima Alizadeh, Dr. Yuyang Wang (Tom), John Hinkle (Tripp), Dr. Prutha Joshi, and Lucila Carias played an important role in my research, including (but limited to) providing scientific insights and feedback, reviewing drafts and many presentations, and giving suggestions on experimental setup and analyses. Also, they played a vital role in cheering me up during difficult times in my graduate life. To Dr. Auad - I don't have enough words to express my gratitude for everything – you are an amazing human being, and I am fortunate to have you as my mentor and adviser for the last five years. You are an incredibly smart individual from whom I learned a lot about research, how to formulate ideas, present them precisely, and effectively execute them. Thank you so much for providing opportunities to travel for conferences and seminars to present my research work at regional and national conferences. I am very grateful to travel with you to Argentina for a technical project. Also, I will never forget the hospitability you provided there and the chance to meet your family. I loved the overall experience there. As I said, I will keep talking about how much your support means to me in my grad life – THANK YOU!

To Dr. Vega – I enjoyed working with you on research projects and learned a lot through experience. Thanks so much for always being available for me to discuss research. To Dr. Farag – you were constant support and help in the lab whenever I required it. Thanks so much for being such great support throughout the last five years. To Dr. Elizabeth Guertal – Thanks for your collaboration and for helping me in crop field studies.

While working on the research, I was fortunate enough to work with other talented and smart individuals, not just from Auburn University but from other places that work in polymer/adhesion research. I want to thank Lorena Alexandra Portilla Villarreal (for being such a great collaborator and friend), Dr. Osei Asafu-Adjaye, Dr. Abiodun Oluseun Alawode, Dr. Vivek Patil, Dr. Tawsif

Rahman, Manish Sakhakarmy, Braden Hahn, Dr. Nicolas Martinez Cuesta (School of Agricultural Sciences, National University of Mar del Plata, Balcarce, Argentina), Tanzina Azad for their contribution through collaboration. I got to learn a lot through these collaborations. Moreover, I received various opportunities to mentor, supervise and train undergraduate colleagues: Christopher Upp, Stephen Adams, Melina Kloster (School of Agricultural Sciences, National University of Mar del Plata, Balcarce, Argentina), and Claire Lindemann (University of Minnesota), I thank them for their contribution and assistance in the various research projects.

Most importantly, I would like to thank my friends who made my stay in Auburn pleasant with their support, friendship, and care – Thank you so much, Vinita (Shinde), for being the cool roommate for a long time. I appreciate your love, care, and support when I needed the most. I am so lucky to have such a wonderful and talented person in my life; huge thank you. Also, thank you, Amod (Parakhi) and Ritvija (Avvari), for your support and friendship – it means a lot. To Tom and Vicky - you guys are awesome in cheering me up and supporting me. Our endless talk on any topic made my days and forget the hard times thank you for introducing authentic Chinese food to me. To Nima – Thanks for being a wonderful friend, your funny comments always made me roll my eyes, but they entertained me (lol). To Tripp – you are such a balanced personality; thanks for teaching me about American culture and things and caring for me.

Also, my friends from back home, Pooja Khairnar, Nikita Mhadeshwar, Bhagyashree Dahifale, Namrata Phulaware, Rucha Patil, and Sangeeta Barwar, for supporting and lifting me in a stressful situations.

Finally, I would like to thank my family: my Father (Shivaji Bansode) and Mother (Usha Bansode) for their constant love, support, and motivation. Pappa – I love you always. Thank you

for understanding me in a challenging situations. You always supported and motivated me, which made me courageous and have a dream big. I would not be here without you and Aai.

Thank you so much, other family members, Sheetal Bansode, Mahesh Rohine, Darshana Bansode, Onkar Kore, and Jayesh Bansode, for all the love, support, care, and encouragement. Also, I would like to thank the little ones, Pari (Shrusti), Arya, and Chiku (Sarth), for making me laugh and reminding me of what is essential in life. Without you guys and your love, I wouldn't have dared to take this giant leap. Also, I would like to thank Dipak Pukale, a wonderful partner, for always supporting and motivating me through many ups and downs.

Table of Contents

List of Tables

List of Figures

List of Abbreviations

ANOVA	Analysis of variance
ATR	Attenuated total reflectance
BNPF	Biobased novolacs phenol-formaldehyde
BO-FP/PW	Bio-oil obtained from fast pyrolysis of pine wood
BO-SL/L	Bio-oil produced from solvent liquefaction of industrial lignin
BPU	Biobased polyurethane
CAD	Computer assisted design
CMR	Carcinogenic, Mutagenic and Reprotoxic
CO_2	Carbon dioxide
CP	Cross-polarization
CRFs	Controlled-release fertilizers
CRM	Calcined red mud
DAC	Dialdehyde cellulose
DGEBA	Diglycidyl ether of bisphenol A
DIW	Direct ink writing
DLP	Digital light processing
DMSO-d_6	Deuterated Dimethyl Sulfoxide
DNPH	2, 4-dinitrophenylhydrazine
DOE	Design of Experiment
DSC	Differential scanning calorimetry
EP	Epoxy

ERs	Epoxy resins
FP	Frontal polymerization
FTIR	Fourier Transform Infrared
G	Guaiacyl
GCMS	Gas Chromatography-Mass Spectroscopy
H	p-hydroxyphenyl
HDI	Hexamethylene diisocyanate
HETCOR	Heteronuclear Correlation
HMTA	Hexamethylenetetramine
HSQC	Heteronuclear single quantum coherence
HTL	Hydrothermal liquefaction
IPDI	Isophorone diisocyanate
K	Potassium
L	Indulin AT kraft lignin
LBL	Layer-by-layer
LC	Lignocellulosic
LCBM	Lignocellulosic biomass
L-KB	Kraft biorefinery
MAS	Magic angle spinning
MDF	Medium density boards
MDI	Methylene diphenyl diisocyanate
MF	Melamine-Formaldehyde
MSS	Municipal sewage sludge

MSS-Bio-oil_E	Municipal bio-oil produced under ethylene atmosphere with no catalyst
MSS-Bio-oil_EC	Municipal bio-oil produced under ethylene atmosphere with catalyst
MSS-Bio-oil_N	Municipal bio-oil produced under nitrogen atmosphere with no catalyst
MSS-Bio-oil_NC	Municipal bio-oil produced under nitrogen atmosphere with catalyst
N	Nitrogen
$NaIO_4$	Sodium periodate
NASA	National Aeronautics and Space Administration
NERL	National Renewable Energy Laboratory
NHND	N-hydroxy-5-norbornene-2,3-dicarboximide
NMR	Nuclear Magnetic Resonance
NPF	Novolac phenol−formaldehyde
OL	Periodate oxidized lignin
OSB	Oriented strand board
P	Phosphorus
PCU	Polymer-coated coated urea
PF	Phenol-formaldehyde
PTMEG: DIOL	Polytetramethylene ether glycol
pMDI	Polymeric methylene diphenyl diisocyanate
PRs	Polymeric Resins
PU	Polyurethane
PUs	Polyurethanes
RRM	Reduced red mud
RH	Relative humidity

S	Syringyl
SD	Standard deviation
SEM	Scanning Electron Microscopy
SLA	Stereolithography
SYP	Southern yellow pine
T_p	Curing peak temperature
TA	Thermal analysis
TCD	Thermal conductivity detector
TDI	Toluene diisocyanate
THF	Tetrahydrofuran
TMDP	2-Chloro-4,4,5,5-tetramethyl-1,3,2-dioxaphospholane
TMS	Tetramethylsilane
TRIOL	2-Ethyl-2-(hydroxymethyl)-1,3-propanediol
TS	Thickness Swelling
UF	Urea-Formaldehyde
WA	Water Absorption
WBPs	Wood-based panels
WWTPs	Wastewater treatment plants
α	Degree of curing
^{31}P-NMR	Phosphorus-31 nuclear Magnetic Resonance
3DP	Three-dimensional printing
100-NPF	Novolac phenol-formaldehyde

50-NPF-L-KB	Novolac phenol-formaldehyde by partial replacement of phenol with lignin
50-NPF-BO-SL/L	Novolac phenol-formaldehyde by partial replacement of phenol with bio-oil derived from solvent liquefaction of industrial lignin
50-NPF-BO-FP/PW	Novolac phenol-formaldehyde by partial replacement of phenol with bio-oil derived from bio-oil obtained from fast pyrolysis of pine wood

Chapter 1

Introduction

1.1 Polymeric Resins

Polymeric resins (PRs) have achieved popularity in the world of materials since the introduction of the first commercial synthetic resin, Bakelite, in the early 1900s.[1–3] The usage of polymer resin materials has expanded to the point that they can be found in almost every product, from critical to nonessential.[4] Several properties of polymeric resin materials, such as being lightweight, structure, and functionality that can be tailored to specific applications, a high strength-to-weight ratio, and relatively low cost, have made them a material of choice and replaced traditional metals, ceramics, and glass-based materials.[5–7] Moreover, this variety of advantageous characteristics makes them ideal for various applications, including adhesives, coatings, 3D printing of structural materials, electrical/electronic laminates, automotive and aerospace parts, molding compounds, flooring and paving high-performance composites, and many more.[8,9] The demand for polymeric resins has increased for manufacturing adhesives, coatings, and 3D printing of structural materials.

1.2 Application of Polymeric Resins in Adhesives, Coatings, and 3D Printing of Structural Materials

1.2.1 Adhesives

One of the polymeric resin's well-known and prominent applications is adhesives, which join or hold two substrates, similar or different, in contact either temporarily or semi-permanently, or permanently by adhesive bonding.[10,11] Polymeric resin usually forms an adhesive bond by a

chemical reaction involving crosslinking triggered by external stimuli such as temperature or solvent evaporation.[10,12] Owing to the structural integrity of adhesive bonds, the polymeric resin adhesives show a diverse range of applications[13] such as construction,[14] packaging materials,[15,16] aerospace,[17] automobile,[18] medicine and healthcare,[19–22] textile[23–28] industries.

1.2.2 Coatings

Polymeric resins have gained much attention in coating technology and surface chemistry.[29,30] As many coating technologies involve the application of a coating layer made of polymeric resin on the surface of the material or substrate to enhance the resistance of the substrate to environmental factors, introduce specific functions into the system by changing surface properties, or even add design factors for an aesthetic look.[31,32] Polymeric resin-based coating shows distinct advantages such as tunable physical and chemical properties, lower material and processing costs, and over serval other materials such as metal, ceramics, and glass.[33,34] As this polymeric resin coating imparts desirable characteristic properties to the engineering substrates,[35] they are widely used in applications including anti-corrosion protection,[36–38] self-healing or self-cleaning capabilities,[39–41] antifogging,[42–44] anti-icing,[45,46] anti-fouling,[47,48] water/oil repellency,[49,50] scratch-resistant,[51,52] non-stick surface[53] and controlled release fertilizer[54–57] coatings.

1.2.3 Three-dimensional (3D) Printing of Structural Materials

Three-dimensional (3D) printing, also known as additive manufacturing, is an advanced manufacturing technique that holds the potential for the customized and on-demand production of parts without needing molds.[58–60] The 3D printer utilizes polymeric resins and fibers, ceramics, metals, and composites to produce three-dimensional models via layer-by-layer or continuous deposition using computer-assisted design (CAD).[59] Due to the versatile polymer chemistry, the

polymeric resin-based 3D printing technique has attracted particular attention in the material world.[61–64] Stereolithography (SLA) and digital light processing (DLP) are the two most common resin 3D printing techniques.[62,65,66] Polymeric resin-based technology has opened applications in various fields such as construction, automobiles, biomedical devices, tissue engineering and drug delivery, soft robotics, electronics, and others.[66–68]

1.3 Common Polymeric Resins used in Adhesives, Coatings, and 3D Printing of Structural Materials

Polymeric resins are of increasing interest in the field of adhesives and coatings because they provide the best properties. Based on their nature, polymeric resins can be classified into two main groups, thermoplastic, and thermoset systems. A full details description of the chemistry and properties of polymeric resin can be found in the following section.

1.3.1 Phenol-formaldehyde Resin

Phenolic resin or phenol-formaldehyde (PF) resin is the first synthetic polymer produced commercially from a low molecular weight compound.[69,70] Bakelite is the first synthetic phenol-formaldehyde resin and became commercialized in 1907.[69] PF resin was obtained by adding and condensing phenol with formaldehyde.[70] Depending on the nature of the catalyst and phenol-to-formaldehyde molar ratio (P/F ratio), there are usually two main categories of phenol-formaldehyde resins, such as resole and novolac. The reaction of phenol with an excess of formaldehyde (P/F molar ratio falls between 1:1.1 and 1:3) in alkaline conditions yields the resols known as heat-reactive PF resin.[71] Therein, the reaction in a basic medium involves the addition of formaldehyde with phenoxide ion, which leads to the formation of *o*- or p-monomethylol phenol, and they can be cured thermally.[72] Novolac PF resin is typically prepared by the addition

and condensation of molar excess of phenol reactant with formaldehyde (P/F molar ratio falls between 1:0.75 and 1:0.85) in the presence of an acid catalyst.[71–74] The reaction between phenol and formaldehyde under acidic conditions proceeds through initial protonation of hydrated formaldehyde followed by electronic substitutions in the electron-rich ortho and para position, which results in the formation of novolac with phenolic moieties predominantly connected by methylene bridges.[72,73] The general reaction scheme for synthesizing resole and novolac PF resin is presented in Figure 1.1. Whereas the formed novolac PF resin is linear or only slightly branched thermoplastic polymer, which can be cured by heating in the presence of hardener, mostly hexamethylenetetramine (HMTA). The curing of the novolac PF resin system leads to insoluble and infusible products with crosslinked structures.[7,70,72,74] The crosslinking of PF resin has high solvent and chemical resistance and thermal stability.

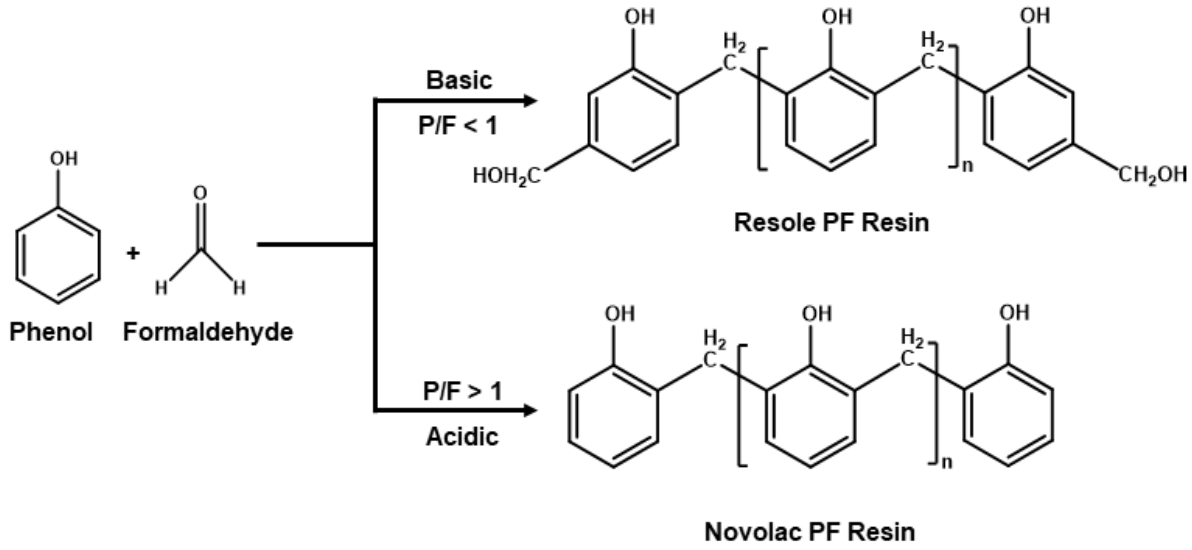

Figure 1.1 General reaction scheme for the synthesis of resole and novolac PF resins.[75] [Adapted by permission from Springer Nature: Springer eBook, Nanofibrillated Cellulose Based Biophenolic Composites, Copyright 2021]

1.3.2 Polyurethane Resin

Polyurethane (PU) is one of the most versatile polymers in the world.[76] Polyurethane was first synthesized by Otto Bayer and his co-workers in 1937 in Germany.[77,78] Polyurethanes (PUs) are widely used in adhesives, coatings, and many other important applications such as rigid foams, elastomers, and insulating materials due to high-performance properties including flexibility, toughness, strength, durable finish, and resistance to chemicals, corrosion, abrasion, and stain.[79–81] PUs are mainly prepared through polyaddition (exothermic reaction) of isocyanate groups (−NCO) of polyisocyanates (or diisocyanates) with other polynucleophiles such as polyols with other terminal hydroxyl groups (−OH) results in the formation of urethane linkage in the back-bone, also called carbamate (−NH−(C=O) −O−).[82] Figure 1.2 represents the general reaction scheme of PU synthesis. The isocyanates are usually difunctional and aromatic, aliphatic, or acyclic in structure.[82] The most important polyisocyanates are methylene diphenyl diisocyanate (MDI), and toluene diisocyanate (TDI), which possess rigid aromatic rings in their chemical structure and hence improve the mechanical strength of the material.[77] On the other hand, hexamethylene diisocyanate (HDI) and isophorone diisocyanate (IPDI) are aliphatic polyisocyanates with alkyl chain in the structure.[77,82] Polyols is the second important component in polyurethane synthesis, the most commonly used polyols with longer alkyl chains are typically polyether, polyester or polycarbonate, with molecular weights ranges between 300 – 4000 g/mol, which make up the soft block or segment in PUs that provides flexibility and elasticity to the material.[4,77,82,83] Whereas polyols with shorter alkyl chains, such as a 1,4-butane diol or 1,6-hexane diol, provide rigidity to materials and are used to control hard segments.[4,77,82,83] Apart from the polyols, using chain extenders such as glycerol, diethanolamine, 2-(methylamino) ethanol, and 1,2-ethylene diol helps to increase the molecular weight, functionality as well as soft/rigid segment ratio.[4,77,82,83]

Theoretically, the polyurethanes are synthesized from the equimolar ratio of polyisocyanate and polyol to achieve the degree of polymerization, whereas, in practice, little excess of isocyanate is utilized to compensate its losses due to the reaction of isocyanate with a water molecule (generally present in the polyol or water).[82] Considering the combination and composition of the soft and hard segments, the PU polymeric material possesses rigid, semirigid, or flexible properties that found promising applications in adhesives and coatings.[4,77,81–83]

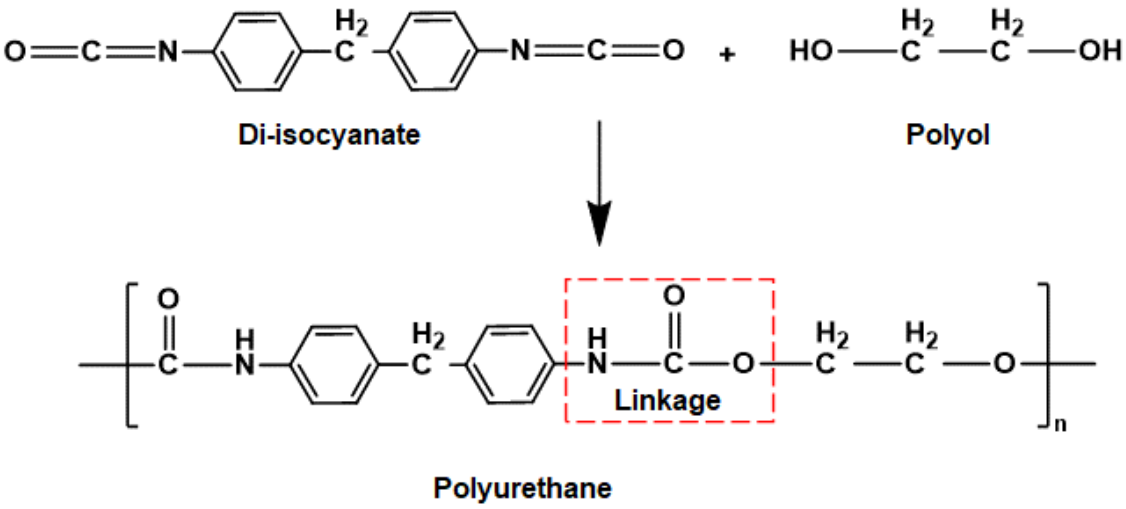

Figure 1.2 General reaction scheme for the synthesis of polyurethane resins.[84] [Adapted by permission from RSC Publishing: RSC Advances, Polyurethane types, synthesis and applications – a review, Copyright 2021]

1.3.3 Epoxy Resin

The epoxy (EP) resin is another important type of polymeric resin that was first discovered in 1909 by Prileschajew[85,86], and their first commercial production started in the late 1940s.[86,87] Two scientists, Pierre Caston and Sylvan Greenlee filed patents for the synthesis of diglycidyl ether of bisphenol A (DGEBA) with the same process but different molecular weights of DGE-

BA in 1938 and 1943, respectively, which accounts for more than 70% of all epoxy resin usage .[88,89] Epoxy resins (EPRs) are composed of two or more 3-membered cyclic structures, the organic chemistry of cyclic structure is also referred to as oxirane (ethylene oxide or epoxide), which is the representative unit of an epoxy polymer.[88,90–92] The epoxide structure consists of one oxygen atom and two carbon atoms, forming a ring-like structure by bonding to each other, as shown in Figure 1.3, whereas carbon and oxygen possess different electronegativity, which makes carbon atoms electrophilic.[85,88,91] This atomic arrangement makes them highly reactive, which undergoes ring opening reactions with nucleophilic functional groups such as −COOH, −OH, $-NH_2$, sulfone etc.[91] There are three different types of epoxy resins such as cycloaliphatic, epoxidized and glycated epoxy resins, in this first two types of epoxy resins are prepared by the direct oxidation of the corresponding olefin.[93] The glycidated epoxy resin i.e., diglycidyl ether of bisphenol-A (DGEBA) is most commonly used and prepared by the coupling reaction of polyhydric compounds having at least two active hydrogen atoms, for instance, bisphenol A with epichlorohydrin in an alkaline medium followed by dehydrohalogenation as presented in Figure 1.4.[85,89,93,94] The curing of epoxy resins is carried out by chemical reaction of epoxide groups with several curing agents (hardener system), the curing agents are selected based on the desired properties needed for the intended applications, they are typically cured in the presence of amines and anhydrides.[83,89,93] The unique abilities of epoxies, such as their excellent mechanical properties, high adhesiveness to many substrate, good heat and chemical resistance, and low shrinkage during cure, they are intensively used across wide range of fields as high performance adhesives and coatings, high performance materials for automobile, aerospace and building construction.[85,88,91,93]

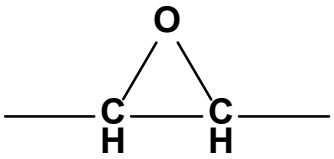

Figure 1.3 Chemical representation of epoxy or oxirane group[93] [Adapted by permission from American Chemical Society: Industrial & Engineering Chemistry Research, Additive Manufacturing of Epoxy Resins: Materials, Methods, and Latest Trends, Copyright 2020]

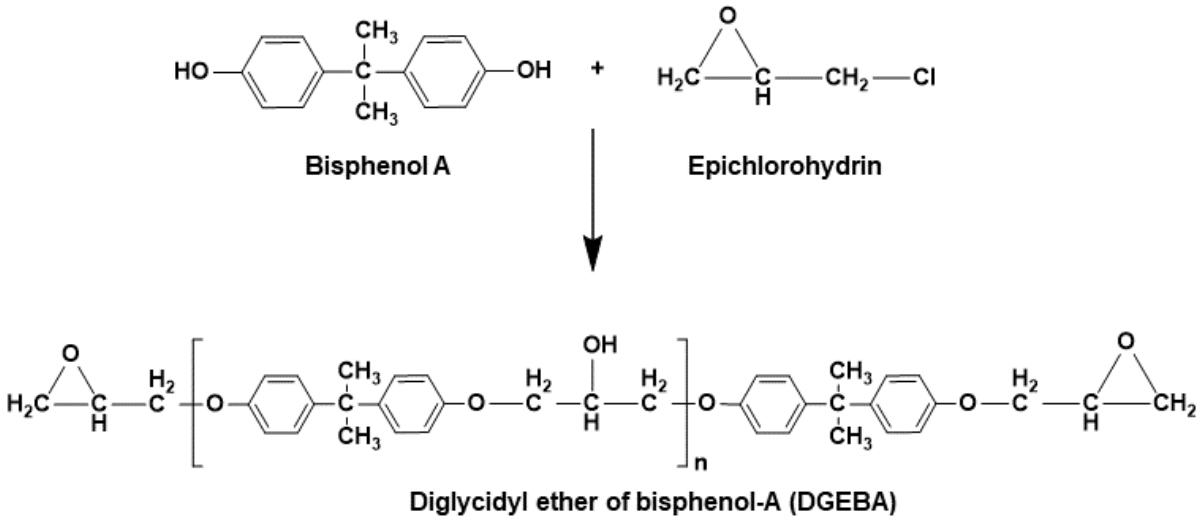

Figure 1.4 General reaction scheme for the synthesis of DGEBA from bisphenol A and epichlorohydrin.[93] [Adapted by permission from American Chemical Society: Industrial & Engineering Chemistry Research, Additive Manufacturing of Epoxy Resins: Materials, Methods, and Latest Trends, Copyright 2020]

1.3.4 Acrylic Resin

Acrylic polymers are commonly known as acrylics[95], and the first acrylic polymeric resin prepared to be commercially was poly (methyl acrylate). Their industrial production began in 1927 by Rohm and Hass AG in Germany.[96,97] The acrylic polymeric resin is prepared by the addition

polymerization technique using a variety of hard and soft monomers (Figure 1.5).[98,99] The acrylic soft monomer most commonly used are N-butyl acrylate, ethyl acrylate, 2-ethyhexyl acrylate. In contrast, the hard acrylic monomer includes methyl methacrylate and isobutyl acrylate, which tend to be brittle.[98,100,101] The proper composition and type of monomer yield desirable flexibility and hardness polymeric resin.[95] Acrylic polymeric resins are extensively employed in the coating and adhesive industries because of their excellent chemical, thermal and mechanical properties, good weather resistance, good adhesion to various substrates, and durability.[81,98,102,103]

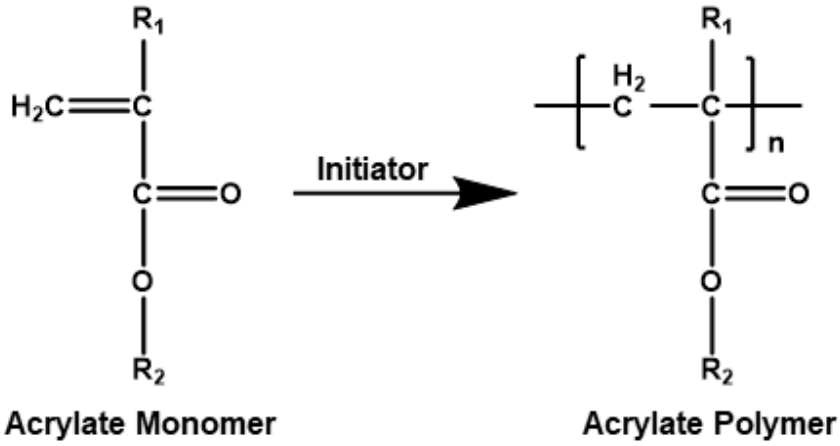

Figure 1.5 General reaction scheme for the synthesis of acrylic resin.[97] [Adapted by permission from Springer Nature: Applied Microbiology and Biotechnology, Current status on the biodegradability of acrylic polymers: microorganisms, enzymes and metabolic pathways involved, Copyright 2021]

As stated in the previous section (Figure 1.1−1.5), the synthesis and development of these polymeric resins can be achieved with the functionality and nature of the coreactive centers of the monomers. The monomers with functional groups (hydroxyls, acids, amines, and isocyanates) in the structural units are the precursors of choice for synthesizing high-performance engineering

polymeric materials. To enable the resin to form polyurethane chains, the monomer molecules should have isocyanate (−NCO) and hydroxyl functionality (−OH) in the structure. Furthermore, the hydroxyl functionality is offered by some commercially available polyols (polyester or polyether), for instance, 2,2-dimethylolpropionic acid and 2-amino-1,3-propanediol.[104,105]

However, these polyols and many other key monomers/chemicals such as phenol, formaldehyde, styrene, and isocyanate employed in synthesizing polymeric resins have predominantly relied on the petroleum hydrocarbon, which is derived from the petroleum biorefinery.[106] If the current reliance on petrochemical feedstocks for the generation of monomers continues, then pessimistic estimates suggest that 20% of the total fuel consumed every year could be utilized to produce plastic within 2050.[105,107–109] In the following section, we address the potential consequences in the utilization of petroleum refinery derived monomers.

1.4 Petroleum Refinery

The petroleum refinery is a highly integrated industry and the largest source of energy products in the world, which heavily depends on crude oil as its primary feedstock to produce chemicals.[110,111] Petroleum is the most important crude oil that consists of a complex mixture of hydrocarbon compounds (organic compounds composed of carbon and hydrogen atoms), including paraffins, naphthenes, and aromatics with small amounts of other (hetero) elements such as sulfur, nitrogen, oxygen, as well as certain metals.[110,112–114] A wide range of products, especially ethylene, propylene, and the mixture of C4 and C5 molecules, can be produced by the cracking of naphtha.[108,115,116] Additionally, aromatics such as benzene, toluene, xylene, and naphthalene are produced through a catalytic reforming process.[108,117] The resultant platform chemicals are the precursor for the production of chemicals. For example, phenol is produced from the oxida-

tion of cumene and benzene, which is further used as a precursor chemical for synthesizing phenol-formaldehyde resin.[108,118,119] The manufacturing flow chart of some common polymeric resin from petroleum resources is shown in Figure 1.6.[120]

Alarmingly, considering that almost 98% of polymeric resins are produced from monomers derived from petroleum refinery-based chemicals, their intensive usage has led to significant issues and concerns.[121] The world's heavy reliance on these resources introduces the concept of petroleum scarcity, as petroleum is nonrenewable due to the geological limitations of petroleum production.[122] From the economic point of view, petroleum scarcity refers to a gap between finite petroleum resources on the one hand and unlimited needs and wants of consumers, on the other hand, corresponding to the rapid growth of the world population and rising demands for commodity plastics.[122,123] Therefore, if the trend is moving towards overusing petroleum-based products, then it will increase scarcity by depletion of resource supply and continuous price fluctuation of nonrenewable resources, affecting the stability of plastic production costs.[105,122,124] This is already happening in some sectors of the petroleum market.[125]

Beyond the economic consequences posed by using petroleum-based precursors for synthesizing materials, there are growing concerns over long-term detrimental environmental impacts due to the continuous production and use of these petroleum-based polymeric resin products.[8,126]

The vigorous production and use of polymeric resin products lead to an unprecedented waste management crisis as the percentage of plastic waste ending up in landfills is very high. This is because these materials possess low biodegradability and persist in the environment for decades and centuries.[127,128] Some predict that the amount of plastic waste will increase by 155-265 million tons per annum by 2060.[129] One promising approach to reducing the environmental impacts of plastic waste accumulation is plastic recycling. Still, only 2% of plastic packaging materials

are recycled into similar-value products, whereas approximately 40% of plastic is landfilled, and one-third end up dispersed or released in the terrestrial environment.[128] About 8 million tons of plastic waste is dumped into the oceanic environment, and more than 150 million tons of plastic debris is currently floating on the ocean surface.[127] Within maritime environments, the submerged plastic pieces, and microplastic particles (<1–5 mm in size) are potentially harmful to marine life.[130,131] Also, these waste leach out toxic chemicals that can eventually pollute the environment.[121,130]

Additionally, the petroleum refining process and their corresponding material production release large amounts of toxic gases into the environment, causing air pollution and the greenhouse effect.[132–134] According to the National Aeronautics and Space Administration (NASA) website, there have been 10% increments of carbon dioxide (CO_2) in the atmosphere from the year 2005 to 2021.[127] The continuous rise of carbon footprint into the atmosphere contributes to environmental concerns and shows negative influence on human lives.[133,135] The petroleum-based monomers that produce polymeric resins such as phenol, formaldehyde, polyols, isocyanates, styrene, and several others are carcinogenic, mutagenic, or reprotoxic (CMR) as classed by European Chemical Agency.[8,136] Hence, it will show serious health concerns if humans are exposed to it during production.[137,138]

To combat these consequences, intensive efforts and essential strategies are being carried out to utilize renewable and sustainable energy to develop biobased chemicals and materials with unique advantages and functionality that are alternatives to petro-derived compounds.

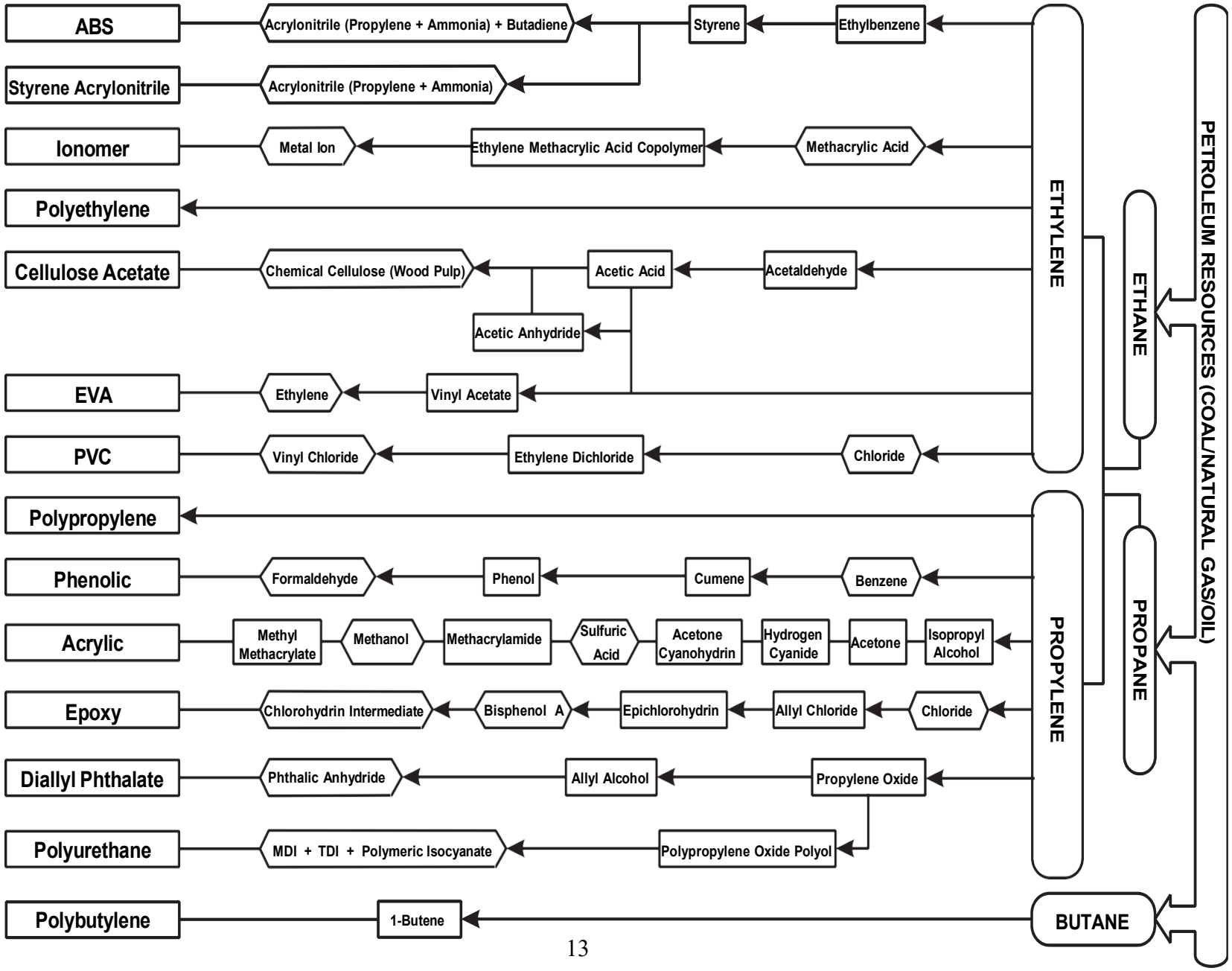
PETROLEUM RESOURCES (COAL/NATURAL GAS/OIL)
ETHANE
PROPANE
BUTANE
ETHYLENE
PROPYLENE
ABS
Acrylonitrile (Propylene + Ammonia) + Butadiene
Styrene
Ethylbenzene
Styrene Acrylonitrile
Acrylonitrile (Propylene + Ammonia)
Ionomer
Metal Ion
Ethylene Methacrylic Acid Copolymer
Methacrylic Acid
Polyethylene
Cellulose Acetate
Chemical Cellulose (Wood Pulp)
Acetic Acid
Acetaldehyde
Acetic Anhydride
EVA
Ethylene
Vinyl Acetate
PVC
Vinyl Chloride
Ethylene Dichloride
Chloride
Polypropylene
Phenolic
Formaldehyde
Phenol
Cumene
Benzene
Acrylic
Methyl Methacrylate
Methanol
Methacrylamide
Sulfuric Acid
Acetone Cyanohydrin
Hydrogen Cyanide
Acetone
Isopropyl Alcohol
Epoxy
Chlorohydrin Intermediate
Bisphenol A
Epichlorohydrin
Allyl Chloride
Chloride
Diallyl Phthalate
Phthalic Anhydride
Allyl Alcohol
Propylene Oxide
Polyurethane
MDI + TDI + Polymeric Isocyanate
Polypropylene Oxide Polyol
Polybutylene
1-Butene

Figure 1.6 Manufacturing flow chart of common polymeric resins from petroleum resources. [Adapted by permission from Elsevier: Elsevier Book, Selection of Polymeric Materials, Polymeric Materials and Properties, Copyright 2008)

1.5 Biorefinery: Emerging Opportunities for the Sustainable Development of Polymeric Resin

Biorefinery is a sustainable and effective alternative to the petroleum refinery industry. The biorefinery began to evolve during the late 1990s and is considered somewhat analogous to the petroleum refinery, except that it utilizes biomass feedstock instead of crude oil to produce marketable products and energy, including materials, the bulk of fine chemicals, transportation fuels, heat, and power.[139,140] According to the National Renewable Energy Laboratory (NERL), the biorefinery is an industrial facility that integrates biomass conversion processes and equipment to produce a spectrum of products and energy.[139,141]

Taking a step further, biorefineries can be described in three different phases: phase I, phase II, and phase II.[139,142,143] Therein, each phase indicates the prowess of biorefining operations.[139,143,144] A phase I biorefinery focuses on the utilizes only one kind of biomass feedstock material, has fixed processing capability, and gives a single primary product.[143] Examples of phase I biorefinery are ethanol from grain, pulp, and paper mills and biodiesel from vegetable oil.[139] Next is the phase II biorefinery which integrates various processes that facilitate the production of different end products using single biomass feedstock.[143] Examples include the production of multiple carbohydrate derivatives and bioethanol from cereal grains.[139] Phase III is the most advanced and developed biorefineries, which will be the powerhouse of the biobased economy.[143] This type of biorefinery utilizes various types of biomass feedstocks and processing technologies and yields multiple types of products. This biorefinery is further classified into four types of phase III biorefinery systems and can be identified as (1) whole crop biorefinery (2) green biorefinery (3) lignocellulosic biorefinery, and (4) Integrated biorefinery.[139,144,145]

1.5.1 Biomass as Feedstock for Biorefinery

Biomass is organic matter and the only renewable organic carbon resource in nature, which can be recognized as a most promising substitute for crude oil.[146] Besides, it should be noted that biomass generates heat and power, accounting for about 14% of the world's energy supply. It is the fourth most significant energy source after oil, coal, and natural gas.[146,147] Examples of such renewable biomass include woody biomass (or plant biomass), starch, chitin, chitosan, pectin, hyaluronic acid, terpenes, vegetable oils, proteins (keratin, silk, gelatin, gluten, albumin, etc.), and natural rubber.[148] Among this potential renewable biomass, lignocellulosic is the most abundant form of biomass resource on earth, with an annual production of around 150 – 170 billion metric tons.[146,149] Lignocellulosic (LC) biomass is mainly categorized into three types: virgin LC biomass (plants: tree, brushes, and grasses), waste LC biomass (agricultural residue, municipal and industrial waste), and energy crops LC biomass.[150] The plant-based LC and waste LC biomass produce bulk raw material for biorefineries.

1.5.1.1 Plant LC Biomass as Feedstock

The plant biomass is chemically known as lignocellulosic biomass, comprising cellulose (40-60%), hemicellulose (10-40%), and lignin (15-30%), which makes up about 99% of the composition of wood material.[8,140,151] However, the varying composition of these biopolymers (cellulose, hemicellulose, and lignin) can be observed between biomass types and species, as shown in Figure 1.7.

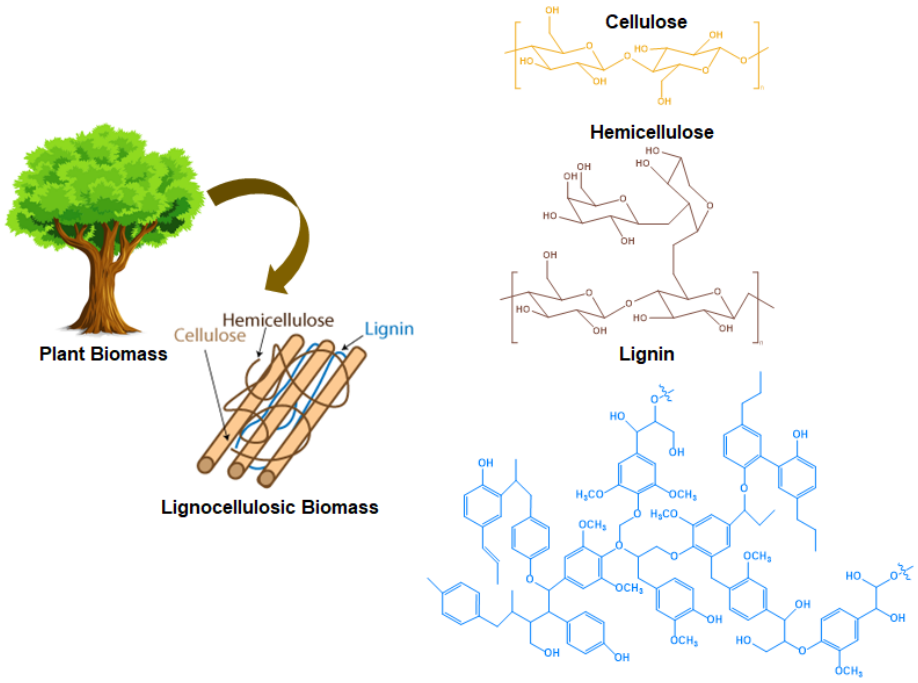

Figure 1.7 Structure of lignocellulosic biomass and its major components

Cellulose

Cellulose is one of the significant components of lignocellulosic biomass.[140] It is a linear homo-polysaccharide, which is linked through the β-1,4-glycosidic bonds of glucose units, that develop strong inter-molecular and intra-molecular hydrogen bonding in the cellulose structure.[140,152,153] This internal organization pattern is known as microfibrils/microfiber, which can be found in crystalline and amorphous structures.[140] The cellulose linearity, crystallinity, and fibrous structure impart mechanical strength to the plant cell that protects the internal structure of the plant cell.[140,153]

Hemicellulose

Hemicellulose is a branched polysaccharide formed from five to six sugar monomers, such as pentose, hexoses, glucose, xylose, mannose, and galactose.[140,151,152] These hemicellulose sugars are held together by glycosidic linkages.[140,153] Unlike cellulose, the hemicellulose structure displays side groups and shorter chains and, in some cases, branched.[140,153]

Lignin

Lignin is a three-dimensional amorphous polymer and the largest natural source of aromatic molecules. In raw lignocellulosic biomass, lignin acts as a binding material that fills the spaces between cellulose and hemicellulose by holding the lignocellulosic matrix together and providing structural integrity to cell walls. It is composed of three basic hydroxy phenylpropane units such as p-coumaryl alcohol (H), coniferyl alcohol (G), and sinapyl alcohol (S), also called monolignols having 0, 1, and 2 methoxy groups at ortho position to the hydroxyl group, respectively.[154] These monolignols go through radical polymerization to form lignin polymer-forming various interunit linkages like α-O-4 (aryl ether), β-O-4 (aryl ether), β-β (resinol), β-5 (phenylcoumaran), 5-5 (biphenyl), β-1 (1,2-diaryl propane) shown in Figure 1.8. The lignin can be extracted from different biomass sources, such as softwood, grass, and hardwood. The structure and physical properties depend strongly on the biomass sources and the extraction process.

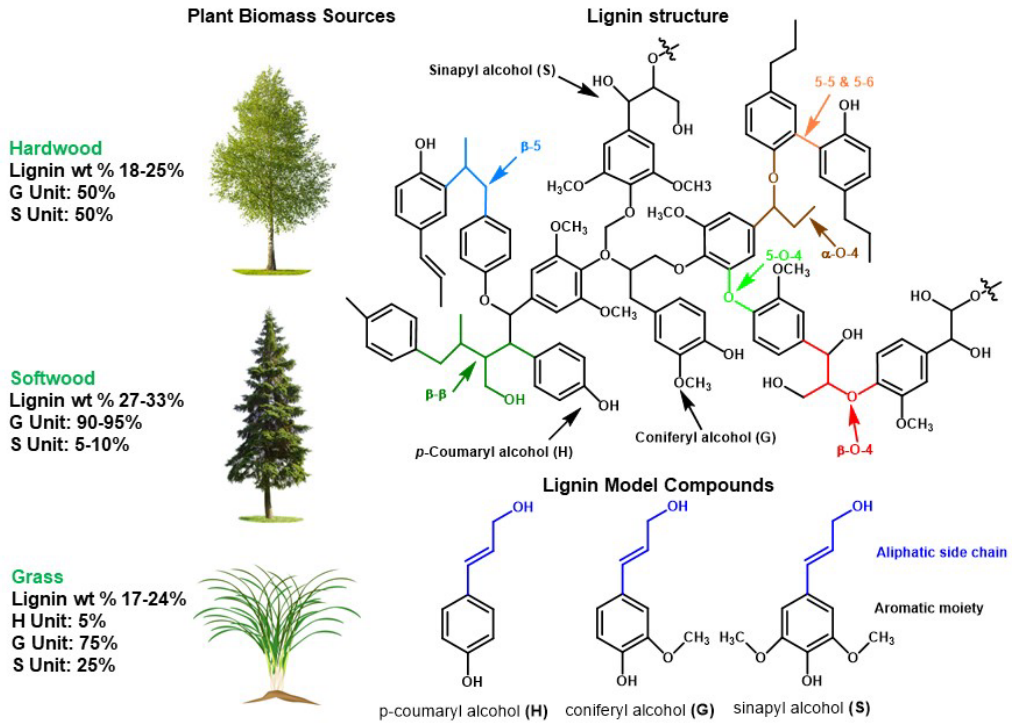

Figure 1.8 Chemical structure of lignin, lignin model compounds, and their composition in the three different types of plant biomass: H, G, and S units.[155] [Adapted by permission from American Chemical Society: Journal of Agricultural and Food Chemistry, Recent Studies on the Preparation and Application of Ionic Amphiphilic Lignin: A Comprehensive Review, Copyright 2022]

1.5.1.2 Waste Lignocellulosic Biomass as Feedstock

The agricultural LC residues and municipal/industrial waste generate significant quantities of biomass waste every day worldwide.[156] The agricultural residue is generated as a byproduct during the harvest and processing of crops, estimated to be 150 Gt annually globally.[149] This waste LC biomass has tremendous potential energy, fertilizer, and materials if used appropriately.[157] Municipal and industrial waste is produced by wastewater treatment plants (WWTPs) through biological and chemical treatment.[158,159]

1.5.2 The Pulp and Paper Industry as Lignocellulosic Biorefineries Platform

Today's traditional pulp and paper manufacturing facilities represent the world's largest woody biomass utilization system.[160–162] Kraft pulping technology has gained considerable attention in paper industries covering more than 80% of pulping capacity.[163] In the pulping industries, lignocellulosic plant biomass (wood chips) is first mechanically broken down into small pieces.[164] Next, the cellulose pulp (a slurry of cellulose fibers in water) is produced by dissolving lignin and hemicellulose (which cleaves the β-O-4 linkages between the C9 units in lignin) from lignocellulosic biomass in an alkaline medium (sodium hydroxide and sodium sulfide) at a temperature around 170 °C.[163,165] At the end of the pulping process, a high solid concentration liquor is produced as a byproduct, also referred to as "black liquor," that contains a significant amount of lignin in addition to hemicellulose and other chemicals.[165,166] processes have been developed to extract lignin from black liquor by acidification.[165,167] These include an existing kraft lignin biorefinery by Westvaco (now called Ingevity) which produces high-purity lignin (e.g., Indulin-Westvaco's trade name).[165,168]

1.5.3 Thermochemical Conversion Process for the conversion of Lignocellulosic Biomass

Bio-oil is a multi-component mixture produced by the thermochemical processes of biomass.[169] Thermochemical technologies (combustion, gasification, liquefaction, and pyrolysis) are an effective method for biomass conversion.[170,171] Bio-oil contains numerous organic compounds like phenols (e.g., guaiacols, cresols, dimethyl phenol), aldehydes (e.g., benzaldehydes and furfurals), acids (e.g., acetic and propanoic acids), ketones (e.g., cyclopentanones) and levoglucosan and complex oxygenated derived from biomass components such as carbohydrates, hemicellulose, and lignin.[169,172,173] Nitrogen and sulfur-containing compounds are also present in the bio-oil, depending on the biomass

source.[172] It typically contains about 15 – 30% of the water from dehydration reactions, and very little ash and char (a few ppm) can be found in the bio-oil.[174] Two basic thermochemical processes, i.e., pyrolysis and hydrothermal liquefaction, are the most advantageous methods for converting wet and dry lignocellulosic biomass to produce high-quality bio-oil, considered a promising feedstock for value-added products.[169,175]

1.5.3.1 Pyrolysis of Lignocellulosic Biomass

Pyrolysis is a thermochemical process for the thermal decomposition of lignocellulosic biomass in the absence of molecular oxygen.[169,176] Pyrolysis is usually carried out at a reactor's temperature ranging from 300 to 700 °C at atmospheric pressure.[177] Fixed-bed, fluidized-bed, microwave, or solar pyrolysis reactors are used.[178] The heating rates employed during the pyrolysis process can be classified into fast and slow pyrolysis (conventional pyrolysis). Fast pyrolysis has been widely employed and studied because it is a productive method that converts biomass to high-yield bio-oil at high temperatures in a very short residence time. This offers advantages in transport and storage, leading to low investment costs.[165,178] The main pyrolytic products include organic liquid (crude oil), solid (char), and a low calorific value gas (pyrogas).[177] The liquid fraction of bio-oil shows two different phases. The upper phase has a higher affinity to water which is derived from the deconstruction of carbohydrates. Whereas the lower phase originated from lignin compounds (pyrolytic lignin).[165,179] The lower organic phase pyrolytic lignin is an attractive platform for producing value-added materials.[170,179]

1.5.3.2 Liquefaction of Lignocellulosic Biomass

The liquefaction can be defined as a physical and chemical conversion of biomass in an aqueous environment (hydrothermal liquefaction) or organic solvents (solvent liquefaction) at modest temperatures (105−400 °C) and elevated pressures (2−20 MPa).[165,169,180] The main product of the liquefaction pro-

cess are liquid biocrude, gaseous stream, and solid residue byproduct.[177,178] Liquefaction shows an advantage over pyrolysis in that the former has the potential to process wet biomass feedstock directly without energy-intensive drying operations.[169,180]

1.5.4 Chemical and Catalytic Upgrading of Lignin

Finally, let's take a look at possible opportunities regarding the use of lignocellulosic biomass. The simplified summary of processes for lignin conversion is presented in Figure 1.9.[146] The hydroprocessing of lignin involves thermal reduction at temperatures ranging from 100 to 350 °C in the presence of a hydrogen source (Figure 1.9).[146] This process has the potential to create simple bulk aromatic compounds such as phenols, benzene, toluene, and xylene through hydrogen participated upgrading.[146] The oxidation process has been carried out at lower temperatures, from 0 to 250 °C, which can produce aromatic alcohols, aldehydes, and acids.[146] The depolymerization of lignin catalyzed by both acid and base at a temperature ranges from 0 to 200 °C and 100 to 300 °C, respectively.[146] Depolymerization occurs by breaking the C–O or C–C linkages between lignin units, producing small fragment molecules, including monomeric phenols.[146] Hydrogen and light gas have been produced from the liquid-phase reforming at a temperature ranging from 250 to 400 °C.[146] The gasification process of lignin produces synthesis gases such as CO and H_2.[146] The pyrolysis of lignin performed in the temperature range of 450 to 700 °C produces bio-oil.[146] Several academic groups are researching using these lignin-derived compounds for new products for a wide range of applications in favor of renewable and safer compounds.

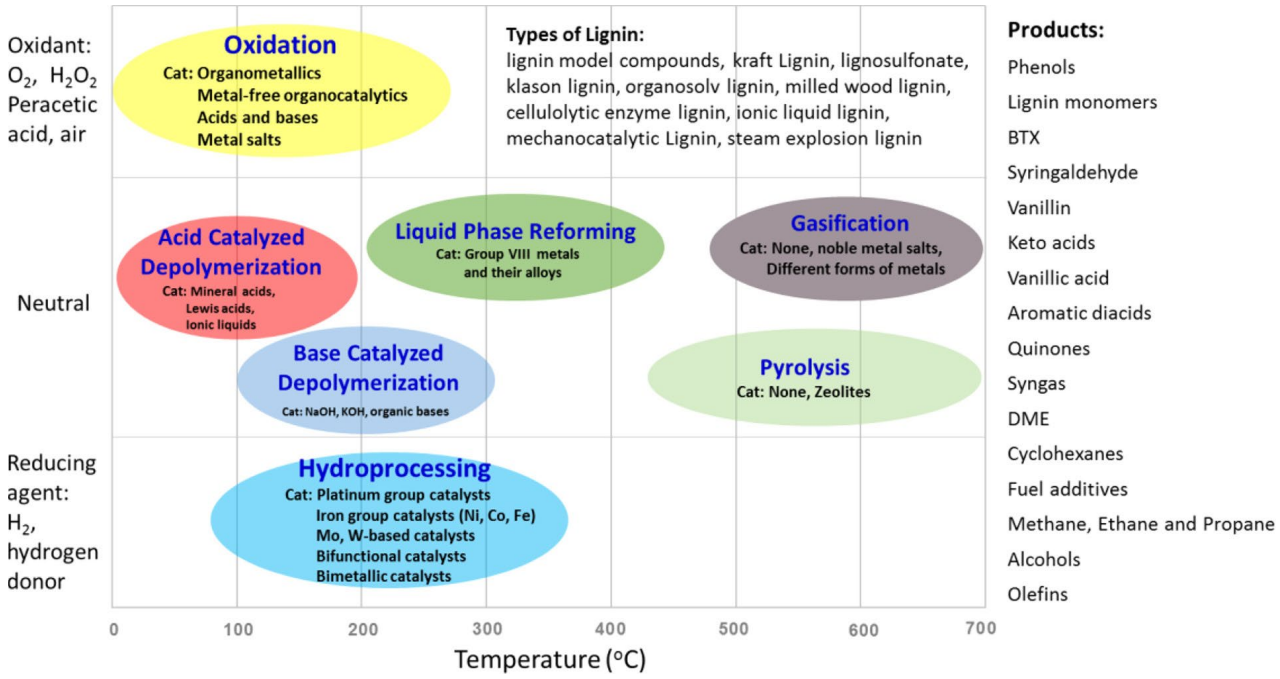

Figure 1.9 Summary of processes for conversion of lignin (abscissa represents the typical temperature range of the lignin conversion processes) [Reprinted by permission American Chemical Society: ACS Chemical Review from Author of Catalytic Transformation of Lignin for the Production of Chemicals and Fuels,[146] Copyright 2015]

1.6 Research Objectives

The current research focuses on utilizing biomass derived from biorefinery processes for synthesizing phenol-formaldehyde and polyurethane resins. Different characterization methods have been employed to examine the detailed chemical structures of biorefinery-derived biomass kraft lignin and bio-oils. The developed biobased polymeric resins have been used to replace traditional polymeric resin in applications such as wood adhesives and functional coatings for fertilizers in the following research objectives.

Chapter 2: Synthesis of Biobased Novolac Phenol-Formaldehyde Wood Adhesives from Biorefinery Derived Lignocellulosic Biomass

In chapter 2 of this dissertation, lignin recovered from kraft biorefinery (L-KB) and two bio-oils prepared from laboratory-scale solvent liquefaction of lignin (BO-SL/L) and fast pyrolysis of pinewood (BO-FP/PW), respectively, have been used to substitute 50% (w/w) of phenol in a novolac phenol−formaldehyde (NPF) resin system. The L-KB, BO-SL/L, and BO-FP/PW molecular structures were characterized via FTIR, $^{13}C-^{1}H$ HSQC 2D-NMR, GCMS, and carbohydrate analysis. The obtained resin adhesive structures were examined by FTIR and ^{1}H NMR spectroscopy, which confirmed the formation of methylene bridges during the resin preparation. Subsequently, DSC analysis was performed to understand the curing behavior of each NPF resin with a hexamethylenetetramine (HMTA) curing agent, which helped optimize the bonding process. Attempts have been made to determine the bonding strength of each developed resin adhesive by tensile shear strength analysis. The objective of the current chapter is to synthesize biobased NPF resins from potential biomass by verifying their functioning as an adhesive.

Chapter 3: Kraft Lignin Functionalization through Periodate Oxidation for the Development of Biobased Novolac Phenol-formaldehyde Resins for Wood-based Panels

In chapter 3 of this dissertation, biobased novolac phenol-formaldehyde (BNPF) resins were developed by partially replacing petroleum-based phenol and formaldehyde with lignin derived from kraft biorefinery and modified kraft biorefinery-derived lignin, respectively. The lignin's chemical modification was performed through the periodate oxidation process using sodium periodate ($NaIO_4$) as an oxidizing agent, aiming to oxidize the aromatic hydroxyl groups in lignin into quinoid groups and further oxidize them into muconic acid. The structure of oxidized lignin

was validated by the FTIR, elemental analysis, solid-state $^{1}H-^{13}C$ 2D HETCOR NMR, and aldehyde content analysis. In addition, the adhesion strength of the adhesive was determined using the tensile shear strength analysis and compared with commercially available lab-made NPF resin. This modification is expected to add new functionality to the lignin structure with the intention of sustainable PF resin wood adhesive, which is the objective of this chapter.

Chapter 4: Application of Hydrothermal Liquified Municipal Sewage Sludge as a Functional Reactive Filler in pMDI Wood Adhesive

In chapter 4 of this dissertation, we explore the possibility of bio-oils derived from the hydrothermal liquefaction (HTL) of municipal sewage sludge at different processing conditions as a natural filler for polymeric methylene diphenyl diisocyanate (pMDI) resin systems for wood adhesive applications. Several characterizations have been performed to analyze the chemical composition of municipal sewage sludge bio-oils. The bonding performance showed that the MSS Bio-oil usage allows pMDI to become a more versatile wood adhesive. This research aims to develop an eco-friendly and economical wood adhesive.

Chapter 5: Non-isothermal Curing Kinetics of Novolac type Phenol-Formaldehyde Resin for 3D Printing of Sustainable Building Design

In chapter 5 of this dissertation, the curing kinetics of the resins synthesized in chapter 1 were investigated, which was aimed to use in 3D printing manufacturing. The curing kinetic analysis of both NPF and BNPF resins cured with hexamethylenetetramine (HMTA) curing agent was studied and assessed using the differential scanning calorimetry (DSC) method. In addition, the thermal curing kinetics were studied through model-fitting, and model-free (iso-conversional)

approaches. This chapter aims to provide valuable curing kinetic information for applying BNPR resins developed from renewable resources, promoting sustainability.

Chapter 6: Biobased Polyurethane Derived from Lignin as a Coating Material for Urea Fertilizer to achieve Controlled Release of Nutrients

In the final chapter of this dissertation, biobased polyurethane was synthesized from lignin as the primary polyol, the most abundant aromatic biopolymer with potential hydroxyl group functionalities. At the same time, DIOL and TRIOL were selected as secondary polyols. At a fixed NCO/OH ratio (1:1), biobased polyurethanes were prepared for coating urea prills from the polyaddition reaction between polyol and isocyanate (p-MDI), with a typical urethane linkage characterized by FTIR. The morphology of the coated fertilizers was examined by SEM analysis. The mechanical properties of the coated particle were determined in terms of crushing strength. The nutrient release behavior of developed coated fertilizers was systematically studied both in water and soil environment. We hope this chapter can offer a sustainable approach by using lignin biomacromolecule to design and develop controlled-release fertilizer with desired nutrient-release properties.

1.7 References

(1) Baekeland, L. H. Original Papers: The Synthesis, Constitution, and Uses of Bakelite. *Ind. Eng. Chem.* **1909**, *1* (3), 149–161. https://doi.org/10.1021/ie50003a004.

(2) Jawerth, M. *Thermoset Resins Using Technical Lignin as a Base Constituent*; 2020.

(3) Patterson, G. D. Materia Polymerica: Bakelite. *ACS Symp. Ser.* **2011**, *1080*, 21–29. https://doi.org/10.1021/bk-2011-1080.ch003.

(4) Hai, T. A. P.; Tessman, M.; Neelakantan, N.; Samoylov, A. A.; Ito, Y.; Rajput, B. S.;

Pourahmady, N.; Burkart, M. D. Renewable Polyurethanes from Sustainable Biological Precursors. *Biomacromolecules* **2021**, *22* (5), 1770–1794. https://doi.org/10.1021/acs.biomac.0c01610.

(5) Sikder, A.; Pearce, A. K.; Parkinson, S. J.; Napier, R.; O'Reilly, R. K. Recent Trends in Advanced Polymer Materials in Agriculture Related Applications. *ACS Applied Polymer Materials*. 2021, pp 1203–1217. https://doi.org/10.1021/acsapm.0c00982.

(6) Morelli, A.; Hawker, M. J. Utilizing Radio Frequency Plasma Treatment to Modify Polymeric Materials for Biomedical Applications. *ACS Biomater. Sci. Eng.* **2021**. https://doi.org/10.1021/acsbiomaterials.0c01673.

(7) Kay, R. *Developments in Reinforced Plastics. 1—Resin Matrix Aspects*; 1981; Vol. 3. https://doi.org/10.1016/0141-3910(81)90028-8.

(8) Mahajan, J. S.; O'Dea, R. M.; Norris, J. B.; Korley, L. S. T. J.; Epps, T. H. Aromatics from Lignocellulosic Biomass: A Platform for High-Performance Thermosets. *ACS Sustain. Chem. Eng.* **2020**, *8* (40), 15072–15096. https://doi.org/10.1021/acssuschemeng.0c04817.

(9) Sztorch, B.; Brząkalski, D.; Pakuła, D.; Frydrych, M.; Špitalský, Z.; Przekop, R. E. Natural and Synthetic Polymer Fillers for Applications in 3D Printing—FDM Technology Area. *Solids* **2022**, *3* (3), 508–548. https://doi.org/10.3390/solids3030034.

(10) Dwivedi, P.; Singh, K.; Chaudhary, K.; Mangal, R. Biomimetic Polymer Adhesives. *ACS Appl. Polym. Mater.* **2022**, *4* (7), 4588–4608. https://doi.org/10.1021/acsapm.1c01285.

(11) Critchlow, G. W.; Litchfield, R. E.; Sutherland, I.; Grandy, D. B.; Wilson, S. A Review and Comparative Study of Release Coatings for Optimised Abhesion in Resin Transfer Moulding Applications. *Int. J. Adhes. Adhes.* **2006**, *26* (8), 577–599.

https://doi.org/10.1016/j.ijadhadh.2005.09.003.

(12) Cudjoe, E.; Herbert, K. M.; Rowan, S. J. Strong, Rebondable, Dynamic Cross-Linked Cellulose Nanocrystal Polymer Nanocomposite Adhesives. *ACS Applied Materials and Interfaces*. 2018, pp 30723–30731. https://doi.org/10.1021/acsami.8b10520.

(13) Dinte, E.; Sylvester, B. Adhesives: Applications and Recent Advances. *Appl. Adhes. Bond. Sci. Technol.* **2018**. https://doi.org/10.5772/intechopen.71854.

(14) Lacoste, C.; El Hage, R.; Bergeret, A.; Corn, S.; Lacroix, P. Sodium Alginate Adhesives as Binders in Wood Fibers/Textile Waste Fibers Biocomposites for Building Insulation. *Carbohydr. Polym.* **2018**, *184* (December 2017), 1–8. https://doi.org/10.1016/j.carbpol.2017.12.019.

(15) Al-Moghazy, M.; Mahmoud, M.; Nada, A. A. Fabrication of Cellulose-Based Adhesive Composite as an Active Packaging Material to Extend the Shelf Life of Cheese. *Int. J. Biol. Macromol.* **2020**, *160*, 264–275. https://doi.org/10.1016/j.ijbiomac.2020.05.217.

(16) Wang, C.; Yusufu, D.; Mills, A. A Smart Adhesive “consume within” (CW) Indicator for Food Packaging. *Food Packag. Shelf Life* **2019**, *22* (September), 100395. https://doi.org/10.1016/j.fpsl.2019.100395.

(17) Scarselli, G.; Corcione, C.; Nicassio, F.; Maffezzoli, A. Adhesive Joints with Improved Mechanical Properties for Aerospace Applications. *Int. J. Adhes. Adhes.* **2017**, *75* (March), 174–180. https://doi.org/10.1016/j.ijadhadh.2017.03.012.

(18) Ciardiello, R.; Belingardi, G.; Martorana, B.; Brunella, V. Physical and Mechanical Properties of a Reversible Adhesive for Automotive Applications. *Int. J. Adhes. Adhes.* **2019**, *89* (December 2018), 117–128. https://doi.org/10.1016/j.ijadhadh.2018.12.005.

(19) Nam, S.; Mooney, D. Polymeric Tissue Adhesives. *Chem. Rev.* **2021**, *121* (18), 11336–

11384. https://doi.org/10.1021/acs.chemrev.0c00798.

(20) Ayyıldız, S. N.; Ayyıldız, A. Cyanoacrylic Tissue Glues: Biochemical Properties and Their Usage in Urology. *Turk Urol. Derg.* **2017**, *43* (1), 14–24. https://doi.org/10.5152/tud.2017.09465.

(21) Imam, S. H.; Bilbao-Sainz, C.; Chiou, B. Sen; Glenn, G. M.; Orts, W. J. Biobased Adhesives, Gums, Emulsions, and Binders: Current Trends and Future Prospects. *J. Adhes. Sci. Technol.* **2013**, *27* (18–19), 1972–1997. https://doi.org/10.1080/01694243.2012.696892.

(22) Liu, X.; Shi, L.; Wan, X.; Dai, B.; Chen, Y.; Wang, S. Recent Progress of Spider-Silk-Inspired Adhesive Materials. *ACS Materials Letters*. 2021, pp 1453–1467. https://doi.org/10.1021/acsmaterialslett.1c00378.

(23) Tian, Y.; Huang, X.; Cheng, Y.; Niu, Y.; Ma, J.; Zhao, Y.; Kou, X.; Ke, Q. Applications of Adhesives in Textiles: A Review. *Eur. Polym. J.* **2022**, *167* (December 2021), 111089. https://doi.org/10.1016/j.eurpolymj.2022.111089.

(24) Zhang, B.; Chen, S.; Wang, W.; Tian, M.; Ning, N.; Zhang, L. Polyester (PET) Fabrics Coated with Environmentally Friendly Adhesive and Its Interface Structure and Adhesive Properties with Rubber. *Compos. Sci. Technol.* **2020**, *195* (December 2019), 108171. https://doi.org/10.1016/j.compscitech.2020.108171.

(25) Pukale, D. D.; Bansode, A. S.; Pinjari, D. V.; Sayed, U.; Kulkarni, R. R. Development of Nanoemulsion of Silicone Oil and Pine Oil Using Binary Surfactant System for Textile Finishing. *J. Surfactants Deterg.* **2017**, *20* (5), 1061–1073. https://doi.org/10.1007/s11743-017-1970-8.

(26) Pukale, D. D.; Bansode, A. S.; Pinjari, D. V.; Kulkarni, R. R.; Sayed, U. Application of

Silicone Surfactant Along with Hydrocarbon Surfactants to Textile Washing for the Removal of Different Complex Stains. *J. Surfactants Deterg.* **2017**, *20* (1), 287–295. https://doi.org/10.1007/s11743-016-1901-0.

(27) Bansode, A. S.; Pukale, D. D.; Jadhav, N. L.; Sayed, U.; Pinjari, D. V. Sonochemical Enzymatic Esterification of Oleic Acid and Tri-Ethanolamine for a Fabric Softener in Textile Application. *Chem. Eng. Process. - Process Intensif.* **2019**, *137* (February), 128–136. https://doi.org/10.1016/j.cep.2019.02.013.

(28) Pukale, D. D.; Bansode, A. S.; Jadhav, N. L.; Pinjari, D. V; Kulkarni, R. R. Review on Silicone Surfactants: Silicone-Based Gemini Surfactants, Physicochemical Properties and Applications. *Tenside Surfactants Deterg.* **2019**, *56* (4), 268–278. https://doi.org/10.3139/113.110617.

(29) Frick, N. H.; Gerhart, H. L.; Gilbert, H. E.; Parker, E. E. *Polymer Coatings*; 1969; Vol. 61. https://doi.org/10.1021/ie50716a010.

(30) Lyu, Q.; Hsueh, N.; Chai, C. L. L. The Chemistry of Bioinspired Catechol(Amine)-Based Coatings. *ACS Biomater. Sci. Eng.* **2019**, *5* (6), 2708–2724. https://doi.org/10.1021/acsbiomaterials.9b00281.

(31) Barroso, G.; Li, Q.; Bordia, R. K.; Motz, G. Polymeric and Ceramic Silicon-Based Coatings-a Review. *J. Mater. Chem. A* **2019**, *7* (5), 1936–1963. https://doi.org/10.1039/c8ta09054h.

(32) Upadhyay, R. K.; Kumar, A. Micro-Indentation Studies of Polymers. *Encycl. Mater. Plast. Polym.* **2022**, *2* (2013), 928–937. https://doi.org/10.1016/b978-0-12-820352-1.00104-8.

(33) Wagle, P. G.; Tamboli, S. S.; More, A. P. Peelable Coatings: A Review. *Prog. Org.*

Coatings **2021**, *150* (August 2020), 106005. https://doi.org/10.1016/j.porgcoat.2020.106005.

(34) Mitra, D.; Kang, E. T.; Neoh, K. G. Polymer-Based Coatings with Integrated Antifouling and Bactericidal Properties for Targeted Biomedical Applications. *ACS Applied Polymer Materials*. 2021, pp 2233–2263. https://doi.org/10.1021/acsapm.1c00125.

(35) Wang, C.; Brown, G. O.; Burris, D. L.; Korley, L. S. T. J.; Epps, T. H. Coating Architects: Manipulating Multiscale Structures to Optimize Interfacial Properties for Coating Applications. *ACS Appl. Polym. Mater.* **2019**, *1* (9), 2249–2266. https://doi.org/10.1021/acsapm.9b00302.

(36) Ates, M. A Review on Conducting Polymer Coatings for Corrosion Protection. *J. Adhes. Sci. Technol.* **2016**, *30* (14), 1510–1536. https://doi.org/10.1080/01694243.2016.1150662.

(37) Andreeva, D. V.; Fix, D.; Möhwald, H.; Shchukin, D. G. Self-Healing Anticorrosion Coatings Based on PH-Sensitive Polyelectrolyte/Inhibitor Sandwichlike Nanostructures. *Adv. Mater.* **2008**, *20* (14), 2789–2794. https://doi.org/10.1002/adma.200800705.

(38) Chang, C. H.; Huang, T. C.; Peng, C. W.; Yeh, T. C.; Lu, H. I.; Hung, W. I.; Weng, C. J.; Yang, T. I.; Yeh, J. M. Novel Anticorrosion Coatings Prepared from Polyaniline/Graphene Composites. *Carbon N. Y.* **2012**, *50* (14), 5044–5051. https://doi.org/10.1016/j.carbon.2012.06.043.

(39) Cho, S. H.; White, S. R.; Braun, P. V. Self-Healing Polymer Coatings. *Adv. Mater.* **2009**, *21* (6), 645–649. https://doi.org/10.1002/adma.200802008.

(40) van Benthem, R. A. T. M.; Ming, W. (Marshall); de With, G. (Bert). Self Healing Polymer Coatings. *Springer Ser. Mater. Sci.* **2007**, *100*, 139–159. https://doi.org/10.1007/978-1-4020-6250-6_7.

(41) Howarter, J. A.; Youngblood, J. P. Self-Cleaning and next Generation Anti-Fog Surfaces and Coatings. *Macromol. Rapid Commun.* **2008**, *29* (6), 455–466. https://doi.org/10.1002/marc.200700733.

(42) Cebeci, F. Ç.; Wu, Z.; Zhai, L.; Cohen, R. E.; Rubner, M. F. Nanoporosity-Driven Superhydrophilicity: A Means to Create Multifunctional Antifogging Coatings. *Langmuir* **2006**, *22* (6), 2856–2862. https://doi.org/10.1021/la053182p.

(43) Tahk, D.; Kim, T. Il; Yoon, H.; Choi, M.; Shin, K.; Suh, K. Y. Fabrication of Antireflection and Antifogging Polymer Sheet by Partial Photopolymerization and Dry Etching. *Langmuir* **2010**, *26* (4), 2240–2243. https://doi.org/10.1021/la904768e.

(44) Zhao, J.; Ma, L.; Millians, W.; Wu, T.; Ming, W. Dual-Functional Antifogging/Antimicrobial Polymer Coating. *ACS Appl. Mater. Interfaces* **2016**, *8* (13), 8737–8742. https://doi.org/10.1021/acsami.6b00748.

(45) Li, J.; Zhao, Y.; Hu, J.; Shu, L.; Shi, X. Anti-Icing Performance of a Superhydrophobic PDMS/Modified Nano-Silica Hybrid Coating for Insulators. *J. Adhes. Sci. Technol.* **2012**, *26* (4–5), 665–679. https://doi.org/10.1163/016942411X574826.

(46) Peng, C.; Xing, S.; Yuan, Z.; Xiao, J.; Wang, C.; Zeng, J. Preparation and Anti-Icing of Superhydrophobic PVDF Coating on a Wind Turbine Blade. *Appl. Surf. Sci.* **2012**, *259*, 764–768. https://doi.org/10.1016/j.apsusc.2012.07.118.

(47) Banerjee, I.; Pangule, R. C.; Kane, R. S. Antifouling Coatings: Recent Developments in the Design of Surfaces That Prevent Fouling by Proteins, Bacteria, and Marine Organisms. *Adv. Mater.* **2011**, *23* (6), 690–718. https://doi.org/10.1002/adma.201001215.

(48) Chambers, L. D.; Stokes, K. R.; Walsh, F. C.; Wood, R. J. K. Modern Approaches to Marine Antifouling Coatings. *Surf. Coatings Technol.* **2006**, *201* (6), 3642–3652.

https://doi.org/10.1016/j.surfcoat.2006.08.129.

(49) Das, S.; Kumar, S.; Samal, S. K.; Mohanty, S.; Nayak, S. K. A Review on Superhydrophobic Polymer Nanocoatings: Recent Development and Applications. *Ind. Eng. Chem. Res.* **2018**, *57* (8), 2727–2745. https://doi.org/10.1021/acs.iecr.7b04887.

(50) Xue, Z.; Liu, M.; Jiang, L. Recent Developments in Polymeric Superoleophobic Surfaces. *J. Polym. Sci. Part B Polym. Phys.* **2012**, *50* (17), 1209–1224. https://doi.org/10.1002/polb.23115.

(51) Charitidis, C.; Laskarakis, A.; Kassavetis, S.; Gravalidis, C.; Logothetidis, S. Optical and Nanomechanical Study of Anti-Scratch Layers on Polycarbonate Lenses. *Superlattices Microstruct.* **2004**, *36* (1–3), 171–179. https://doi.org/10.1016/j.spmi.2004.08.015.

(52) Joo, W.; Kim, Y.; Jang, S.; Kim, J. K. Antireflection Coating with Enhanced Anti-Scratch Property from Nanoporous Block Copolymer Template. *Thin Solid Films* **2011**, *519* (11), 3804–3808. https://doi.org/10.1016/j.tsf.2011.01.107.

(53) Tsibouklis, J.; Stone, M.; A. Thorpe, A.; Graham, P.; Nevell, T. G.; Ewen, R. J. Inhibiting Bacterial Adhesion onto Surfaces: The Non-Stick Coating Approach. *Int. J. Adhes. Adhes.* **2000**, *20* (2), 91–96. https://doi.org/10.1016/S0143-7496(99)00034-2.

(54) Siepmann, F.; Siepmann, J.; Walther, M.; MacRae, R. J.; Bodmeier, R. Polymer Blends for Controlled Release Coatings. *J. Control. Release* **2008**, *125* (1), 1–15. https://doi.org/10.1016/j.jconrel.2007.09.012.

(55) Zhang, S.; Yang, Y.; Gao, B.; Li, Y. C.; Liu, Z. Superhydrophobic Controlled-Release Fertilizers Coated with Bio-Based Polymers with Organosilicon and Nano-Silica Modifications. *J. Mater. Chem. A* **2017**, *5* (37), 19943–19953. https://doi.org/10.1039/c7ta06014a.

(56) Tian, H.; Liu, Z.; Zhang, M.; Guo, Y.; Zheng, L.; Li, Y. C. Biobased Polyurethane, Epoxy Resin, and Polyolefin Wax Composite Coating for Controlled-Release Fertilizer. *ACS Appl. Mater. Interfaces* **2019**, *11* (5), 5380–5392. https://doi.org/10.1021/acsami.8b16030.

(57) Yang, Y. C.; Zhang, M.; Li, Y.; Fan, X. H.; Geng, Y. Q. Improving the Quality of Polymer-Coated Urea with Recycled Plastic, Proper Additives, and Large Tablets. *J. Agric. Food Chem.* **2012**, *60* (45), 11229–11237. https://doi.org/10.1021/jf302813g.

(58) Sanchez-Rexach, E.; Johnston, T. G.; Jehanno, C.; Sardon, H.; Nelson, A. Sustainable Materials and Chemical Processes for Additive Manufacturing. *Chem. Mater.* **2020**, *32* (17), 7105–7119. https://doi.org/10.1021/acs.chemmater.0c02008.

(59) Ligon, S. C.; Liska, R.; Stampfl, J.; Gurr, M.; Mülhaupt, R. Polymers for 3D Printing and Customized Additive Manufacturing. *Chem. Rev.* **2017**, *117* (15), 10212–10290. https://doi.org/10.1021/acs.chemrev.7b00074.

(60) Xu, W.; Jambhulkar, S.; Zhu, Y.; Ravichandran, D.; Kakarla, M.; Vernon, B.; Lott, D. G.; Cornella, J. L.; Shefi, O.; Miquelard-Garnier, G.; Yang, Y.; Song, K. 3D Printing for Polymer/Particle-Based Processing: A Review. *Compos. Part B Eng.* **2021**, *223* (June), 109102. https://doi.org/10.1016/j.compositesb.2021.109102.

(61) Bagheri, A.; Jin, J. Photopolymerization in 3D Printing. *ACS Appl. Polym. Mater.* **2019**, *1* (4), 593–611. https://doi.org/10.1021/acsapm.8b00165.

(62) Mu, X.; Bertron, T.; Dunn, C.; Qiao, H.; Wu, J.; Zhao, Z.; Saldana, C.; Qi, H. J. Porous Polymeric Materials by 3D Printing of Photocurable Resin. *Mater. Horizons* **2017**, *4* (3), 442–449. https://doi.org/10.1039/c7mh00084g.

(63) Ishutov, S.; Hasiuk, F. J.; Jobe, D.; Agar, S. Using Resin-Based 3D Printing to Build Geometrically Accurate Proxies of Porous Sedimentary Rocks. *Groundwater* **2018**, *56* (3),

482–490. https://doi.org/10.1111/gwat.12601.

(64) Wang, B.; Zhang, Z.; Pei, Z.; Qiu, J.; Wang, S. Current Progress on the 3D Printing of Thermosets. *Adv. Compos. Hybrid Mater.* **2020**, *3* (4), 462–472. https://doi.org/10.1007/s42114-020-00183-z.

(65) Ravichandran, D.; Xu, W.; Jambhulkar, S.; Zhu, Y.; Kakarla, M.; Bawareth, M.; Song, K. Intrinsic Field-Induced Nanoparticle Assembly in Three-Dimensional (3D) Printing Polymeric Composites. *ACS Appl. Mater. Interfaces* **2021**, *13* (44), 52274–52294. https://doi.org/10.1021/acsami.1c12763.

(66) Arefin, A. M. E.; Khatri, N. R.; Kulkarni, N.; Egan, P. F. Polymer 3D Printing Review: Materials, Process, and Design Strategies for Medical Applications. *Polymers (Basel).* **2021**, *13* (9), 1–24. https://doi.org/10.3390/polym13091499.

(67) Shahzadi, L.; Maya, F.; Breadmore, M. C.; Thickett, S. C. Functional Materials for DLP-SLA 3D Printing Using Thiol-Acrylate Chemistry: Resin Design and Postprint Applications. *ACS Appl. Polym. Mater.* **2022**. https://doi.org/10.1021/acsapm.2c00358.

(68) Black, H. T.; Celina, M. C.; Mcelhanon, J. R. Additive Manufacturing of Polymers : Materials Opportunities and Emerging Applications. *Sandia Natl. Lab.* **2016**, No. April, 40.

(69) Poliskie, M.; Poliskie, M. *Introduction to Polymers*; 2011. https://doi.org/10.1201/b10941-1.

(70) Valdez, D.; Nagy, E. *Analyses/Testing*; 2010. https://doi.org/10.1007/978-3-642-04714-5_5.

(71) Milazzo, M.; Amoresano, A.; Pasquino, R.; Grizzuti, N.; Auriemma, F.; De Stefano, F.; Sin Xicola, A.; Iodice, V.; De Rosa, C. Curing Efficiency of Novolac-Type Phenol–

Formaldehyde Resins from Viscoelastic Properties. *Macromolecules* **2021**, *54* (24), 11372–11383. https://doi.org/10.1021/acs.macromol.1c01598.

(72) Gibson, G. *Epoxy Resins*; 2017. https://doi.org/10.1016/B978-0-323-35824-8.00027-X.

(73) Upton, B. M.; Kasko, A. M. Strategies for the Conversion of Lignin to High-Value Polymeric Materials: Review and Perspective. *Chem. Rev.* **2016**, *116* (4), 2275–2306. https://doi.org/10.1021/acs.chemrev.5b00345.

(74) Lin, C. C.; Teng, H. Influence of the Formaldehyde-to-Phenol Ratio in Resin Synthesis on the Production of Activated Carbons from Phenol-Formaldehyde Resins. *Ind. Eng. Chem. Res.* **2002**, *41* (8), 1986–1992. https://doi.org/10.1021/ie010610n.

(75) Ismail, M. F.; Hawa, A. *Phenolic Polymers Based Composite Materials*; 2021. https://doi.org/10.1007/978-981-15-8932-4.

(76) Liang, C.; Gracida-Alvarez, U. R.; Gallant, E. T.; Gillis, P. A.; Marques, Y. A.; Abramo, G. P.; Hawkins, T. R.; Dunn, J. B. Material Flows of Polyurethane in the United States. *Environ. Sci. Technol.* **2021**, *55* (20), 14215–14224. https://doi.org/10.1021/acs.est.1c03654.

(77) Mehravar, S.; Ballard, N.; Tomovska, R.; Asua, J. M. Polyurethane/Acrylic Hybrid Waterborne Dispersions: Synthesis, Properties and Applications. *Ind. Eng. Chem. Res.* **2019**, *58* (46), 20902–20922. https://doi.org/10.1021/acs.iecr.9b02324.

(78) Wu, X.; Wu, J.; Mu, C.; Wang, C.; Lin, W. Advances in Antimicrobial Polymer Coatings in the Leather Industry: A Comprehensive Review. *Ind. Eng. Chem. Res.* **2021**, *60* (42), 15004–15018. https://doi.org/10.1021/acs.iecr.1c02600.

(79) Wang, Y.; Chen, G.; Zhang, H.; Zhao, C.; Sun, L.; Zhao, Y. Emerging Functional Biomaterials as Medical Patches. *ACS Nano*. 2021, pp 5977–6007.

https://doi.org/10.1021/acsnano.0c10724.

(80) Wazarkar, K.; Kathalewar, M.; Sabnis, A. Reactive Modification of Thermoplastic and Thermoset Polymers Using Flame Retardants: An Overview. *Polymer - Plastics Technology and Engineering*. 2016, pp 71–91. https://doi.org/10.1080/03602559.2015.1038839.

(81) Singh, M.; Kadian, S.; Manik, G. Polymers in Adhesive Applications. *Encycl. Mater. Plast. Polym.* **2022**, *4*, 370–381. https://doi.org/10.1016/b978-0-12-820352-1.00124-3.

(82) Yadav, A.; Souza, F. M. De; Dawsey, T.; Gupta, R. K. Recent Advancements in Flame-Retardant Polyurethane Foams : A Review. *Ind. Eng. Chem. Res.* **2022**.

(83) Rudlong, A. M.; Koga, Y. T.; Goddard, J. M. Advances in Nonfouling and Antimicrobial Coatings: Perspectives for the Food Industry. *ACS Food Sci. Technol.* **2022**, *2* (9), 1401–1416. https://doi.org/10.1021/acsfoodscitech.2c00148.

(84) Akindoyo, J. O.; Beg, M. D. H.; Ghazali, S.; Islam, M. R.; Jeyaratnam, N.; Yuvaraj, A. R. Polyurethane Types, Synthesis and Applications-a Review. *RSC Adv.* **2016**, *6* (115), 114453–114482. https://doi.org/10.1039/c6ra14525f.

(85) Jin, F. L.; Li, X.; Park, S. J. Synthesis and Application of Epoxy Resins: A Review. *J. Ind. Eng. Chem.* **2015**, *29*, 1–11. https://doi.org/10.1016/j.jiec.2015.03.026.

(86) Myers, R. R. *Epoxy Resins: Chemistry and Technology*; 1974; Vol. 49. https://doi.org/10.1016/0021-9797(74)90319-1.

(87) Auvergne, R.; Caillol, S.; David, G.; Boutevin, B.; Pascault, J. P. Biobased Thermosetting Epoxy: Present and Future. *Chem. Rev.* **2014**, *114* (2), 1082–1115. https://doi.org/10.1021/cr3001274.

(88) Salunke, A.; Sasidharan, S.; Gopinathapanicker, J. C.; Kandasubramanian, B.; Anand, A.

Cyanate Ester Epoxy Blends for Structural and Functional Composites. *Ind. Eng. Chem. Res.* **2021**, *60* (8), 3260–3277. https://doi.org/10.1021/acs.iecr.0c05008.

(89) Gibson, G. Epoxy Resins. *Brydson's Plast. Mater. Eighth Ed.* **2017**, 773–797. https://doi.org/10.1016/B978-0-323-35824-8.00027-X.

(90) Capricho, J. C.; Fox, B.; Hameed, N. Multifunctionality in Epoxy Resins. *Polym. Rev.* **2020**, *60* (1), 1–41. https://doi.org/10.1080/15583724.2019.1650063.

(91) Saba, N.; Jawaid, M.; Alothman, O. Y.; Paridah, M. T.; Hassan, A. Recent Advances in Epoxy Resin, Natural Fiber-Reinforced Epoxy Composites and Their Applications. *J. Reinf. Plast. Compos.* **2016**, *35* (6), 447–470. https://doi.org/10.1177/0731684415618459.

(92) Yang, K.; Wu, S.; Guan, J.; Shao, Z.; Ritchie, R. O. Enhancing the Mechanical Toughness of Epoxy-Resin Composites Using Natural Silk Reinforcements. *Sci. Rep.* **2017**, *7* (1), 1–9. https://doi.org/10.1038/s41598-017-11919-1.

(93) Peerzada, M.; Abbasi, S.; Lau, K. T.; Hameed, N. Additive Manufacturing of Epoxy Resins: Materials, Methods, and Latest Trends. *Ind. Eng. Chem. Res.* **2020**, *59* (14), 6375–6390. https://doi.org/10.1021/acs.iecr.9b06870.

(94) Riemenschneider, W.; Bolt, H. M. Epoxy Resins. *Ullmann's Encycl. Ind. Chem.* **2005**, *13*. https://doi.org/10.1002/14356007.a09_565.pub2.

(95) Jalal Uddin, A. Coatings for Technical Textile Yarns. *Tech. Text. Yarns* **2010**, 140–184. https://doi.org/10.1533/9781845699475.1.140.

(96) Saunders, K. J. *Organic Polymer Chemistry*; 1973. https://doi.org/10.1007/978-94-017-2504-0.

(97) Gaytán, I.; Burelo, M.; Loza-Tavera, H. Current Status on the Biodegradability of Acrylic Polymers: Microorganisms, Enzymes and Metabolic Pathways Involved. *Applied*

Microbiology and Biotechnology. 2021, pp 991–1006. https://doi.org/10.1007/s00253-020-11073-1.

(98) Maiti, T. K.; Parvate, S.; Pragya; Singh, J.; Dixit, P.; Bhuvanesh, E.; Vennapusa, J. R.; Chattopadhyay, S. Plastics in Coating Applications. *Encycl. Mater. Plast. Polym.* **2022**, *4*, 126–135. https://doi.org/10.1016/b978-0-12-820352-1.00176-0.

(99) Gerhart, H. THERMOSETTING ACRYLIC RESINS Introduction. *Industrial & Engineering Chemistry*. 1961, pp 458–459. https://doi.org/10.1021/ie50618a028.

(100) Joseph, P.; Ebdon, J. R. *Recent Developments in Flame-Retarding Thermoplastics and Thermosets*; Woodhead Publishing Ltd, 2001. https://doi.org/10.1533/9781855737464.220.

(101) Cheng, W.; Wu, D.; Liu, Y. Michael Addition Polymerization of Trifunctional Amine and Acrylic Monomer: A Versatile Platform for Development of Biomaterials. *Biomacromolecules* **2016**, *17* (10), 3115–3126. https://doi.org/10.1021/acs.biomac.6b01043.

(102) Foyer, G.; Barriol, M.; Negrell, C.; Caillol, S.; David, G.; Boutevin, B. Aldehyde Functional Monomer as Efficient Cross-Linkable Comonomer with Biobased Phenols in Acrylic Coatings. *Prog. Org. Coatings* **2015**, *84*, 1–8. https://doi.org/10.1016/j.porgcoat.2015.02.006.

(103) Ebnesajjad, S. *Characteristics of Adhesive Materials*; Elsevier Inc., 2011. https://doi.org/10.1016/B978-1-4377-4461-3.10008-2.

(104) Bramhecha, I.; Sheikh, J. Development of Sustainable Citric Acid-Based Polyol to Synthesize Waterborne Polyurethane for Antibacterial and Breathable Waterproof Coating of Cotton Fabric. *Industrial and Engineering Chemistry Research*. 2019, pp 21252–21261.

https://doi.org/10.1021/acs.iecr.9b05195.

(105) Sardon, H.; Mecerreyes, D.; Basterretxea, A.; Avérous, L.; Jehanno, C. From Lab to Market: Current Strategies for the Production of Biobased Polyols. *ACS Sustain. Chem. Eng.* **2021**, *9* (32), 10664–10677. https://doi.org/10.1021/acssuschemeng.1c02361.

(106) Nagalakshmaiah, M.; Afrin, S.; Malladi, R. P.; Elkoun, S.; Robert, M.; Ansari, M. A.; Svedberg, A.; Karim, Z. Biocomposites: Present Trends and Challenges for the Future. *Green Compos. Automot. Appl.* **2018**, 197–215. https://doi.org/10.1016/B978-0-08-102177-4.00009-4.

(107) Geyer, R.; Jambeck, J. R.; Law, K. L. Production, Use, and Fate of All Plastics Ever Made. *Sci. Adv.* **2017**, *3* (7), 25–29. https://doi.org/10.1126/sciadv.1700782.

(108) Schneiderman, D. K.; Hillmyer, M. A. 50th Anniversary Perspective: There Is a Great Future in Sustainable Polymers. *Macromolecules* **2017**, *50* (10), 3733–3749. https://doi.org/10.1021/acs.macromol.7b00293.

(109) Zheng, J.; Suh, S. Strategies to Reduce the Global Carbon Footprint of Plastics. *Nature Climate Change*. 2019, pp 374–378. https://doi.org/10.1038/s41558-019-0459-z.

(110) The International Council On Clean Transportation. An Introduction To Petroleum Refining and the Production of Ultra Low Sulfur Gasoline. *Energy Econ. Appl. Optim.* **2011**, 1–38.

(111) Shah, N. K.; Li, Z.; Ierapetritou, M. G. Petroleum Refining Operations: Key Issues, Advances, and Opportunities. *Ind. Eng. Chem. Res.* **2011**, *50* (3), 1161–1170. https://doi.org/10.1021/ie1010004.

(112) Lucas, E. F.; Mansur, C. R. E.; Spinelli, L.; Queirós, Y. G. C. Polymer Science Applied to Petroleum Production. *Pure Appl. Chem.* **2009**, *81* (3), 473–494.

https://doi.org/10.1351/PAC-CON-08-07-21.

(113) Goud, D.; Gupta, R.; Maligal-Ganesh, R.; Peter, S. C. Review of Catalyst Design and Mechanistic Studies for the Production of Olefins from Anthropogenic CO2. *ACS Catalysis*. 2020, pp 14258–14282. https://doi.org/10.1021/acscatal.0c03799.

(114) Bojkovic, A.; Vermeire, F. H.; Kuzmanović, M.; Dao Thi, H.; Van Geem, K. M. Analytics Driving Kinetics: Advanced Mass Spectrometric Characterization of Petroleum Products. *Energy and Fuels* **2022**, *36* (1), 6–59. https://doi.org/10.1021/acs.energyfuels.1c02355.

(115) Corma, A.; Corresa, E.; Mathieu, Y.; Sauvanaud, L.; Al-Bogami, S.; Al-Ghrami, M. S.; Bourane, A. Crude Oil to Chemicals: Light Olefins from Crude Oil. *Catal. Sci. Technol.* **2017**, *7* (1), 12–46. https://doi.org/10.1039/c6cy01886f.

(116) Artetxe, M.; Lopez, G.; Elordi, G.; Amutio, M.; Bilbao, J.; Olazar, M. Production of Light Olefins from Polyethylene in a Two-Step Process: Pyrolysis in a Conical Spouted Bed and Downstream High-Temperature Thermal Cracking. *Ind. Eng. Chem. Res.* **2012**, *51* (43), 13915–13923. https://doi.org/10.1021/ie300178e.

(117) Gholami, Z.; Gholami, F.; Tišler, Z.; Tomas, M.; Vakili, M. A Review on Production of Light Olefins via Fluid Catalytic Cracking. *Energies* **2021**, *14* (4), 1–36. https://doi.org/10.3390/en14041089.

(118) EGLOFF, G.; ALEXANDER, M.; ZIMMER, C. Commercial Development of Hydrocarbons From Petroleum and Natural Gas. **1954**, 360–369. https://doi.org/10.1021/ba-1954-0010.ch038.

(119) Pasch, H.; Schrod, M. Preparation and Analysis of Phenol-Formaldehyde Resins by High-Throughput Techniques. *Macromol. Rapid Commun.* **2004**, *25* (1), 224–230. https://doi.org/10.1002/marc.200300145.

(120) Campo, E. A. Polymeric Materials and Properties. In *Selection of Polymeric Materials*; Elsevier, 2008; pp 1–39. https://doi.org/10.1016/b978-081551551-7.50003-6.

(121) Soni, V. K.; Singh, G.; Vijayan, B. K.; Chopra, A.; Kapur, G. S.; Ramakumar, S. S. V. Thermochemical Recycling of Waste Plastics by Pyrolysis: A Review. *Energy and Fuels* **2021**, *35* (16), 12763–12808. https://doi.org/10.1021/acs.energyfuels.1c01292.

(122) Schwartz, B. S.; Parker, C. L.; Hess, J.; Frumkin, H. Public Health and Medicine in an Age of Energy Scarcity: The Case of Petroleum. *Am. J. Public Health* **2011**, *101* (9), 1560–1567. https://doi.org/10.2105/AJPH.2010.205187.

(123) Makhdoum, H.; Pouransari, Z. Analytical Study of Iran Nonrenewable Energy Resources Using Hubbert Theory. *ACS Omega* **2022**, *7* (2), 1772–1784. https://doi.org/10.1021/acsomega.1c04696.

(124) Robbins, Lord. An Essay on the Nature and Significance of Economic Science. *An Essay Nat. Significance Econ. Sci.* **1984**. https://doi.org/10.1007/978-1-349-17510-9.

(125) Kirsch, S. Running out? Rethinking Resource Depletion. *Extr. Ind. Soc.* **2020**, *7* (3), 838–840. https://doi.org/10.1016/j.exis.2020.06.002.

(126) Fagnani, D. E.; Tami, J. L.; Copley, G.; Clemons, M. N.; Getzler, Y. D. Y. L.; McNeil, A. J. 100th Anniversary of Macromolecular Science Viewpoint: Redefining Sustainable Polymers. *ACS Macro Lett.* **2021**, *10* (1), 41–53. https://doi.org/10.1021/acsmacrolett.0c00789.

(127) Tripathi, N.; Misra, M.; Mohanty, A. K. Durable Polylactic Acid (PLA)-Based Sustainable Engineered Blends and Biocomposites: Recent Developments, Challenges, and Opportunities. *ACS Eng. Au* **2021**, *1* (1), 7–38. https://doi.org/10.1021/acsengineeringau.1c00011.

(128) Fortman, D. J.; Brutman, J. P.; De Hoe, G. X.; Snyder, R. L.; Dichtel, W. R.; Hillmyer, M. A. Approaches to Sustainable and Continually Recyclable Cross-Linked Polymers. *ACS Sustain. Chem. Eng.* **2018**, *6* (9), 11145–11159. https://doi.org/10.1021/acssuschemeng.8b02355.

(129) Jiang, H.; Zhang, Y.; Wang, H. Surface Reactions in Selective Modification: The Prerequisite for Plastic Flotation. *Environ. Sci. Technol.* **2020**, *54* (16), 9742–9756. https://doi.org/10.1021/acs.est.9b07861.

(130) Rosenboom, J. G.; Langer, R.; Traverso, G. Bioplastics for a Circular Economy. *Nat. Rev. Mater.* **2022**, *7* (2), 117–137. https://doi.org/10.1038/s41578-021-00407-8.

(131) Sardon, H.; Dove, A. P. Plastics Recycling with a Difference. *Science (80-.).* **2018**, *360* (6387), 380–381. https://doi.org/10.1126/science.aat4997.

(132) Flores, J.; Laura Cunico, M.; Rodriguez, M. A.; Vecchietti, A. Optimizing the Energy Production Infrastructure Considering Uncertainty in Fossil Resource Availability. *Ind. Eng. Chem. Res.* **2014**, *53* (44), 16984–17001. https://doi.org/10.1021/ie500459a.

(133) Cabernard, L.; Pfister, S.; Oberschelp, C.; Hellweg, S. Growing Environmental Footprint of Plastics Driven by Coal Combustion. *Nature Sustainability*. 2022, pp 139–148. https://doi.org/10.1038/s41893-021-00807-2.

(134) Awodumi, O. B.; Adewuyi, A. O. The Role of Non-Renewable Energy Consumption in Economic Growth and Carbon Emission: Evidence from Oil Producing Economies in Africa. *Energy Strateg. Rev.* **2020**, *27*, 100434. https://doi.org/10.1016/j.esr.2019.100434.

(135) Whipple, D. T.; Kenis, P. J. A. Prospects of CO2 Utilization via Direct Heterogeneous Electrochemical Reduction. *J. Phys. Chem. Lett.* **2010**, *1* (24), 3451–3458. https://doi.org/10.1021/jz1012627.

(136) Aziz, N. A.; Latip, A. F. A.; Peng, L. C.; Latif, N. H. A.; Brosse, N.; Hashim, R.; Hussin, M. H. Reinforced Lignin-Phenol-Glyoxal (LPG) Wood Adhesives from Coconut Husk. *Int. J. Biol. Macromol.* **2019**, *141*, 185–196. https://doi.org/10.1016/j.ijbiomac.2019.08.255.

(137) Van Nieuwenhove, I.; Renders, T.; Lauwaert, J.; De Roo, T.; De Clercq, J.; Verberckmoes, A. Biobased Resins Using Lignin and Glyoxal. *ACS Sustain. Chem. Eng.* **2020**, *8* (51), 18789–18809. https://doi.org/10.1021/acssuschemeng.0c07227.

(138) Foyer, G.; Chanfi, B. H.; Virieux, D.; David, G.; Caillol, S. Aromatic Dialdehyde Precursors from Lignin Derivatives for the Synthesis of Formaldehyde-Free and High Char Yield Phenolic Resins. *Eur. Polym. J.* **2016**, *77*, 65–74. https://doi.org/10.1016/j.eurpolymj.2016.02.018.

(139) Takkellapati, S.; Li, T.; Gonzalez, M. A. An Overview of Biorefinery-Derived Platform Chemicals from a Cellulose and Hemicellulose Biorefinery. *Clean Technol. Environ. Policy* **2018**, *20* (7), 1615–1630. https://doi.org/10.1007/s10098-018-1568-5.

(140) Zakzeski, J.; Bruijnincx, P. C. A.; Jongerius, A. L.; Weckhuysen, B. M. The Catalytic Valorization of Lignin for the Production of Renewable Chemicals. *Chem. Rev.* **2010**, *110* (6), 3552–3599. https://doi.org/10.1021/cr900354u.

(141) Wenger, J.; Stern, T. Reflection on the Research on and Implementation of Biorefinery Systems – a Systematic Literature Review with a Focus on Feedstock. *Biofuels, Bioprod. Biorefining* **2019**, *13* (5), 1347–1364. https://doi.org/10.1002/bbb.2021.

(142) Gavrilescu, M. Biorefinery Systems: An Overview. *Bioenergy Res. Adv. Appl.* **2014**, 219–241. https://doi.org/10.1016/B978-0-444-59561-4.00014-0.

(143) Hwang, H. L.; Jadhav, S. R.; Silverman, J. R.; John, G. Sweet and Sustainable: Teaching

the Biorefinery Concept through Biobased Gelator Synthesis. *J. Chem. Educ.* **2014**, *91* (10), 1563–1568. https://doi.org/10.1021/ed3007764.

(144) Kamm, B.; Kamm, M. Principles of Biorefineries. *Appl. Microbiol. Biotechnol.* **2004**, *64* (2), 137–145. https://doi.org/10.1007/s00253-003-1537-7.

(145) Fernando, S.; Adhikari, S.; Chandrapal, C.; Murali, N. Biorefineries: Current Status, Challenges, and Future Direction. *Energy and Fuels* **2006**, *20* (4), 1727–1737. https://doi.org/10.1021/ef060097w.

(146) Li, C.; Zhao, X.; Wang, A.; Huber, G. W.; Zhang, T. Catalytic Transformation of Lignin for the Production of Chemicals and Fuels. *Chem. Rev.* **2015**, *115* (21), 11559–11624. https://doi.org/10.1021/acs.chemrev.5b00155.

(147) Zhang, Y.; Wan, L.; Guan, J.; Xiong, Q.; Zhang, S.; Jin, X. A Review on Biomass Gasification: Effect of Main Parameters on Char Generation and Reaction. *Energy and Fuels* **2020**, *34* (11), 13438–13455. https://doi.org/10.1021/acs.energyfuels.0c02900.

(148) Ates, B.; Koytepe, S.; Ulu, A.; Gurses, C.; Thakur, V. K. Chemistry, Structures, and Advanced Applications of Nanocomposites from Biorenewable Resources. *Chem. Rev.* **2020**, *120* (17), 9304–9362. https://doi.org/10.1021/acs.chemrev.9b00553.

(149) Bayat, H.; Cheng, F.; Dehghanizadeh, M.; Brewer, C. E. Recovery of Nitrogen from Low-Cost Plant Feedstocks Used for Bioenergy: A Review of Availability and Process Order. *Energy and Fuels* **2021**, *35* (18), 14361–14381. https://doi.org/10.1021/acs.energyfuels.1c02140.

(150) Yousuf, A.; Pirozzi, D.; Sannino, F. *Fundamentals of Lignocellulosic Biomass*; INC, 2019. https://doi.org/10.1016/B978-0-12-815936-1.00001-0.

(151) Xu, H.; Wang, Z.; Huang, J.; Jiang, Y. Thermal Catalytic Conversion of Biomass-Derived

Glucose to Fine Chemicals. *Energy and Fuels* **2021**, *35* (10), 8602–8616. https://doi.org/10.1021/acs.energyfuels.1c00715.

(152) Zoghlami, A.; Paës, G. Lignocellulosic Biomass: Understanding Recalcitrance and Predicting Hydrolysis. *Front. Chem.* **2019**, *7* (December). https://doi.org/10.3389/fchem.2019.00874.

(153) Bussemaker, M. J.; Zhang, D. Effect of Ultrasound on Lignocellulosic Biomass as a Pretreatment for Biorefinery and Biofuel Applications. *Ind. Eng. Chem. Res.* **2013**, *52* (10), 3563–3580. https://doi.org/10.1021/ie3022785.

(154) Thallada, B.; Kumar, A.; Jindal, M.; Maharana, S. Lignin Biorefinery: New Horizons in Catalytic Hydrodeoxygenation for the Production of Chemicals. *Energy and Fuels* **2021**, *35* (21), 16965–16994. https://doi.org/10.1021/acs.energyfuels.1c01651.

(155) Sun, H.; Xu, Q.; Ren, M.; Wang, S.; Kong, F. Recent Studies on the Preparation and Application of Ionic Amphiphilic Lignin: A Comprehensive Review. *J. Agric. Food Chem.* **2022**, *70* (29), 8871–8891. https://doi.org/10.1021/acs.jafc.2c02798.

(156) Clauser, N. M.; González, G.; Mendieta, C. M.; Kruyeniski, J.; Area, M. C.; Vallejos, M. E. Biomass Waste as Sustainable Raw Material for Energy and Fuels. *Sustain.* **2021**, *13* (2), 1–21. https://doi.org/10.3390/su13020794.

(157) Nagarajan, S.; Ranade, V. V. Valorizing Waste Biomass via Hydrodynamic Cavitation and Anaerobic Digestion. *Ind. Eng. Chem. Res.* **2021**, *60* (46), 16577–16598. https://doi.org/10.1021/acs.iecr.1c03177.

(158) Djandja, O. S.; Wang, Z. C.; Wang, F.; Xu, Y. P.; Duan, P. G. Pyrolysis of Municipal Sewage Sludge for Biofuel Production: A Review. *Ind. Eng. Chem. Res.* **2020**, *59* (39), 16939–16956. https://doi.org/10.1021/acs.iecr.0c01546.

(159) Zhang, X.; Li, X.; Li, R.; Wu, Y. Hydrothermal Carbonization and Liquefaction of Sludge for Harmless and Resource Purposes: A Review. *Energy and Fuels* **2020**, *34* (11), 13268–13290. https://doi.org/10.1021/acs.energyfuels.0c02467.

(160) Mongkhonsiri, G.; Gani, R.; Malakul, P.; Assabumrungrat, S. Integration of the Biorefinery Concept for the Development of Sustainable Processes for Pulp and Paper Industry. *Comput. Chem. Eng.* **2018**, *119*, 70–84. https://doi.org/10.1016/j.compchemeng.2018.07.019.

(161) Larson, E. D.; Larson, E. D.; Consonni, S.; Consonni, S.; Katofsky, R. E.; Katofsky, R. E.; Consulting, N.; Consulting, N.; Iisa, K.; Iisa, K.; Frederick, W. J.; Frederick, W. J. A Cost-Benefit Assessment of Gasification-Based Biorefining in the Kraft Pulp and Paper Industry Volume 1 Main Report. *Main* **2006**, *1*.

(162) Bajpai, P. *Biorefinery Opportunities in the Pulp and Paper Industry*; 2013. https://doi.org/10.1016/b978-0-12-409508-3.00002-x.

(163) Hu, J.; Zhang, Q.; Lee, D. J. Kraft Lignin Biorefinery: A Perspective. *Bioresour. Technol.* **2018**, *247* (September 2017), 1181–1183. https://doi.org/10.1016/j.biortech.2017.08.169.

(164) Mccance, K. R.; Suarez, A.; Mcalexander, S. L.; Davis, G.; Blanchard, M. R.; Venditti, R. A. Modeling a Biorefinery: Converting Pineapple Waste to Bioproducts and Biofuel. *J. Chem. Educ.* **2021**, *98* (6), 2047–2054. https://doi.org/10.1021/acs.jchemed.1c00020.

(165) Bansode, A.; Barde, M.; Asafu-Adjaye, O.; Patil, V.; Hinkle, J.; Via, B. K.; Adhikari, S.; Adamczyk, A. J.; Farag, R.; Elder, T.; Labbé, N.; Auad, M. L. Synthesis of Biobased Novolac Phenol-Formaldehyde Wood Adhesives from Biorefinery-Derived Lignocellulosic Biomass. *ACS Sustain. Chem. Eng.* **2021**, *9* (33), 10990–11002. https://doi.org/10.1021/acssuschemeng.1c01916.

(166) Eugenia Eugenio, M.; Ibarra, D.; Martín-Sampedro, R.; Espinosa, E.; Bascón, I.; Rodríguez, A. Alternative Raw Materials for Pulp and Paper Production in the Concept of a Lignocellulosic Biorefinery. *Cellulose* **2019**. https://doi.org/10.5772/intechopen.90041.

(167) Mazar, A.; Ajao, O.; Benali, M.; Jemaa, N.; Wafa Al-Dajani, W.; Paleologou, M. Integrated Multiproduct Biorefinery for Furfural Production with Acetic Acid and Lignin Recovery: Design, Scale-Up Evaluation, and Technoeconomic Analysis. *ACS Sustain. Chem. Eng.* **2020**, *8* (47), 17345–17358. https://doi.org/10.1021/acssuschemeng.0c04871.

(168) Kouisni, L.; Gagné, A.; Maki, K.; Holt-Hindle, P.; Paleologou, M. LignoForce System for the Recovery of Lignin from Black Liquor: Feedstock Options, Odor Profile, and Product Characterization. *ACS Sustain. Chem. Eng.* **2016**, *4* (10), 5152–5159. https://doi.org/10.1021/acssuschemeng.6b00907.

(169) Liu, W. J.; Yu, H. Q. Thermochemical Conversion of Lignocellulosic Biomass into Mass-Producible Fuels: Emerging Technology Progress and Environmental Sustainability Evaluation. *ACS Environ. Au* **2022**, *2* (2), 98–114. https://doi.org/10.1021/acsenvironau.1c00025.

(170) Liu, Q.; Chmely, S. C.; Abdoulmoumine, N. Biomass Treatment Strategies for Thermochemical Conversion. *Energy and Fuels* **2017**, *31* (4), 3525–3536. https://doi.org/10.1021/acs.energyfuels.7b00258.

(171) Fatehi, H.; Weng, W.; Li, Z.; Bai, X. S.; Aldén, M. Recent Development in Numerical Simulations and Experimental Studies of Biomass Thermochemical Conversion. *Energy and Fuels* **2021**, *35* (9), 6940–6963. https://doi.org/10.1021/acs.energyfuels.0c04139.

(172) Elliott, D. C.; Meier, D.; Oasmaa, A.; Van De Beld, B.; Bridgwater, A. V.; Marklund, M. Results of the International Energy Agency Round Robin on Fast Pyrolysis Bio-Oil

Production. *Energy and Fuels* **2017**, *31* (5), 5111–5119. https://doi.org/10.1021/acs.energyfuels.6b03502.

(173) Pattiya, A. *1 - Fast Pyrolysis*; Elsevier Ltd., 2018. https://doi.org/10.1016/B978-0-08-101029-7.00001-1.

(174) Wang, D.; Czernik, S.; Montané, D.; Mann, M.; Chornet, E. Hydrogen from Biomass via Fast Pyrolysis and Catalytic Steam Reforming. *ACS Div. Fuel Chem. Prepr.* **1997**, *42* (2), 779–782.

(175) Miyata, Y.; Sagata, K.; Hirose, M.; Yamazaki, Y.; Nishimura, A.; Okuda, N.; Arita, Y.; Hirano, Y.; Kita, Y. Fe-Assisted Hydrothermal Liquefaction of Lignocellulosic Biomass for Producing High-Grade Bio-Oil. *ACS Sustain. Chem. Eng.* **2017**, *5* (4), 3562–3569. https://doi.org/10.1021/acssuschemeng.7b00381.

(176) De Wild, P.; Reith, H.; Heeres, E. *Biomass Pyrolysis for Chemicals*; 2011; Vol. 2. https://doi.org/10.4155/bfs.10.88.

(177) Chiaramonti, D.; Prussi, M.; Buffi, M.; Rizzo, A. M.; Pari, L. Review and Experimental Study on Pyrolysis and Hydrothermal Liquefaction of Microalgae for Biofuel Production. *Appl. Energy* **2017**, *185*, 963–972. https://doi.org/10.1016/j.apenergy.2015.12.001.

(178) Megia, P. J.; Vizcaino, A. J.; Calles, J. A.; Carrero, A. Hydrogen Production Technologies: From Fossil Fuels toward Renewable Sources. A Mini Review. *Energy and Fuels* **2021**, *35* (20), 16403–16415. https://doi.org/10.1021/acs.energyfuels.1c02501.

(179) Azadi, P.; Inderwildi, O. R.; Farnood, R.; King, D. A. Liquid Fuels, Hydrogen and Chemicals from Lignin: A Critical Review. *Renew. Sustain. Energy Rev.* **2013**, *21*, 506–523. https://doi.org/10.1016/j.rser.2012.12.022.

(180) Ghosh, A.; Haverly, M. R. Solvent Liquefaction. *Thermochem. Process. Biomass* **2019**,

257–306. https://doi.org/10.1002/9781119417637.ch8.

Chapter 2

Synthesis of Biobased Novolac Phenol-Formaldehyde Wood Adhesives from Biorefinery Derived Lignocellulosic Biomass

2.1 Introduction

The large-scale production and use of adhesives to develop wood-based composites have been rapidly expanding over the years.[1] These adhesives are mainly produced from petroleum-derived monomers. However, the utilization of these monomers and their corresponding materials are growing concerns owing to environmental pollution and future shortages of energy supplies.[2] In this context, integrated biorefineries have been proposed at the industrial and laboratory scale to facilitate the production of sustainable chemicals and fuels through renewable feedstocks.[3] Lignocellulose is one of the most desirable renewable feedstocks, composed of three biopolymers: cellulose, hemicellulose, and lignin. These biopolymers are generally derived from residues of industrial (e.g., black liquor), agricultural (e.g., wheat straw), forestry waste (e.g., sawdust) as well as energy crops.[4,5]

---

[1] Bansode, A.; Barde, M.; Asafu-Adjaye, O.; Patil, V.; Hinkle, J.; Via, B. K.; Adhikari, S.; Adamczyk, A. J.; Farag, R.; Elder, T.; Labbé, N.; Auad, M. L. Synthesis of Biobased Novolac Phenol-Formaldehyde Wood Adhesives from Biorefinery Derived Lignocellulosic Biomass, ACS Sustainable Chem. Eng. 2021, 9, 10990−11002.

In the quest to utilize lignocellulosic biomass (LCBM), the kraft biorefinery represents cost-effective and zero-waste strategies.[6] Kraft is a pulping process of transforming wood into wood pulp; during this operation, cellulose is separated by dissolving lignin from lignocellulosic biomass in an alkaline medium (NaOH and Na_2S). At the end of the process, a high solids concentration called black liquor is generated as a byproduct, which contains a significant lignin concentration in addition to hemicellulose and other chemicals.[7] In this line, several technically feasible processes have been pioneered to extract lignin from black liquor by acidification. For instance, Westvaco (now called Ingevity) is the most established technology for kraft lignin recovery at a commercial scale, enabling high-purity lignin (e.g., Indulin-Westvaco's trade name) production.[8,9] This lignin is a highly functionalized biomacromolecule that contains various reactive groups such as acidic, aliphatic, and aromatic hydroxyl, whose relative chemistry is applicable in the synthesis of bio-based materials.[10]

Thermochemical conversion processes are another explicitly endorsed biorefinery strategy to convert biomass to energy. Intensive reaction conditions are employed to break the bonds of organic matter and provide a wide range of chemical compounds that can be used to produce biobased materials.[11] This includes technologies such as pyrolysis, liquefaction, gasification, and combustion. Whereas liquefaction and pyrolysis are considered high-efficiency conversion technologies, which produces bio-oil (a mixture of oxygenated compounds) as a predominant product with a high energy density compared to solid biomass.[12] Liquefaction is performed in an aqueous environment (hydrothermal liquefaction) or organic solvents (solvent liquefaction). [13] Usually, solvent liquefaction can be performed at modest temperatures (105−400 °C) and elevated pressures (2−20 MPa) in the presence of a suitable solvent.[14] The performance of the liquefaction process depends on the selection of a suitable solvent. In this case, alcohols are proved to be

a suitable solvent as it suppresses side reactions by providing hydrogen sources during the reaction.[15] With that regard, research work in the literature reported that solvent liquefaction of lignin, using alcohol as a solvent, showed a higher conversion efficiency. This is important in the case of lignin as there can be a chance of getting a high amount of solid fraction recoupling of phenolic compounds.[16]

Aforementioned, pyrolysis is a robust thermochemical process of materializing biomass into valuable and flexible bio-liquids, which is commonly performed at moderate temperatures (450−600°C) under oxygen-free conditions.[17] According to the pyrolysis process parameters, two main pyrolysis processes are listed: slow pyrolysis (conventional pyrolysis) and fast pyrolysis. Fast pyrolysis is a productive method in which the biomass is rapidly heated to high temperatures for a very short residence time, leading to the low investment cost and high-yield bio-oil.[18] The obtained fast pyrolysis liquid fraction shows phase-separated bio-oil. The lower phase is classified as organic and mainly originates from pyrolytic lignin, while the upper phase is more of aqueous fractions.[19] The main reason for phase separation is excess water, which resulted in a byproduct of condensation and esterification reactions at elevated temperatures.

Interestingly, the organic phase of bio-oil can be practically useful in producing aromatic chemicals due to the high concentration of phenolic compounds. However, the chemical composition of bio-oil depends on the feedstock used during fast pyrolysis.[20,21] For the explained reasons, these noteworthy biorefinery materials (kraft recovery lignin and thermochemical conversion bio-oils) hold the potential to replace the petroleum-based monomer in conventional adhesive production.

Phenol-formaldehyde (PF) resin is a widely used adhesive in various wood industries and synthesized via condensation polymerization of phenol and formaldehyde using either acid (oxalic

acid or hydrochloric acid) or base (sodium hydroxide) catalyst to produce novolac or resol PF resin, respectively.[22] However, novolac PF resins are produced with an excess of phenol, classified as a hazardous substance derived from petroleum sources.[23] Therefore, the substitution of phenol with biobased phenolic structures becomes an alternative sustainable strategy to produce biobased novolac PF wood adhesives. Several studies have reported biobased resole PF resins from lignocellulosic biomass (LCBM) for wood adhesive application.[24–27] However, limited literature has reported the substitution of phenol by LCBM in novolac PF resin preparation.[28,29] A wide variety of lignocellulosic biomass has been proposed in the literature for producing biobased wood adhesives. Among these, the softwood and grass containing LCBM considered as a prime choice for PF adhesive, as they possess more guaiacyl (G) and p-hydroxyphenyl (H) units into their structure, which can react with formaldehyde in PF resin synthesis.[24]

In this study we have selected phenolic structures from three different biorefineries: lignin from kraft biorefinery (L-KB), bio-oil produced from solvent liquefaction of industrial lignin (BO-SL/L), and bio-oil obtained from fast pyrolysis of pine wood (BO-FP/PW) for the synthesis of NPF resin adhesive. The first two sources are lignin powder and bio-oil from lignin, so they are lignin-based. In contrast, the BO-FP/PW is obtained from the organic phase of bio-oil, mainly pyrolytic lignin, as demonstrated by previous work from this group.[30] In addition, kraft lignin (L-KB) and the BO-FP/PW are produced from softwood sources. All of the biobased sources were characterized and compared in the first part of this work. We then use these phenolic sources to substitute 50% (w/w) of phenol in the Novolac phenol-formaldehyde (NPF) resin system. Finally, these biobased NPF resins are compared to 100-NPF resin (lab-made novolac PF) as a reference. The adhesion properties were determined using tensile shear strength analysis on the wood

sample under dry and wet conditions using the proper standard method. The performance of adhesives was discussed with the help of two-way ANOVA followed by Tukey's post hoc test.

2.2 Experimental Section

2.2.1 Materials

The kraft lignin (Indulin AT) used in this work was generously provided by Ingevity Corporation, South Carolina, USA. Deuterated dimethyl sulfoxide (DMSO-d6, with TMS 0.1 vol % deuteration degree min. 99.9%), pyridine (99+%), acetic anhydride (≥97.0%), tetrahydrofuran (THF, 99.0%), glucose, sulfuric acid (70%), phenol (99%), formalin solution (37% formaldehyde in water with 10-15% methanol as stabilizer), hexamethylenetetramine (HMTA, 99+%) and acetone (99.5%) were purchased from VWR International, USA. Oxalic acid (anhydrous crystal, 98.0%) was supplied by Spectrum Chemical Mfg. Corp., USA. Southern yellow pine (Pinus spp.) wood was used in the adhesion properties studies. The solvent liquefaction bio-oil (BO-SL/L) and fast pyrolysis (BO-FP/PW) were obtained from lignin and pine wood, respectively. The relevant biorefinery processes were performed in our Biosystems Engineering Laboratory, Auburn University, and the Center for Renewable Carbon Laboratory, University of Tennessee, USA, as described in the Methods section.

2.2.2 Solvent Liquefaction Methodology

The lignin used for solvent liquefaction was provided by Renmatix Incorporation, USA. The lignin was made using a proprietary supercritical water extraction technology. The details of feed biomass were not provided by the supplier. A 1.8 L capacity high-pressure Parrr® 4680 reactor was used for solvent liquefaction to produce bio-oil from lignin. 100 g of lignin thoroughly mixed with 500 mL ethanol (reagent grade, 95%, VWR International, USA) was loaded into the

reactor vessel.[31] The reactor was then pressurized and depressurized with 300 psi nitrogen (ultra-high purity, 99.999%) thrice and then heated to 250 °C with stirring at 500 rpm. The maximum pressure attained by the reactor was ~1400 psi at 250 °C. The reactor was then washed with ethyl acetate (VWR International, USA) to remove any product stuck on the impeller, and this mixture was added to the product.[32] The product mixture was filtered with Whatman filter paper (#42) to separate the char. The filtrate was subjected to rotary evaporation at 40 °C under vacuum to remove ethyl acetate and ethanol. The resulting bio-oil was removed from the round bottom flask by mixing it with dichloromethane (≥99.5%, VWR International, USA) and then keeping it under vacuum at room temperature for 24 hours. The bio-oil was obtained in ~55 wt% yields (based on the initial dry mass of lignin). The exact process was repeated twice, and the bio-oil was combined.

2.2.3 Fast Pyrolysis Methodology

A semi-pilot scaled auger reactor was used for the fast pyrolysis experiment, and the details about reactor design are explained previously.[33] For the experiment, pinewood biomass with particles less than 4 mm in size was fed into a pyrolyzer reactor at a rate of 7.3 kg/h. The pyrolysis reaction occurred at 500 °C under oxygen-free conditions by continuously passing N_2 at a flow rate of 50 L/min. After condensation of pyrolysis vapors in the quench system, the liquid products were allowed to settle down, to separate the organic phase of bio-oil from the aqueous phase. The related properties of bio-oil are reported in previously published articles from our research group.[30,34]

2.2.4 Characterization of L-KB, BO-SL/L, and BO-FP/PW

2.2.4.1 FTIR Spectroscopy

FTIR measurements were performed using a Thermo Scientific Nicolet 6700 FTIR instrument equipped with attenuated total reflection (ATR). Each spectrum was collected with 64 scans in the wavenumber range of 4000 cm^{-1} - 400 cm^{-1} at a resolution of 4 cm^{-1}. Background spectra were recorded before every sampling. The spectra were analyzed using the OMNIC 7.3 software.

2.2.4.2 ^{13}C-^{1}H HSQC 2D-NMR

For the 2D HSQC-NMR experiment, around 156.6 mg of the sample was fully dissolved in 1 mL of DMSO-d_6 solvent. The spectra were recorded on Bruker Ultrashied^{TM} 500 MHz plus spectrometer using hsqcetgpsisp 2.2 pulse program with other parameters: 90° pulse angle, 0.11 s acquisition time, 1.5 s pulse delay, and 16 number of scans. The $^{1}J_{CH}$ used was 145 Hz. The number of collected complex points was 1024 for the ^{1}H-dimension, and 256 increments were recorded in ^{13}C-dimension. The spectral width of 13.02 and 220.00 ppm used for ^{1}H and ^{13}C, respectively. Data processing was performed using Mnova V.14 software.

2.2.4.3 Py-GCMS/GCMS

Pyrolysis of the lignin (L-KB) sample was performed using a CDS Pyroprobe® 5200 (CDS Analytical LLC, Pennsylvania, USA) micro-pyrolyzer. This was done by loading 1 mg of the sample into a glass pyroprobe. The pyroprobe was initially heated to 100 °C and held at that temperature for 5 seconds, followed by heating at 10 °C/mS to 750 ^{0}C with a 5-second hold. For GC/MS analysis, an Agilent 7890A GC/ 5975C gas chromatography unit was used, and the separation was made using 30 m X 0.25 mm i.d. X 0.25 mm film thickness DB-1701 mass spectroscopy column with an injection temperature of 300 °C and 70eV electron impact. The MS scan range

of m/z (mass to charge ratio) was 30-550, and the split ratio of 10:1 was used for the analysis. The GC oven temperature was held at 60 °C for 1 min and then heated to 280 °C at 15 °C /min, and the final temperature was maintained for 10 minutes. Helium gas was used as the carrier gas with a flow rate of 3 ml/min. The identification and analysis of the peaks were performed using the MS NIST library.

The GC-MS/FID analysis of BO-SL/L was carried out with the same instrument but without connecting the Pyroprobe. About 20 mg of bio-oil was dissolved in ~2 g of ethanol to achieve 100x dilution, and the solution was filtered. Agilent 7890A GC/ 5975C gas chromatography-mass spectrometry unit was used for the analysis, with an initial temperature of 60 °C held for 1 min, and then ramping up to 280 °C at 15 °C/min, which was held for 10 minutes. 3 ml/min of helium was used as a carrier gas in a DB-1701 column (30 m X 0.25 mm i.d. X 0.25 mm film thickness). The GCMS analysis of BO-FP/PW was mentioned in a previously published article.[30]

2.2.4.4 Colorimetric quantification of carbohydrates in bio-oils

The amount of carbohydrates was determined by phenol-sulfuric acid assay. Dubois et al.[35] mentioned this as a well-known colorimetric method for carbohydrates. The procedure of this method is referred to from literature [36,37] as follows. A 0.5 mL of bio-oil (each bio-oil diluted with acetone as 0.01 g/ml) sample was mixed with 0.5 mL of 4% aqueous solution of phenol in a sample tube. The mixture was shaken for 30 seconds. Subsequently, 2.5 mL concentrated H_2SO_4 was added to the mixture and allowed to stand for 10 minutes at room temperature. After that, the mixture was placed in a static water bath for another 10 minutes. Bio-oil samples were hydrolyzed in triplicate. Glucose standards of 0, 20, 40, and 60 µg/ml were prepared, and each stand-

ard was subjected to the hydrolysis procedure outlined above. A Genesys 150 UV-Visible spectrophotometer was used for the measurement of absorbance.

2.2.5 Synthesis and Characterization of NPF Resins

The NPF resins used as wood adhesives were synthesized using a 1:0.8 molar ratio of phenol to formaldehyde with 0.05 moles of oxalic acid per mole of phenol as a catalyst. Oxalic acid was selected to avoid potential corrosion to the system as it is a weak acid.[38,39] The synthesis was conducted at 90 °C for 3 hours in a four-necked flask equipped with a dropping funnel at one end for dropwise addition of the formaldehyde solution (37% formalin solution) and a condenser at another neck to prevent formaldehyde escape through the system at high temperature. The whole assembly was placed in a silicone oil bath to maintain a constant temperature throughout the reaction under continuous stirring. After 3 hours of synthesis, the water generated as a byproduct in the reaction was removed using a rotary evaporator at 60 °C under reduced pressure to recover the PF resin. The obtained resin was labeled as 100-NPF. A similar procedure was used to synthesize resin from L-KB, BO-SL/L, and BO-FP/PW by substituting 50% (w/w) of phenol by each of the phenolic sources as described above. The synthesized resins were labeled as 50-NPF-L-KB, 50-NPF-BO-SL/L, and 50-NPF-BO-FP/PW, respectively. Further, the resins were characterized by FTIR and ^{1}H NMR spectroscopy.

2.2.5.1 ^{1}H NMR spectroscopy

The chemical structures of NPF resins were analyzed through ^{1}H NMR spectrometry using a Bruker 600 MHz NMR spectrophotometer equipped with a triple resonance cryoprobe and an automatic sample changer. Spectra were acquired by dissolving 100 mg of the sample in 1 mL of deuterated DMSO-d_6 containing 0.03% tetramethylsilane (TMS), which is used as an internal

standard for referencing the chemical shifts. ^{1}H NMR spectra were recorded using 16 scans with 2.7262 sec acquisition time, 1 sec delay time, and 65536 transients. Spectral data were analyzed using the Mnova V.14 software.

2.2.6 Crosslinking of NPF resins and Thermal study by DSC

For the crosslinking reaction, NPF resin samples were ground with the HMTA curing agent using mortar and pestle in the desired proportion (9% w/w HMTA/NPF resin) to achieve a homogenous mixture. The subsequent mixture was then used for DSC analysis to study the curing properties. The combinations of each resin with HMTA were labeled as 100-NPF adhesive, 50-NPF-L-KB adhesive, 50-NPF-BO-SL/L adhesive and 50-NPF-BO-FP/PW adhesive, respectively.

The DSC measurements were performed using a TA Q2000 (TA instruments, DE, USA) with nitrogen purge gas at 50mL/min. 5-6 mg of samples were measured in DSC standard aluminum pans with a small hole punctured in the aluminum lid, the purpose of doing that to collect the blown-out sample in the upper lid. The modulated DSC experiment was performed for each sample between 25 °C to 200 °C at a heating/cooling rate of 10 °C/min with two heating and cooling cycles with modulation of +/- 1 °C every 60 seconds. The first heating cycle was used to interrogate the curing phenomenon by using TA instrument analysis software.

2.2.7 Preparation of glued wood specimens

The board of southern yellow pine (Pinus spp.) wood was cut into eight panels of dimensions 40 × 7 × 0.035 cm^3 (L × W × H). After that, these panels were conditioned at 62% relative humidity (RH) and 22 °C temperature for 24 hours. Then, the adhesive was spread uniformly to one side of the wood panel with a glue spread rate of 200 g/m^2, and the other wood panel was placed on top of it. Before application, the NPF resin was grounded with HMTA (9% on weight of NPF

resin), then the homogenous mixture was dissolved in the desired amount of acetone for ease of application on wood substrate. In total, four glued panels were prepared corresponding to each NPF resin adhesive type using the same procedure. Afterward, all the four glued wood panels were pressed at 150 °C for 15 minutes with 2 MPa pressure and then allowed to cool and conditioned as before. From each bonded panel, eight wood specimens were produced according to standard procedure ASTM D906-98 (2017), as illustrated in Figure 2.1a-b, out of which four wood specimens were used for wet shear bonding strength and physical analysis of each adhesive. The wood specimens were placed underwater using a metal grid at room temperature for 24 hours. After 24 hours, the wood specimens were removed from the water and wiped using a paper towel.

Water Absorption (WA) and Thickness Swelling (TS)

The weight and thickness of the wood specimen before immersing and after immersing in water were measured using electric balance and vernier caliper, respectively, to calculate water absorption and thickness swelling.

The water absorption (WA %) was calculated according to equation 2.1.[40]

$$\text{WA } \% = \frac{W_{24} - W_0}{W_0} \times 100 \qquad [2.1]$$

Where W_0 is the weight of the wood specimen before immersion, and W_{24} is the weight of the wood specimen after immersing for 24 hours.

The thickness swelling (TS %) of the wood specimen was calculated using equation 2.2.[40]

$$\text{TS } \% = \frac{T_{24} - T_0}{T_0} \times 100 \qquad [2.2]$$

Where T_0 is the average thickness taken at three different places across the wood specimen before immersion, and T_{24} is the average thickness measured after immersion for 24 hours.

Tensile Shear Strength

The dry and wet shear strength tests for each NPF resin adhesive were carried out following ASTM D 906-98 (2017)[41] standard using universal testing machine INSTRON 5565 at a constant loading speed of 1.0 mm/min and loading capacity of 10 kN.

The tensile shear strength is calculated according to equation 2.3.[40]

$$\tau = \frac{F_{Max}}{l_2 b} \qquad [2.3]$$

Where τ is the tensile-shear strength (MPa), F_{max} is the maximum loading force recorded at the breaking point (N), l_2 is the length of the shear area (mm), and b is the width of the shear area (mm).

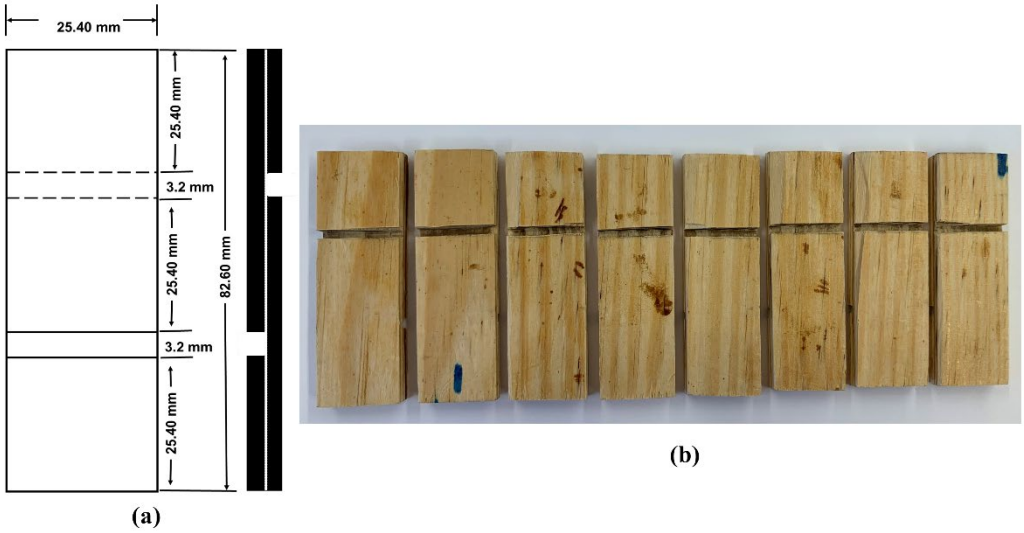

Figure 2.1 (a) Schematic illustration for the dimension of the wood specimen (ASTM D906-98 2017)[41] (b) wood specimens glued with NPF resin adhesives.

2.2.8 Statistical Analysis

Statistical analysis of water absorption and thickness swelling was performed using one-way analysis of variance (ANOVA) in conjunction with Tukey's *post-hoc* test. The results were expressed as means ± standard deviations. Two-way ANOVA followed by Tukey's *post-hoc* test was conducted for tensile shear strength analysis of each of the adhesive and at the dry and wet conditions. All data were analyzed using Minitab 19 software.

2.3 Results and Discussion

2.3.1 Characterization of L-KB, BO-SL/L, and BO-FP/PW

In this study, we used lignin and bio-oils obtained from three different biorefineries. So, to understand their chemistry and structural reactivity, selective characterization was performed and presented further in the following sections.

The functional groups present in the L-KB, BO-SL/L, and BO-FP/PW were analyzed by FTIR as shown in Figure 2.2. The representative peaks were assigned as per previously reported literature. [42,43] Each of them exhibited a broad peak in the region of 3500−3300 cm^{-1} which are related to −OH stretching vibrations from phenolic and aliphatic –OH presents in lignin and polysaccharides (cellulose and hemicellulose). [43] The absorption bands in the region (2900−2800 cm^{-1}) representing symmetric (*vs*) and asymmetric (*vas*) C−H stretching vibrations in CH_2 (methylene) and CH_3 (methyl) groups: 2934 cm^{-1} ($_{vas}CH_2$, L-KB), 2872 cm^{-1} ($_{vs}CH_3$, L-KB), 2970 cm^{-1} ($_{vas}CH_3$, BO-SL/L), 2935 cm^{-1} ($_{vas}CH_2$, BO-SL/L), 2845 cm^{-1} ($_{vs}CH_2$, BO-SL/L), 2928 cm^{-1} ($_{vas}CH_2$, BO-FP/PW), 2855 cm^{-1} ($_{vs}CH_2$, BO-FP/PW). The BO-FP/PW and BO-SL/L have high-intensity CH_2 and CH_3 peaks, which indicates the highest proportion of CH group than L-KB. The peaks at 1703 cm^{-1} for BO-SL/L and 1705 cm^{-1} for BO-FP/PW are more likely associated

with C=O stretching vibration of unconjugated ketones and carboxyl groups. The appearance of these peaks for bio-oils shows the depolymerization of lignin during the liquefaction and pyrolysis process, which generate more carbonyl functional groups. The absorption peaks at 1590 and 1515 cm^{-1} were assigned to aromatic skeleton vibrations (guaiacyl units in LCBM). The intensity of 1270 cm^{-1} is related to the C−O stretching in guaiacyl. [44] The characteristic band for C−O−C asymmetric stretching has been seen at 1152 cm^{-1} (weak) in the case of BO-FP/PW and BO-SL/L. The band detected at 1033 cm^{-1} is linked to aromatic C−H in-plane deformation in G units. A band at 732 cm^{-1} can be ascribed to the C−H out of a plane in p-hydroxyl phenolic unit.

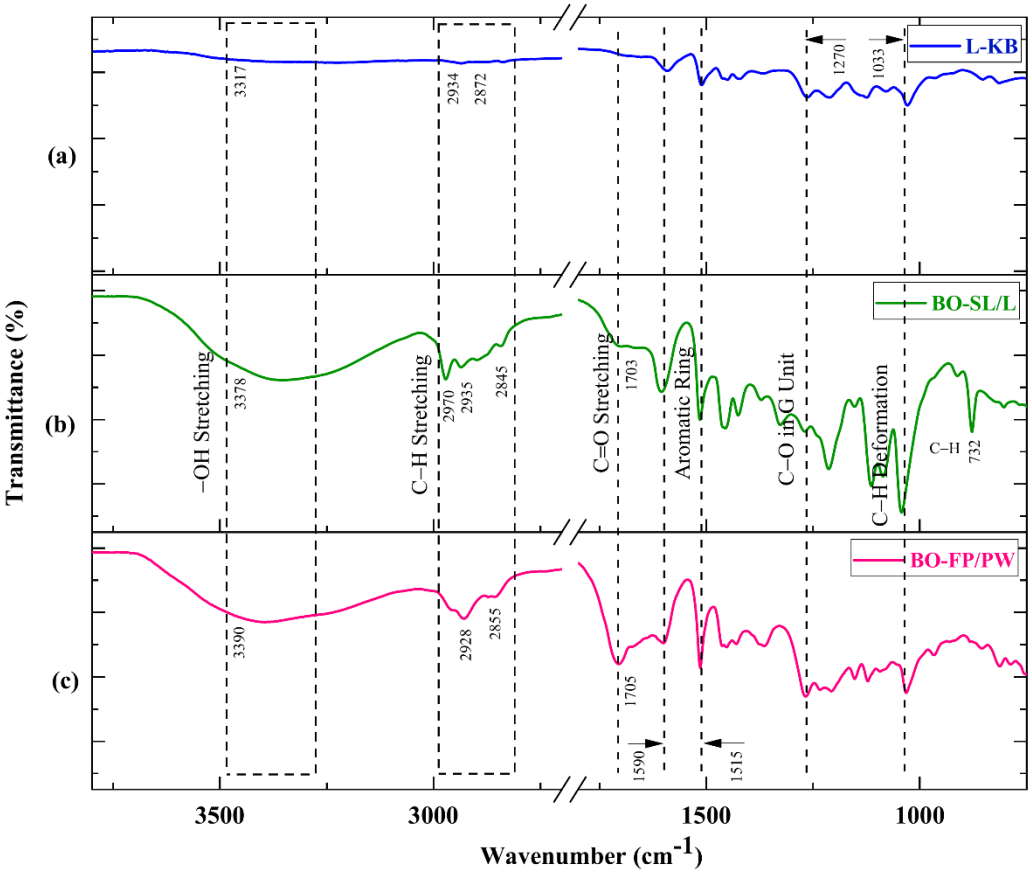

Figure 2.2 FTIR spectra of (a) L-KB, (b) BO-SL/L, and (c) BO-FP/PW.

2D HSQC NMR experiment was run for L-KB, BO-SL/L and BO-FP/PW sample and their spectra with designated peaks and structures according to previously published articles[45] are displayed in Figure 2.3, which shows informative peaks in the aromatic (δC/δH 90.0-150.0/4.0-8.0), interunit aliphatic lignin (δC/δH 52.5-90.0/2.8-5.7) and aliphatic (δC/δH 8.0-52.5/0.5-4.5) region. Figure 2.3a represents the spectrum of L-KB. Lignin is a complex macromolecule consisting of the *p*-coumaryl, coniferyl, and sinapyl alcohol. These monolignols undergo radical polymerization forming various interunit linkages, α-O-4 (aryl ether), β-O-4 (aryl ether), β-β (pinoresinol), β-5 (phenylcoumaran), 5-5 (biphenyl), β-1 (1,2-diaryl propane).[46] The aromatic region of kraft lignin (Figure 2.3a) shows strong signals related to guaiacyl (G) unit at C2–H2 (δC/δH 109.5-112.8/6.7–7.2 ppm) and C6–H6 (δC/δH 118.7–121.8/6.5–7.3 ppm). This is because the kraft lignin used in this study was originated from softwood. Whereas, in the case of BO-SL/L (Figure 2.3b), both guaiacyl (G) and p-hydroxyphenyl (H) units related peaks were observed. In Figure 2.3c (BO-FP/PW), mainly guaiacyl (G) units are observed. Also, signals related to carbohydrates C_1−H_1 in 4−O−methyl−β−D−gluconic acid at δC/δH 97.50/4.56 detected, which may be associated with carbohydrates present in bio-oil.

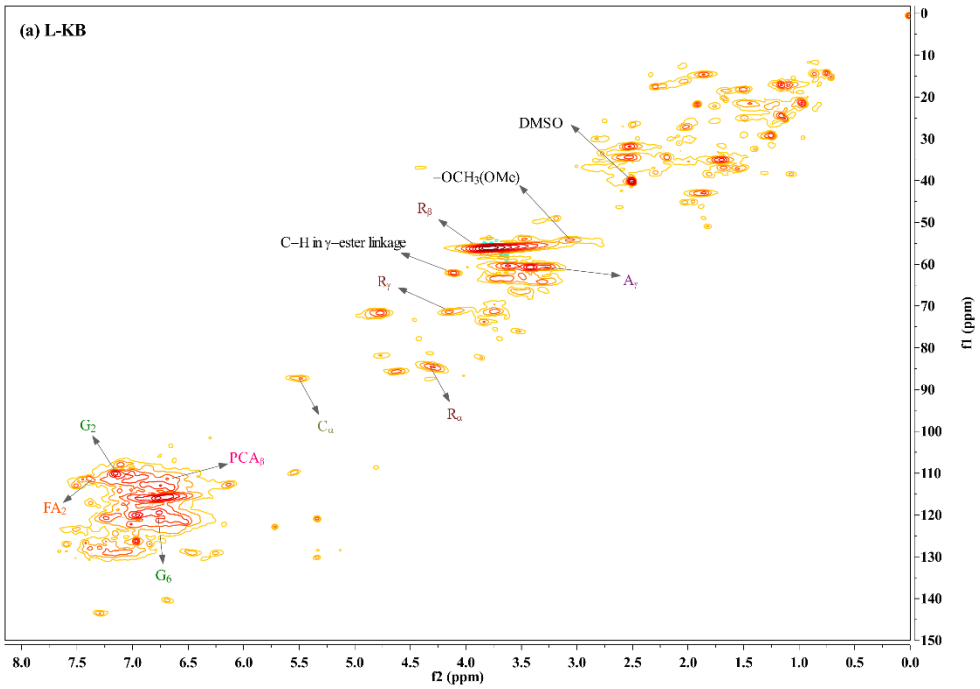
(a) L-KB
DMSO
–OCH3(OMe)
Rβ
C–H in γ–ester linkage
Aγ
Rγ
Cα
Rα
G2
PCA8
FA2
G6
f2 (ppm)
f1 (ppm)

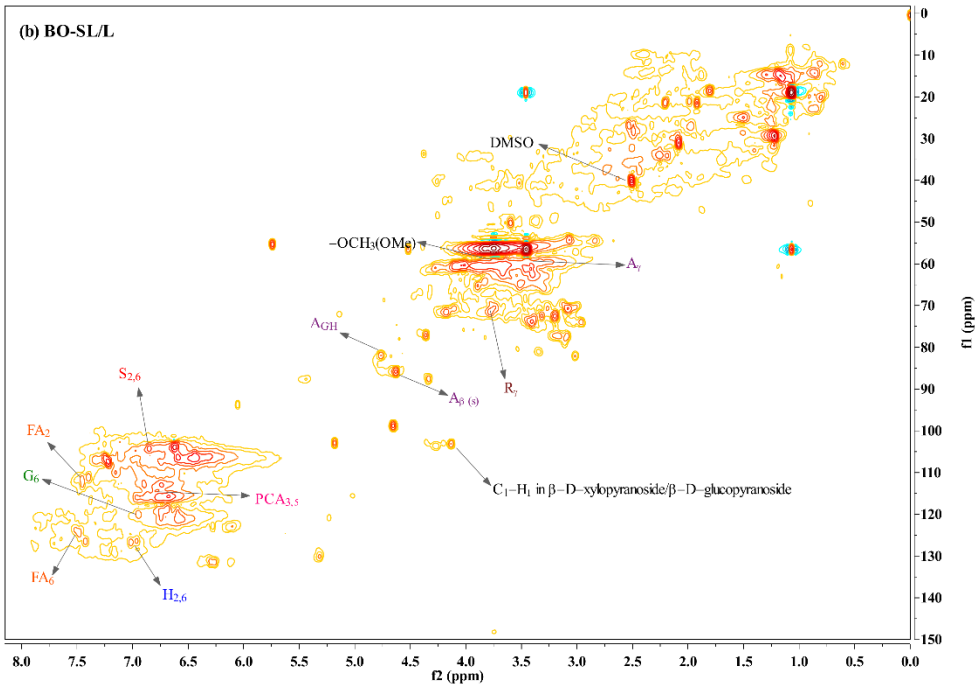
(b) BO-SL/L
DMSO
–OCH3(OMe)
Aγ
AGH
Rγ
Aβ (s)
S2,6
FA2
G6
PCA3,5
FA6
H2,6
C1–H1 in β–D–xylopyranoside/β–D–glucopyranoside
f2 (ppm)
f1 (ppm)

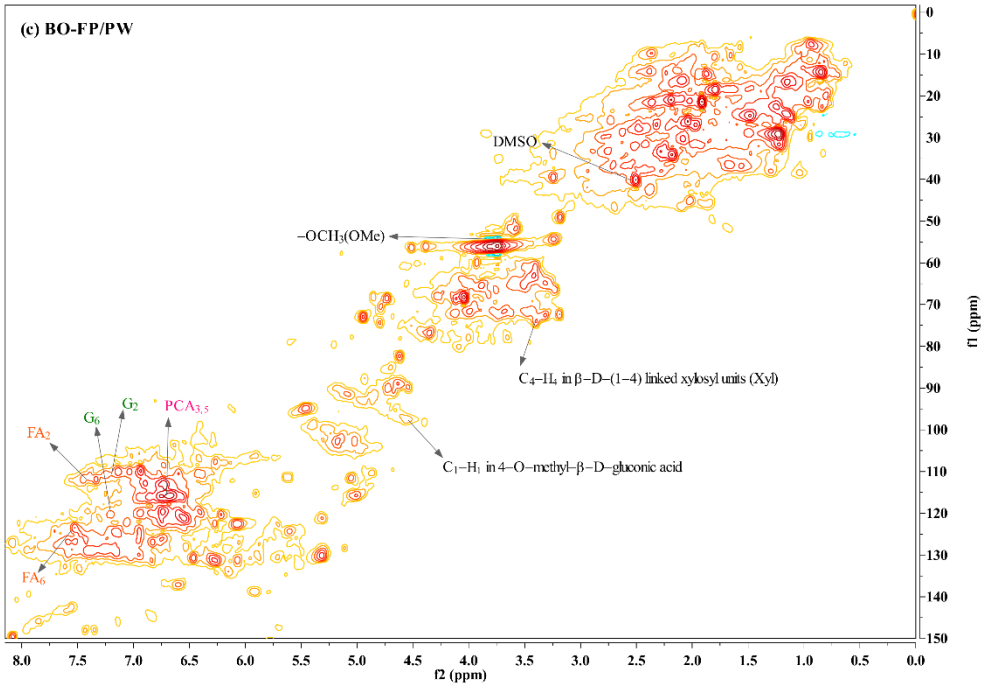
(c) BO-FP/PW
DMSO
–OCH3(OMe)
C4–H4 in β–D–(1–4) linked xylosyl units (Xyl)
C1–H1 in 4–O–methyl–β–D–gluconic acid
FA2
G6
G2
PCA3,5
FA6
f2 (ppm)
f1 (ppm)

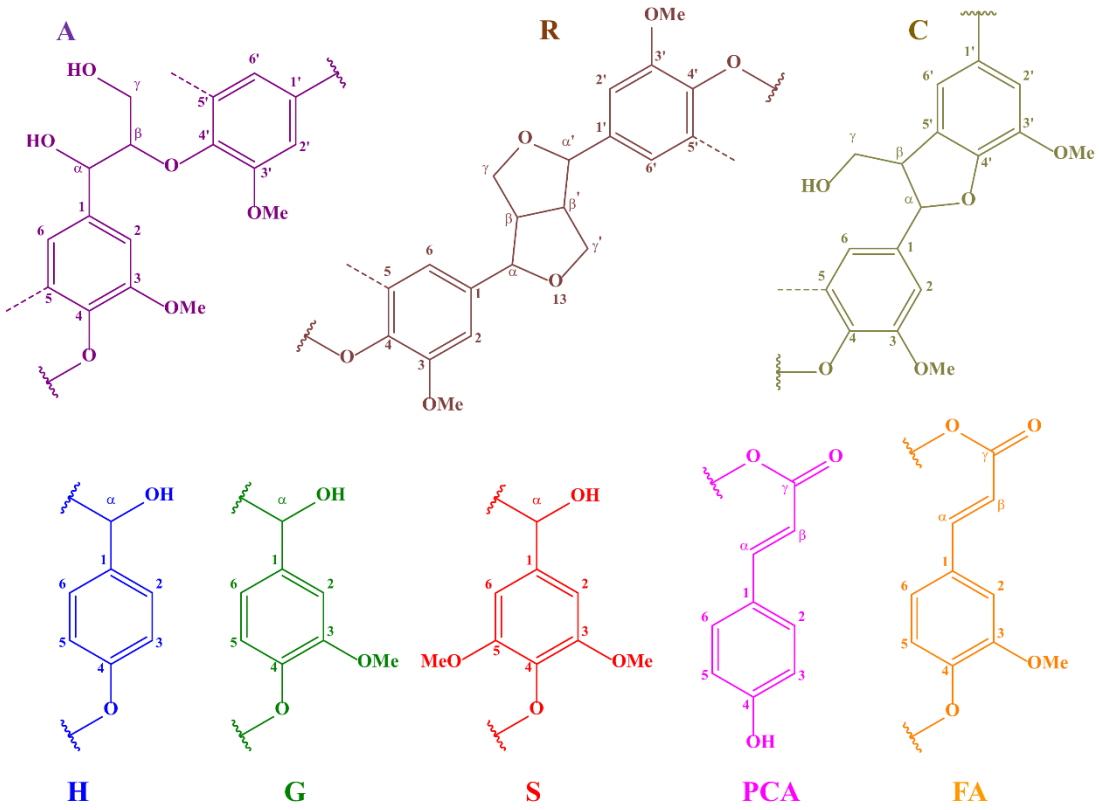

Figure 2.3 ^{13}C-^{1}H HSQC 2D-NMR spectra of (a) L-KB, (b) BO-SL/L, (c) BO-FP/PW, and possible structure presents in the compounds: (A) β−O−4 (aryl ether) (R) Resinol (C) Coumarate (H) p-Hydroxyphenyl (G) Guaiacyl (S) Syringyl (PCA) p-Coumarate (FA) Ferculate.

The monomeric components present in the L-KB, BO-SL/L, and BO-FP/PW were identified using GCMS analysis as depicted in Figure 2.4. The L-KB lignin was subjected to pyrolysis to shows GCMS peaks (Figure 2.4a). However, the peaks were generated through light vapors produced during pyrolysis that is the reason why we did not observe any peaks after 15 minutes of retention time. The main diagnostic products shown through pyrolysis vapors are G units because the kraft lignin originated from softwood species.[47] The GCMS spectrum of BO-SL/L (Figure 2.4b) shows peaks of compounds produced during the depolymerization of lignin using

ethanol solvent under the thermal environment. The compounds identified are alcohols, ketones, substituted phenols, nitrogen-containing compounds.[48,49] The ester-containing compounds are generated from the esterification reaction between ethanol and acids. The substituted phenols are G and H (p-hydroxyphenyl) type. The bio-oil (BO-FP/PW) yield from fast pyrolysis of pinewood contains a majority of aromatic and few nonaromatic compounds, as presented in Figure 2.4c (GCMS spectra of BO-FP/PW). It could be seen that the phenolic compounds are mostly 2-methoxy phenol, also denoted as G units, which can be derived from pyrolytic lignin (lignin-derived fragments) present in the organic phase of bio-oil, and is also known to be prevalent in pine from softwood species.[50] Whereas, the oxygenated compounds such as acids, esters, and heterocyclic organics also detected due to breakage of side chains in lignin and decomposition of cellulose and hemicellulose.

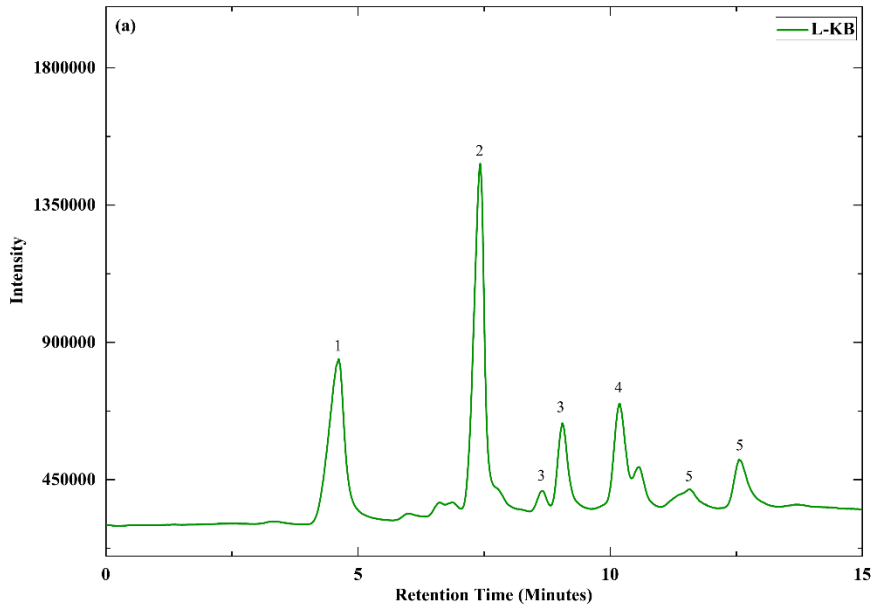

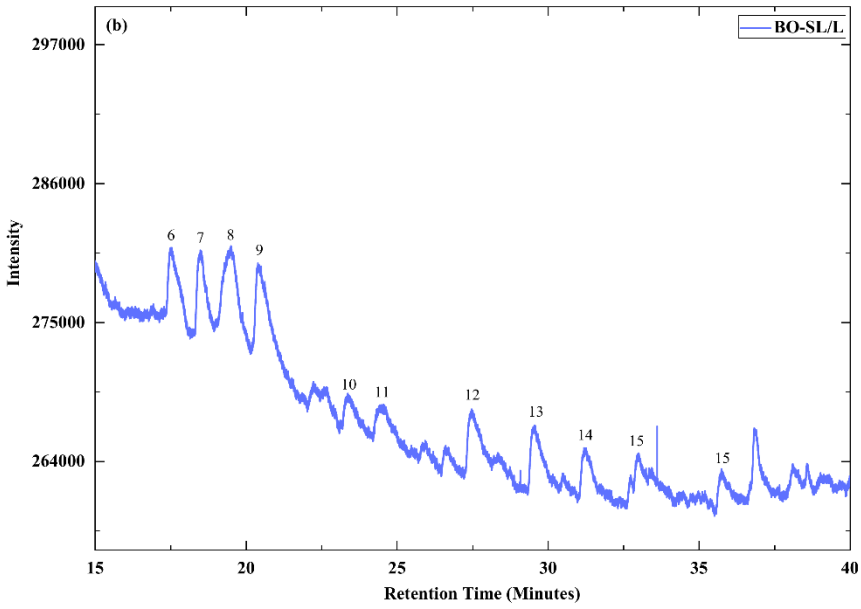
(b)
BO-SL/L
297000
286000
275000
264000
Intensity
6
7
8
9
10
11
12
13
14
15
15
15
20
25
30
35
40
Retention Time (Minutes)

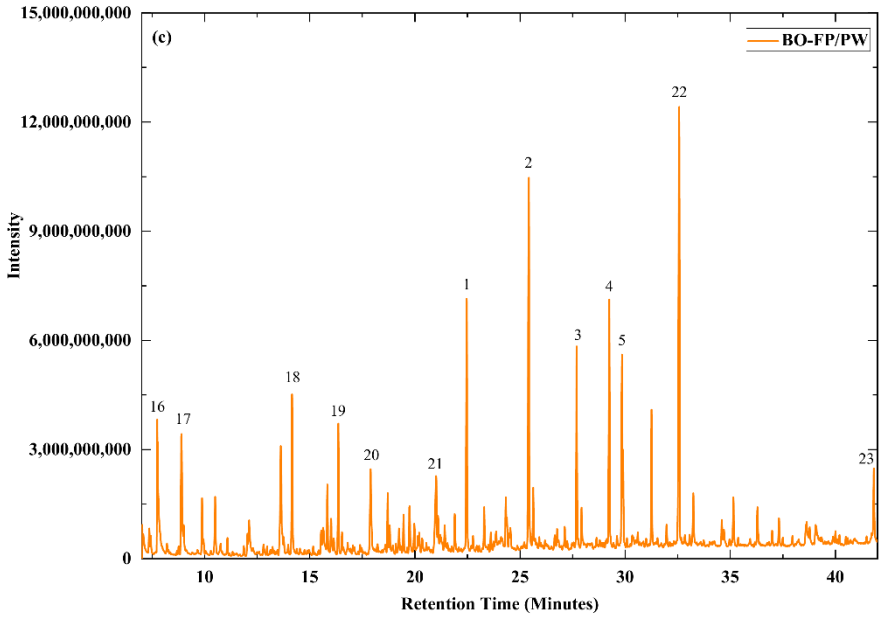
(c)
BO-FP/PW
15,000,000,000
12,000,000,000
9,000,000,000
6,000,000,000
3,000,000,000
0
Intensity
16
17
18
19
20
21
1
2
3
4
5
22
23
10
15
20
25
30
35
40
Retention Time (Minutes)

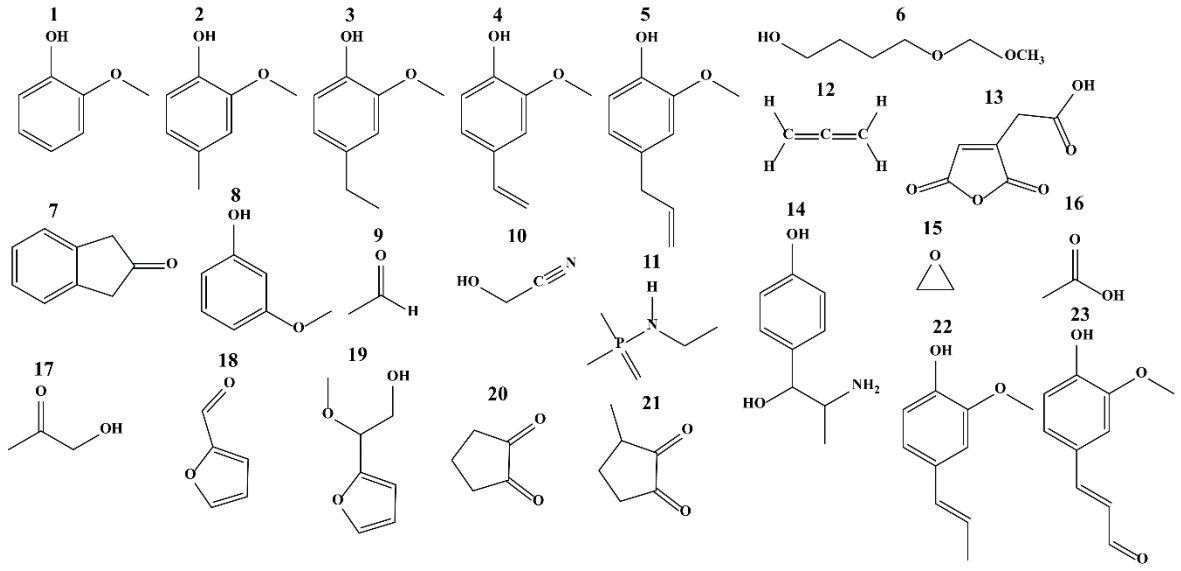

Figure 2.4 GCMS spectra of (a) L-KB, (b) BO-SL/L, (c) BO-FP/PW, and compounds observed in the structures.

Quantitative analysis of the carbohydrates present in the BO-SL/L and BO-FP/PW was carried out using the phenol-sulfuric acid colorimetric method. Here, in the study, glucose was used as a calibration standard because, after acid hydrolysis, the polymeric/oligomeric sugars present in the bio-oils are converted into glucose.[51,52] The absorbance maximum for glucose measured by UV-visible spectrophotometer was observed at 488 nm (Figure 2.5a). The generated calibration curve (Figure 2.5c) showed a linear relationship between absorbance and glucose concertation. Further, the calibration curve was used to measure the amount of carbohydrates in bio-oil using the maximum absorbance at 488 nm shown in Figure 2.5b.

Table 2.1 summarizes the carbohydrate content resulting from two bio-oils. The BO-FP/PW has an average of 24.05% of sugars in the structure. As outlined in the method, BO-FP/PW was produced from the fast pyrolysis of pine wood. During pyrolysis of biomass (pine wood), a high yield of anhydrosugars was generated through the cleavage of glycosidic bonds in cellulose.[53]

However, the organic phase of bio-oil was used having high polarity compounds such as sugars. Therefore, carbohydrates in the organic phase of BO-FP/PW could be associated with the water-insoluble sugars linked to the pyrolytic lignin. An average of 33.61% carbohydrate (sugar) was obtained for BO-SL/L, which was produced from solvent liquefaction of lignin. The authors are unaware of the source of the lignin, but the 2D HSQC spectrum (Figure 2.3b), provided information on the presence of ferculate units in the lignin structure. According to Ghaffar et al.[54], lignin crosslinked with the carbohydrates via ferculate, and during liquefaction, the carbohydrates entered the bio-oil.

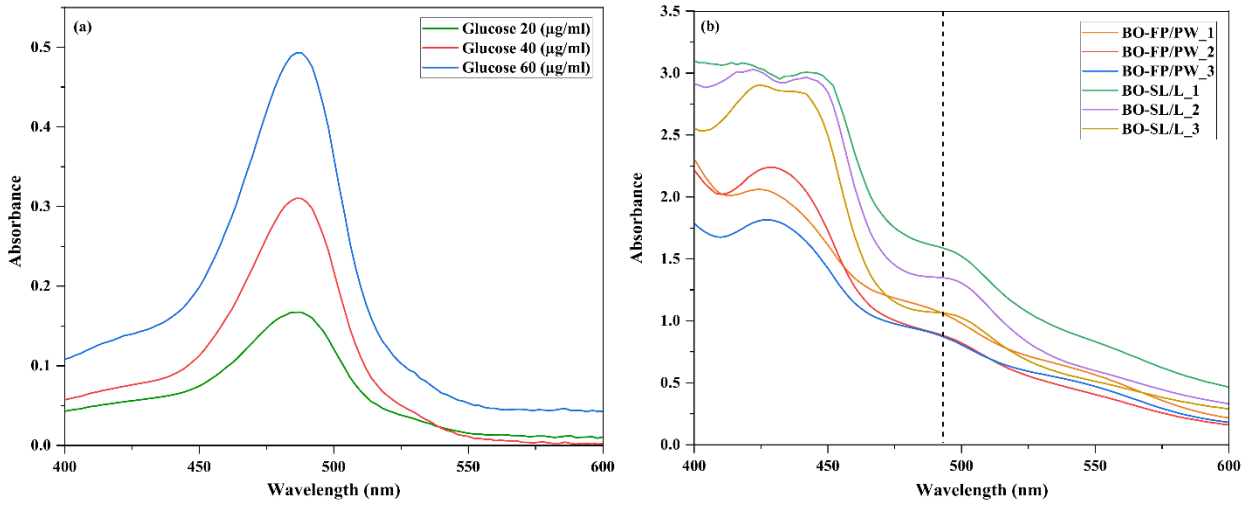

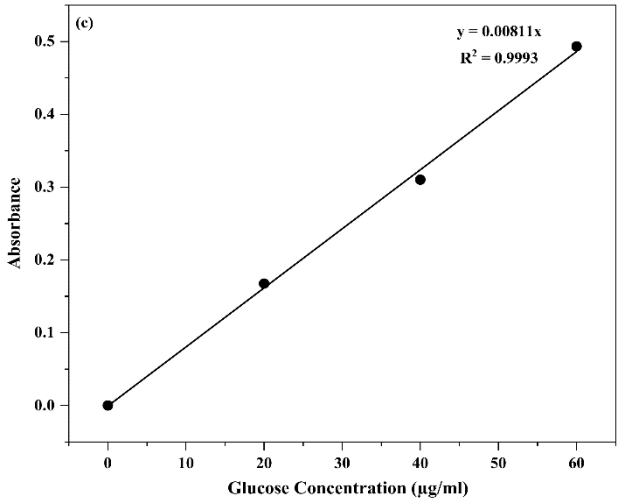

Figure 2.5 Carbohydrates measurement by phenol-sulfuric acid assay (a) Ultraviolet spectra of different concertation of glucose sugar (b) ultraviolet spectra of bio-oils: BO-SL/L and BO-FP/PW (c) ultraviolet calibration curve of glucose sugar.

Table 2.1 Carbohydrate in bio-oil analyzed by the phenol-sulfuric acid assay

	Bio-oils	
	BO-SL/L	BO-FP/PW
Carbohydrate content (%)	33.61 ± 6.79	24.05 ± 2.71

2.3.2 Characterization of NPF Resins

The four different NPF resins were prepared by polymerization reaction between reactive sites in phenol or substituted phenol and formaldehyde under the influence of temperature and catalyst. This forms methylene bridges between ortho and para sites of phenolates in the NPF resin structure. Thus, the chemical structures of the synthesized NPF resins were investigated by FTIR and ^{1}H NMR techniques.

The FTIR spectra for 100-NPF, 50-NPF-L-KB, 50-NPF-BO-SL/L and 50-NPF-BO-FP/PW resins are shown in Figure 2.6 with the respective assignment according to literature data.[55,56] The peaks between 3500−3300 cm^{-1} belonged to stretching vibrations of –OH presents in aromatic and aliphatic hydroxyl. The peaks in the C–H stretching region were assigned to methyl/methylene (CH_3/CH_2) groups. The carbonyl peak was observed in biobased NPF resin spectra (Figure 2.6b-d). This was expected since the biobased NPF resins were synthesized from lignin and bio-oils. The peaks that appeared at 1600 cm^{-1} and 1515 cm^{-1} corresponds to the aromatic ring vibrations of phenyl units.[57]

The presence of signals in the region of 1470−1430 cm^{-1} confirmed the formation of a methylene bridge (CH_2) in the phenolic rings.[58] In the biobased NPF resin spectra, a peak at 1020 cm^{-1} can be seen related to the C–H deformation for the guaiacyl unit. The absorption peaks at 815 cm^{-1} and 750 cm^{-1} were attributed to para and ortho position addition in the phenolic rings, respectively. Whereas the ortho position signal is more prominent in all the spectra with oxalic acid catalyst system as proposed by Jing et al.[59]

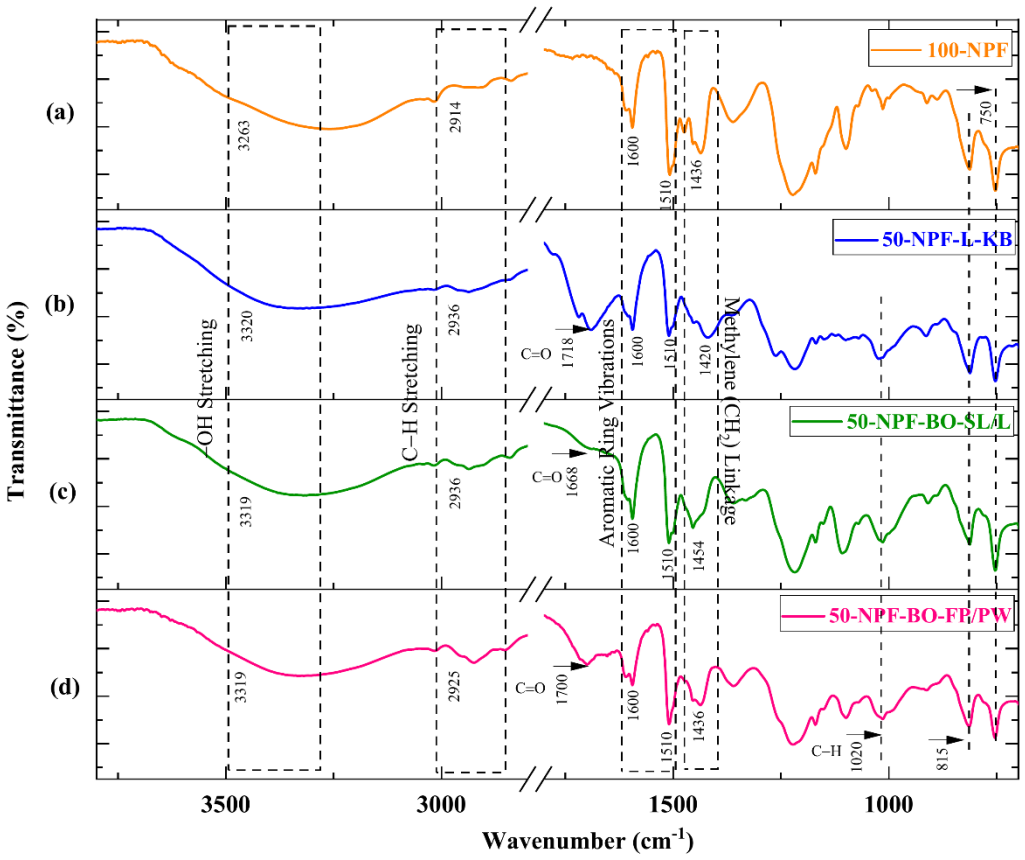

Figure 2.6 FTIR spectra of (a) 100-NPF, (b) 50-NPF-L-KB, (c) 50-NPF-BO-SL/L, and (d) 50-NPF-BO-FP/PW.

^{1}H NMR spectra of synthesized NPF resins are presented in Figure 2.7. Each resin spectrum was segmented and integrated. The signal with the chemical shift of 2.5 ppm related to the DMSO-d_6 solvent. The peaks between 7.34−6.5 ppm are attributed to the aromatic protons of all benzene rings and unconjugated alkene protons. Signals at 5.45−4.45 ppm arose from the aliphatic and aromatic hydroxyl protons. At the same time, the high-intensity signals in this region for bio-obased NPF resins (Figure 2.7b-d) suggest the presence of aliphatic hydroxyl groups. The protons related to the methylene linkages (*o-o*, *o-p* and *p-p*) formed during resin synthesis were noticed between 4.2−3.2 ppm. A similar observation was found in the literature for phenol-

formaldehyde resins.[60–64] However, the peaks in this region overlapped with the protons from the methoxyls functional group attached to phenolic rings of G, S, and H units of LCBM.[65] The peaks in 50-NPF-BO-SL/L are more crowded as it comes from the methoxy H of syringyl units. The 2D HSQC NMR spectrum confirms the presence of syringyl units in BO-SL/L. The 50-NPF-BO-SL/L and 50-NPF-BO-FP/PW show high-intensity signals at 1.5−0.8 ppm, which might be due to the H of aliphatic side chains. The integral area ratio (peaks at 7.34−6.5 ppm to that 4.2−3.2 ppm) for all the NPF resins are 1:0.79 (Figure 2.7a), 0.99:0.71 (Figure 2.7b), 0.99:1.15 (Figure 2.7c) and 0.98:0.98 (Figure 2.7d). The discrepancy between the aromatic-H and methylene-H ratios was due to the overlapping of peaks.

The results from FTIR and ^{1}H NMR suggested that methylene linkages have formed during the polymerization of the respective NPF resins.

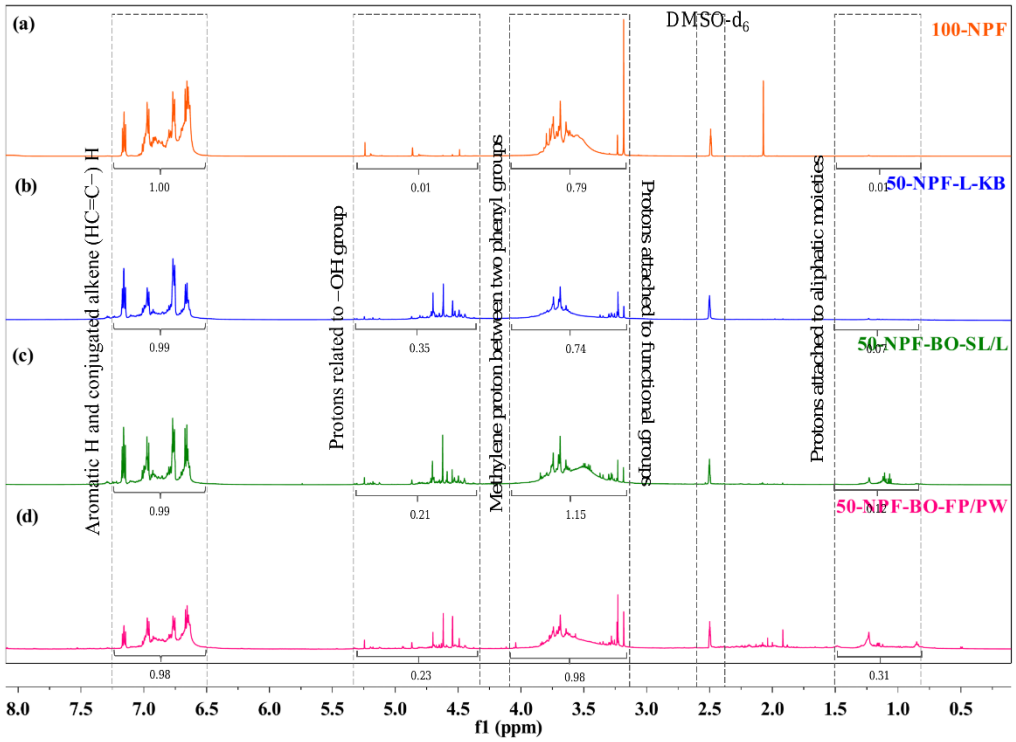

Figure 2.7 1H NMR spectra of (a) 100-NPF, (b) 50-NPF-L-KB, (c) 50-NPF-BO-SL/L, and (d) 50-NPF-BO-FP/PW.

2.3.3 Crosslinking of NPF resins and Thermal study by DSC

In general, NPF resin needs to be crosslinked by adding a curing agent, hexamethylenetetramine (HMTA). This curing process happened in two stages. In the first stage, NPF resin reacts with HMTA and forms initial intermediates such as benzoxazines and benzylamines. Further thermal decomposition of these curing intermediates generates methylene bridge for phenolic rings.[66,67] The DSC data in Table 2.2 reported exothermic heat (ΔH_c) developed during the curing process NPF resins, which attributed to the formation of methylene bridges.

The biobased NPF adhesive exhibited different curing properties from the 100-NPF adhesive. The decrease in ΔH_c (31.85 J/g, 14.51 J/g and 19.68 J/g)) were evident when 50% (w/w) of phenol is replaced by L-KB, BO-SL/L, and BO-FP/PW, respectively, which could be due to the

lower chemical reactivity of the phenolic rings in the LCBM structure causing steric hindrance during the curing process. The same observation may be connected with curing peak temperature (T_p) of biobased NPF adhesive. However, compared to the data in Table 2.2, the 50-NPF-L-KB adhesive has similar values of ΔH_c and T_p as 100-NPF adhesive, which suggests that L-KB has more accessible sites in the structure for the curing process compared to the bio-oils, which the previous characterization has confirmed. The endothermic peak (Figure 2.8) observed during the curing process might be due to the condensation reaction of methylol group with phenol.

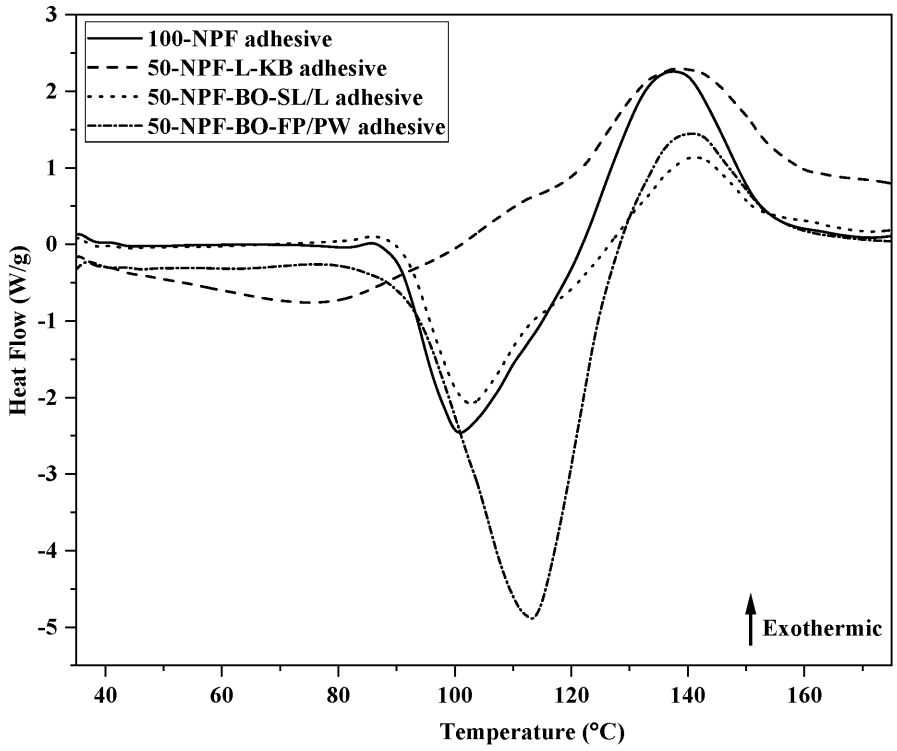

Figure 2.8 DSC thermograms of the NPF resin adhesives.

Table 2.2 DSC Data for NPF resins [a]

Adhesives	ΔH_c (J/g)	T_p (°C)
100-NPF adhesive	36.31	137.53
50-NPF-L-KB adhesive	31.85	138.59
50-NPF-BO-SL/L adhesive	14.51	141.31
50-NPF-BO-FP/PW adhesive	19.68	140.98

[a] ΔH_c = curing exotherm enthalpy and T_p = curing peak temperature

2.3.4 Bonding Performance of NPF resin Adhesives on Wood Substrates

2.3.4.1 Water Absorption and Thickness Swelling

One of the main concerns in applying wood adhesives for exterior applications is the impact of water or humid environment on the wood bonding. To understand the effect, we have measured the mass and thickness gain of the wood panels after soaking them in water for 24 hours, and the values are listed in Table 2.3. The result showed that the WA values of the biobased NPF resins are relatively high. Among them, the wood samples glued with 50-BO-FP/PW adhesive absorbed more water compared to other adhesives ($p < 0.05$, Table 2.3). This behavior may be correlated with carbohydrates (sugar) in the structure (as evidenced by Table 2.1). The same observation can be valid for 50-NPF-BO-SL/L adhesive glued wood. At the same time, the 43.96% of WA in 50-NPF-L-KB was due to the hydroxyl group in the lignin. Similar results were also observed in another biobased adhesive in the literature.[68,69]

The thickness swelling data in Table 2.3 displays clear evidence of dimensional change of the wood matrix due to interaction of the hydrophilic group present in the adhesive with the water molecule. In contrast, the wood sample bonded with the 100-NPF adhesive showed a high TS

value ($p < 0.05$, Table 2.3), this might have been due to the penetration of water into the voids of the wood itself.[70]

Table 2.3 Water Absorption (WA %) and Thickness Swelling (% TS) of the wood specimens prepared with different adhesives[a]

Adhesives	Mean ± Standard Deviation	
	Water Absorption (%)	% Thickness Swelling
100-NPF adhesive	42.80 ± 1.25 b	11.15 ± 2.94 a
50-NPF-L-KB adhesive	43.96 ± 2.72 b	07.95 ± 1.08 b
50-NPF-BO-SL/L adhesive	43.06 ± 2.55 b	09.01 ± 2.53 ab
50-NPF-BO-FP/PW adhesive	49.00 ± 1.64 a	11.04 ± 1.71 a

[a]Water absorption (WA %) and thickness swelling (% TS) of the glued wood specimens were analyzed with one-way ANOVA followed by Tukey's *post-hoc* test. Different letters for each column represent significantly different water absorption and thickness swelling respectively ($p < 0.05$).

2.3.4.2 Tensile Shear Strength

Tensile shear strength (wet and dry) has been conducted on each glued wood sample and presented in Figure 2.9. There was no significant difference found between the wood specimens bonded with 100-NPF and 50-NPF-L-KB adhesive ($p > 0.05$, Figure 2.9). This suggests that there is a benefit in replacing 50% of phenol with kraft biorefinery obtained lignin. The 50-NPF-L-KB adhesive glued wood product gave the highest strength (3.46 ± 0.55 MPa) among all the tested adhesives. This high adhesion strength could be ascribed to the functional macromolecular structure of lignin having high molar mass, which facilitates the bonding with the wood substrate

during the curing process. This observation is in good agreement with the literature reported for lignin-based wood adhesives.[24,71,72] Furthermore, the bonding strength of wood samples pressed with 50-NPF-BO-SL/L and 50-NPF-BO-FP/PW adhesive were significantly lower than 50-NPF-L-KB adhesive ($p < 0.05$, Figure 2.9). The possible reason should be that along with phenolic compounds (H, G, and S units), other compounds such as aliphatic fractions and carbohydrates are detected in the bio-oils as discussed in characterization, limiting the reactivity and interaction between functional groups in the resin.[73,74]

Regarding the wet strength, after water soaking in water for 24 hours, the strength of all glued samples drastically decreased ($p < 0.05$, Figure 2.9). This would be because the cohesion within the adhesive is destroyed by absorbed moisture. Overall, the shear strength values obtained at dry and wet conditions can meet the standard specified by the Engineering Wood Association (APA) except for 50-NPF-BO-SL/L adhesive at the wet condition.

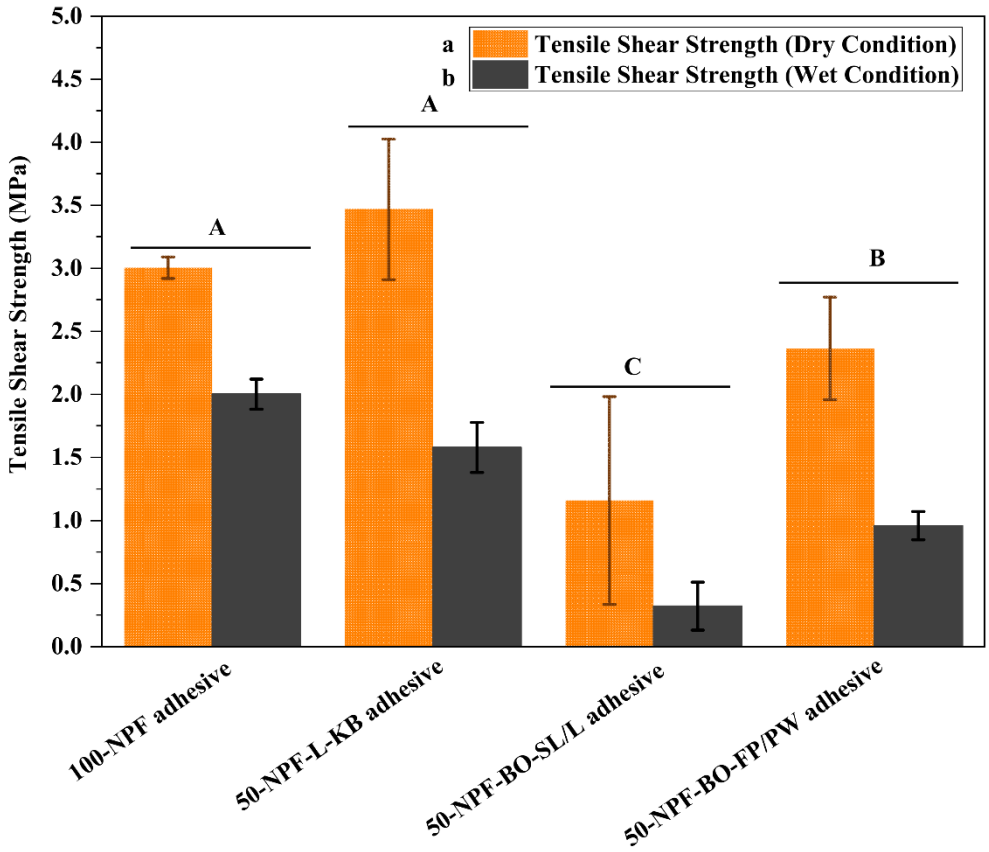

Figure 2.9 The dry and wet shear bonding strength of the wood specimens bonded with different adhesives: 100-NPF adhesive, 50-NPF-L-KB adhesive, 50-NPF-BO-SL/L adhesive, and 50-NPF-BO-FP/PW adhesive. Four wood samples per adhesive for each strength measurement were prepared. The data are the means of five replicates, and the error bars represent standard deviation (SD). The obtained adhesion data was analyzed using two-way ANOVA followed by Tukey's post-hoc test. Different letters on the bar represent significantly different adhesion strengths ($p < 0.05$).

2.4 Conclusions

This experimental work represents different biorefinery approaches to produce phenolic sources (L-KB, BO-SL/L, and BO-FP/PW) substitution to develop wood adhesives. The structure of

these LCBM phenolic sources was analyzed using FTIR, ^{13}C-^{1}H HSQC 2D-NMR, GCMS, and carbohydrate analysis techniques. The 2D-NMR and GCMS results demonstrate that most 'G-type' units are present in every structure which makes them suitable for NPF resin synthesis. Using FTIR and ^{1}H-NMR, it was possible to explain that the NPF resins are successfully synthesized, forming methylene linkages in their structures. DSC analysis was used to investigate the curing process of the NPF resin, and with the generated data, we designed an optimized curing temperature for wood bonding. The ANOVA analysis clarified a statistically significant difference between the bonding strength of biobased NPF resin adhesives. The dry bonding strength of all NPF resins was significantly higher than the wet bonding strength. Overall, lignin-derived from kraft biorefinery (L-KB) was the appropriate substitute for petroleum-based phenol in NPF resin synthesis because it shows high bonding strength with moderate curing energy.

2.5 References

(1) A. Pizzi and K. L. Mittal. *Handbook of Adhesive Technology Third Edition*; 2018.

(2) López, F. J. D.; Montalvo, C. A Comprehensive Review of the Evolving and Cumulative Nature of Eco-Innovation in the Chemical Industry. *J. Clean. Prod.* **2015**, *102*, 30–43. https://doi.org/10.1016/j.jclepro.2015.04.007.

(3) Cherubini, F. The Biorefinery Concept: Using Biomass Instead of Oil for Producing Energy and Chemicals. *Energy Convers. Manag.* **2010**, *51* (7), 1412–1421. https://doi.org/10.1016/j.enconman.2010.01.015.

(4) Takkellapati, S.; Li, T.; Gonzalez, M. A. An Overview of Biorefinery-Derived Platform Chemicals from a Cellulose and Hemicellulose Biorefinery. *Clean Technol. Environ. Policy* **2018**, *20* (7), 1615–1630. https://doi.org/10.1007/s10098-018-1568-5.

(5) Limayem, A.; Ricke, S. C. Lignocellulosic Biomass for Bioethanol Production: Current Perspectives, Potential Issues and Future Prospects. *Prog. Energy Combust. Sci.* **2012**, *38* (4), 449–467. https://doi.org/10.1016/j.pecs.2012.03.002.

(6) Hu, J.; Zhang, Q.; Lee, D. J. Kraft Lignin Biorefinery: A Perspective. *Bioresour. Technol.* **2018**, *247* (September 2017), 1181–1183. https://doi.org/10.1016/j.biortech.2017.08.169.

(7) Azadi, P.; Inderwildi, O. R.; Farnood, R.; King, D. A. Liquid Fuels, Hydrogen and Chemicals from Lignin: A Critical Review. *Renew. Sustain. Energy Rev.* **2013**, *21*, 506–523. https://doi.org/10.1016/j.rser.2012.12.022.

(8) Kouisni, L.; Gagné, A.; Maki, K.; Holt-Hindle, P.; Paleologou, M. LignoForce System for the Recovery of Lignin from Black Liquor: Feedstock Options, Odor Profile, and Product Characterization. *ACS Sustain. Chem. Eng.* **2016**, *4* (10), 5152–5159. https://doi.org/10.1021/acssuschemeng.6b00907.

(9) Lake, M. A.; Blackburn, J. C. SLRP™ - An Innovative Lignin-Recovery Technology. *Cellul. Chem. Technol.* **2014**, *48* (9–10), 799–804.

(10) Richter, A. P.; Bharti, B.; Armstrong, H. B.; Brown, J. S.; Plemmons, D.; Paunov, V. N.; Stoyanov, S. D.; Velev, O. D. Synthesis and Characterization of Biodegradable Lignin Nanoparticles with Tunable Surface Properties. *Langmuir* **2016**, *32* (25), 6468–6477. https://doi.org/10.1021/acs.langmuir.6b01088.

(11) Medoff Marschal, Masterman Thomas, F. M. *Processing of Biomass Materials*; 2016.

(12) Doassans-Carrère, N.; Ferrasse, J. H.; Boutin, O.; Mauviel, G.; Lédé, J. Comparative Study of Biomass Fast Pyrolysis and Direct Liquefaction for Bio-Oils Production: Products Yield and Characterizations. *Energy and Fuels* **2014**, *28* (8), 5103–5111. https://doi.org/10.1021/ef500641c.

(13) Brand, S.; Hardi, F.; Kim, J.; Suh, D. J. Effect of Heating Rate on Biomass Liquefaction: Differences between Subcritical Water and Supercritical Ethanol. *Energy* **2014**, *68*, 420–427. https://doi.org/10.1016/j.energy.2014.02.086.

(14) Arpa Ghosh, M. R. H. Solvent Liquefaction. In *Thermochemical Processing of Biomass: Conversion into Fuels, Chemicals and Power, Second Edition*; Brown, R. C., Ed.; 2019; pp 257–306. https://doi.org/org/10.1002/9781119417637.ch8.

(15) Kim, J.; Won, H.; Min, S.; Jae, J.; Park, Y. Bioresource Technology Overview of the Recent Advances in Lignocellulose Liquefaction for Producing Biofuels , Bio-Based Materials and Chemicals. *Bioresour. Technol.* **2019**, *279* (January), 373–384. https://doi.org/10.1016/j.biortech.2019.01.055.

(16) Kirtania, K. Thermochemical Conversion Processes for Waste Biorefinery. In *Waste Biorefinery: Potential and Perspectives*; Bhaskar, T., Pandey, A., Mohan, S. V., Lee, D.-J., Khanal, S. K., Eds.; 2018; pp 129–156. https://doi.org/org/10.1016/B978-0-444-63992-9.00004-5.

(17) Chiaramonti, D.; Prussi, M.; Buffi, M.; Rizzo, A. M.; Pari, L. Review and Experimental Study on Pyrolysis and Hydrothermal Liquefaction of Microalgae for Biofuel Production. *Appl. Energy* **2017**, *185*, 963–972. https://doi.org/10.1016/j.apenergy.2015.12.001.

(18) Balat, M.; Balat, M.; Kirtay, E.; Balat, H. Main Routes for the Thermo-Conversion of Biomass into Fuels and Chemicals. Part 1: Pyrolysis Systems. *Energy Convers. Manag.* **2009**, *50* (12), 3147–3157. https://doi.org/10.1016/j.enconman.2009.08.014.

(19) Alsbou, E.; Helleur, B. Accelerated Aging of Bio-Oil from Fast Pyrolysis of Hardwood. *Energy and Fuels* **2014**, *28* (5), 3224–3235. https://doi.org/10.1021/ef500399n.

(20) Mohan, D.; Pittman, C. U.; Steele, P. H. Pyrolysis of Wood/Biomass for Bio-Oil: A

Critical Review. *Energy and Fuels* **2006**, *20* (3), 848–889. https://doi.org/10.1021/ef0502397.

(21) Effendi, A.; Gerhauser, H.; Bridgwater, A. V. Production of Renewable Phenolic Resins by Thermochemical Conversion of Biomass: A Review. *Renew. Sustain. Energy Rev.* **2008**, *12* (8), 2092–2116. https://doi.org/10.1016/j.rser.2007.04.008.

(22) Hocking, M. B. Commercial Polycondensation (Step-Growth) Polymers. *Handb. Chem. Technol. Pollut. Control* **2005**, 689–712. https://doi.org/10.1016/b978-012088796-5/50024-7.

(23) Granado, L.; Tavernier, R.; Henry, S.; Auke, R. O.; Foyer, G.; David, G.; Caillol, S. Toward Sustainable Phenolic Thermosets with High Thermal Performances. *ACS Sustain. Chem. Eng.* **2019**, *7* (7), 7209–7217. https://doi.org/10.1021/acssuschemeng.8b06286.

(24) Wang, L.; Lagerquist, L.; Zhang, Y.; Koppolu, R.; Tirri, T.; Sulaeva, I.; Schoultz, S. von; Vähäsalo, L.; Pranovich, A.; Rosenau, T.; Eklund, P. C.; Willför, S.; Xu, C.; Wang, X. Tailored Thermosetting Wood Adhesive Based on Well-Defined Hardwood Lignin Fractions. *ACS Sustain. Chem. Eng.* **2020**, *8* (35), 13517–13526. https://doi.org/10.1021/acssuschemeng.0c05408.

(25) Kalami, S.; Arefmanesh, M.; Master, E.; Nejad, M. Replacing 100% of Phenol in Phenolic Adhesive Formulations with Lignin. *Journal of Applied Polymer Science*. 2017. https://doi.org/10.1002/app.45124.

(26) Jin, Y.; Cheng, X.; Zheng, Z. Preparation and Characterization of Phenol-Formaldehyde Adhesives Modified with Enzymatic Hydrolysis Lignin. *Bioresour. Technol.* **2010**, *101* (6), 2046–2048. https://doi.org/10.1016/j.biortech.2009.09.085.

(27) Sarika, P. R.; Nancarrow, P.; Khansaheb, A.; Ibrahim, T. Bio-Based Alternatives to

Phenol and Formaldehyde for the Production of Resins. *Polymers*. 2020, pp 1–24. https://doi.org/10.3390/polym12102237.

(28) Yan, N.; Zhang, B.; Zhao, Y.; Farnood, R. R.; Shi, J. Application of Biobased Phenol Formaldehyde Novolac Resin Derived from Beetle Infested Lodgepole Pine Barks for Thermal Molding of Wood Composites. *Ind. Eng. Chem. Res.* **2017**, *56* (22), 6369–6377. https://doi.org/10.1021/acs.iecr.7b00353.

(29) Pan, H. Wood Liquefaction in the Presence of Phenol with a Weak Acid Catalyst and Its Potential for Novolac Type Wood Adhesives. Ph.D. Dissertation, Louisiana State University and Agricultural and Mechanical College, Baton Rouge, LA, 2007.

(30) Barde, M.; Edmunds, C. W.; Labbé, N.; Auad, M. L. Fast Pyrolysis Bio-Oil from Lignocellulosic Biomass for the Development of Bio-Based Cyanate Esters and Cross-Linked Networks. *High Perform. Polym.* **2019**, *31* (9–10), 1140–1152. https://doi.org/10.1177/0954008319829517.

(31) Fan, D.; Xie, X.; Li, Y.; Li, L.; Sun, J. Aromatic Compounds from Lignin Liquefaction over ZSM-5 Catalysts in Supercritical Ethanol. *Chem. Eng. Technol.* **2018**, *41* (3), 509–516. https://doi.org/10.1002/ceat.201700396.

(32) Nandiwale, K. Y.; Danby, A. M.; Ramanathan, A.; Chaudhari, R. V.; Subramaniam, B. Dual Function Lewis Acid Catalyzed Depolymerization of Industrial Corn Stover Lignin into Stable Monomeric Phenols. *ACS Sustain. Chem. Eng.* **2019**, *7* (1), 1362–1371. https://doi.org/10.1021/acssuschemeng.8b05077.

(33) Kim, P.; Weaver, S.; Noh, K.; Labbé, N. Characteristics of Bio-Oils Produced by an Intermediate Semipilot Scale Pyrolysis Auger Reactor Equipped with Multistage Condensers. *Energy and Fuels* **2014**, *28* (11), 6966–6973.

https://doi.org/10.1021/ef5016186.

(34) Barde, M.; Avery, K.; Edmunds, C. W.; Labbé, N.; Auad, M. L. Cross-Linked Acrylic Polymers from the Aqueous Phase of Biomass Pyrolysis Oil and Acrylated Epoxidized Soybean Oil. *ACS Sustain. Chem. Eng.* **2019**, *7* (2), 2216–2224. https://doi.org/10.1021/acssuschemeng.8b04897.

(35) M, D.; SMITH, G. J. K. H. P. A. R. F. A New Paper Chromatography Solvent For. **2008**, *499* (4265), 4265.

(36) Albalasmeh, A. A.; Berhe, A. A.; Ghezzehei, T. A. A New Method for Rapid Determination of Carbohydrate and Total Carbon Concentrations Using UV Spectrophotometry. *Carbohydr. Polym.* **2013**, *97* (2), 253–261. https://doi.org/10.1016/j.carbpol.2013.04.072.

(37) Fournier, E. Colorimetric Quantification Of Carbohydrates. *Handb. Food Anal. Chem.* **2005**, *1–2*, 653–660. https://doi.org/10.1002/0471709085.ch15.

(38) Conner, A. Wood: Adhesives. Encyclopedia of Materials: Science and Technology. *Adhes. wood* **2001**, 17.

(39) Jing, Z.; Lihong, H.; Bingchuan, L.; Caiying, B.; Puyou, J.; Yonghong, Z. Preparation and Characterization of Novolac Phenol-Formaldehyde Resins with Enzymatic Hydrolysis Lignin. *Journal of the Taiwan Institute of Chemical Engineers*. 2015, pp 178–182. https://doi.org/10.1016/j.jtice.2015.03.023.

(40) Efhamisisi, D.; Thevenon, M. F.; Hamzeh, Y.; Karimi, A. N.; Pizzi, A.; Pourtahmasi, K. Induced Tannin Adhesive by Boric Acid Addition and Its Effect on Bonding Quality and Biological Performance of Poplar Plywood. *ACS Sustain. Chem. Eng.* **2016**, *4* (5), 2734–2740. https://doi.org/10.1021/acssuschemeng.6b00230.

(41) Conshohocken, W. Standard Test Method for Strength Properties of Adhesives in Plywood Type Construction in Shear by Tension Loading 1. **2020**, *i*, 1–4. https://doi.org/10.1520/D0906-20.responsibility.

(42) Passauer, L.; Salzwedel, K.; Struch, M.; Herold, N.; Appelt, J. Quantitative Analysis of the Etherification Degree of Phenolic Hydroxyl Groups in Oxyethylated Lignins: Correlation of Selective Aminolysis with FTIR Spectroscopy. *ACS Sustain. Chem. Eng.* **2016**, *4* (12), 6629–6637. https://doi.org/10.1021/acssuschemeng.6b01495.

(43) Moghaddam, L.; Rencoret, J.; Maliger, V. R.; Rackemann, D. W.; Harrison, M. D.; Gutiérrez, A.; Del Río, J. C.; Doherty, W. O. S. Structural Characteristics of Bagasse Furfural Residue and Its Lignin Component. An NMR, Py-GC/MS, and FTIR Study. *ACS Sustain. Chem. Eng.* **2017**, *5* (6), 4846–4855. https://doi.org/10.1021/acssuschemeng.7b00274.

(44) Zhao, J.; Xiuwen, W.; Hu, J.; Liu, Q.; Shen, D.; Xiao, R. Thermal Degradation of Softwood Lignin and Hardwood Lignin by TG-FTIR and Py-GC/MS. *Polym. Degrad. Stab.* **2014**, *108*, 133–138. https://doi.org/10.1016/j.polymdegradstab.2014.06.006.

(45) Rencoret, J.; Prinsen, P.; Gutiérrez, A.; Mart;nez, Á. T.; Del R;o, J. C. Isolation and Structural Characterization of the Milled Wood Lignin, Dioxane Lignin, and Cellulolytic Lignin Preparations from Brewer?S Spent Grain. *J. Agric. Food Chem.* **2015**, *63* (2), 603–613. https://doi.org/10.1021/jf505808c.

(46) Glasser, W. G. About Making Lignin Great Again—Some Lessons From the Past. *Frontiers in Chemistry*. 2019. https://doi.org/10.3389/fchem.2019.00565.

(47) Hita, I.; Heeres, H. J.; Deuss, P. J. Insight into Structure–Reactivity Relationships for the Iron-Catalyzed Hydrotreatment of Technical Lignins. *Bioresour. Technol.* **2018**, *267*

(July), 93–101. https://doi.org/10.1016/j.biortech.2018.07.028.

(48) Leng, L.; Zhang, W.; Peng, H.; Li, H.; Jiang, S.; Huang, H. Nitrogen in Bio-Oil Produced from Hydrothermal Liquefaction of Biomass: A Review. *Chem. Eng. J.* **2020**, *401* (April), 126030. https://doi.org/10.1016/j.cej.2020.126030.

(49) Guo, K.; Cheng, Q.; Jiang, J.; Xu, J.; Tan, W. Qualitative Analysis of Liquid Products Generated from Lignocellulosic Biomass Using Post-Target and Nontarget Analysis Methods and Liquefaction Mechanism Research. *ACS Sustainable Chemistry and Engineering*. 2020, pp 11099–11113. https://doi.org/10.1021/acssuschemeng.0c00539.

(50) Vitasari, C. R.; Meindersma, G. W.; de Haan, A. B. Water Extraction of Pyrolysis Oil: The First Step for the Recovery of Renewable Chemicals. *Bioresour. Technol.* **2011**, *102* (14), 7204–7210. https://doi.org/10.1016/j.biortech.2011.04.079.

(51) Johnston, P. A.; Brown, R. C. Quantitation of Sugar Content in Pyrolysis Liquids after Acid Hydrolysis Using High-Performance Liquid Chromatography without Neutralization. *J. Agric. Food Chem.* **2014**, *62* (32), 8129–8133. https://doi.org/10.1021/jf502250n.

(52) Rover, M. R. Analysis of Sugars and Phenolic Compounds in Bio-Oil. Ph.D. Dissertation, Iowa State University, 2013.

(53) Yu, Y.; Chua, Y. W.; Wu, H. Characterization of Pyrolytic Sugars in Bio-Oil Produced from Biomass Fast Pyrolysis. *Energy and Fuels* **2016**, *30* (5), 4145–4149. https://doi.org/10.1021/acs.energyfuels.6b00464.

(54) Ghaffar, S. H.; Fan, M. Structural Analysis for Lignin Characteristics in Biomass Straw. *Biomass and Bioenergy* **2013**, *57*, 264–279. https://doi.org/10.1016/j.biombioe.2013.07.015.

(55) Dante, R. C.; Santamaria, D. A.; Gil, J. M. Crosslinking and Thermal Stability of Thermosets Based on Novolak and Melamine. *J. Appl. Polym. Sci.* **2009**, *114* (6), 4059–4065. https://doi.org/10.1002/app.31114.

(56) Kumar, H.; Tripathi, S. K.; Mistry, S.; Bajpai, G. Synthesis, Characterization and Application of Coatings Based on Epoxy Novolac and Liquid Rubber Blend. *E-Journal Chem.* **2009**, *6* (4), 1253–1259. https://doi.org/10.1155/2009/826071.

(57) Guo, Z.; Liu, Z.; Ye, L.; Ge, K.; Zhao, T. The Production of Lignin-Phenol-Formaldehyde Resin Derived Carbon Fibers Stabilized by BN Preceramic Polymer. *Mater. Lett.* **2015**, *142*, 49–51. https://doi.org/10.1016/j.matlet.2014.11.068.

(58) Chen, Y.; Chen, Z.; Xiao, S.; Liu, H. A Novel Thermal Degradation Mechanism of Phenol-Formaldehyde Type Resins. *Thermochim. Acta* **2008**, *476* (1–2), 39–43. https://doi.org/10.1016/j.tca.2008.04.013.

(59) Jing, Z.; Lihong, H.; Bingchuan, L.; Caiying, B.; Puyou, J.; Yonghong, Z. Preparation and Characterization of Novolac Phenol-Formaldehyde Resins with Enzymatic Hydrolysis Lignin. *J. Taiwan Inst. Chem. Eng.* **2015**, *54*, 178–182. https://doi.org/10.1016/j.jtice.2015.03.023.

(60) Koley, R.; Kasilingam, R.; Sahoo, S.; Chattopadhyay, S.; Bhowmick, A. K. Synthesis and Characterization of Phenol Furfural Resin from Moringa Oleifera Gum and Biophenol and Its Application in Styrene Butadiene Rubber. *Ind. Eng. Chem. Res.* **2019**, *58* (40), 18519–18532. https://doi.org/10.1021/acs.iecr.9b03684.

(61) Yelle, D. J.; Ralph, J. Characterizing Phenol-Formaldehyde Adhesive Cure Chemistry within the Wood Cell Wall. *Int. J. Adhes. Adhes.* **2016**, *70*, 26–36. https://doi.org/10.1016/j.ijadhadh.2016.05.002.

(62) Huang, J.; Xu, M.; Ge, Q.; Lin, M.; Lin, Q.; Chen, Y.; Chu, J.; Dai, L.; Zou, Y. Controlled Synthesis of High-Ortho-Substitution Phenol-Formaldehyde Resins. *J. Appl. Polym. Sci.* **2005**, *97* (2), 652–658. https://doi.org/10.1002/app.21808.

(63) Kandola, B. K.; Krishnan, L.; Deli, D.; Luangtriratana, P.; Ebdon, J. R. Fire and Mechanical Properties of a Novel Free-Radically Cured Phenolic Resin Based on a Methacrylate-Functional Novolac and of Its Blends with an Unsaturated Polyester Resin. *RSC Adv.* **2015**, *5* (43), 33772–33785. https://doi.org/10.1039/c5ra01813g.

(64) Scariah, K. J.; Usha, K. M.; Narayanaswamy, K.; Shanmugam, K.; Sastri, K. S. Evaluation of Isomeric Composition of Resol-Type Phenol Formaldehyde Matrix Resins for Silica-Phenolic Composites and Its Effect on Cure Characteristics of the Resin. *Journal of Applied Polymer Science*. 2003, pp 2517–2524. https://doi.org/10.1002/app.12918.

(65) Wang, Y.; Wang, S.; Leng, F.; Chen, J.; Zhu, L.; Luo, Z. Separation and Characterization of Pyrolytic Lignins from the Heavy Fraction of Bio-Oil by Molecular Distillation. *Sep. Purif. Technol.* **2015**, *152*, 123–132. https://doi.org/10.1016/j.seppur.2015.08.011.

(66) Patel, J. P.; Xiang, Z. G.; Hsu, S. L.; Schoch, A. B.; Carleen, S. A.; Matsumoto, D. Characterization of the Crosslinking Reaction in High Performance Adhesives. *Int. J. Adhes. Adhes.* **2017**, *78* (August), 256–262. https://doi.org/10.1016/j.ijadhadh.2017.08.006.

(67) Wang, L.; Lagerquist, L.; Zhang, Y.; Koppolu, R.; Tirri, T.; Sulaeva, I.; von Schoultz, S.; Vahasalo, L.; Pranovich, A.; Rosenau, T.; Eklund, P. C.; Willfor, S.; Xu, C.; Wang, X. Tailored Thermosetting Wood Adhesive Based on Well-Defined Hardwood Lignin Fractions. *ACS Sustain. Chem. Eng.* **2020**.

https://doi.org/10.1021/acssuschemeng.0c05408.

(68) Mekonnen, T. H.; Mussone, P. G.; Choi, P.; Bressler, D. C. Adhesives from Waste Protein Biomass for Oriented Strand Board Composites: Development and Performance. *Macromol. Mater. Eng.* **2014**, *299* (8), 1003–1012. https://doi.org/10.1002/mame.201300402.

(69) Bandara, N.; Wu, J. Randomly Oriented Strand Board Composites from Nanoengineered Protein-Based Wood Adhesive. *ACS Sustain. Chem. Eng.* **2018**, *6* (1), 457–466. https://doi.org/10.1021/acssuschemeng.7b02686.

(70) Sarmin, S. N.; Zakaria, S. A. K. Y.; Kasim, J.; Shafie, A. Influence of Resin Content and Density on Thickness Swelling of Three-Layered Hybrid Particleboard Composed of Sawdust and Acacia Mangium. *BioResources* **2013**, *8* (4), 4864–4872. https://doi.org/10.15376/biores.8.4.4864-4872.

(71) Griffini, G.; Passoni, V.; Suriano, R.; Levi, M.; Turri, S. Polyurethane Coatings Based on Chemically Unmodified Fractionated Lignin. *ACS Sustain. Chem. Eng.* **2015**, *3* (6), 1145–1154. https://doi.org/10.1021/acssuschemeng.5b00073.

(72) Zhu, X.; Wang, D.; Li, N.; Sun, X. S. Bio-Based Wood Adhesive from Camelina Protein (a Biodiesel Residue) and Depolymerized Lignin with Improved Water Resistance. *ACS Omega* **2017**, *2* (11), 7996–8004. https://doi.org/10.1021/acsomega.7b01093.

(73) Zheng, P.; Chen, N.; Mahfuzul Islam, S. M.; Ju, L. K.; Liu, J.; Zhou, J.; Chen, L.; Zeng, H.; Lin, Q. Development of Self-Cross-Linked Soy Adhesive by Enzyme Complex from Aspergillus Niger for Production of All-Biomass Composite Materials. *ACS Sustain. Chem. Eng.* **2019**, *7* (4), 3909–3916. https://doi.org/10.1021/acssuschemeng.8b04993.

(74) Hemmilä, V.; Adamopoulos, S.; Karlsson, O.; Kumar, A. Development of Sustainable

Bio-Adhesives for Engineered Wood Panels-A Review. *RSC Adv.* **2017**, *7* (61), 38604–38630. https://doi.org/10.1039/c7ra06598a.

Chapter 3

Kraft Lignin Functionalization through Periodate Oxidation for the Development of Biobased Novolac Phenol-formaldehyde Resins for Wood-based Panels

This chapter is being prepared for submission[2]

3.1 Introduction

Engineered wood-based panels show a wide range of applications in internal wall partitioning, sheathing, roofing, ceilings, furniture, and structural insulated panels due to their design flexibility, durability, strength, and cost-effectiveness.[1,2] Laminated veneer lumber, plywood, particle boards, medium density boards (MDF), and oriented strand board (OSB) used mainly wood-based panels (WBPs).[3,4] In addition, wood adhesives have contributed to the fabrication and preparation of WBPs, accounting for nearly 65% of the total world adhesives.[5–7] Various wood adhesives on the market are thermoplastics and thermoset resins, such as phenol-formaldehyde (PF), melamine-formaldehyde (MF), urea-formaldehyde (UF), polyurethane and polymeric methylene diphenyl diisocyanate (pMDI).[8,9] Moreover, most of these resins are aldehyde-based adhesives, which have long dominated the wood adhesive industry owing to their high adhesion

[2] Bansode, A.; Portilla Villarreal L.; Auad, M. L.; Asafu-Adjaye O.; Via B. K.; Farag, R.; Vega Erramuspe I. B.; Kraft Lignin Functionalization through Periodate Oxidation for the Development of Biobased Novolac Phenol-formaldehyde Resins for Wood-based Panels, In Preparation, 2022

strength and low cost.[10] Among them, phenol-formaldehyde resins are predominantly used due to the broad range of commercially available phenol and formaldehyde; therefore, PF resins have gained more potential.[11,12] Depending on the structure and curing process, the PF resins are classified as resol type PF resin or novolac type PF resin. Resole-type PF resin is produced by the polycondensation reaction of phenol with the molar excess of formaldehyde (P/F molar ratio of 1:1.1 or more) under an alkaline catalyst. In contrast, the reaction of excess phenol with formaldehyde (P/F molar ratio 1:0.75 or less) in acidic conditions yields novolacs.[13–15]

However, the formation of these resins still relies on nonrenewable petrochemicals such as phenol and formaldehyde, which would release formaldehyde and other complex toxic substances at high concentration levels identified as hazardous to humans and pollute the environment during their production and use process. Thus, extensive research is being conducted in academia and industry for replacing phenol and formaldehyde with potential biobased renewable resources to produce greener wood adhesives.[14,16]

Within this context, "lignin" have acquired significant interest as a promising sustainable alternative for replacing phenol in PF resin due to their structural similarities of having active H from the aromatic hydroxyl-containing group (Ar–OH).[16] Lignin is one of the three polymers of lignocellulosic biomass, which is primarily composed of cellulose, hemicellulose, and lignin, found principally in the middle lamella that "glue" the cell wall of plants. This polyphenolic and amorphous macromolecule is the second most abundant resource after cellulose, and it is formed through radical polymerization of phenylpropane units: p-hydroxyphenyl (H), guaiacyl (G), and syringyl (S). The monomeric units H, G, and S are randomly linked through different linkages, including β-O-4, β-β and β-5 covalent bonds, depending upon the botanic origin and extraction process, resulting in versatile functionality.[17,18] In the pulp and paper mills, lignin is generated as

a waste byproduct (black liquor) during the delignification of the lignocellulosic biomass by immersing it in an aqueous solution with alkaline chemicals at elevated temperatures (cooking).[19] However, the lignin-containing black liquor, separated from the fibrous material after the cooking process, is underutilized and usually combusted for energy and heat production.[20] To this end, some processes are employed to recover lignin from black liquor. In this respect, Ingevity (formerly known as Westvaco) has been recovering lignin (marketed as INDULIN® trademark) from black liquor.[21] Also, an industrial kraft lignin marketed by Stora Enso (Finland) under the name Lineo™ used as a sustainable material for replacing a variety of phenol-resins and oil-based binders in asphalt.[22]

In recent decades, numerous research studies have been reported on exploiting lignin as a phenol replacement in PF resin synthesis for wood adhesives applications.[16,19,23–28] In our prior work, we successfully used kraft lignin (Indulin AT from Ingevity) as a partial replacement for phenolic monomer synthesis of biobased Novolac PF (BNPF) resin for wood bonding. The work showed that synthesized lignin-based PF resin exhibited the highest adhesion strength compared to the standard Novolac PF resin (NPF).[29] Despite these achievements in reducing phenol consumption in PF resin synthesis, using the second primary ingredient, i.e., formaldehyde, has remained a significant concern due to its high toxicity.[30] Hence, to further enhance the sustainability of the PF resin and broaden the utilization of lignin, the substitution of formaldehyde with a chemical modification of lignin has become an exciting area of research to explore different strategies.[31]

Among the various chemical modification routes, oxidation is a promising technique that selectively cleaves the chemical bonds and allows the addition of new functionalities (i.e., aldehydes and carboxylate groups). In this regard, periodate oxidation processes have been reported where highly reactive aldehyde groups are introduced into the structure by oxidizing the hydroxyl

groups. In the past, the cellulose is subjected to a reaction with the sodium periodate ($NaIO_4$), leading to a highly oxidized form of dialdehyde cellulose (DAC) through oxidation on C2 and C3 positions of the anhydroglucose units.[8,32,33] Considering the diversity of functional groups, specific oxidation of lignin has been carried out under mild conditions. Therein, β-O-4 linkages present in the lignin are selectively cleaved by a periodate oxidant, thereby adding aldehyde functionality to the lignin structure.[34] Zhang et al.[35] reported a two-step periodate oxidation of carbohydrate-enriched hydrolysis lignin leading to the formation of muconic functional groups in the lignin structure. Further, the periodate oxidized network can react with the hydroxyl and activates reactive phenolic sites during respective synthesis to yield environmental friendly biobased wood adhesives.[34,36]

Herein, this work intends to develop more sustainable PF resin wood adhesives. We describe the oxidation of hydroxyl vicinal to β-O-4 bond in the lignin structure using sodium periodate ($NaIO_4$) as an oxidizing agent under mild conditions. To better understand the chemical structure of the oxidized lignin, FTIR, elemental analysis, aldehyde content, and solid-state $^{1}H–^{13}C$ 2D HETCOR NMR techniques were used to investigate the structural features. A series of BNPF resins were synthesized by first replacing phenol with lignin (BNPLF), then by replacing formaldehyde with oxidized lignin (BNPFOL), and later by replacing both phenol and formaldehyde with lignin and oxidized lignin (BNPLFOL), respectively. The prepared resin adhesive was applied on the wood substrate, and respective adhesion strength was measured.

3.2 Experimental Section

3.2.1 Materials

Indulin AT lignin from a kraft pulping process was generously supplied by Ingevity Corporation, South Carolina. Phenol (99%), formalin solution (37% formaldehyde in water), ethanol (200 proof), methanol (99.8%), sulfuric acid (H_2SO_4; 95.0-98.0%), deuterated dimethyl sulfoxide (DMSO-d6, 99.9%), and hexamethylenetetramine (HMTA, 99+%) were supplied by VWR International, USA. Sodium periodate ($NaIO_4$, 99.0%) was purchased from Acros Organics, USA. 2, 4-dinitrophenylhydrazine (DNPH) and oxalic acid (anhydrous crystal, 98.0%) were acquired from Spectrum Chemical Manufacturing Corporation, USA.

3.2.2 Periodate Oxidation of Lignin

The periodate oxidation has been performed to introduce the aldehyde groups in the lignin by oxidizing the hydroxyl groups. Briefly, for each batch of periodate oxidized lignin, 20 g of Indulin AT kraft lignin (IN) was mixed with the 50 g $NaIO_4$ and added to the 500 mL ethanol (15%). Further, this mixture was loaded into the pressure-resistant bottle and wrapped with a layer of aluminum foil to prevent the decomposition of $NaIO_4$ by exposure to light. The reaction was carried out under mild stirring at room temperature allowing the oxidation to proceed overnight (or for 24 hours). The product was then purified using methanol by centrifuging and decanting at least three times. After that, the product was dried at 40 °C in a vacuum oven.

3.2.3 Structural Characterization of Periodate Oxidized Lignin

3.2.3.1 Fourier Transform Infrared (FTIR) Spectroscopy

FTIR analysis of Indulin AT lignin (L) and periodate oxidized lignin (OL) were carried out on Nicolet 6700 FTIR spectrophotometer (Thermo Fisher Scientific Instrument., USA) equipped

with attenuated total reflectance (ATR) accessory containing a diamond crystal. The spectrum was collected in transmission mode over a region of 4000 − 600 cm^{-1} using 64 scans at a resolution of 4 cm^{-1}. Before every sampling, the background spectrum was collected. The software used for FTIR evaluation was OMNIC Version 7.3.

3.2.3.2 Elemental Analysis

Elemental analysis (C, H, and N) of Indulin AT lignin (L) and periodate oxidized lignin (OL) were performed in a Flash 2000 Elemental Analyzer (Thermo Fisher Scientific, Bremen, Germany) operating with the dynamic flash combustion of the samples. The aspartic acid weight used as a standard was 3.00-4.00 mg, and the weight of the unknown samples. All samples were weighed in aluminum tin capsules and dropped into the combustion reactor (left furnace) from the Thermo Scientific™ MAS Plus Autosampler. The samples were combusted in the reactor initially set at 950 °C in oxygen and helium (carrier gas). The elemental gases were carried out into the gas chromatography column set at 75 °C and detected in a highly sensitive thermal conductivity detector (TCD) set at 1000 μV. The collected data were analyzed using Eager Xperience for flash elemental analyzers software (EA111X F/W Ver. 1.12, EA111x OCX Ver. 01.02). All the samples were analyzed in three replicate specimens. The results were reported as averaged values in percent by weight.

3.2.3.3 Determination of Aldehyde Content

In the analysis of aldehyde groups, often 2, 4-dinitrophenylhydrazine (DNPH) reagent is used, and the subsequent reagent solution was prepared using the procedure in the literature.[37,38] Briefly, 143 mg of DNPH has dissolved in 15 mL of concentrated sulfuric acid in 500 mL of a volumetric flask, and then 156.25 mL of ethanol (96%) in this mixture, and the final volume was

made up to the mark with distilled water. Later, the solution was placed in the ultrasonic bath for 15 minutes to achieve a homogenized solution. Alternatively, a blank solution was prepared with the same procedure except for adding the DNPH reagent. A series of standard solutions 20, 40, 60, 80, and 100 mg/mL were prepared using DNPH reagent solution to generate a calibration curve. After that, the quantitative aldehyde analysis of Indulin AT lignin (L) and periodate oxidized lignin (OL) was performed by weighing 30 mg of sample in 10 mL of the centrifuge tube, followed by the addition of 10 mL freshly prepared DNPH reagent solution. The subsequent reactive mixture was centrifuged for 10 minutes using 4200 rpm. Finally, the aldehyde content was investigated by measuring absorbance with a Genesys 150 UV−Visible spectrophotometer in the range of 200-800 nm using a blank solution as background. The amount of aldehyde generated was calculated using equation 3.1.[37]

$$\text{Aldehyde Concentration (mmol/g)} = \frac{\frac{\text{Reacted DNPH(mmol/g)}}{198.14}}{\text{Concentration (\%)}\times 10^{-4}} \quad [3.1]$$

where 198.14 is the molecular weight of DNPH.

3.2.3.4 Solid-state Two-Dimensional Heteronuclear Correlation Nuclear Magnetic Resonance (ss $^{1}H-^{13}C$ 2D HETCOR NMR)

Solid-state $^{1}H-^{13}C$ 2D HETCOR NMR experiment of Indulin AT lignin (L) and periodate oxidized lignin (OL) were performed Bruker AVIII-HD 500 nuclear magnetic resonance (NMR) spectrometer equipped with standard Bruker 3.2 mm CP-MAS at Magnetic Resonance Imaging Core Facility at Georgia Institute of Technology, Atlanta. The combination of cross-polarization (CP) with magic angle spinning (MAS) is commonly used to perform solid-state NMR. The HETCOR measurements were recorded using “lghetfq” pulse program from the Bruker library

for homonuclear decoupling of ^{1}H. All the spectra ran with a contact time of 2 ms under CP conditions, and the spinning speed was set to 14.0 kHZ. The total experimental time for each sample is 12.34 h. The initial spectral processing was done using Bruker's Topspin 3.2 software, and structure analysis was done later using Mestrelab Research (MestReNova Version 7.1.1) software.

3.2.4 Synthesis and Characterization of Biobased NPF resins (BNPF)

The acid-catalyzed condensation reaction between phenol and formaldehyde for the synthesis of a Novolac Phenol Formaldehyde resin NPF was carried out following the procedure reported in the previously published article.[29] Briefly, phenol (94 g, 1.0 mol) and oxalic acid (4.7 g, 0.05 mol) were added into a 500 mL four-necked round bottom flask. Later, the flask equipped with a mechanical stirrer, condenser, and dropping funnel was placed in a silicone oil bath under magnetic stirring. First, the reaction mixture was heated to 90 °C, and then 37% formalin solution (64.87 g, 0.8 mol of formaldehyde: 24 g) was slowly added to this mixture through an attached funnel dropwise. After the complete addition of formaldehyde, the reaction continued for 3 hours at 90 °C. Once the reaction was completed, the reaction product was cooled down to room temperature and washed to remove the unreacted reaction component with distilled water (DI), followed by freeze-drying. Furthermore, three different biobased-NPF resins (BNPF) were prepared according to the recipe reported in Table 3.1 by following the same reaction conditions described above. Finally, the prepared NPF and BNPF resins were characterized using FTIR and $^{13}C–^{1}H$ HSQC 2D-NMR techniques.

Table 3.1 Reaction recipe of acid-catalyzed condensation polymerization reaction of four NPF resins and their designations ((*) BNPF resins)

Resin Samples	Phenolic monomer		Aldehyde monomer	
	Phenol (g)	Lignin (g)	Formaldehyde (g)	Oxidized Lignin (g)
NPF	94	-	24	-
PLF*	49	49	24	-
PFOL*	94	-	12	12
PLFOL*	49	49	12	12

3.2.4.1 Solution-State Two-Dimensional Heteronuclear Single Quantum Coherence NMR (Solution-state $^{1}H-^{13}C$ 2D HSQC NMR) Analysis

NPF and BNPF resins were thoroughly identified by the solution-state $^{1}H-^{13}C$ 2D HSQC NMR analysis technique. The NMR spectra were recorded using hsqctgpsisp 2.2. pulse program on Bruker Ultrashield Plus 500 MHz spectrometer with a broadband nitrogen-cooled prodigy probe. For each NMR experiment, approximately 155 mg of the sample was dissolved entirely in 1000 μL DMSO-d_6 solvent. The mixture was transferred into 5 mm NMR tubes, and the experiment was performed with the following parameters: spectral width from 0 to 13 ppm in the F2 (^{1}H) with 1024 data points (TD1) and spectral width from 0 to 220 ppm in F1 (^{13}C) with 256 data points (TD2), 90° pulse angle, a pulse delay of 1.5 s, $^{1}J_{CH}$ used was 145 Hz, an acquisition time of 0.11 s, scan number of 16, dummy scan number of 16. The chemical shifts were referenced to the central solvent DMSO-d_6 peak (δ = 2.49 ppm) and δ = 39.5 ppm) for ^{1}H NMR and ^{13}C NMR, respectively. The NMR data were analyzed using Mestrelab Research software (MestReNova Version 7.1.1).

3.2.5 Thermal study of NPF and BNPF resins by Differential Scanning Calorimetry (DSC)

The prepared NPF and BNPF resins were further reacted with the HMTA curing agent to form a crosslinked structure. Differential Scanning Calorimetry (DSC) was performed on TA Instruments (TA Q2000, DE, and USA) to determine the peak exothermic temperature associated with the curing process. For DSC analysis, each resin sample was grounded with the HMTA curing agent (9% w/w HMTA/NPF resin) using mortar and pestle, yielding four wood adhesive mixtures: NPF-HMTA, NPLF-HMTA, NPFOL-HMTA, and NPLFOL-HMTA. Next, about 5-6 mg of the subsequent adhesive was loaded into the DSC standard aluminum pans and sealed with DSC standard aluminum lid, and then heated from 25 °C to 200 °C at a rate of 10 °C/min under a nitrogen atmosphere with a flow rate of 50 mL/min. The generated curing thermograms were analyzed using TA instrument analysis software.

3.2.6 Preparation of Different Phenol-Formaldehyde Resin-Glued Wood Specimens

All the biobased PF resins adhesion testing was conducted on southern yellow pine (SYP) wood specimens cut into a size of 320 × 46 × 10.5 mm^3 (L × W × H), which have been widely used for adhesive testing. After being conditioned at a relative humidity of (65 ± 5%) and at 22 ± 2 °C for 7 days, the biobased PF resin was spread with an adhesive content of about 200 g/m^2 on the single side of the veneer, and then the uncoated veneer was overlapped on the coated veneer by applying light pressure manually. Subsequently, assembled wood strips were hot-pressed at 200 °C for 5 min with the applied pressure of 2 MPa. After hot pressing, the glued wood specimens were cooled down and maintained for 24 hours to release internal stress before cutting them into the desired size. Eight specimens per bonded adhesives were cut as illustrated in Figure 3.1a, b. from

this group of cut eight wood specimens, four samples were chosen for the dry bonding strength, and the remaining samples were submersion in water at room temperature for 24 hours to perform the wet bonding strength followed by air drying of wood specimens for 15 minutes.

3.2.7 Characterization of the Phenol-Formaldehyde Resin-Glued Wood Specimens

Tensile Shear Strength

The biobased PF adhesives bonded wood specimens were tested at a speed of 1.0 mm/mm on an Instron 5900 Universal Material Testing Instrument (Bluehill, Instron, MA, USA) attached with a 100 kN load cell and the collected data was processed using a Bluhill 3.0 software.

The tensile shear strength was calculated using equation 3.2.

$$\tau = \frac{F}{A} \qquad [3.2]$$

where τ is the tensile shear strength (N/mm^2 or MPa), F is the maximum force to break the adhesive (N), and A is the shear area (mm^2).

The tensile shear strength of the NPF and BNPF resins were measured in quartets and expressed as the mean value ± the corresponding standard deviation value (SD). Further, data were subjected to using two-way analysis of variance (ANOVA) with Tukey's *post-hoc* test for statistical significance analysis. The statistical analysis was carried out using Minitab 19 software.

3.3 Results and Discussion

3.3.1 Characterization of periodate oxidized lignin

The structure of the lignin after periodate oxidation (Figure 3.1) was evaluated by the analytical techniques, including FTIR, elemental analysis, $^{1}H–^{13}C$ 2D HETCOR NMR technique, and al-

dehyde content and further compared with the unmodified lignin. Later, the results of each characterization technique are discussed hereafter.

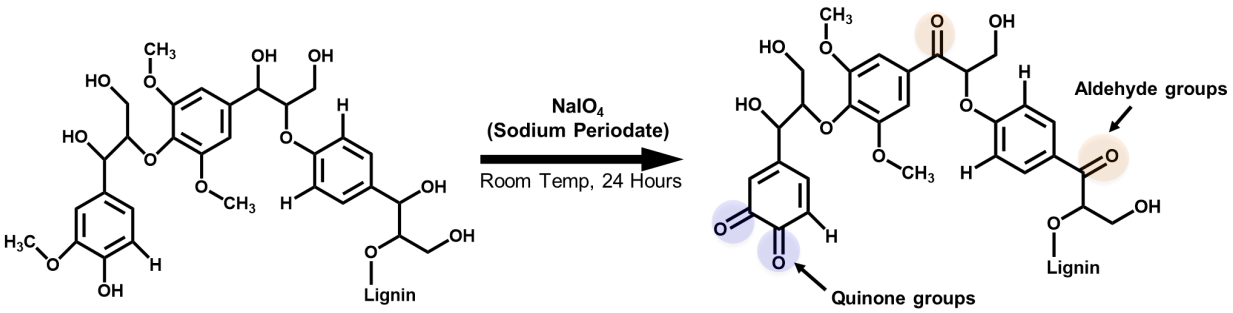

Figure 3.1 Periodate oxidation of lignin.

The FTIR-ATR analysis first examined the influence of periodate oxidation on the lignin structure, and the spectra are shown in Figure 3.2. The two peaks at 2935 and 2840 cm^{-1} belong to the methoxy group linked to the C−H stretching (Figure 3.2a). In the oxidized lignin structure (Figure 3.2b), the band intensity of the C−H stretching decreased at 2935 and 2840 cm^{-1}, indicating the removal of the methoxy group from the aromatic lignin ring. The increased intensity of peaks at 1733 cm^{-1} highlighted the introduction of the carbonyl (C=O) group (unconjugated and conjugated aldehyde and ketones) that are formed during the oxidation of hydroxyl groups present in the interunit linkages (β-O-4 bond) in the lignin structure. A new peak observed in Figure 3.1b at 1630 cm^{-1} highlighted the presence of the quinone group. A similar observation was reported in the literature with the periodate oxidation of softwood lignin.[36] The peaks around 1509, 1450, and 1425 cm^{-1} were attributed to aromatic skeleton vibrations. The absorption bands at 1218, 1125, and 1029 cm^{-1} were due to the C−O stretching vibration deriving from the guaiacyl ring, and secondary and primary alcohols (C−OH), respectively, which weakened in intensity after undergoing oxidation. The peaks detected in the region 1000 – 750 cm^{-1} were assigned to the aromatic C−H out-of-plane deformations. The characteristic peaks associated with lignin detected

were also observed in the FTIR-ATR spectrum of oxidized lignin, indicating that there are limited changes in the lignin chemical structure after oxidation.

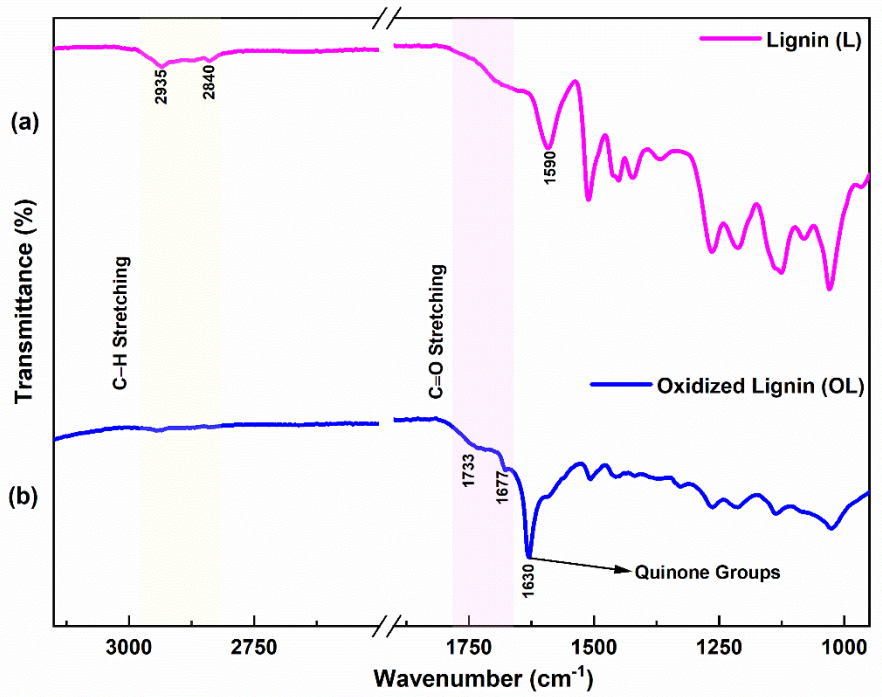

Figure 3.2 FTIR spectra of (a) Lignin (L) and (b) Periodate Oxidized Lignin (OL).

The elemental compositions (C, H, O) of the lignin and oxidized lignin were determined (Table 3.2), and the relation of H/C vs. O/C atomic ratios was presented in Figure 3.3. A relatively smaller amount of nitrogen element was detected in the plant resource-based lignin. The contents of carbon (59.80 to 19.34%) and hydrogen (5.71 to 2.31%) decreased. Still, oxygen content increased from 34.088 to 79.186% in oxidized lignin compared to the lignin due to the oxidation hydroxyl groups present in the interunit linkages (β-O-4 bond) in the lignin structure and partial conversion of lignin to quinone groups.

Additionally, the atomic H/C and O/C ratios of the oxidized lignin distinctively increased, possibly due to the oxidation of the lignin side chains.

Table 3.2 Elemental Compositions of Lignin and Oxidized Lignin

Samples	elemental composition (wt %)			atomic ratio		
	C %	H %	N%	O/C	H/C	O/H
Lignin	59.80 ± 0.06	5.71 ± 0.01	0.385 ± 0.005	0.570	0.095	5.97
Oxidized Lignin	19.34 ± 3.31	2.31 ± 0.44	0.051 ± 0.020	4.094	0.119	34.28

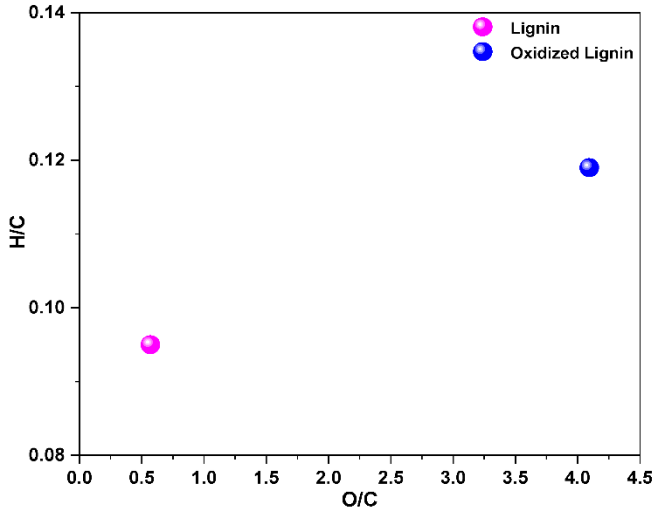

Figure 3.3 H/C vs. O/C of Lignin (L) and Periodate Oxidized Lignin (OL).

The synthesized oxidized lignin was partially soluble in the desired NMR solvents compared with the lignin as the molecular weight of the lignin increases after the periodate oxidation process.[39] In this respect, the solid-state $^{1}H–^{13}C$ 2D HETCOR NMR technique is considered an advantageous method for elucidating the structure of lignin, which is not limited by its insolubility. To gain insights into the oxidative transformations of lignin, a 2D HETCOR NMR experiment was performed, as shown in Figure 3.4 (a, b). Further, the corresponding peak assignments are carried out by the following literature.[40,41] According to the 2D HETCOR, the peaks representing

the aromatic carbon (δC/δH 110−122/6.3−6.9 ppm) are relatively reduced in intensity in the case of oxidized lignin, which could be due to the low availability of protons for the crosspolarization of aromatic carbons.[42] During the periodate oxidation of lignin, aldehyde groups, are likely to introduce into the lignin structure. Herein, we hypothesized that the oxidation is expected to occur at hydroxyl groups attached to β-O-4 bond in the lignin, which can be confirmed by the disappearance of the peaks related to the hydroxyl groups (δC/δH 74.61−77.20/4.57−5.84 ppm) in β-O-4 linkages (Figure 3.4b).

Additionally, the emergence of the cross signals at 215 ppm (δC) and above ~ 153 ppm in Figure 3.4b, clearly demonstrated the presence of oxidized carbon in the structure. The same cannot be seen in the lignin Figure 3.4a. Whereas the methoxyls groups in the lignin are remained unaffected, since the oxidized HETCOR spectrum reveals no signals related to the quinones groups (δC 183 ppm).

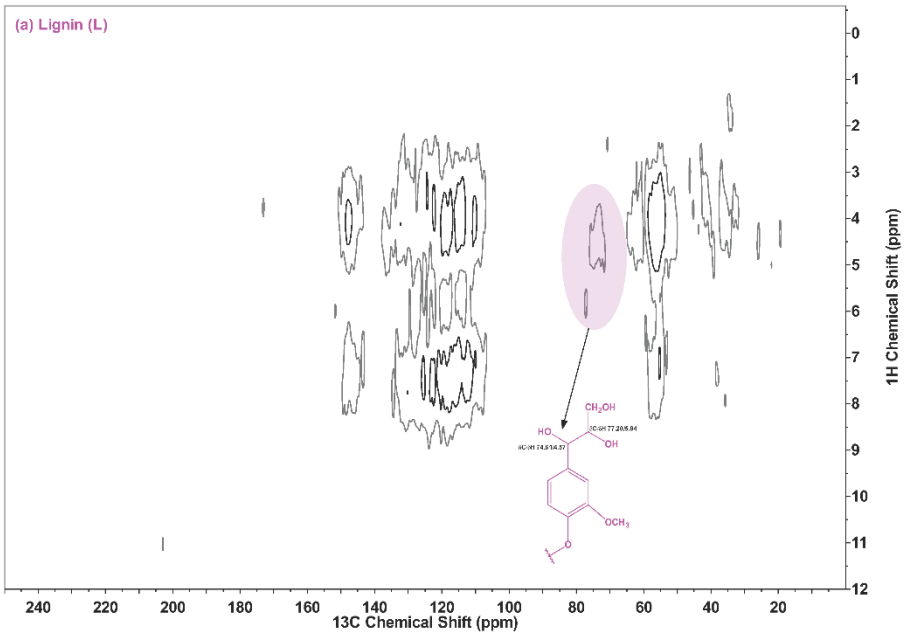

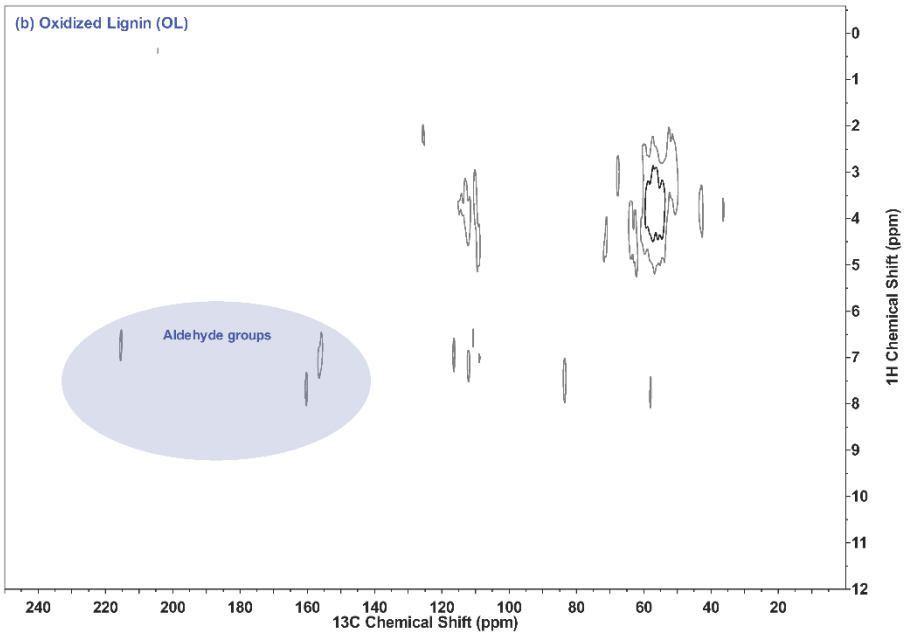

Figure 3.4 Solid-state $^{1}H-^{13}C$ 2D HETCOR NMR spectra of (a) Lignin (L) and (b) Oxidized Lignin (OL).

In the current study, a UV-Vis-based analytical approach was applied by derivatization with 2,4-dinitrophenylhydrazine (DNPH) to investigate the possibility of the formation of aldehyde groups in the lignin structure after periodate oxidation. DNPH is the most efficient derivatization reagent that has been used extensively for aldehyde. The aldehyde content was calculated based on the calibration curve Figure 3.5 (a, b) generated using different concentrations of the DNPH reagent solutions (20, 40, 60, 80, and 100 mg/ml), where a strong UV band is attributed to the excited resonance state of the DNPH in solution. Subsequently, the lignin and oxidized lignin samples were reacted with the DNPH solution, respectively. During this reaction, nucleophilic addition of the $-NH_2$ group to the carbonyl groups takes place, which results in the formation of the yellow precipitate. The UV-Vis spectra of the supernatant from the DNPH-reacted lignin and oxidized sample solutions were presented in Figure 3.5 c. The result demonstrates a distinct shift

in the absorption maximum for DNPH, which is an unreacted DNPH present in the supernatant after the reaction with an aldehyde in the lignin and oxidized lignin, respectively.

Furthermore, the lignin structure observed an increase in the aldehyde content (0.0200 to 0.1116 mmol/g) after oxidation treatment (as shown in Table 3.3). Therefore, it could be seen that periodate oxidation treatment introduces the aldehyde functionality in the lignin structure. During the periodate oxidation, the hydroxyl groups at the interunit linkages (β-O-4 bond) transformed into aldehyde groups, while lignin methoxy groups converted to a quinone.

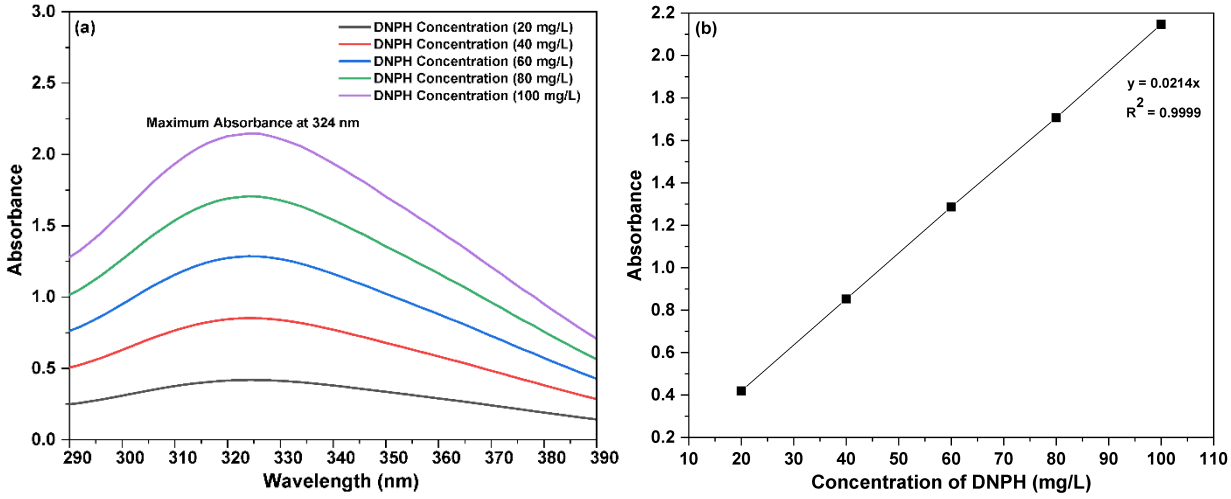

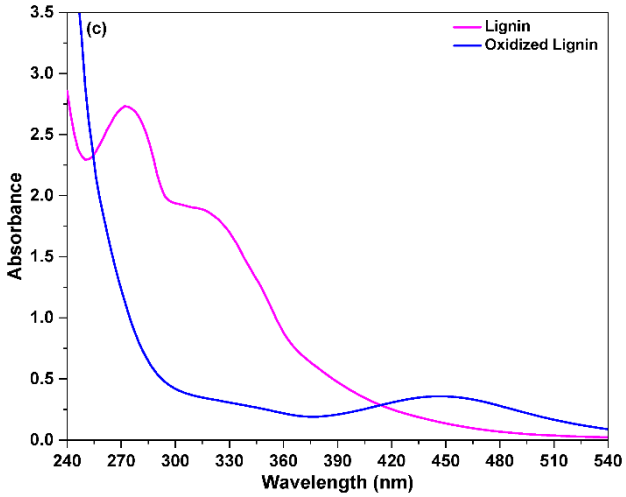

Figure 3.5 Aldehyde content measurement (a) Ultraviolet spectra of different concentrations of DNPH (b) ultraviolet calibration curve of DNPH (c) Ultraviolet spectra of lignin and oxidized lignin.

Table 3.3 Aldehyde content of Lignin and Oxidized Lignin

	Samples	
	Lignin	Oxidized Lignin
Aldehyde Content (mmol/g)	0.0200 ± 0.00073	0.1116 ± 0.00038

3.3.2 Synthesis and Characterization of NPF and BNPF resins

The NPF and BNPF resins were synthesized by forming the methylene bridges through the reaction between OH-groups of a phenol and formaldehyde (CH_2O) under the acid-catalyzed process. Further, the structures of the NPF and BNPF resins were examined using FTIR and ^{13}C-^{1}H HSQC 2D NMR analysis techniques.

The FTIR spectra of the NPF and BNPF resins were demonstrated in Figure 3.6. The peaks were assigned to the corresponding functional groups based on the previous findings.[43,44] The FTIR

spectra (Figure 3.6 a-d) show the –OH bending and stretching vibrations peaks around 3500 – 3300 cm^{-1} regions. The peak at ~1594 and 1510 cm^{-1} correspond to C=C stretching vibration of the aromatic ring. The signals in the region 1460 – 1420 cm^{-1} attributed to the methylene (–CH_2–) stretching vibrations after the successful addition of formaldehyde on the phenolic rings. The FTIR spectra of the BNPF resins show relatively different intensity peaks in the regions 917 – 912 cm^{-1}, 855 – 820 cm^{-1}, and 794 – 753 cm^{-1} which are associated with para and ortho position addition in the phenolic units, respectively.

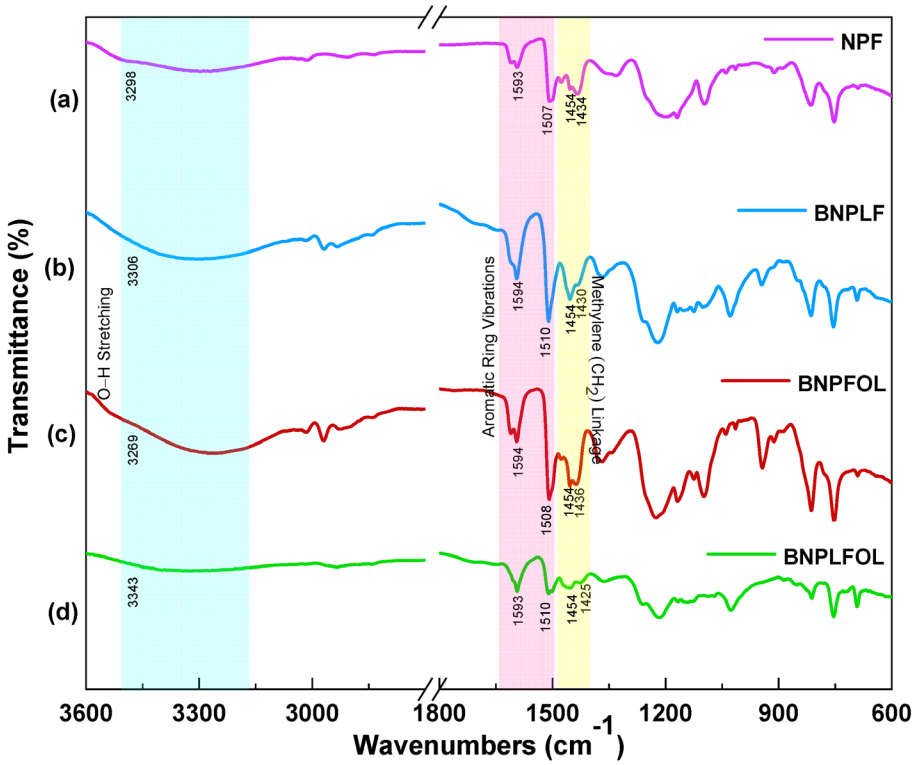

Figure 3.6 FTIR spectra of (a) NPF, (b) BNPLF, (c) BNPFOL, and (d) BNPLFOL.

To further understand the chemical structure, NPF and BNPF resins were characterized by the ^{13}C-^{1}H HSQC 2D NMR analysis experiment, and the spectra are shown in Figure 3.7. The obtained HSQC spectra revealed the presence of a series of characteristic peaks related to meth-

ylene bridges (Ar – CH_2 – Ar) in the region (δC/δH 28.5 – 41.5/3.5 – 4.5 ppm), which originated from the acid-catalyzed condensation polymerization reaction between phenolate moieties and aldehyde functionality. Each of the NPF and BNPF resins shows peaks related to the ortho-ortho methylene linkages (*o–o'*) in the region (δC/δH 29.5/3.75 ppm), ortho-para methylene linkages (*o–p'*) in the region (δC/δH 34.3/3.75 ppm) and para-para methylene linkages (*p–p'*) in the region (δC/δH 29.5/3.75 ppm), respectively. Overall, the 2D HSQC characterization indicates that BNPF resin structures were significantly different from standard NPF resin.

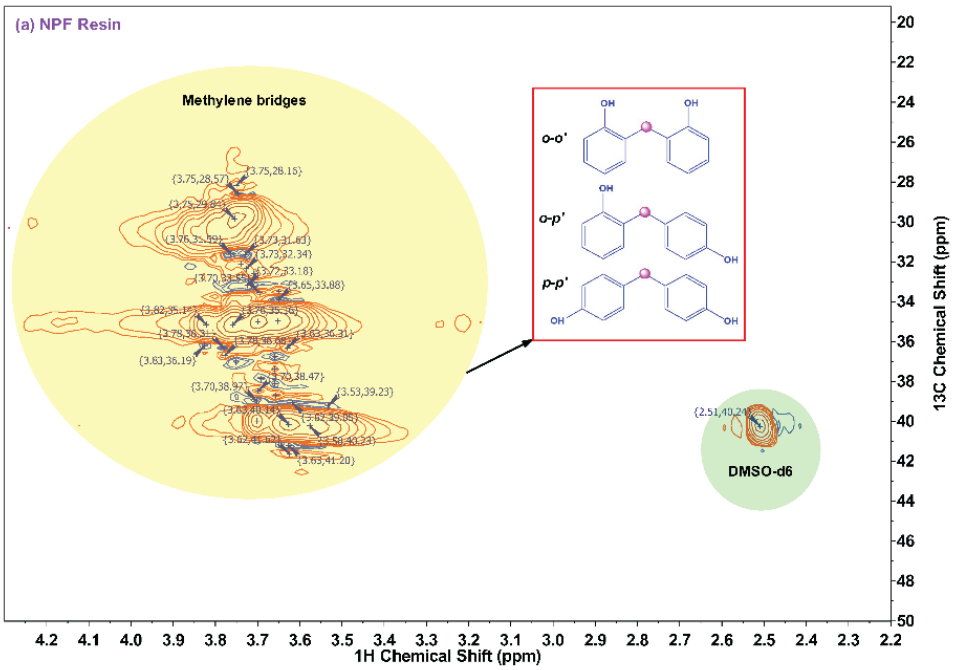

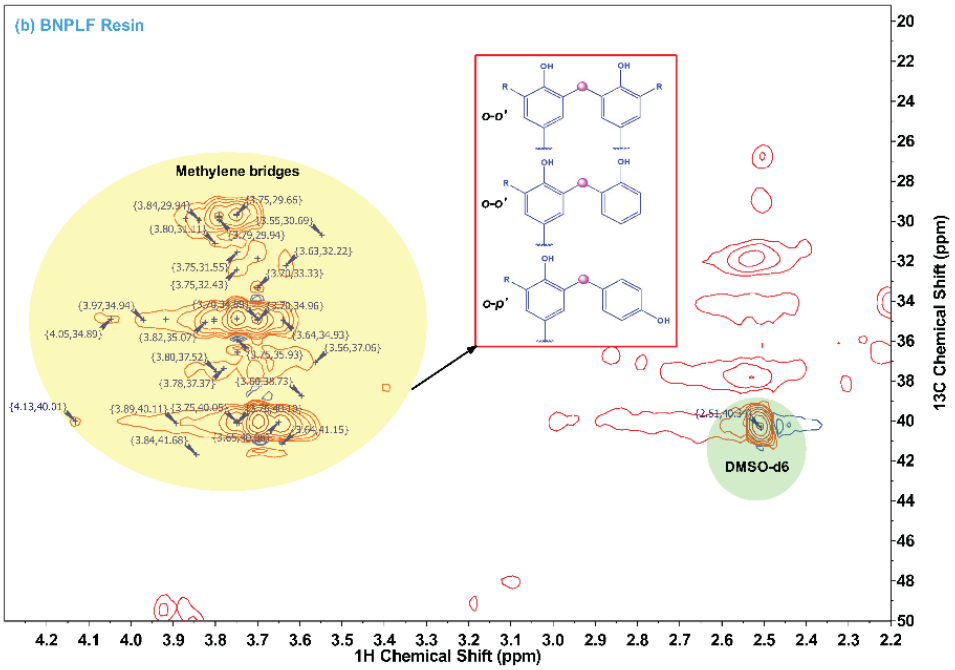
(b) BNPLF Resin
Methylene bridges
o-o'
o-p'
DMSO-d6
1H Chemical Shift (ppm)
13C Chemical Shift (ppm)

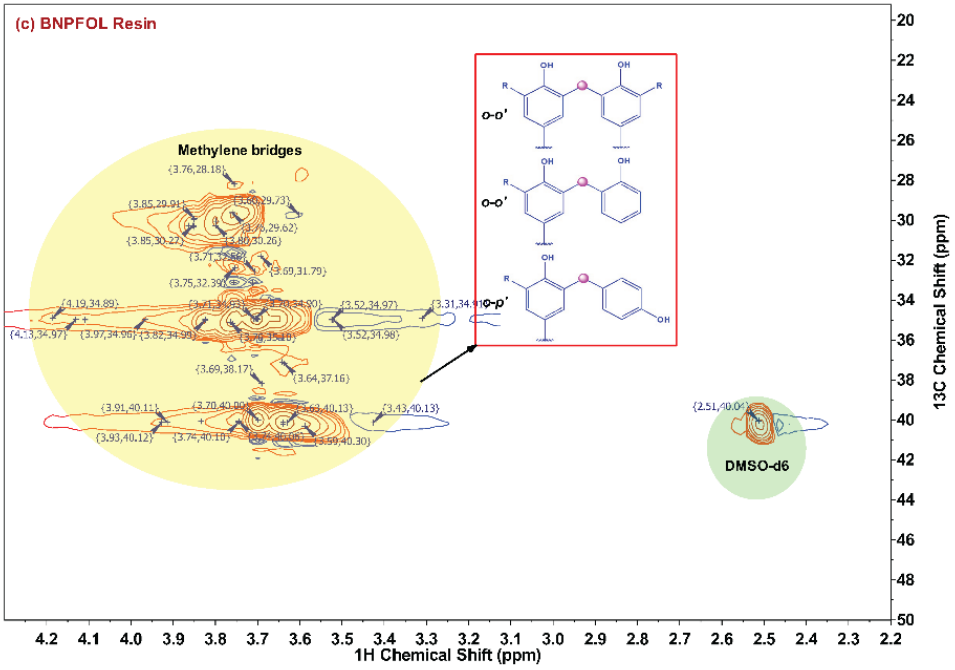
(c) BNPFOL Resin
Methylene bridges
o-o'
o-p'
DMSO-d6
1H Chemical Shift (ppm)
13C Chemical Shift (ppm)

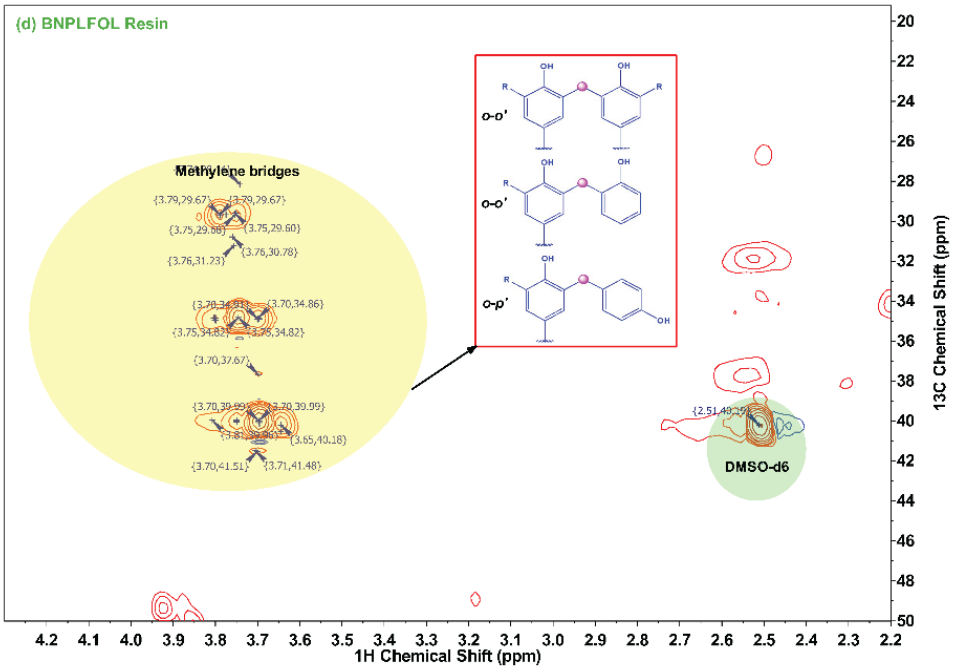

Figure 3.7 ^{13}C-^{1}H HSQC 2D-NMR spectra of (a) NPF, (b) BNPLF, (c) BNPFOL, and (d) BNPLFOL.

3.3.3 Thermal study of NPF and BNPF resins by Differential Scanning Calorimetry (DSC)

In the wood processing industries, evaluation of the curing temperature of the adhesive is crucial to obtain adequate curing temperature for heat pressing of wood panels. DSC analysis was used to determine the curing temperature of the adhesive. The DSC thermograms of four synthesized NPF and BNPF resins were reported in Figure 3.8. It can be seen that all the resins showed curing peak temperature fall in the range of 130–160 °C. A broad and intense exothermic peak occurred due to the heat generated during the polymerization reaction between reactive sites in phenol and formaldehyde. The results turned out that the NPF and BNPF resins have different reactivities, from which it can be concluded that with the replacement of both phenol and for-

maldehyde by lignin and oxidized lignin, respectively, the curing peak temperature was shifted to a higher temperature (159.37 °C). This could be assigned to the lower reactivity of lignin and oxidized lignin than phenol and formaldehyde. The partial replacement of phenol by lignin (BNPLF) or formaldehyde by oxidized lignin (BNPFOL), shifted the exotherm to a lower temperature. This reduction could be beneficial to save energy consumed for the curing process of the resin. This shows that lignin and oxidized lignin provide more reactive sites than phenol or formaldehyde during BNPF resin synthesis.

For our study, wood panels glued with all NPF and BNPF adhesives were hot pressed at 200 °C to ensure the adhesion performance comparison performed under identical conditions.

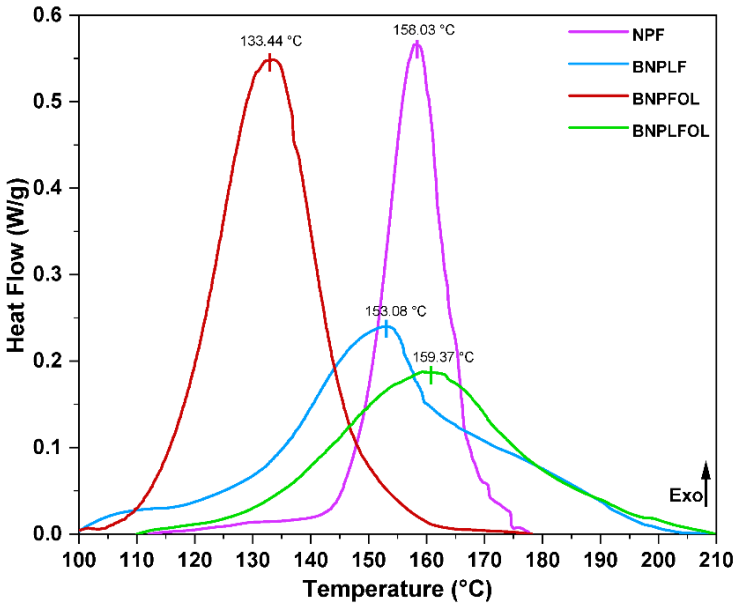

Figure 3.8 DSC thermograms of NPF and BNPF resins.

3.3.4 NPF and BNPF Resin Adhesives Bonding Performance

The adhesion ability of the NPF and BNPF resins on wood specimens was evaluated by the tensile shear strength, which is defined as the adhesion strength required to rupture the bonds between the wood strands bonded by resin. The adhesion shear strength (dry and wet) of each ad-

hesive resin is presented in Figure 3.9. For comparison purposes, we duplicated the BNPLF resin adhesive used in our previous work[29] and prepared it by replacing 50% (w/w) phenol with lignin and the control resin (NPF or 100% PF resin). In this study, among all the tested adhesives, BNPLF resin adhesive showed the highest dry shear strength (2.75 MPa). This suggests that replacing phenolic moieties with lignin would be beneficial.

In contrast, the pairwise comparisons using the Tukey method indicate that the adhesion strength was statistically different for the resin prepared by replacing formaldehyde with oxidized lignin (BNPFOL). A possible explanation for this could be that during BNPFOL resin synthesis, the hydroxyl groups of the phenols could not form stronger covalent interactions with the aldehyde groups of the oxidized lignin structure due to the increasing amount of the reactive sites and steric hindrance. Furthermore, the BNPLFOL resin adhesive performed better than the BNPFOL, owing to the growing number of polar groups which could trigger solid intermolecular interactions.

To further illustrate the versatility of the prepared BNPF resins for wood adhesive applications, the adhesion performance in a wet environment (wet shear strength) was studied. The pairwise comparisons using the Tukey method indicate that the adhesive strength of the wood panels was relatively reduced (NPF: 2.57 to 1.87 MPa, BNPLF: 2.76 to 1.66, BNPFOL: 2.26 to 1.3 MPa, and BNPLFOL: 2.42 to 1.54 MPa) after soaking in water for 24 h, this would be because in the humid environment the hydrogen bonds formed between the wood surface and adhesion layer are easy to break. Whereas, in the case of BNPF resins, wet strength is drastically decreased ($p < 0.05$, Figure 3.9). This is because lignin has hydroxyl groups in its structure.

Overall, the bonded wood panels' dry and wet bonding strength showed their acceptable tensile shear strength, as specified by the GB/T 14732-2006 National standard (> 0.7 MPa)[19], which shows the potential of the BNPF resins as wood adhesives.

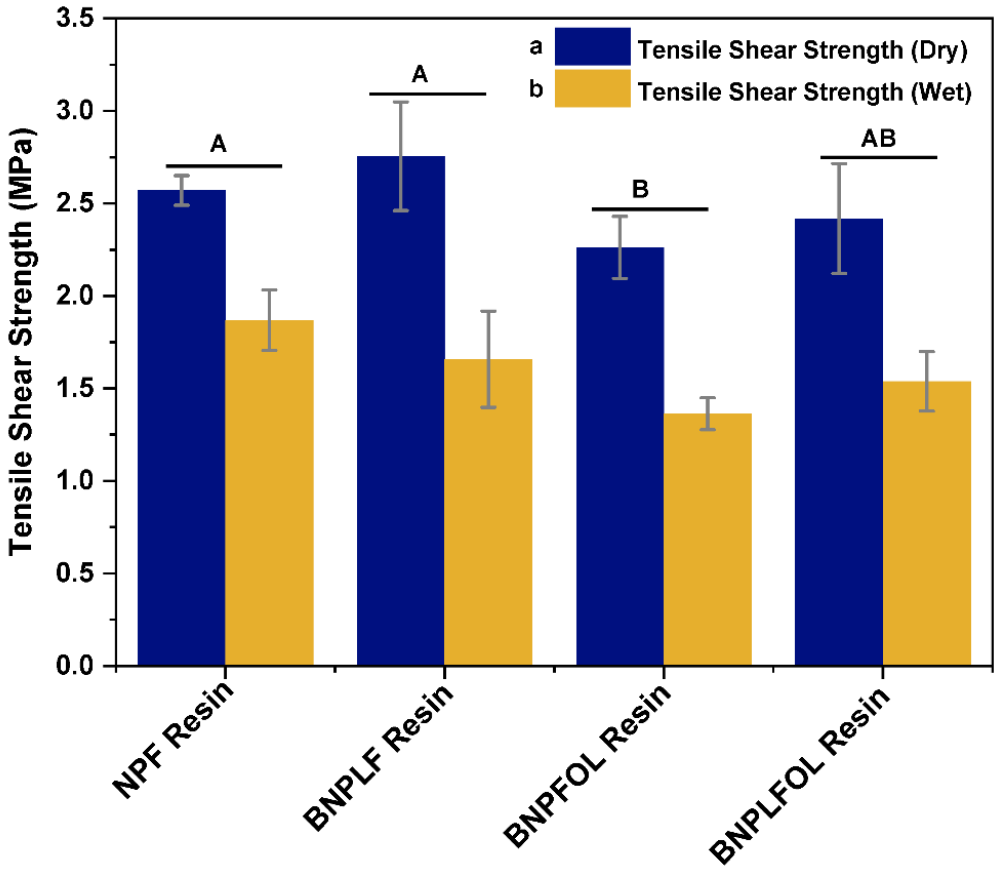

Figure 3.9 The dry and wet shear bonding strength of the wood specimens bonded with different adhesives: NPF Resin, BNPLF Resin, BNPFOL Resin, and BNPLFOL Resin. Four wood-bonded specimens were tested and reported for each adhesive measurement in the form of means and standard deviation (error bars). The statistical analysis was performed with the Two-way ANOVA, followed by the Tukey's post hoc test. The means that do not present the same letters show significantly different adhesion strengths ($p < 0.05$).

3.4 Conclusions

In this experimental work, we presented the functionalization of kraft biorefinery-derived lignin for synthesizing biobased novolac phenol-formaldehyde (BNPF) resin for application as wood adhesives. The functionalization of lignin was performed by oxidation of the hydroxyl groups of the lignin using sodium periodate, leading to what can be called oxidized lignin. Lignin and oxidized lignin were characterized for their chemical compositions and molecular structures using FTIR, elemental analysis, solid-state $^{1}H–^{13}C$ 2D HETCOR NMR, and aldehyde content analysis. The BNPF resins were synthesized in one step through a polycondensation reaction between reactive sites present in the phenol and formaldehyde by replacing 50% (w/w) phenol with lignin and formaldehyde with oxidized lignin. FTIR characterized the obtained BNPF resins and ^{13}C-^{1}H HSQC 2D NMR techniques, and the observed results provide evidence of the formation of methylene linkages. The results observed in the FTIR and ^{13}C-^{1}H HSQC 2D NMR analysis provide evidence of the formation of methylene linkages. The dry bonding strength of the BNPF resin adhesive was comparable to the conventional (PF) adhesives. The dry adhesive bonding strength of the BNPF resins, including BNPLF, BNPFOL, and BNPLFOL was presented by tensile shear strengths of 2.76, 2.26, and 2.42 MPa, respectively. The BNPF resin adhesives prepared in this study could be effectively used as a green alternative for the NPF resin adhesives in developing environmentally friendly wood-based panels.

3.5 References

(1) Aladejana, J. T.; Wu, Z.; Li, D.; Guelifack, K.; Wei, W.; Wang, X. A.; Xie, Y. Facile Approach for Glutaraldehyde Cross-Linking of PVA/Aluminophosphate Adhesives for Wood-Based Panels. *ACS Sustain. Chem. Eng.* **2019**, *7* (22), 18524–18533.

https://doi.org/10.1021/acssuschemeng.9b04555.

(2) Bandara, N.; Wu, J. Randomly Oriented Strand Board Composites from Nanoengineered Protein-Based Wood Adhesive. *ACS Sustain. Chem. Eng.* **2018**, *6* (1), 457–466. https://doi.org/10.1021/acssuschemeng.7b02686.

(3) Pang, B.; Li, M. K.; Yang, S.; Yuan, T. Q.; Du, G. Ben; Sun, R. C. Eco-Friendly Phenol-Urea-Formaldehyde Co-Condensed Resin Adhesives Accelerated by Resorcinol for Plywood Manufacturing. *ACS Omega* **2018**, *3* (8), 8521–8528. https://doi.org/10.1021/acsomega.8b01286.

(4) Rebollar, M.; Pérez, R.; Vidal, R. Comparison between Oriented Strand Boards and Other Wood-Based Panels for the Manufacture of Furniture. *Mater. Des.* **2007**, *28* (3), 882–888. https://doi.org/10.1016/j.matdes.2005.10.012.

(5) Yang, H.; Du, G.; Li, Z.; Ran, X.; Zhou, X.; Li, T.; Gao, W.; Li, J.; Lei, H.; Yang, L. Superstrong Adhesive of Isocyanate-Free Polyurea with a Branched Structure. *ACS Appl. Polym. Mater.* **2021**, *3* (3), 1638–1651. https://doi.org/10.1021/acsapm.1c00056.

(6) Yin, H.; Zhang, E.; Zhu, Z.; Han, L.; Zheng, P.; Zeng, H.; Chen, N. Soy-Based Adhesives Functionalized with Pressure-Responsive Crosslinker Microcapsules for Enhanced Wet Adhesion. *ACS Appl. Polym. Mater.* **2021**, *3* (2), 1032–1041. https://doi.org/10.1021/acsapm.0c01295.

(7) Pizzi, A. Wood Products and Green Chemistry. *Ann. For. Sci.* **2016**, *73* (1), 185–203. https://doi.org/10.1007/s13595-014-0448-3.

(8) Zhang, H.; Liu, P.; Musa, S. M.; Mai, C.; Zhang, K. Dialdehyde Cellulose as a Bio-Based Robust Adhesive for Wood Bonding. *ACS Sustain. Chem. Eng.* **2019**, *7* (12), 10452–10459. https://doi.org/10.1021/acssuschemeng.9b00801.

(9) A. Pizzi and K. L. Mittal. *Handbook of Adhesive Technology Third Edition*; 2018.

(10) Zhang, J.; Zhang, M.; Zhang, Y.; Shi, S. Q.; Zhan, X.; Li, J.; Luo, J.; Gao, Q. Improving Bond Performance and Reducing Cross-Linker Dosage for Soy Flour Adhesives Inspired by Spider Silk. *ACS Sustain. Chem. Eng.* **2021**, *9* (1), 168–179. https://doi.org/10.1021/acssuschemeng.0c06333.

(11) Zhao, Y.; Yan, N.; Feng, M. W. Biobased Phenol Formaldehyde Resins Derived from Beetle-Infested Pine Barks - Structure and Composition. *ACS Sustain. Chem. Eng.* **2013**, *1* (1), 91–101. https://doi.org/10.1021/sc3000459.

(12) Chai, Y.; Liu, J.; Zhao, Y.; Yan, N. Characterization of Modified Phenol Formaldehyde Resole Resins Synthesized in Situ with Various Boron Compounds. *Ind. Eng. Chem. Res.* **2016**, *55* (37), 9840–9850. https://doi.org/10.1021/acs.iecr.6b02156.

(13) Milazzo, M.; Amoresano, A.; Pasquino, R.; Grizzuti, N.; Auriemma, F.; De Stefano, F.; Sin Xicola, A.; Iodice, V.; De Rosa, C. Curing Efficiency of Novolac-Type Phenol–Formaldehyde Resins from Viscoelastic Properties. *Macromolecules* **2021**, *54* (24), 11372–11383. https://doi.org/10.1021/acs.macromol.1c01598.

(14) Gao, Z.; Lang, X.; Chen, S.; Zhao, C. Mini-Review on the Synthesis of Lignin-Based Phenolic Resin. *Energy and Fuels* **2021**, *35* (22), 18385–18395. https://doi.org/10.1021/acs.energyfuels.1c03177.

(15) Gustin, J. L. Vent Sizing for the Phenol + Formaldehyde Reaction. *Org. Process Res. Dev.* **2006**, *10* (6), 1263–1274. https://doi.org/10.1021/op068007+.

(16) Wang, L.; Lagerquist, L.; Zhang, Y.; Koppolu, R.; Tirri, T.; Sulaeva, I.; von Schoultz, S.; Vahasalo, L.; Pranovich, A.; Rosenau, T.; Eklund, P. C.; Willfor, S.; Xu, C.; Wang, X. Tailored Thermosetting Wood Adhesive Based on Well-Defined Hardwood Lignin

Fractions. *ACS Sustain. Chem. Eng.* **2020**. https://doi.org/10.1021/acssuschemeng.0c05408.

(17) Yao, J.; Odelius, K.; Hakkarainen, M. Microwave Hydrophobized Lignin with Antioxidant Activity for Fused Filament Fabrication. *ACS Appl. Polym. Mater.* **2021**, *3* (7), 3538–3548. https://doi.org/10.1021/acsapm.1c00438.

(18) He, Q.; Ziegler-Devin, I.; Chrusciel, L.; Obame, S. N.; Hong, L.; Lu, X.; Brosse, N. Lignin-First Integrated Steam Explosion Process for Green Wood Adhesive Application. *ACS Sustain. Chem. Eng.* **2020**, *8* (13), 5380–5392. https://doi.org/10.1021/acssuschemeng.0c01065.

(19) Jedrzejczyk, M. A.; Kouris, P. D.; Boot, M. D.; Hensen, E. J. M.; Bernaerts, K. V. Renewable Thiol-Yne "Click" Networks Based on Propargylated Lignin for Adhesive Resin Applications. *ACS Appl. Polym. Mater.* **2022**, *4* (4), 2544–2552. https://doi.org/10.1021/acsapm.1c01853.

(20) Sun, Y. C.; Liu, X. N.; Wang, T. T.; Xue, B. L.; Sun, R. C. Green Process for Extraction of Lignin by the Microwave-Assisted Ionic Liquid Approach: Toward Biomass Biorefinery and Lignin Characterization. *ACS Sustain. Chem. Eng.* **2019**, *7* (15), 13062–13072. https://doi.org/10.1021/acssuschemeng.9b02166.

(21) Lake, M. A.; Blackburn, J. C. SLRP^{TM} - An Innovative Lignin-Recovery Technology. *Cellul. Chem. Technol.* **2014**, *48* (9–10), 799–804.

(22) Borrega, M.; Päärnilä, S.; Greca, L. G.; Jääskeläinen, A. S.; Ohra-Aho, T.; Rojas, O. J.; Tamminen, T. Morphological and Wettability Properties of Thin Coating Films Produced from Technical Lignins. *Langmuir* **2020**, *36* (33), 9675–9684. https://doi.org/10.1021/acs.langmuir.0c00826.

(23) Journal, I. Use of Organosolv Lignin in Phenol-Formaldehyde Resins for Particleboard Production II . Particleboard Production and Properties. **2002**, *22*, 481–486.

(24) Pizzi, A. Recent Developments in Eco-Efficient Bio-Based Adhesives for Wood Bonding: Opportunities and Issues. *J. Adhes. Sci. Technol.* **2006**, *20* (8), 829–846. https://doi.org/10.1163/156856106777638635.

(25) Kouisni, L.; Fang, Y.; Paleologou, M.; Ahvazi, B.; Hawari, J.; Zhang, Y.; Wang, X. M. Kraft Lignin Recovery and Its Use in the Preparation of Lignin-Based Phenol Formaldehyde Resins for Plywood. *Cellul. Chem. Technol.* **2011**, *45* (7–8), 515–520.

(26) Solt, P.; Rößiger, B.; Konnerth, J.; van Herwijnen, H. W. G. Lignin Phenol Formaldehyde Resoles Using Base-Catalysed Depolymerized Kraft Lignin. *Polymers*. 2018. https://doi.org/10.3390/polym10101162.

(27) Zhang, Y.; Wu, J. Q.; Li, H.; Yuan, T. Q.; Wang, Y. Y.; Sun, R. C. Heat Treatment of Industrial Alkaline Lignin and Its Potential Application as an Adhesive for Green Wood-Lignin Composites. *ACS Sustain. Chem. Eng.* **2017**, *5* (8), 7269–7277. https://doi.org/10.1021/acssuschemeng.7b01485.

(28) Karthäuser, J.; Biziks, V.; Mai, C.; Militz, H. Lignin and Lignin-Derived Compounds for Wood Applications—A Review. *Molecules* **2021**, *26* (9). https://doi.org/10.3390/molecules26092533.

(29) Bansode, A.; Barde, M.; Asafu-Adjaye, O.; Patil, V.; Hinkle, J.; Via, B. K.; Adhikari, S.; Adamczyk, A. J.; Farag, R.; Elder, T.; Labbé, N.; Auad, M. L. Synthesis of Biobased Novolac Phenol-Formaldehyde Wood Adhesives from Biorefinery-Derived Lignocellulosic Biomass. *ACS Sustain. Chem. Eng.* **2021**, *9* (33), 10990–11002. https://doi.org/10.1021/acssuschemeng.1c01916.

(30) Deng, S.; Du, G.; Li, X.; Pizzi, A. Performance and Reaction Mechanism of Zero Formaldehyde-Emission Urea-Glyoxal (UG) Resin. *J. Taiwan Inst. Chem. Eng.* **2014**, *45* (4), 2029–2038. https://doi.org/10.1016/j.jtice.2014.02.007.

(31) Van Nieuwenhove, I.; Renders, T.; Lauwaert, J.; De Roo, T.; De Clercq, J.; Verberckmoes, A. Biobased Resins Using Lignin and Glyoxal. *ACS Sustain. Chem. Eng.* **2020**, *8* (51), 18789–18809. https://doi.org/10.1021/acssuschemeng.0c07227.

(32) Liimatainen, H.; Visanko, M.; Sirviö, J. A.; Hormi, O. E. O.; Niinimaki, J. Enhancement of the Nanofibrillation of Wood Cellulose through Sequential Periodate-Chlorite Oxidation. *Biomacromolecules* **2012**, *13* (5), 1592–1597. https://doi.org/10.1021/bm300319m.

(33) Esen, E.; Meier, M. A. R. Sustainable Functionalization of 2,3-Dialdehyde Cellulose via the Passerini Three-Component Reaction. *ACS Sustain. Chem. Eng.* **2020**, *8* (41), 15755–15760. https://doi.org/10.1021/acssuschemeng.0c06153.

(34) Chen, X.; Xi, X.; Pizzi, A.; Fredon, E.; Du, G.; Gerardin, C.; Amirou, S. Oxidized Demethylated Lignin as a Bio-Based Adhesive for Wood Bonding. *J. Adhes.* **2021**, *97* (9), 873–890. https://doi.org/10.1080/00218464.2019.1710830.

(35) Zhang, Y.; Fatehi, P. Periodate Oxidation of Carbohydrate-Enriched Hydrolysis Lignin and Its Application as Coagulant for Aluminum Oxide Suspension. *Ind. Crops Prod.* **2019**, *130* (November 2018), 81–95. https://doi.org/10.1016/j.indcrop.2018.12.052.

(36) Gosselink, R. J. A.; Van Dam, J. E. G.; De Jong, E.; Gellerstedt, G.; Scott, E. L.; Sanders, J. P. M. Effect of Periodate on Lignin for Wood Adhesive Application. *Holzforschung* **2011**, *65* (2), 155–162. https://doi.org/10.1515/HF.2011.025.

(37) Tummalapalli, M.; Gupta, B. A UV-Vis Spectrophotometric Method for the Estimation of

Aldehyde Groups in Periodate-Oxidized Polysaccharides Using 2,4-Dinitrophenyl Hydrazine. *J. Carbohydr. Chem.* **2015**, *34* (6), 338–348. https://doi.org/10.1080/07328303.2015.1068793.

(38) Kandrac, M. Factors Affecting the 2,4-Dinitrophenyl Hydrazine Reaction With Lipid Carbonyls. **2018**, No. October.

(39) Zhang, Y.; Fatehi, P. Periodate Oxidation of Carbohydrate-Enriched Hydrolysis Lignin and Its Application as Coagulant for Aluminum Oxide Suspension. *Ind. Crops Prod.* **2019**, *130* (August 2018), 81–95. https://doi.org/10.1016/j.indcrop.2018.12.052.

(40) Knicker, H.; Velasco-Molina, M.; Knicker, M. 2D Solid-State Hetcor1H-13C Nmr Experiments With Variable Cross Polarization Times As a Tool for a Better Understanding of the Chemistry of Cellulose-Based Pyrochars—a Tutorial. *Appl. Sci.* **2021**, *11* (18). https://doi.org/10.3390/app11188569.

(41) Le Brech, Y.; Delmotte, L.; Raya, J.; Brosse, N.; Gadiou, R.; Dufour, A. High Resolution Solid State 2D NMR Analysis of Biomass and Biochar. *Anal. Chem.* **2015**, *87* (2), 843–847. https://doi.org/10.1021/ac504237c.

(42) Cao, X.; Drosos, M.; Leenheer, J. A.; Mao, J. Secondary Structures in a Freeze-Dried Lignite Humic Acid Fraction Caused by Hydrogen-Bonding of Acidic Protons with Aromatic Rings. *Environ. Sci. Technol.* **2016**, *50* (4), 1663–1669. https://doi.org/10.1021/acs.est.5b02859.

(43) Chen, S.; Xin, Y.; Zhao, C. Multispectroscopic Analysis in the Synthesis of Lignin-Based Biophenolic Resins. *ACS Sustain. Chem. Eng.* **2021**, *9* (46), 15653–15660. https://doi.org/10.1021/acssuschemeng.1c06135.

(44) Siahkamari, M.; Emmanuel, S.; Hodge, D. B.; Nejad, M. Lignin-Glyoxal: A Fully

Biobased Formaldehyde-Free Wood Adhesive for Interior Engineered Wood Products. *ACS Sustain. Chem. Eng.* **2022**, *10* (11), 3430–3441. https://doi.org/10.1021/acssuschemeng.1c06843.

Chapter 4

Application of Hydrothermal Liquified Municipal Sewage Sludge as a Functional Filler in pMDI Wood Adhesive

This chapter is being prepared for submission[3]

4.1 Introduction

Engineered wood products, such as plywood, particleboard, fiberboard-oriented strand boards (OSBs), and medium-density fiberboards (MDFs), are intensively used in various fields, including the home furnishing, packaging, and building and construction industry.[1–3] In addition to the wood itself, adhesives used in processing these wood products have made an essential contribution to determining the quality and mechanical properties.[4] In the wood industry, polymeric methylene diphenyl diisocyanate (pMDI) resins are predominantly used as adhesives along with other thermosetting and thermoplastic polymeric resin adhesives such as phenol-formaldehyde (PF), melamine-formaldehyde (MF), urea-formaldehyde (UF), and polyurethane (PU).[5–7]

pMDI is dark brown viscous one-component isocyanate adhesive, which contains 30-80% of the monomer (methylene diphenyl diisocyanate) together with oligomers having a degree of polymerization from 3 to 5, resulting in ~2.7 isocyanate groups per molecule.[8] pMDI resin adhesive has gained a significant market. As shown, advantages like excellent wet and dry bonding strengths, water-resistant properties, and good dimensional stability render them suitable for ex-

[3] Bansode, A.; Carias L.; Rahman T.; Vega Erramuspe I. B.; Alawode AO.; Asafu-Adjaye O.; Adhikari S.; Via B. K.; Farag, R.; Auad, M. L.; Application of Hydrothermal Liquified Municipal Sewage Sludge as a Functional Filler in pMDI Wood Adhesive, In Preparation, 2022

terior and structural applications.[9,10] Theoretically, the isocyanate groups R–N=C=O in the pMDI can reacts with the compounds containing active hydrogen atoms present in the wood substrates (wood cell-wall polymers) to form irreversible urethane linkages.[11,12] The covalent bonds formed between pMDI adhesive and wood polymer establish strong bonding during wood adhesive application.[13,14] However, there are still some challenges of isocyanate-based pMDI adhesives, which limits their application as wood adhesives.[15] They are highly toxic compounds synthesized from toxic reagents that harm humans and the environment during handling uncured adhesives.[15,16] Due to their viscosity and tackiness, they tend to adhere to the steel platens during the hot-pressing operations.[17,18] In addition, pMDI adhesive can over-penetrate into the wood substrate resulting in poor bonding. Thus pMDI adhesive is generally unsuitable for situations where continuous bonding is required, such as plywood and laminated veneer lumber.[15,17,19] A critical limitation of pMDI adhesive is its limited gap-filling ability, which leads to poor bonding with gaps and defects.[17] Functional fillers and extenders are often used in pMDI adhesive formulations to lower the usage of pMDI and reduce the cost by increasing solid content and improving the bonding formation and adhesion performance while maintaining the original pMDI properties.[9,15,17] Serval mineral particles (fumed silicas, sepiolite, and chalk) were used as a filler to improve the thermal stability of pMDI-derived adhesives.[15] Additionally, using organic particles (modified montmorillonite clay and tungsten disulphide nanoparticles) and polyamide powder showed enhanced bonding performance.[15] There is strong interest in academic and industry communities in utilizing renewable biomass for achieving higher sustainability and a lower carbon footprint.[10,15,17,20] In this regard, chemicals produced from waste and residues derived from domestic and industrial activities are gaining importance to substitute fossil fuel resources.[21]

Rapid urbanization and economic development with a growing population have increased the volume of municipal wastewater, which must be treated before recirculation into the civil wastewater pipeline for water resource protection.[22] The biological and chemical treatment of municipal wastewater through wastewater treatment plants (WWTPs) generates a semisolid by-product called sewage sludge.[23–25] This produced municipal sewage sludge is a valuable renewable energy and nutrient source.[26] Concerning a circular economy, utilizing this potential feedstock to generate sustainable chemicals and fuels is crucial.[27,28] However, these materials also contain pathogens, hazardous metals, and some persistent organic contaminants, limiting their direct disposal into landfill sites, incineration, and agriculture applications due to sticker regulation and environmental concerns.[29] Accounting for all these impacts, sustainable, economical, and efficient technology for the conversion of municipal sewage sludge has become an essential goal in developing sustainable chemicals and materials.[30]

Thermochemical conversion processes, such as pyrolysis and hydrothermal liquefaction (HTL), are valuable technologies for transforming biomass feedstocks into liquid fuel products (so-called biocrude oil).[31,32] Hydrothermal liquefaction has its advantages when compared to pyrolysis in the application of wet feedstocks like sewage sludge (typically >75 wt % water), that it can enhance the yield of liquid products, suppress the formation of char, and does not require predrying.[33–35] HTL can effectively convert biomass (sewage sludge) in the presence of sub- and supercritical conditions in water or an organic solvent media at high temperatures (250−250 °C) and high pressures (2−22 MPa) for a certain time in an inert or reducing atmosphere.[36] During liquefaction, solid biopolymeric structures associated with the sludge undergoes different reactions such as hydrolysis, depolymerization, and condensation to produce energy-dense biofuels (bio-oil).[37] The bio-oil from HTL composes of macromolecular compounds, aromatic hydrocar-

bons, oxygen, nitrogen-containing chemicals, heteroatom-containing species, and complex compounds of diverse polarity and boiling points, increasing the viscosity and lowering the heating value of bio-oils.[36,38,39] Therefore, an extensive upgrade is required to minimize the amount of N-containing compounds and heteroatoms present in the sewage sludge to improve the quality of sewage sludge-derived bio-oil.[34,40]

In the previous article[41] published by our collaborator, hydrothermal liquefaction of municipal sewage sludge was conducted at different adequate reaction conditions such as catalysts (calcined red mud; CRM, reduced red mud at 500°C; RRM500, and reduced red mud 700°C; RRM700) and reaction atmosphere (nitrogen and ethylene) to find optimal conditions for improving municipal sewage sludge bio-oils yield and quality. Tawsif and coworkers demonstrated that bio-oils prepared under an ethylene atmosphere and RRM500 catalyst are favorable conditions to produce bio-oil. Based on these findings, the current research aims to explore the possibility of these municipal sewage sludge bio-oil as a functional filler for polymeric methylene diphenyl diisocyanate (pMDI) resin systems for wood adhesive applications. The bio-oils derived from the municipal sewage sludge consist of several organic compounds; hence to analyze the chemical functional groups' several characterizations have been performed. Furthermore, the effect of MSS-Bio-oil/pMDI weight ratio on the bonding performance of the resulting MSS bio-oil/pMDI adhesives was investigated and compared with neat pMDI adhesive.

4.2 Experimental Section

4.2.1 Materials

Polymeric methylene diphenyl diisocyanate (Rubinate M, identified as pMDI) utilized in this work was kindly received by Huntsman Corporation, Texas, USA. Deuterated chloroform (with

0.03 v/v% TMS, 99.8+ atom% D), chromium (III) acetylacetonate (98.0%), N-hydroxy-5-norbornene-2,3-dicarboximide (NHND, 99.0%), pyridine (>99%), acetone (99.5%), and dichloromethane were acquired from VWR International, USA. 2-Chloro-4,4,5,5-tetramethyl-1,3,2-dioxaphospholane (TMDP, 95%) was obtained from Sigma-Aldrich, USA. Southern yellow pine (SYP, pinus ssp) veneers were used for the wood adhesive test. Red mud was procured from Almatis Burnside, Inc., Louisiana, USA. Gases such as high-purity nitrogen and ethylene used in the hydrothermal liquefaction process were purchased from Airgas Inc., Alabama, USA. The municipal sewage sludge sample used in the study was collected from H.C. Morgan Water Pollution Control Facility (a local wastewater treatment facility in Auburn, Alabama, USA). The received municipal sewage sludge details are reported in previously published articles.[41]

The hydrothermal liquefaction of municipal sewage sludge was performed in our Biosystems Engineering Laboratory at Auburn University, as described in the following methodology.

4.2.2 Hydrothermal Liquefaction of Municipal Sewage Sludge

All hydrothermal liquefaction experiments were conducted in Parr reactor model 4578 (Illinois, USA) with an internal volume capacity of 1.8 L, designed to have the maximum temperature and pressure. The details of the reactor design are described in a previous study.[41] Briefly, in each HTL experiment, 600 g of municipal sewage sludge (solid content of 17-19%) was loaded into the HTL reactor and sealed. In the case of catalytic HTL reactions, a catalyst to municipal sewage sludge feedstock loading was kept at 1:3. The loaded HTL reactor vessel was then purged with the desired gas (nitrogen or ethylene gas) three times to remove existing air and then repressurized the reactor with the initial gas pressure of 200 psi. The HTL reactor was then heated to the desired temperature of 350 °C at a heating rate of 4 °C/min for a holding time of 60 minutes,

followed by reactor cooling. After the reactor cooling, the reaction products, such as gas, solid, aqueous phase, and biocrude, were separated, as reported in the previous literature.[41] To ensure accuracy, all experiments were performed in duplicates. This procedure was followed for two different reaction atmospheres (nitrogen and ethylene gas) and with (reduced red mud at 500°C; RRM500) and without catalyst, so there was a total of 4 runs (4 municipal sewage sludge bio-oils): MSS-Bio-oil_N (nitrogen atmosphere with no catalyst), MSS-Bio-oil_NC (nitrogen atmosphere with catalyst), MSS-Bio-oil_E (ethylene atmosphere with no catalyst), and MSS-Bio-oil_EC (ethylene atmosphere with catalyst).

4.2.3 Structural Characterization of Municipal Sewage Sludge Bio-oils

4.2.3.1 Fourier Transform Infrared (FTIR) Spectroscopy

Bio-oils obtained from municipal sewage sludge were analyzed on Nicolet 6700 FTIR spectrophotometer (Thermo Scientific Inc., USA) equipped with a diamond attenuated total reflection (ATR) crystal. The spectral information of each bio-oils was collected in the wavenumber range between 4000 − 600 cm^{-1} with a resolution of 4 cm^{-1} and 64 scans. In addition, the background spectrum of ambient air was recorded before each sampling and subtracted from the measured spectra using OMNIC software (Thermo Scientific, v7.3).

4.2.3.2 Elemental Analysis

The organic elements in municipal sewage sludge bio-oils were performed on an elemental analyzer (Vario MICRO cube, Elementar, New York, USA). The elemental compositions such as carbon (C), hydrogen (H), and nitrogen (N) were directly measured. The oxygen (O) content was calculated by difference with respect to the total sample.

4.2.3.3 Nuclear Magnetic Resonance (NMR) Spectroscopy Analysis

The NMR experiments of municipal sewage sludge bio-oil were performed on Bruker Ultrashield Plus 500 MHz spectrometer with a broadband nitrogen-cooled prodigy probe. The NMR data were processed with Mestrelab Research (MestReNova Version 7.1.1) software.

Phosphorus-31 (^{31}P) NMR Spectroscopy

^{31}P-NMR analysis of municipal sewage sludge bio-oil was carried out according to a slightly modified method reported in a published article.[42] For each qualitative ^{31}P-NMR analysis, about 25 mg of sample was dissolved in 750 µL of the stock solution. The stock solution was prepared by mixing 3 mL of pyridine and 2 mL of deuterated chloroform. N-hydroxy-5-norbornene-2,3-dicarboximide (NHND) 20 mg as an internal standard and chromium (III) acetylacetonate 20 mg, used as a relaxation agent, were dissolved in the same mixture solvent of pyridine/$CDCl_3$ (1.5:1 v/v) and then the whole stock solution was stirred at room temperature. The dissolved sample was then phosphitylated with 200 µL 2-chloro-4,4,5,5-tetramethyl-1,3,2-dioxaphospholane (TMDP) and transferred into a dry 5 mm NMR tube and measured to perform subsequent NMR analysis. The ^{31}P NMR spectra were acquired using 90° pulse angle, 25 seconds pulse delay, 128 scans and an inverse gated proton decoupling pulse to eliminate the nuclear overhauser effects for quantitative purposes.

Two-Dimensional Heteronuclear Single Quantum Coherence NMR ($^{1}H-^{13}C$ 2D HSQC NMR) Analysis

For each ^{1}H–^{13}C 2D HSQC NMR of municipal sewage sludge bio-oil, around 155 mg of the sample was dissolved entirely in 1000 µL $CDCl_3$ solvent, and then the mixture was transferred into 5 mm NMR tubes. The spectra were recorded using hsqctgpsisp 2.2. pulse program with

spectral widths from 0 to 13 ppm (6578 Hz) and from 0 to 220 ppm (27679 Hz) for ^{1}H and ^{13}C, respectively. The other parameters used are listed below: an acquisition time of 0.11 s, 90° pulse angle, a pulse delay of 1.5 s, $^{1}J_{CH}$ used was 145 Hz, 16 scans with an additional 16 dummy scans, acquisition of 1024 data points for ^{1}H and 256 increments for ^{13}C. The chemical shifts were referenced to $CDCl_3$ (δ = 7.26 ppm) for ^{1}H NMR and (δ = 77.16 ppm) for ^{13}C NMR.

4.2.4 Preparation of Municipal sludge bio-oil/Polymeric methylene diphenyl diisocyanate (MSS bio-oil/pMDI) Adhesives

The preparation of the final MSS bio-oil/pMDI wood adhesives was carried out by mixing the two-component solutions, the MSS bio-oil, and pMDI. Therein, a series of biobased MSS bio-oil/pMDI resin adhesives were synthesized with MSS Bio-oil/pMDI weight ratio: of 0.18, 0.33, and 0.54, first by weighing MSS bio-oil into the beaker, followed by the addition of pMDI using a disposable plastic dropper as per recipe presented in Table 4.1. The final mixture was further homogenized by manually mixing it with a glass rod for about 3 minutes. Furthermore, the prepared adhesive resins were applied for wood bonding.

Table 4.1 Composition of MSS bio-oil/pMDI wood adhesives with a three different MSS Bio-oil/pMDI Weight Ratio

Sr. No.	MSS Bio-oils (g)	pMDI (g)	MSS Bio-oil/pMDI Weight Ratio
MSS-Bio-oil_N (Nitrogen)			
1	0.4485	2.5500	0.18
2	0.7471	2.2400	0.33
3	1.0460	1.9400	0.54
MSS-Bio-oil_NC (Nitrogen & Catalyst)			
1	0.4140	2.3460	0.18
2	0.6900	2.0700	0.33
3	0.9660	1.7940	0.54
MSS-Bio-oil_E (Ethylene)			
1	0.4800	2.72	0.18
2	0.8000	2.40	0.33
3	1.1200	2.09	0.54
MSS-Bio-oil_EC (Ethylene & Catalyst)			
1	0.6900	3.9100	0.18
2	1.1500	3.4500	0.33
3	1.6100	3.0100	0.54

4.2.5 Preparation and Adhesion Performance of biobased MSS bio-oil/pMDI glued Wood Specimens

To test the bonding performance of each formulated biobased MSS bio-oil/pMDI resin adhesives, southern yellow pine (SYP, pinus ssp) veneers wood specimens were cut into several panels of dimensions 320 × 46 × 10.5 mm^3 (L × W × H). The cut wooden samples were conditioned at 22 ± 2 °C and at a relative humidity of (65 ± 5%) for 7 days before applying adhesives. After

that, the adhesive joins were prepared by spreading the formulated biobased MSS bio-oil/pMDI resin viscous material on a single veneer surface with a glue spread rate of 200 g/m^2. The un-coated veneer wooden strip was placed over coated wooden strip by applying light pressure manually. Afterward, the assembled wood panels were hot-pressed at 160°C for 5 min under the pressure of 2 MPa. After cooling down at room temperature, the samples were maintained and stored for 24 hours for internal stress release before cutting into a specific size for the adhesive bonding test. Then, each bonded adhesive panel was cut into eight wood specimens with a glued area of 40 mm × 22 mm, out of which four wood specimens were tested for dry bonding strength, and the other four specimens were immersed in the water at room temperature for 24 hours. After soaking in water for 24 hours, wood specimens were naturally dried in air for 15 minutes for subsequent wet bonding strength analysis.

Tensile Shear Strength

The dry and wet shear strength of biobased MSS bio-oil/pMDI adhesives bonded wood specimens were performed on universal material testing machine (INSTRON 5900) equipped with 100 kN load cell and Bluhill 3.0 software. The adhesive strength of each bonded specimen was tested at a constant loading speed of 1.0 mm/mm, and the maximum load was recorded.

The tensile shear strength was calculated using equation 4.1[43]

$$\tau = \frac{P}{A} \qquad [4.1]$$

where τ is the tensile shear strength (N/mm^2 or MPa), P is the maximum loading force to break the bonded wood specimen (N), A represents the gluing area of adhesive joints, which is the length × width of the shear area (mm^2).

4.2.6 Adhesive Bondline Interfaces Observation through Optical Microscope

The optical microscope images of the MSS-Bio-oil/pMDI adhesive and pMDI bonded wood specimens were viewed and captured under the OLYMPUS 52X7 optical microscope at varied magnifications. The cross-sectional slices of wood joints after the bonding test were placed on the glass slide.

4.3 Results And Discussion

4.3.1 Structural Characterization of Municipal Sewage Sludge Bio-oils

Several characterizations have been performed to analyze the main chemical functions and structures present in the bio-oils derived from municipal sewage sludge hydrothermal liquefaction at four different processing conditions: MSS-Bio-oil_N MSS-Bio-oil_NC, MSS-Bio-oil_E, and MSS-Bio-oil_EC.

The FTIR analytical method helps identify the functional groups in the municipal sewage sludge bio-oils using specific absorption bands associated with the fundamental vibrations of individual molecules. Figure 4.1 presented the FTIR spectra of all the municipal sewage sludge bio-oils, and the related peak assignments were performed according to the published studies.[44–46] The peaks in the region 3500−3300 cm^{-1} correspond to the −OH stretching vibrations which indicate the presence of the hydrogen-bonded hydroxyl groups in alcohols, phenols, and acids along with the hydrogen-bonded N−H groups. A sharp triplet peak at 3000−2800 cm^{-1} is attributed to C−H stretching vibrations in methyl and methylene groups. The appearance of the characteristic peaks between 1800−1600 cm^{-1} was related to the C=O stretching vibrations of the carboxylic acid/ester or aldehydes/ketones components derived from the proteins, lipids, carbohydrates, and lignin fragments of the sewage sludge. The absorption peak observed at 1285 cm^{-1} is more likely

associated with the C−O−C stretching vibration of aliphatic and aromatic esters in the organic compounds of the sludge. In addition, some absorbance peaks with low intensities observed at 900−800 cm^{-1} were due to the C−H_2 bending vibrations, which suggested the aromaticity of the MSS bio-oils. Overall, the FTIR spectrum of each MSS bio-oil showed a similar characteristic peak with a little difference in the peak intensities owing to their hydrothermal liquefaction conditions.

To further characterize the chemical functionalities in the municipal sewage sludge bio-oils, elemental analysis and NMR techniques were performed and presented in the next section.

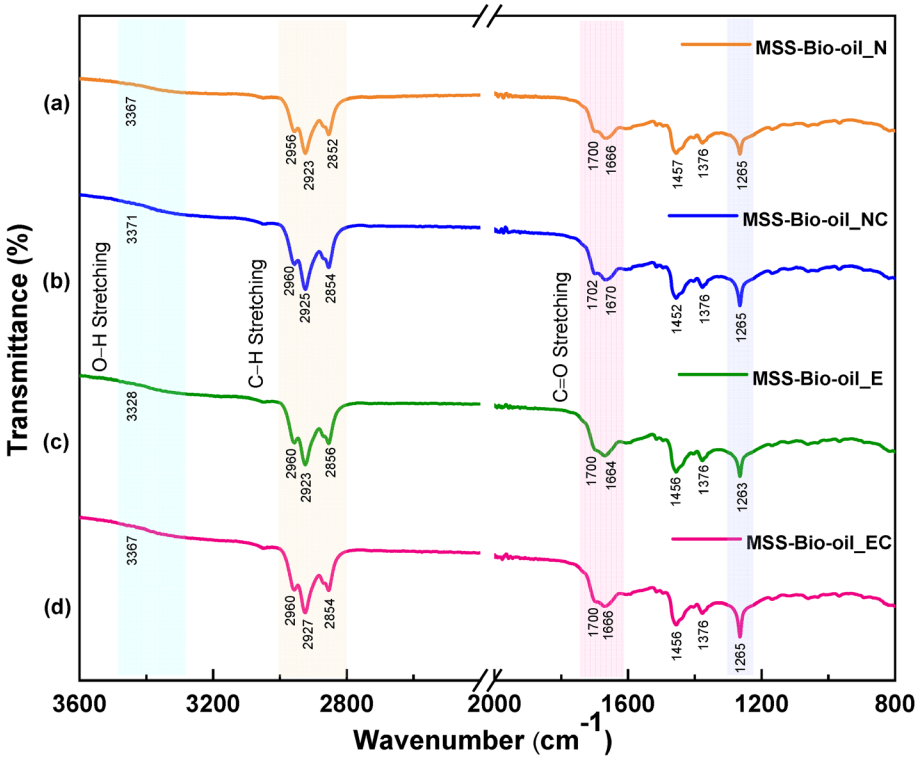

Figure 4.1 FTIR spectra of municipal sewage sludge bio-oils (a) MSS-Bio-oil_N (b) MSS-Bio-oil_NC (c) MSS-Bio-oil_E, and (d) MSS-Bio-oil_EC.

The bio-oils obtained from the hydrothermal liquefaction of municipal sewage sludge were dark-ish brown-colored, highly viscous liquid with a characteristic smell of sewage sludge comprising of a mixture of organic compounds. The elemental compositions of the MSS bio-oils are listed in Table 4.2. As seen from the Table, the C and H contents of the MSS bio-oils prepared under a nitrogen atmosphere were slightly increased with the influence of the catalyst. Additionally, hydrothermal liquefaction of the MSS under an ethylene atmosphere enhanced the carbon content (54.13 to 59.37%) and hydrogen content (6.55 to 7.62 %), irrespective of catalytic activity. The observed changes in the elemental compositions are due to the interaction between the ethylene gases and the organic compounds in the sewage sludge, which leads to increased hydrocarbon compounds.

Inorganic species such as N, S, and O are considered energy deficient as they affect the quality of bio-oils. The catalytic hydrothermal liquefaction process helps reduce the MSS bio-oils N, S and O content. One possible explanation is that the presence of the catalyst promotes the loss of inorganic elements in the form of gases by accelerating the deoxygenation reactions.[47] This phenomenon was not observed for contrast increase in S and O elements during the catalytic HTL process under an ethylene atmosphere, which was well described by the previous work.[41]

Table 4.2 Elemental Analysis (C, H, N, S, and O) of municipal sewage sludge bio-oils

Municipal Sewage Sludge Bio-oils	**Elemental Composition (wt %)**				
	C (%)	**H (%)**	**N (%)**	**S (%)**	**O (%)**
MSS-Bio-oil_N	72.5 ± 0.1	7.9 ± 0.2	5.3 ± 0.1	0.7 ± 0.1	13.6 ± 0.2
MSS-Bio-oil_NC	72.4 ± 1.4	7.7 ± 0.3	5.1 ± 0.1	0.6 ± 0.1	14.1 ± 1.4
MSS-Bio-oil_E	72.8 ± 0.3	8.1 ± 0.1	4.8 ± 0.2	0.7 ± 0.1	13.6 ± 0.4
MSS-Bio-oil_EC	72.3 ± 0.9	7.9 ± 0.3	5.0 ± 0.1	0.6 ± 0.1	14.2 ± 1.2

The amount of specific hydroxyl functional groups in the municipal sewage sludge bio-oils was quantitatively determined by the ^{31}P-NMR analysis. The MSS bio-oil samples were derivatized by the TMDP, which reacts with the OH moieties, and the resultant ^{31}P-NMR spectra were presented in Figure 4.2. Based on the internal standard (NHND) and integration of the peak area at 150.8−151.5 ppm, the concentration of each hydroxyl group was calculated, and the results are summarized in Table 4.3. This data showed that the phenolic hydroxyl groups (145.0−137.0 ppm) were the dominant type of hydroxyl group in all the bio-oil samples. The bio-oil prepared under the nitrogen atmosphere with no catalyst (MSS-Bio-oil_N) has the highest content of the phenolic hydroxyl groups, followed by the bio-oil prepared under the ethylene atmosphere with no catalyst (MSS-Bio-oil_E). It seems that the reaction atmosphere and the catalyst's presence influence the number of hydroxyl groups.

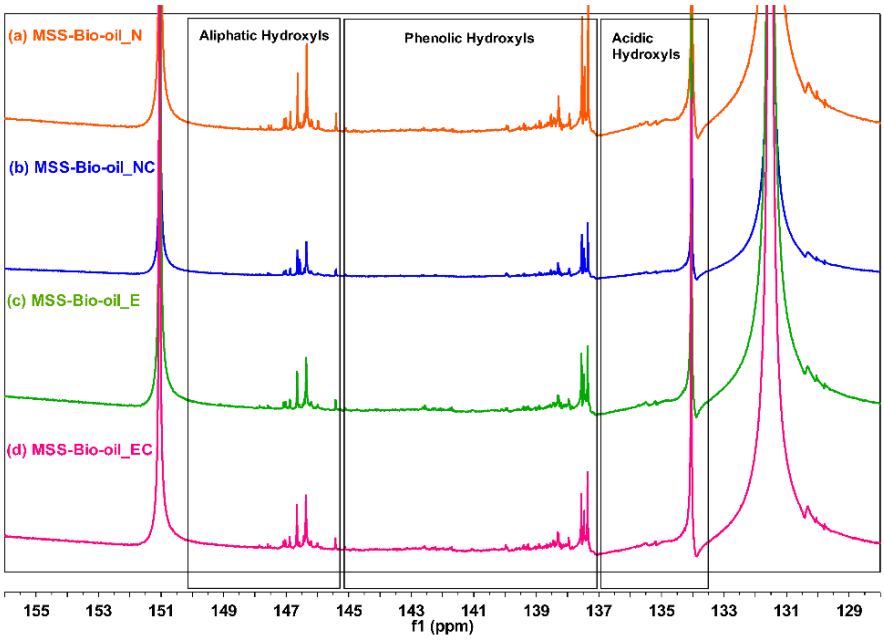

Figure 4.2 ^{31}P NMR spectra and signal assignments of municipal sewage sludge bio-oils (a) MSS-Bio-oil_N (b) MSS-Bio-oil_NC (c) MSS-Bio-oil_E, and (d) MSS-Bio-oil_EC phosphitylated with TMDP.

Table 4.3 Municipal Sewage Sludge bio-oils Hydroxyl groups evaluated by ^{31}P NMR analysis

Type of Hydroxyl Groups	Hydroxyl Group (mmol/g)			
	MSS-Bio-oil_N	**MSS-Bio-oil_NC**	**MSS-Bio-oil_E**	**MSS-Bio-oil_EC**
Aliphatic	0.447	0.354	0.284	0.304
Phenolic	0.674	0.489	0.526	0.476
Acidic	0.445	0.391	0.383	0.364
Total Hydroxyl Groups	1.566	1.233	1.192	1.145

The 2D HSQC NMR spectroscopy analysis was performed to characterize further the chemical structure of the municipal sewage sludge bio-oils, and the spectra are reported in Figure 4.3. The peaks and regions of each spectrum were assigned and labeled according to the literature sources.[48,49]

The 2D HSQC NMR spectra were divided into three regions, non-oxygenated aliphatic C–H: region 1 (δC/δH 0.0-40.0/0.0-3.20), oxygenated aliphatic C–H region: 2 (δC/δH 40-100.0/2.5-5.5), and aromatic and unsaturated C–H: region 3 (δC/δH 100.0-150.0/4.75-9.20).[50] Upon examining the HSQC spectrum of all bio-oils clearly, it can be seen that region 1, which corresponds to the C–H of alkanes (Area 1), Ar-Me (Area 2), and Allylic/benzylic (Area 2) is the most crowded region with a broad hump of overlapping weak peaks. This suggested that the bio-oil composed of a large portion of the aliphatic products originated from the lipids, proteins, and carbohydrates of the sewage sludge. Moreover, a notable difference has been observed between the HSQC spectrum of noncatalytic HTL (Figure 4.3 a and Figure 4.3c) and catalytic HTL (Figure 4.3 b and Figure 4.3d) in region 2 (Area 1: OMe, Area 2: Ar–OMe, Area 3: R–OH and Area 4: RO), an elimination of signals corresponds to the oxygenated aliphatic, this is because in the presence of

the catalyst compositions of the sewage sludge promotes the deoxygenation reactions.[49] In the region of aromatic/saturated region of HSQC spectra, we observed several distinct peaks attributed to the alkenes (Area 1), guaiacolics (Area 2), phenolics (Area 3), aromatic (Area 4), and polycyclic (Area 5). These results are in accordance with the elemental analysis and quantitative ^{31}P-NMR results of the municipal sewage sludge bio-oils.

Overall, it can be seen that the structure of the municipal sewage sludge bio-oils differs, and the reason for this is the different processing conditions, as discussed through the characterization techniques.

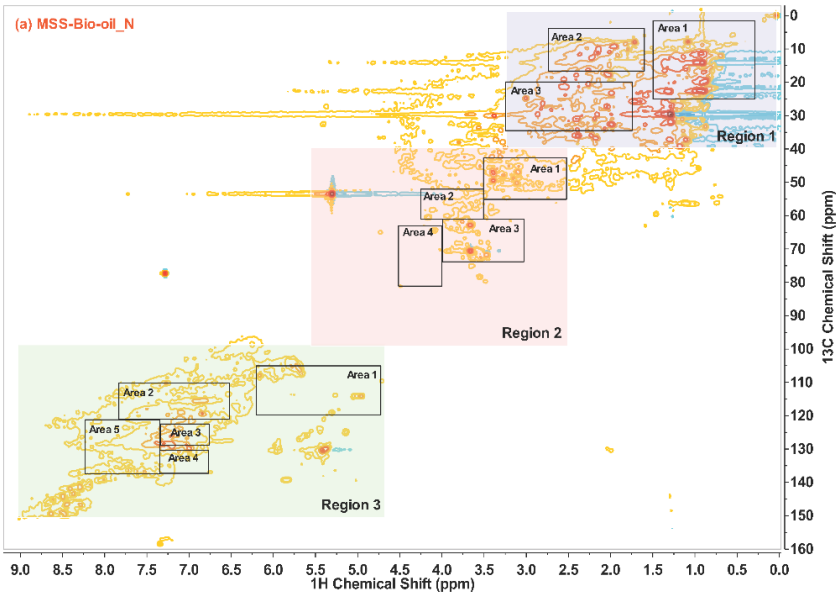

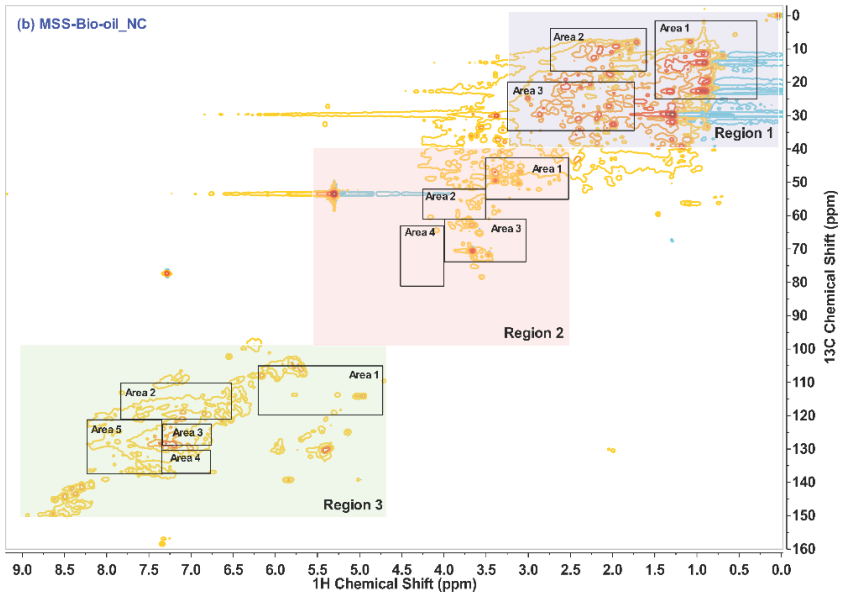
(b) MSS-Bio-oil_NC
Region 1
Region 2
Region 3
Area 1
Area 2
Area 3
Area 4
Area 5
1H Chemical Shift (ppm)
13C Chemical Shift (ppm)

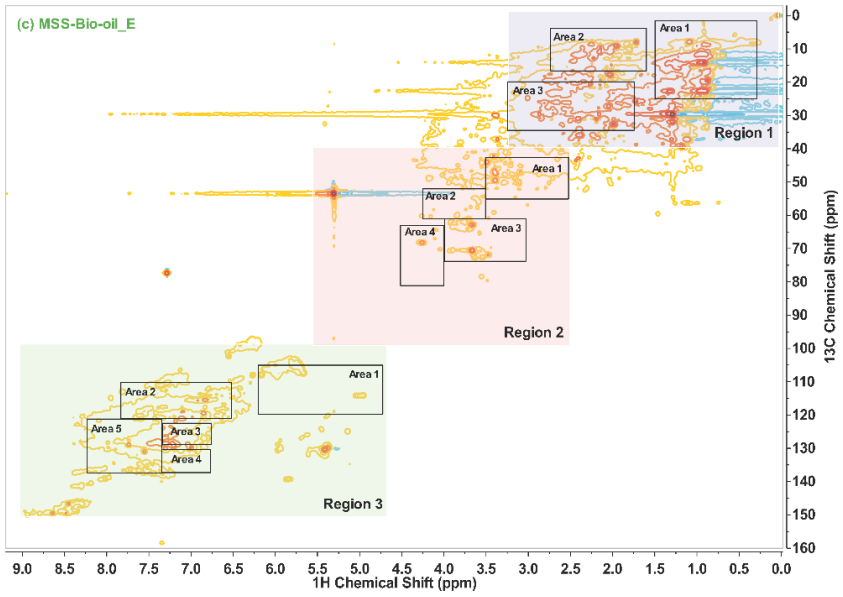
(c) MSS-Bio-oil_E
Region 1
Region 2
Region 3
Area 1
Area 2
Area 3
Area 4
Area 5
1H Chemical Shift (ppm)
13C Chemical Shift (ppm)

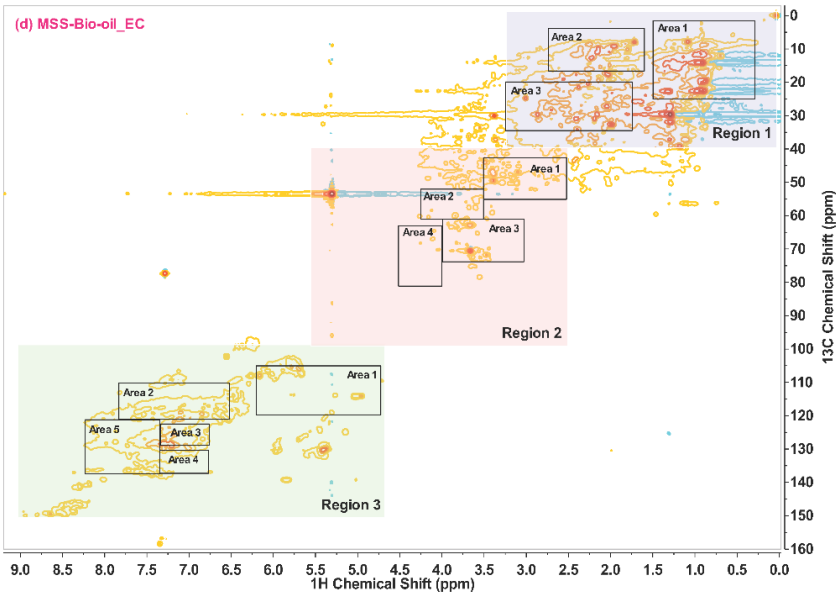

Figure 4.3 ^{13}C-^{1}H HSQC 2D-NMR spectra of municipal sewage sludge bio-oils (a) MSS-Bio-oil_N (b) MSS-Bio-oil_NC (c) MSS-Bio-oil_E, and (d) MSS-Bio-oil_EC.

4.3.2 Bonding Performance of the MSS bio-oil/pMDI Adhesives on Wood Specimens

A variety of biobased MSS bio-oil/pMDI adhesive formulations were prepared by directly mixing each of the MSS bio-oil with the pMDI (MSS Bio-oil/pMDI weight ratio: 0.18, 0.33, and 0.54) as per the method reported in the experimental section and summarized data in Table 4.1. Further, to investigate the performance of these adhesives, the prepared formulation was applied on wood panels with an adhesive spread of 200 g/m^2. The tensile shear strength evaluates the force to rupture the bonds between wood strands, which is a direct indication of adhesion strength.

In practice, pMDI reacts with the wood substrate through urethane linkage, which is formed by noncovalent bonding between the isocyanate groups (–N=C=O) of the pMDI and hydroxyl groups (−OH) on the wood surface as schematically shown in Figure 4.4a. As pMDI adhesives penetrate the amorphous region of wood, increasing the interlocking between the pMDI and

wood, hence leading to high strength.[51,52] Furthermore, different MSS bio-oils were introduced in this system as a functional filler to add sustainability and determine the effect of diverse functional groups present in the bio-oil on the wood bonding. The mechanism responsible for how the MSS bio-oil contained in the pMDI wood adhesive contributed to the bonding need to clarify. According to the characterization results, it is revealed that the MSS bio-oils used in this study contain –OH groups, which could interact with the –N=C=O groups in pMDI (Figure 4.4b) and form crosslinked thermoset structure which helps to improve wood bonding. When MSS bio-oil component is introduced in pMDI wood adhesive for bonding wood substrates, the bio-oil functional groups (MSS-bio-oil−OH groups) can form a chemical bond with pMDI and hence promote the bondline formation. Moreover, pMDI will also react with the hydroxyl groups on the wood surface under hot pressing curing conditions.

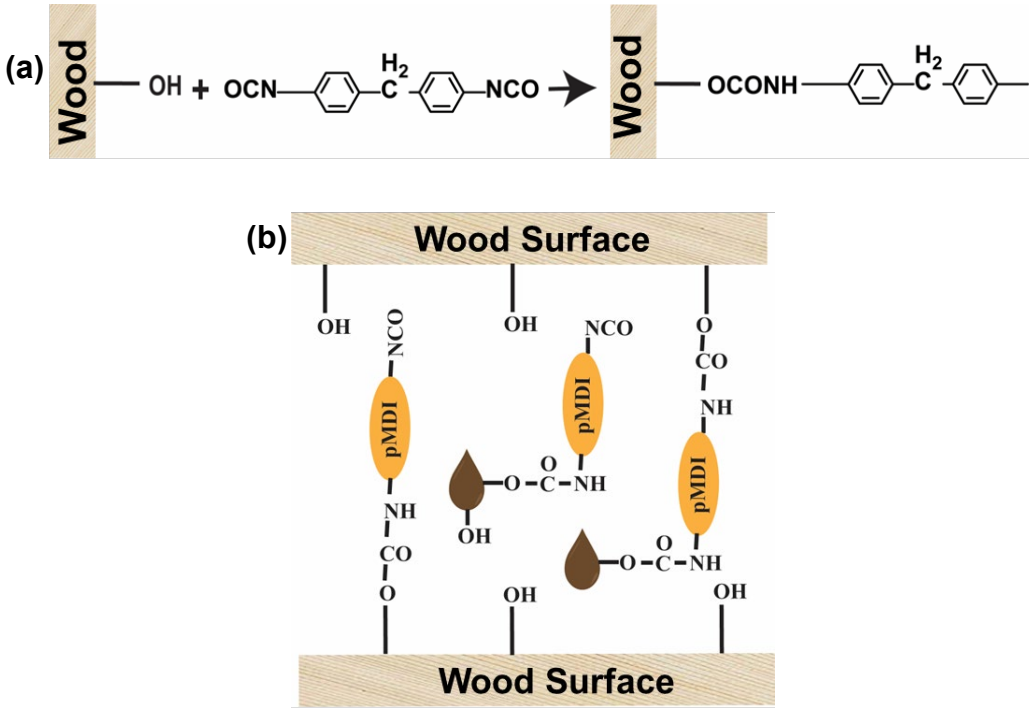

Figure 4.4 Reaction of (a) pMDI adhesive with wood (b) MSS Bio-oil/pMDI adhesive with wood.

The bonding results of pMDI control and MSS Bio-oil/pMDI wood adhesive bonded wood specimens are summarized in Figure 4.5. The wood panels bonded with the pMDI adhesive showed a dry shear strength of 3.39 ± 0.47 MPa. Chen et al. reported 2.3 MPa shear strength for neat pMDI.[17] It is observed from the ^{31}P NMR characterization results the MSS-Bio-oil_N showed relatively high hydroxyl groups (1.566 mmol/g), as reported in Figure 4.2 and Table 4.3, which provides more –OH functionalities to the isocyanate groups. Whereas, among MSS-Bio-oil_N/pMDI adhesive, the adhesive with 0.33 MSS Bio-oil/pMDI weight ratio had dry tensile shear bonding strength (3.45 ± 0.70 MPa) higher than the pMDI control. This is because even if pMDI wood adhesive was considered fast curing, the consumption of all the isocyanate groups takes time, the residual isocyanate groups remained in the adhesive formulation.[15] When the bio-oil is inserted into the system, the residual hydroxyl groups can react with the bio-oil and hence strengthen the bonding strength. Adding MSS-Bio-oil to pMDI can potentially help to reduce pMDI penetration into wood substrate and help to improve the bondline formation.

Interestingly, there was a slight drop in the dry bonding strength of MSS-Bio-oil_N/pMDI wood adhesive with 0.54 (MSS Bio-oil/pMDI weight ratio). Therefore, the amount of MSS-Bio-oil needed to optimize to avoid having adverse effects on the wood bonding strength. An excess of MSS Bio-oil filler in pMDI could overconsume pMDI isocyanate groups, resulting in insufficient reactive groups for the curing reactions and poor bonding performance. Also, too much MSS Bio-oil filler could cause application difficulties, such as uneven distribution of adhesive on the wood surface as adhesive traveled far from the wood surface and thickly coated at edges. The other MSS-Bio-oil containing pMDI adhesive formulations showed relatively lower bonding strength than pMDI which is attributed to their structural characteristics.

Apart from the dry adhesion strength, it is essential to study water resistance properties that influence the dimensional stability of glued wood products. As wood adhesive pMDI stands out for its outstanding water resistance[10,15], it is important to see how MSS Bio-oil affects the wet bonding strength. Figure 4.5b presents the tensile shear strength data obtained under wet conditions. The bonding performance of the MSS-Bio-oil_N, MSS-Bio-oil_E, MSS-Bio-oil_EC, and neat pMDI adhesives after the water soaking displayed a lower tensile shear strength values, compared to the corresponding dry shear strength. In contrast, the tensile shear strength wood specimen bonded with the MSS-Bio-oil_NC adhesive formulation increased after soaking in water. This is because residual isocyanate could react with water and form polyurea linkages to further strengthen the adhesive bond, which is also referred to as the post-curing process. A similar observation is reported in the literature for the lignin-containing cellulose nanofibril filler in pMDI adhesive for wood bonding.[17]

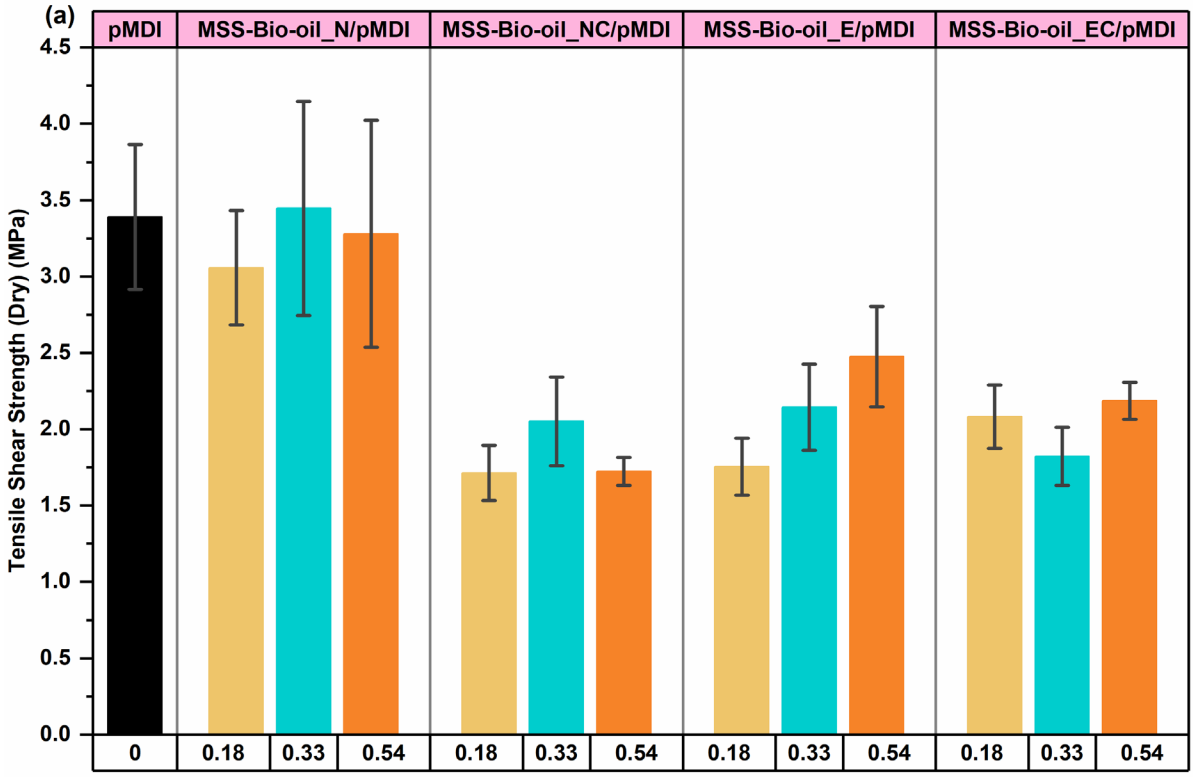

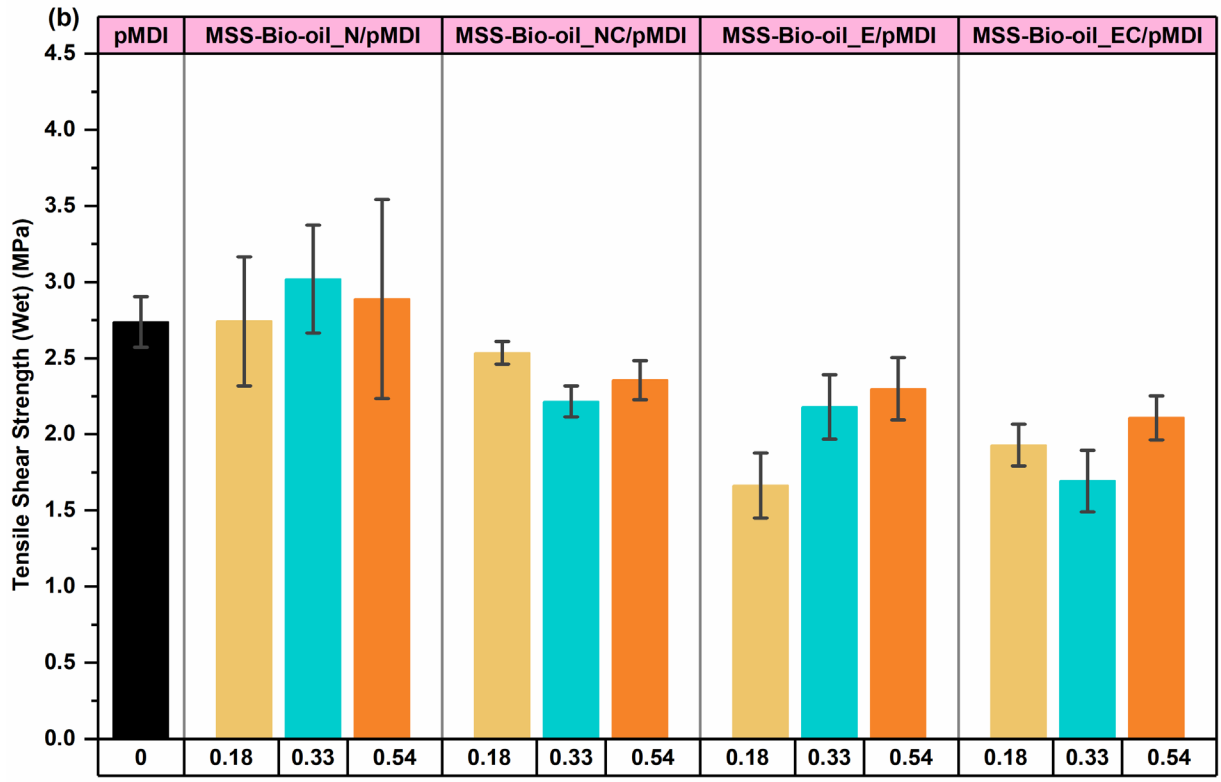

Figure 4.5 The (a) dry and (b) wet tensile shear bonding strength of the wood specimens bonded with different MSS bio-oil/pMDI adhesives. Four wood-bonded specimens were tested and reported for each adhesive measurement in the form of mean and SD (error bars).

4.3.3 Adhesive Bondline Interfaces Observation

The optical images of the bondline of the cross-sectional slice of the wood joints bonded with neat pMDI and MSS-Bio-oil_N/pMDI are shown in Figure 4.6. The pMDI (control sample) showed a thin continuous line. However, inconsistency observed was observed due to the over-penetration of pMDI into the wood substrate, the over-penetration leads to starvation of adhesive on bondline. A similar phenomenon was observed in the literature.[11] In Figure 7B–D, MSS-Bio-oil_N/pMDI adhesive formed a thicker bondline in the bonded specimen. The MSS-Bio-oil is

physically retained on the wood substrate surface and maintains pMDI in the bondline. This fills the gaps and voids on the interfaces, resulting in a continuous and robust bondline.

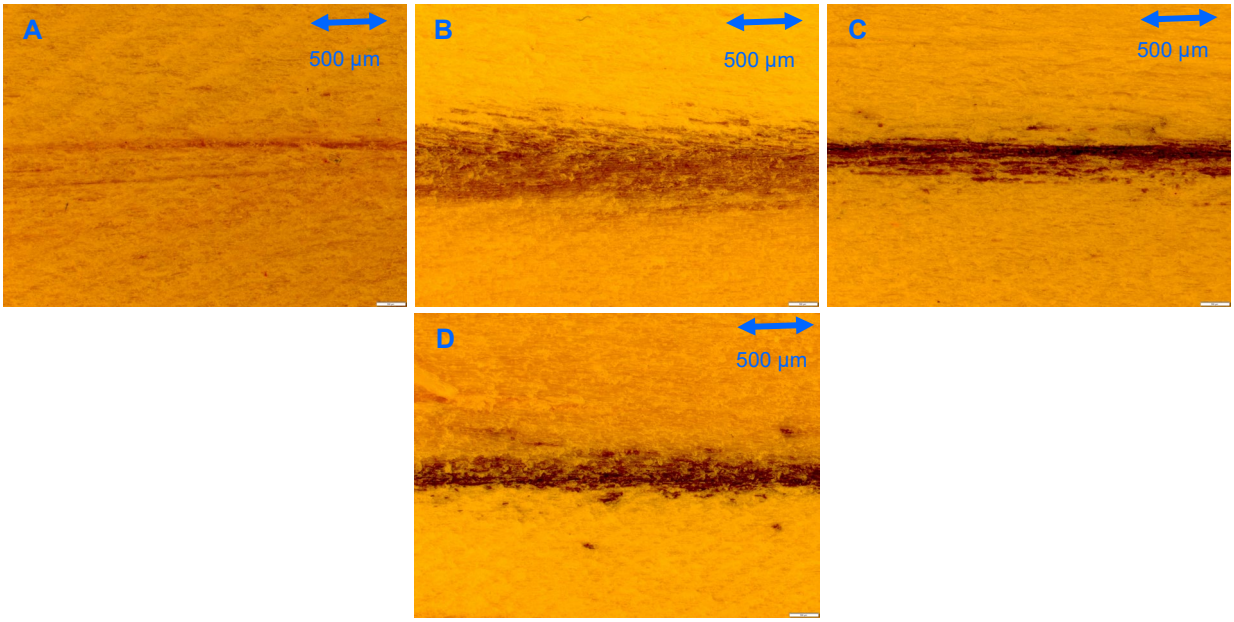

Figure 4.6 Optical microscope images of bondline of the wood pieces bonded with adhesives (A) pMDI (B) MSS-Bio-oil_N/pMDI (ratio: 0.18) (C) MSS-Bio-oil_N/pMDI (ratio: 0.33) (D) MSS-Bio-oil_N/pMDI (ratio: 0.54).

4.4 Conclusions

In this study, we presented the crucial role of bio-oils produced from municipal sewage sludge hydrothermal liquefaction, which is generated as a byproduct during wastewater treatment plants. The chemical structure of the municipal sewage sludge bio-oils prepared under four different HTL processing conditions was analyzed using FTIR, elemental analysis, ^{31}P-NMR, and 2D HSQC-NMR. The results from the analysis study provide evidence of the presence of desired functional groups. Three types of MSS-Bio-oil/pMDI adhesive were prepared for each set of MSS-Bio-oils (MSS-Bio-oil_N, MSS-Bio-oil_NC, MSS-Bio-oil_E, and MSS-Bio-oil_EC) with

MSS Bio-oil/pMDI weight ratio: of 0.18, 0.33, and 0.54, respectively. The bonding performance of MSS bio-oil/pMDI adhesives indicated that the addition of MSS Bio-oil in pMDI formed an interaction between bio-oil, pMDI, and wood substrate. MSS-Bio-oil_N/pMDI wood adhesive with 0.33 (MSS Bio-oil/pMDI weight ratio) enhances the bonding performance of the pMDI wood adhesive owing to the hydroxyl functionality of MSS Bio-oil. This work demonstrated the efficiency and potential of using MSS-Bio-oil as a biobased sustainable functional filler in a pMDI wood adhesive system to enhance the bonding performance of engineered wood products.

4.5 References

(1) Chen, T.; Wu, Z.; Wang, X. A.; Wang, W.; Huang, D.; Wei, Q.; Wu, B.; Xie, Y. Hierarchical Lamellar Aluminophosphate Materials with Porosity as Ecofriendly Inorganic Adhesive for Wood-Based Boards. *ACS Sustain. Chem. Eng.* **2018**, *6* (5), 6273–6280. https://doi.org/10.1021/acssuschemeng.8b00078.

(2) Yin, H.; Zhang, E.; Zhu, Z.; Han, L.; Zheng, P.; Zeng, H.; Chen, N. Soy-Based Adhesives Functionalized with Pressure-Responsive Crosslinker Microcapsules for Enhanced Wet Adhesion. *ACS Appl. Polym. Mater.* **2021**, *3* (2), 1032–1041. https://doi.org/10.1021/acsapm.0c01295.

(3) Bandara, N.; Wu, J. Chemically Modified Canola Protein-Nanomaterial Hybrid Adhesive Shows Improved Adhesion and Water Resistance. *ACS Sustain. Chem. Eng.* **2018**, *6* (1), 1152–1161. https://doi.org/10.1021/acssuschemeng.7b03457.

(4) Zheng, P.; Chen, N.; Mahfuzul Islam, S. M.; Ju, L. K.; Liu, J.; Zhou, J.; Chen, L.; Zeng, H.; Lin, Q. Development of Self-Cross-Linked Soy Adhesive by Enzyme Complex from Aspergillus Niger for Production of All-Biomass Composite Materials. *ACS Sustain.*

Chem. Eng. **2019**, *7* (4), 3909–3916. https://doi.org/10.1021/acssuschemeng.8b04993.

(5) Bandara, N.; Wu, J. Randomly Oriented Strand Board Composites from Nanoengineered Protein-Based Wood Adhesive. *ACS Sustain. Chem. Eng.* **2018**, *6* (1), 457–466. https://doi.org/10.1021/acssuschemeng.7b02686.

(6) Park, S.; Jeong, B.; Park, B. D. A Comparison of Adhesion Behavior of Urea-Formaldehyde Resins with Melamine-Urea-Formaldehyde Resins in Bonding Wood. *Forests* **2021**, *12* (8), 1–11. https://doi.org/10.3390/f12081037.

(7) Edition, S. *Handbook of Adhesion Technology*; 2011. https://doi.org/10.1007/978-3-642-01169-6.

(8) Sánchez-Ferrer, A.; Soprunyuk, V.; Engelhardt, M.; Stehle, R.; Gilg, H. A.; Schranz, W.; Richter, K. Polyurea Networks from Moisture-Cure, Reaction-Setting, Aliphatic Polyisocyanates with Tunable Mechanical and Thermal Properties. *ACS Appl. Polym. Mater.* **2021**, *3* (8), 4070–4078. https://doi.org/10.1021/acsapm.1c00578.

(9) Zhang, C.; Yu, L.; Ferdosian, F.; Vijayaraghavan, S.; Mesnager, J.; Jollet, V.; Zhao, B. Behavior of Water/Pmdi Emulsion Adhesive on Bonding Wood Substrates with Varied Surface Properties. *Ind. Eng. Chem. Res.* **2018**, *57* (48), 16318–16326. https://doi.org/10.1021/acs.iecr.8b03485.

(10) Yan, N.; Chen, H.; Gnanasekar, P.; Nair, S. S.; Xu, W.; Chauhan, P. Lignin as a Key Component in Lignin-Containing Cellulose Nanofibrils for Enhancing the Performance of Polymeric Diphenylmethane Diisocyanate Wood Adhesives. *ACS Sustain. Chem. Eng.* **2020**, *8* (46), 17165–17176. https://doi.org/10.1021/acssuschemeng.0c05642.

(11) Chen, H.; Yan, N. Application of Western Red Cedar (Thuja Plicata) Tree Bark as a Functional Filler in PMDI Wood Adhesives. *Ind. Crops Prod.* **2018**, *113* (August 2017),

1–9. https://doi.org/10.1016/j.indcrop.2018.01.005.

(12) Solt, P.; Libowitzky, S.; van Herwijnen, H. W. G.; Konnerth, J. Improved Method for Analyzing Cohesive Strength Development of PMDI. *Wood Science and Technology*. 2020, pp 7–17. https://doi.org/10.1007/s00226-019-01143-7.

(13) Yelle, D. J.; Service, U. F.; Jakes, J. E.; Frihart, C. R. Characterizing Polymeric Methylene Diphenyl Diisocyanate Reactions with Wood : 1 . High- Resolution Solution-State NMR Spectroscopy. **1996**, 338–342.

(14) Nuryawan, A.; Alamsyah, E. M. A Review of Isocyanate Wood Adhesive: A Case Study in Indonesia. *Appl. Adhes. Bond. Sci. Technol.* **2018**. https://doi.org/10.5772/intechopen.73115.

(15) Chen, H.; Yan, N. Application of Western Red Cedar (Thuja Plicata) Tree Bark as a Functional Filler in PMDI Wood Adhesives. *Ind. Crops Prod.* **2018**, *113* (January), 1–9. https://doi.org/10.1016/j.indcrop.2018.01.005.

(16) Ménard, R.; Caillol, S.; Allais, F. Chemo-Enzymatic Synthesis and Characterization of Renewable Thermoplastic and Thermoset Isocyanate-Free Poly(Hydroxy)Urethanes from Ferulic Acid Derivatives. *ACS Sustain. Chem. Eng.* **2017**, *5* (2), 1446–1456. https://doi.org/10.1021/acssuschemeng.6b02022.

(17) Chen, H.; Nair, S. S.; Chauhan, P.; Yan, N. Lignin Containing Cellulose Nanofibril Application in PMDI Wood Adhesives for Drastically Improved Gap-Filling Properties with Robust Bondline Interfaces. *Chem. Eng. J.* **2019**, *360* (November 2018), 393–401. https://doi.org/10.1016/j.cej.2018.11.222.

(18) Papadopoulos, A. N.; Hill, C. A. S.; Traboulay, E.; Hague, J. R. B. Isocyanate Resins for Particleboard: PMDI vs EMDI. *Holz als Roh - und Werkst.* **2002**, *60* (2), 81–83.

https://doi.org/10.1007/s00107-001-0275-8.

(19) Mittal, K. L. *Progress in Adhesion and Adhesives*; Scrivener Publishin, 2018.

(20) Quienne, B.; Kasmi, N.; Dieden, R.; Caillol, S.; Habibi, Y. Isocyanate-Free Fully Biobased Star Polyester-Urethanes: Synthesis and Thermal Properties. *Biomacromolecules* **2020**, *21* (5), 1943–1951. https://doi.org/10.1021/acs.biomac.0c00156.

(21) Asafu-Adjaye, O. A.; Street, J.; Bansode, A.; Auad, M. L.; Peresin, M. S.; Adhikari, S.; Liles, T.; Via, B. K. Fast Pyrolysis Bio-Oil-Based Epoxy as an Adhesive in Oriented Strand Board Production. *Polymers (Basel).* **2022**, *14* (6). https://doi.org/10.3390/polym14061244.

(22) Tang, S.; Yan, F.; Zheng, C.; Zhang, Z. Novel Calcium Oxide-Enhancement Phosphorus Recycling Technique through Sewage Sludge Pyrolysis. *ACS Sustain. Chem. Eng.* **2018**, *6* (7), 9167–9177. https://doi.org/10.1021/acssuschemeng.8b01492.

(23) Demirbas, A.; Edris, G.; Alalayah, W. M. Sludge Production from Municipal Wastewater Treatment in Sewage Treatment Plant. *Energy Sources, Part A Recover. Util. Environ. Eff.* **2017**, *39* (10), 999–1006. https://doi.org/10.1080/15567036.2017.1283551.

(24) Nascimento, A. L.; Souza, A. J.; Andrade, P. A. M.; Andreote, F. D.; Coscione, A. R.; Oliveira, F. C.; Regitano, J. B. Sewage Sludge Microbial Structures and Relations to Their Sources, Treatments, and Chemical Attributes. *Front. Microbiol.* **2018**, *9* (JUL), 1–11. https://doi.org/10.3389/fmicb.2018.01462.

(25) Barrett, H.; Sun, J.; Gong, Y.; Yang, P.; Hao, C.; Verreault, J.; Zhang, Y.; Peng, H. Triclosan Is the Predominant Antibacterial Compound in Ontario Sewage Sludge. *Environ. Sci. Technol.* **2022**. https://doi.org/10.1021/acs.est.2c00406.

(26) Seiple, T. E.; Coleman, A. M.; Skaggs, R. L. Municipal Wastewater Sludge as a Sustainable Bioresource in the United States. *J. Environ. Manage.* **2017**, *197*, 673–680. https://doi.org/10.1016/j.jenvman.2017.04.032.

(27) Cobo, S.; Dominguez-Ramos, A.; Irabien, A. Minimization of Resource Consumption and Carbon Footprint of a Circular Organic Waste Valorization System. *ACS Sustain. Chem. Eng.* **2018**, *6* (3), 3493–3501. https://doi.org/10.1021/acssuschemeng.7b03767.

(28) Srivastava, R. K.; Shetti, N. P.; Reddy, K. R.; Aminabhavi, T. M. Sustainable Energy from Waste Organic Matters via Efficient Microbial Processes. *Sci. Total Environ.* **2020**, *722*, 137927. https://doi.org/10.1016/j.scitotenv.2020.137927.

(29) Franco, A.; Fernandes De Souza, J.; Pinheiro Do Nascimiento, P. F.; Mendes Pedroza, M.; De Carvalho, L. S.; Rodriguez-Castellón, E.; Luque, R. Sewage Sludge-Derived Materials as Efficient Catalysts for the Selective Production of Vanillin from Isoeugenol. *ACS Sustain. Chem. Eng.* **2019**, *7* (8), 7519–7526. https://doi.org/10.1021/acssuschemeng.8b05105.

(30) Djandja, O. S.; Wang, Z. C.; Wang, F.; Xu, Y. P.; Duan, P. G. Pyrolysis of Municipal Sewage Sludge for Biofuel Production: A Review. *Ind. Eng. Chem. Res.* **2020**, *59* (39), 16939–16956. https://doi.org/10.1021/acs.iecr.0c01546.

(31) Tian, X.; Richardson, R. E.; Tester, J. W.; Lozano, J. L.; You, F. Retrofitting Municipal Wastewater Treatment Facilities toward a Greener and Circular Economy by Virtue of Resource Recovery: Techno-Economic Analysis and Life Cycle Assessment. *ACS Sustain. Chem. Eng.* **2020**, *8* (36), 13823–13837. https://doi.org/10.1021/acssuschemeng.0c05189.

(32) Chen, W. T.; Haque, M. A.; Lu, T.; Aierzhati, A.; Reimonn, G. A Perspective on

Hydrothermal Processing of Sewage Sludge. *Curr. Opin. Environ. Sci. Heal.* **2020**, *14*, 63–73. https://doi.org/10.1016/j.coesh.2020.02.008.

(33) Miyata, Y.; Sagata, K.; Hirose, M.; Yamazaki, Y.; Nishimura, A.; Okuda, N.; Arita, Y.; Hirano, Y.; Kita, Y. Fe-Assisted Hydrothermal Liquefaction of Lignocellulosic Biomass for Producing High-Grade Bio-Oil. *ACS Sustain. Chem. Eng.* **2017**, *5* (4), 3562–3569. https://doi.org/10.1021/acssuschemeng.7b00381.

(34) Wu, B.; Berg, S. M.; Remucal, C. K.; Strathmann, T. J. Evolution of N-Containing Compounds during Hydrothermal Liquefaction of Sewage Sludge. *ACS Sustain. Chem. Eng.* **2020**, *8* (49), 18303–18313. https://doi.org/10.1021/acssuschemeng.0c07060.

(35) Li, L.; Xu, Z. R.; Zhang, C.; Bao, J.; Dai, X. Quantitative Evaluation of Heavy Metals in Solid Residues from Sub- and Super-Critical Water Gasification of Sewage Sludge. *Bioresour. Technol.* **2012**, *121*, 169–175. https://doi.org/10.1016/j.biortech.2012.06.084.

(36) Li, R.; Teng, W.; Li, Y.; Liu, E. Liquefaction of Sewage Sludge to Produce Bio-Oil in Different Organic Solvents with in Situ Hydrogenation. *Energy and Fuels* **2019**, *33* (8), 7415–7423. https://doi.org/10.1021/acs.energyfuels.9b01434.

(37) Zhang, W.; Cao, H.; Mahadevan Subramanya, S.; Savage, P.; Liang, Y. Destruction of Perfluoroalkyl Acids Accumulated in Typha Latifolia through Hydrothermal Liquefaction. *ACS Sustain. Chem. Eng.* **2020**, *8* (25), 9257–9262. https://doi.org/10.1021/acssuschemeng.0c03249.

(38) Jarvis, J. M.; Albrecht, K. O.; Billing, J. M.; Schmidt, A. J.; Hallen, R. T.; Schaub, T. M. Assessment of Hydrotreatment for Hydrothermal Liquefaction Biocrudes from Sewage Sludge, Microalgae, and Pine Feedstocks. *Energy and Fuels* **2018**, *32* (8), 8483–8493. https://doi.org/10.1021/acs.energyfuels.8b01445.

(39) Chang, Y. C.; Xiao, X. F.; Huang, H. J.; Xiao, Y. D.; Fang, H. S.; He, J. B.; Zhou, C. H. Transformation Characteristics of Polycyclic Aromatic Hydrocarbons during Hydrothermal Liquefaction of Sewage Sludge. *J. Supercrit. Fluids* **2021**, *170* (October 2020), 0–2. https://doi.org/10.1016/j.supflu.2020.105158.

(40) Subramaniam, S.; Santosa, D. M.; Brady, C.; Swita, M.; Ramasamy, K. K.; Thorson, M. R. Extended Catalyst Lifetime Testing for HTL Biocrude Hydrotreating to Produce Fuel Blendstocks from Wet Wastes. *ACS Sustain. Chem. Eng.* **2021**, *9* (38), 12825–12832. https://doi.org/10.1021/acssuschemeng.1c02743.

(41) Rahman, T.; Jahromi, H.; Roy, P.; Adhikari, S.; Hassani, E.; Oh, T. S. Hydrothermal Liquefaction of Municipal Sewage Sludge: Effect of Red Mud Catalyst in Ethylene and Inert Ambiences. *Energy Convers. Manag.* **2021**, *245* (May), 114615. https://doi.org/10.1016/j.enconman.2021.114615.

(42) Barde, M.; Celikbag, Y.; Via, B.; Adhikari, S.; Auad, M. L. Semi-Interpenetrating Novolac-Epoxy Thermoset Polymer Networks Derived from Plant Biomass. *J. Renew. Mater.* **2018**, *6* (7), 724–736. https://doi.org/10.32604/JRM.2018.00116.

(43) Bansode, A.; Barde, M.; Asafu-Adjaye, O.; Patil, V.; Hinkle, J.; Via, B. K.; Adhikari, S.; Adamczyk, A. J.; Farag, R.; Elder, T.; Labbé, N.; Auad, M. L. Synthesis of Biobased Novolac Phenol-Formaldehyde Wood Adhesives from Biorefinery-Derived Lignocellulosic Biomass. *ACS Sustain. Chem. Eng.* **2021**, *9* (33), 10990–11002. https://doi.org/10.1021/acssuschemeng.1c01916.

(44) Badrolnizam, R. S.; Elham, O. S. J.; Hadzifah, S. N.; Husain, M. H. N.; Hidayu, A. R.; Mohammad, N. F.; Mohamad Daud, A. R. Sewage Sludge Conversion via Hydrothermal Liquefaction (HTL) - A Preliminary Study. *J. Phys. Conf. Ser.* **2019**, *1349* (1), 0–8.

https://doi.org/10.1088/1742-6596/1349/1/012108.

(45) Faixo, S.; Gehin, N.; Balayssac, S.; Gilard, V.; Mazeghrane, S.; Haddad, M.; Gaval, G.; Paul, E.; Garrigues, J. C. Current Trends and Advances in Analytical Techniques for the Characterization and Quantification of Biologically Recalcitrant Organic Species in Sludge and Wastewater: A Review. *Anal. Chim. Acta* **2021**, *1152*. https://doi.org/10.1016/j.aca.2021.338284.

(46) Tian, K.; Liu, W. J.; Qian, T. T.; Jiang, H.; Yu, H. Q. Investigation on the Evolution of N-Containing Organic Compounds during Pyrolysis of Sewage Sludge. *Environ. Sci. Technol.* **2014**, *48* (18), 10888–10896. https://doi.org/10.1021/es5022137.

(47) Xu, D.; Lin, G.; Liu, L.; Wang, Y.; Jing, Z.; Wang, S. Comprehensive Evaluation on Product Characteristics of Fast Hydrothermal Liquefaction of Sewage Sludge at Different Temperatures. *Energy* **2018**, *159*, 686–695. https://doi.org/10.1016/j.energy.2018.06.191.

(48) Jahromi, H.; Rahman, T.; Roy, P.; Adhikari, S. Hydrotreatment of Solvent-Extracted Biocrude from Hydrothermal Liquefaction of Municipal Sewage Sludge. *Energy Convers. Manag.* **2022**, *263* (March), 115719. https://doi.org/10.1016/j.enconman.2022.115719.

(49) He, S.; Bijl, A.; Rohrbach, L.; Yuan, Q.; Sukmayanda Santosa, D.; Wang, Z.; Jan Heeres, H.; Brem, G. Catalytic Upcycling Paper Sludge for the Recovery of Minerals and Production of Renewable High-Grade Biofuels and Bio-Based Chemicals. *Chem. Eng. J.* **2021**, *420* (P1), 129714. https://doi.org/10.1016/j.cej.2021.129714.

(50) Castello, D.; He, S.; Ruiz, M. P.; Westerhof, R. J. M.; Heeres, H. J.; Seshan, K.; Kersten, S. R. A. Is It Possible to Increase the Oil Yield of Catalytic Pyrolysis of Biomass? A Study Using Commercially-Available Acid and Basic Catalysts in Ex-Situ and in-Situ Modus. *J. Anal. Appl. Pyrolysis* **2019**, *137* (September 2018), 77–85.

https://doi.org/10.1016/j.jaap.2018.11.012.

(51) Paris, J. L.; Kamke, F. A. Quantitative Wood-Adhesive Penetration with X-Ray Computed Tomography. *Int. J. Adhes. Adhes.* **2015**, *61*, 71–80. https://doi.org/10.1016/j.ijadhadh.2015.05.006.

(52) Tan, R. The Use of P-MDI Resin in MDF Manufacture. *Fac. For.* **2012**, 5–6.

Chapter 5

Non-isothermal Curing Kinetics of Novolac type Phenol-Formaldehyde Resin for 3D Printing of Sustainable Building Design

This chapter is being prepared for submission[4]

5.1 Introduction

The rapid increase in the world's population has been accompanied by extensive utilization of building materials and construction-related energy and resource consumption, leading to direct and indirect environmental and human impacts.[1] To reduce energy consumption in building construction, several approaches have been employed. These approaches include the perspective of the sustainable framework, which remarkably alleviates adverse environmental and human impacts through efficient and sustainable material and thoughtful design.[2]

In the material design approach, the use of novolac-type phenol-formaldehyde (NPF) resins is considered advantageous because of the reduced formaldehyde emission and their excellent functional properties: processability, strength, adhesion, and thermal and chemical stability.[3] NPF resins are produced from acid-catalyzed condensation polymerization reaction between phenol and formaldehyde, using an excess of phenol reactant (P/F molar ratio 1:0.8). Novolac resins are linear or partially cross-linked polymers characterized by phenol moieties connected by methylene bridges. The chemical reaction referred to as curing occurs at elevated tempera-

[4] Bansode, A.; Vega Erramuspe I. B.; Portilla Villarreal L.; Hahn B.; Via B. K.; David A.; Labbe N.; Auad, M. L.; Non-isothermal Curing Kinetics of Novolac type Phenol-Formaldehyde Resin for 3D Printing of Sustainable Building Design, In Preparation, 2022

tures in the presence of hardener (typically hexamethylenetetramine, HMTA). During the curing process, three-dimensional network polymer structures are formed.[4] The cross-linking reaction between NPF resin and HMTA occurs in two stages.[5] In the first stage, forming initial intermediates such as benzoxazines and benzylamines. In the second stage, these intermediates decompose and react to form methylene linkages between phenolic rings for chain extension and cross-linking.[6] However, synthesizing these resins still relies on nonrenewable resources, which are associated with the rapid depletion of fossil fuels and increasing concerns for the environment and health during the production and use of phenol-formaldehyde (PF) resins.[7] Thus, substantial research is being conducted in exploring renewable biomass materials to produce sustainable alternative feedstock to replace petroleum-derived materials. In this respect, thermochemically derived materials are considered an advantageous source for bio-based monomers (e.g., phenolic compounds) and can be obtained during the thermochemical conversion of biomass, which can serve as an alternative reactive site during polymer resin synthesis.[8,9]

In addition to material development, the thoughtful structural design also plays a significant role in designing sustainable building components. In this regard, three-dimensional printing (3DP), also known as additive manufacturing (AM), has been proven as one of the critical sustainable technologies compared to the traditional technology of constructing buildings due to the advantages like reduction of material waste and facilitating efficient, customized design with cost effectiveness.[10] 3DP techniques create composite materials and structures layer by layer through cross-linking or curing of thermosets polymeric resins or other materials.[11] Among all the 3DP techniques, direct ink writing (DIW) has been proven effective in the fabrication of thermoset composite, an extrusion-based additive manufacturing method in which materials are deposited layerwise and cured simultaneously or post-printing via photocuring or thermal curing.[12–14]

Thermal curing is especially suitable for thermo-reactive polymeric resins like NPF that cannot be cross-linked by photocuring, which uses ultraviolet light irradiation (UV) to cure the material. In the thermal curing approach, two separate streams of resin and hardener are passively mixed, extruded on the heating bed, and then cured rapidly. However, this curing process is limited to geometries with a few layers of material, not to the 3D printing of freeform structures.[15] One promising curing strategy to overcome these limitations is thermal frontal polymerization (FP), whereby curing polymerization of thermoset polymeric resins occurs rapidly via localized exothermic reaction zone through the coupling of thermal diffusion and Arrhenius reaction kinetics.[15–18]

Considering the discussion above, studying the curing kinetics of the polymeric resin is fundamental to understanding the 3D printing of polymeric materials for transforming polymer resin into a solid polymer structure since the curing reaction mechanism strongly influences the resulting polymer properties.[19] Differential scanning calorimetry (DSC) is the most popular and accurate technique used to study the curing reactions of various thermosetting resins.[20,21] DSC measures the heat flow of the sample as a function of temperature and time. After that, the generated data is extensively applied to find kinetic parameters through two primary thermal kinetic analysis methods: isothermal and non-isothermal.[22,23] In the isothermal method, the reaction mechanism is studied at a specific temperature; however, the non-isothermal method includes a single or multi-heating rate.[24] The non-isothermal process has significant advantages in contrast to the isothermal method.[25] Two approaches, such as the model-free (isoconversional) method and the model-fitting method, are primarily applied to fit the experimental data acquired from isothermal or non-isothermal DSC curves to investigate activation energy and kinetic parameters.[26]

The present work describes the synthesis and curing behavior of two different novolac polymer resin systems, novolac PF (NPF) and bio-based novolac PF (BNPF) resins. The non-isothermal differential scanning calorimetry (DSC) scan method has been used to investigate the behavior of NPF and BNPF throughout the entire curing process. Further, the obtained data were utilized to examine a set of curing kinetic parameters based on non-isothermal experimental runs at different heating rates by model-free (isoconversional) and model-fitting approaches. This work aims to provide valuable curing kinetic information for applying BNPR resins developed from renewable resources, promoting sustainability.

5.2 Experimental Section

5.2.1 Materials

Phenol crystals (99%), formalin solution (37% formaldehyde in water), hexamethylenetetramine (HMTA, >99%), and acetone (99.5%) were obtained from VWR International. Oxalic acid (anhydrous crystal, 98.0%) was purchased from Spectrum Chemical Mfg. Corp. Bio-oil, prepared by the procedure described previously,[27] was received from the Center for Renewable Carbon Laboratory, University of Tennessee.

5.2.2 Synthesis of Novolac PF Resin and Bionovolac PF Resin

Novolac phenol-formaldehyde (NPF) and bio-based novolac phenol-formaldehyde (BNPF) resins were synthesized by phenol reaction with formaldehyde, according to the previously published article.[9] Briefly, a four-necked round 500 mL bottom flask equipped with a condenser, a dropping funnel, and a mechanical stirrer was charged with phenol (94 g, 1 mol) and oxalic acid (4.70 g, 0.05 mol). The mixture was heated to 90 °C, and 37% formalin solution (64.87 g, 0.8 mol of formaldehyde) was dropped into it slowly. The reaction was allowed to continue at 90 °C

for a total time of 3 hours. The reaction product was washed with distilled water and dried in a vacuum oven. The biobased novolac PF was prepared with the same procedure by partially replacing (50% w/w) phenol with bio-oil. Furthermore, as reported previously, NPF and BNPF resins showed similar FTIR and ^{1}H-NMR spectra.[9]

5.2.3 Thermal Analysis

The curing reaction of NPF/HMTA and BNPF/HEXA was studied using a differential scanning calorimeter, DSC TA-Q2000 (Thermal Analysis Instruments, DE, USA), under a nitrogen atmosphere with a gas flux rate of 50 mL/min. Before any sample measurement, the DSC instrument was calibrated with pure indium standard. The samples, NPF/HMTA and BNPF/HMTA were prepared with HMTA to resin weight ratio of 15% and ground manually with mortar and pestle. For each measurement, the sample (3.0 – 5.0 mg) was weighed into the aluminum standard pan and sealed with an aluminum lid.

The DSC non-isothermal technique investigated the curing behavior of NPF/HMTA and BNPF/HMTA resins. First, the thermal data was obtained by increasing heating samples from 25 °C to 250 °C at various heating rates (5, 10, 15, and 25 °C/min). When the curing reaction ended, the samples were cooled to 25 °C with a cooling rate of 5, 10, 15, and 25 °C/min, respectively. In the next step, a non-isothermal curing experiment was performed with the respective heating rates to determine the reaction's residual heat. The curing reactions of NPF/HMTA and BNPF/HMTA resins are presented in Figure 5.1a and Figure 5.1b, respectively.

Origin Pro 2019 software (Origin Lab Corporation, USA) and MATLAB R2022a (version 9.0) were used to analyze thermal curing data.

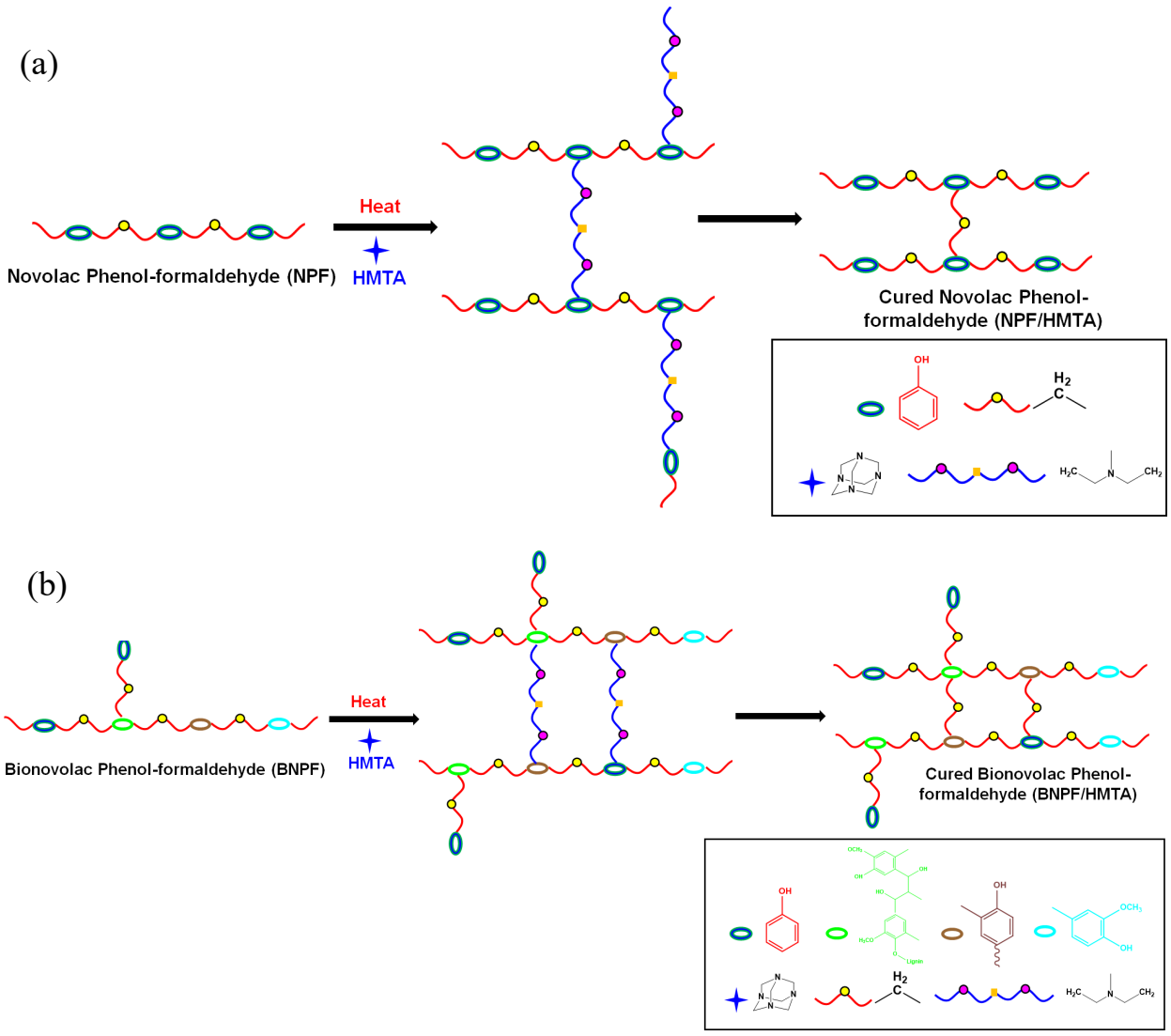

Figure 5.1 The curing process of (a) novolac phenol-formaldehyde resin and HMTA (NPF/HMTA) and (b) bionovolac phenol-formaldehyde resin and HMTA (BNPF/HMTA).

5.2.4 Fundamental Theory of Curing Kinetics

Curing reaction kinetics are performed to present the relationship between the process rates and different experimental parameters. The thermal data obtained from the non-isothermal DSC technique of NPF/HMTA and BNPF/HMTA resins at different heating rates were used to calculate kinetic parameters.

The conversion of the curing reaction or degree of curing (α) is directly proportional to the exothermic heat evolved during the curing process.[28,29] The degree of curing (α) can be expressed from equation 5.1.

$$\alpha(T) = \frac{\Delta H_T}{\Delta H_{total}} \quad [5.1]$$

where, ΔH_T is the heat of reaction at a specific temperature, T, and ΔH_{total} is the total heat of reaction, which is determined by calculation the area under the exothermic curve. The curing reaction was assumed to be complete when the non-isothermal exothermic peak of resins leveled off to the baseline.

The rate of the kinetic process is considered to be directly proportional to the measured heat flow and can be determined by equation 5.2.

$$\frac{d\alpha}{dt} = \frac{\left(\frac{dH}{dt}\right)}{\Delta H_{total}} \quad [5.2]$$

where, $d\alpha/dt$ is the curing kinetic reaction rate, dH/dt is heat flow measured during the kinetic process. For constant heating rate scans, $d\alpha/dt$ can be expressed as$d\alpha/dt = \beta\ d\alpha/dT$ at constant where β is the heating rate (K min^{-1}).

The phenomenological curing kinetic model analysis is parametrized into two main functions[26] according to the following equation 5.3.[30]

$$\frac{d\alpha}{dt} = k(T)f(\alpha) \quad [5.3]$$

where, $k(T)$ temperature-dependent kinetic rate constant and $f(\alpha)$ is the function of curing conversion.[31] The function $k(T)$ can be expressed through Arrhenius relationship as shown by equation 5.4.[30]

$$k(T) = A \exp\left(-\frac{E}{RT}\right) \quad [5.4]$$

where, A is the Arrhenius frequency factor or pre-exponential factor (s^{-1}), E is the activation energy (J mol^{-1}), R is the universal gas constant (8.314 J mol^{-1} K^{-1}), and T is the absolute temperature (K) of the sample. Combining equation 5.3 and equation 5.4 yields kinetic equation 5.5.

$$\frac{d\alpha}{dt} = A \exp\left(-\frac{E}{RT}\right) f(\alpha) \quad [5.5]$$

Curing kinetic reactions are often analyzed by two primary methodologies, i.e., model-fitting kinetic and model-free Isoconversional kinetic methods. The former process kinetic model is used to fit the experimental data to estimate the kinetic parameters.[32] On the other hand, the model-free isoconversional kinetic method obeys the isoconversional principle.[32,33]

5.2.4.1 Model-Free Isoconversional Method

The model-free (isoconversional) is a useful method to determine the mechanism of curing, and the basic assumption of this method is that the reaction rate is merely a function of temperature at a constant extent of curing degree, whose analytical expression can be written by equation 5.6.[32–34]

$$\left[\frac{\partial \ln(d\alpha/dt)}{\partial T^{-1}}\right] = -\frac{E}{R} \quad [5.6]$$

The most commonly used methods include Friedman,[35] Flynn-Wall-Ozawa (FWO),[36,37] Kissinger-Akahira-Sunnose (KAS),[38], and Vyazovkin.[32,39,40] These model-free isoconversional methods are used to calculate the re-activation energy (E) without assuming any specific expression of the reaction model.

5.2.4.2 Model-Fitting Method

The mechanism of curing reaction of resin that is related to the curing kinetic reaction model $f(\alpha)$, can be divided into three kinetic models: the nth-order model, the autocatalytic model, and the Kamal-Sourour model.[31,41,42] These models can be expressed by equation 5.7, equation 5.8, and equation 5.9, respectively.

nth-order kinetics model can be expressed as

$$\frac{d\alpha}{dt} = A \exp\left(-\frac{E}{RT}\right) (1-\alpha)^n \qquad [5.7]$$

The autocatalytic kinetic model can be expressed as

$$\frac{d\alpha}{dt} = A \exp\left(-\frac{E}{RT}\right) (1-\alpha)^n \alpha^m \qquad [5.8]$$

The Kamal kinetic model can be expressed as

$$\frac{d\alpha}{dt} = k_1 (1-\alpha)^n + k_2 (1-\alpha)^n \alpha^m \qquad [5.9]$$

where m and n are the reaction orders, $k_1 = A_1 \exp(-\mathrm{E}_1/\mathrm{RT})$ and $k_2 = A_2 \exp(-\mathrm{E}_2/\mathrm{RT})$ are the kinetic constants. A_1 and A_2 are the corresponding pre-exponential parameters, and E_1 and E_2 are the activation energies.

5.3 Results and Discussion

5.3.1 Non-isothermal DSC analysis of NPF/HMTA and BNPF/HMTA resins.

Isothermal and non-isothermal DSC measurements were performed to measure the heat of the reaction and investigate the curing process of NPF/HMTA and BNPF/HMTA resins and understand the curing behavior of developed NPF/HMTA and BNPF/HMTA resins. The isothermal approach yielded higher testing errors, similar to those previously reported for other systems.[43] Therefore, the non-isothermal DSC technique was adopted.

The non-isothermal DSC thermograms of the NPF/HMTA and BNPF/HMTA resins with different heating rates of 5, 10, 15, and 25 °C/min are shown in Figure 5.2a and Figure 5.2b, respectively. Each of these thermograms displays the exothermic peaks associated with the cross-linking reactions of the NPF/HMTA and BNPF/HMTA resins, and the peak temperature (Tp) inferred from these exothermic peaks is summarized in Table 5.1. All the curing exothermic peaks and characteristic peak temperatures shifted to higher temperatures with the increasing heating rates (β=5-20 °C/min). The increments mentioned before can be attributed to the following: as more heat is released with an increased heating rate, the temperature gradient between the reaction center and the external environment due to thermal inertia increases.[33,43,44] The exothermic peak temperature is believed to shift to a higher temperature zone for compensation.[45] The DSC curves of BNPF/HMTA resin show two distinct exothermic peaks. The first broad exotherm is ascribed to the curing reaction, and the small exotherm at higher temperatures can be attributed to side reactions occurring during the heating process. One possible explanation for the side reactions is that other chemical groups may interact with the HMTA intermediates. Still, the exotherm is very small and was neglected in the present study. Hence, only the exotherm's first curing peak was considered for kinetic analysis.

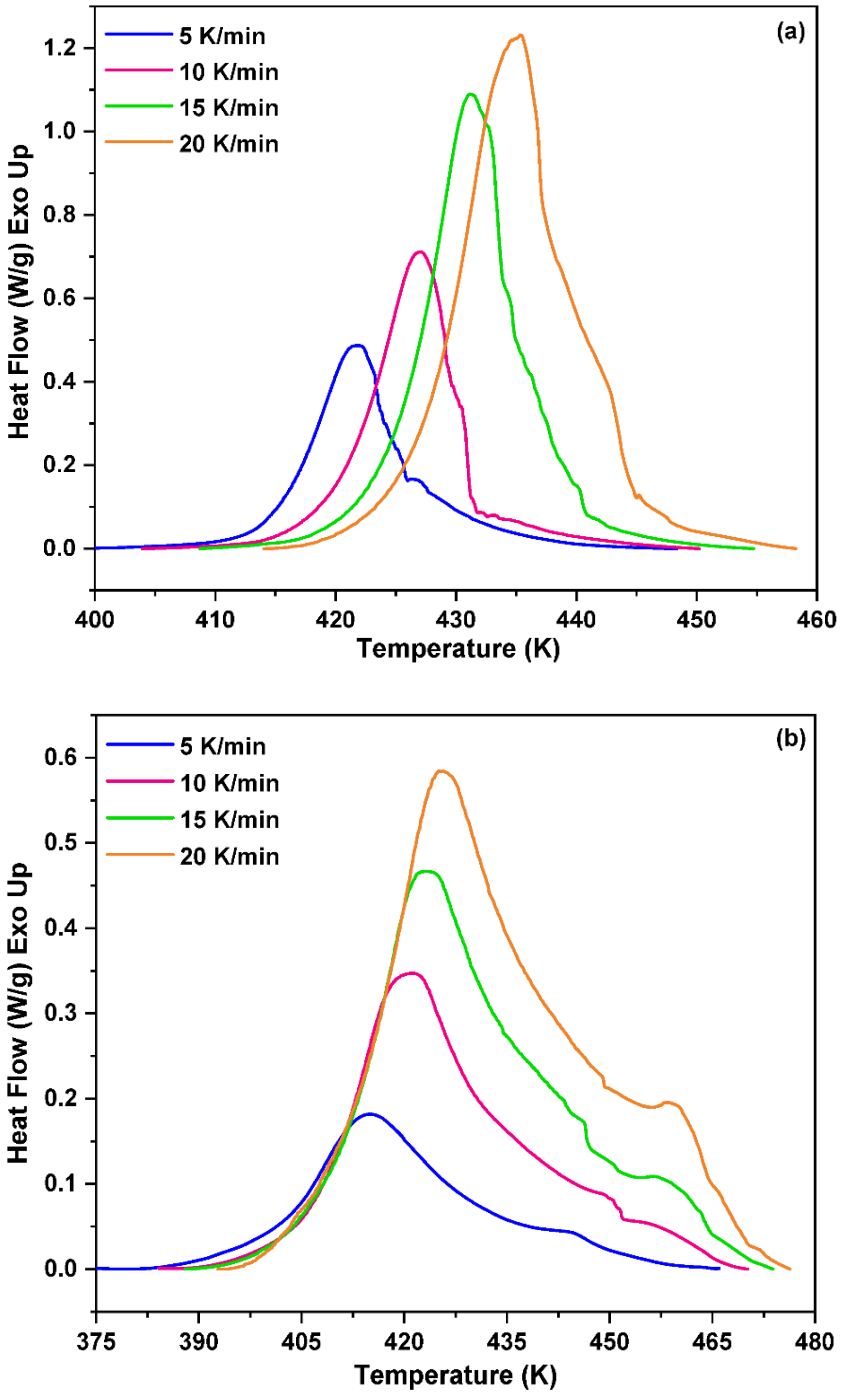

Figure 5.2 Nonisothermal DSC scanning thermograms of the thermal curing reactions of (a) NPF/HMTA resin and (b) BNPF/HMTA resin at different heating rates (5, 10, 15, and 20 K/min).

Table 5.1 Characteristic Parameters of the curing reactions of NPF/HMTA and BNPF/HMTA

Heating rate (β) (K/min)	NPF/HMTA resin	BNPF/HMTA resin
	T_P (K)	T_P (K)
5	421.81	415.11
10	426.97	420.90
15	431.21	423.10
20	435.44	425.72

5.3.2 Model-Fitting Method

The goal in the model-fitting kinetic analysis of NPF/HMTA and BNPF/HMTA resins was to find the four kinetic parameters (A, E, n, m), described in equations 5.7, 5.8, and 5.9 associated with the curing system according to a suitable reaction model. To examine the kinetic model, activation energy (E) is calculated by inserting (β=dT/dt) in equation 5.6 and taking the logarithmic form of it (as reported in equation 5.10) through the relation of the peak temperature (Tp) dependency on the heating rate (β). Assuming an isofractional peak temperature (Tp = Constant), activation energy E is determined by a linear regression analysis of ln(βdα/dTp) against 1/Tp across various heating rates (5, 10, 15, and 25 K/min) as reported in equation 5.10 and shown in Figure 5.3.

$$E = \frac{Rd[-\ln(\beta d\alpha/dT_p)]}{d(1/T_p)} \qquad [5.10]$$

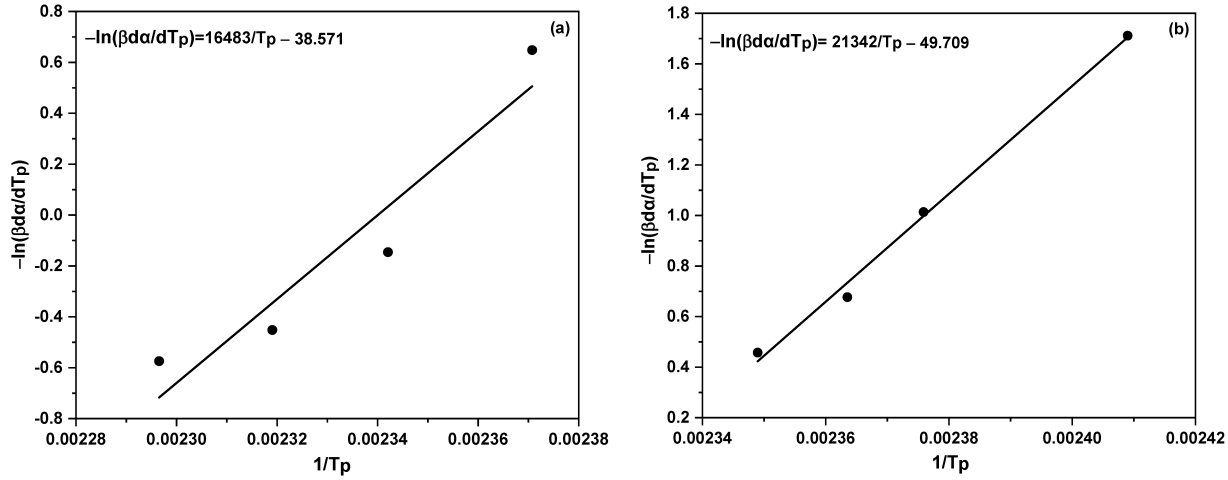

Figure 5.3 Activation energy determination of the (a) NPF/HMTA resin and (b) BNPF/HMTA resin systems.

Using the activation energy and according to the choice of the appropriate kinetic model, the reaction order (n or m) and the frequency factor (A) are calculated.

For the nth-order model, by taking the logarithmic form of equation 5.7, which is reported in the theory section, and expressing it in equation 5.11.

$$\ln\left(\frac{d\alpha}{dt}\right) + \frac{E}{RT} = \mathrm{n}\ \ln(1-\alpha) + \ln A \qquad [5.11]$$

By applying the linear regression method to equation 5.11, the values of n and A are obtained through the slope and intercept (ln A), respectively.

For the autocatalytic model, by taking the logarithmic form of equation 5.8, which is reported in the theory section, and expressing it in equation 5.12.

$$\ln\left(\frac{d\alpha}{dt}\right) + \frac{E}{RT} = \mathrm{n}\ \ln(1-\alpha) + \mathrm{m}\ln\alpha + \ln A \qquad [5.12]$$

A multilinear regression method is applied to equation 5.12 for determining the values of A, n, and m. Here, for the autocatalytic model, the overall order of reactions (m + n) is determined either with constraint (m + n = 2) or without constraint (m + n = 2).

Whereas, in the case of the Kamal model, a nonlinear regression method is used to estimate the kinetic parameters and reaction orders (n and m). In addition, for the Kamal model, the different condition was applied to investigate the kinetic constants k_1 and k_2 ($E_1 = E_2$ & $m + n = 2$, $E_1 = E_2$ & $m + n \neq 2$, $E_1 \neq E_2$ & $m + n = 2$ and $E_1 \neq E_2$ & $m + n \neq 2$). MATLAB R2022a software (version 9.0) is used to evaluate these parameters.

Once the kinetic parameters are determined at each heating rate for the nth-order model (E, A, and n), autocatalytic model (E, A, m, and n), and Kamal model (E_1, E_2, A_1, A_2, m, and n), respectively, the next step is to fit the experimental data using the model and kinetic parameters to obtain the degree of curing (α) and reaction rate (dα/dt) at each temperature.

It can be observed that the extent of conversion (α) plots for both NPF/HMTA and BNPF/HMTA depicted in Figure 5.4 and Figure 5.6 shows the sigmoid profile, i.e., the slow increase in α at the beginning and end of the curing process, while the quick increment at the intermediate stage. Whereas increasing heating rates leads to shifting these conversions (α) curves to higher temperature zones, this behavior shows good agreement with other studies.[43]

According to the model fitting results for NPF/HMTA resin, the autocatalytic model shows a suitable fit for the experimental results, as shown in Figure 5.4 and Figure 5.5. This is because the autocatalytic curing mechanism controls the entire curing reaction of NPF/HMTA resin. The intermediate products generated during the curing process catalyze the reaction with the higher

order of reaction (n), and the reaction rate reaches the maximum at the middle of the reaction stage. Smaller reaction order is observed (m), where the reaction's curing rate decreases. Our results are in accordance with the published works.[41,46,47]

As depicted in Figure 5.6 and Figure 5.7, the Kamal model shows superior predictability for monitoring the curing mechanism of the BNPF/HMTA resin, as the kinetic model shows good agreement with the experimental data. The Kamal model is a combination of the nth-order and autocatalytic models. The initial stage of the curing process, where the curing agent decomposes to produce intermediated that reacts with the novolac resin, is controlled by the autocatalytic reactions in later stages. The nth-order reaction mechanism controls it because the reaction rate decreases due to less availability of the free phenol and phenolic hydroxyl groups.

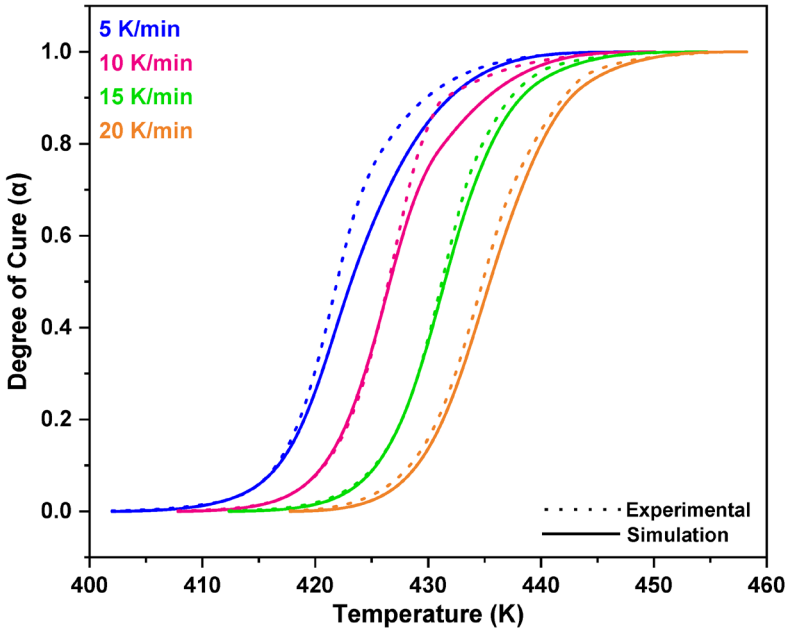

Figure 5.4 Plot for conversion (α) as a function of temperature for the experimental and simulation results for NPF/HMTA resin at different heating rates (autocatalytic model m+n=2).

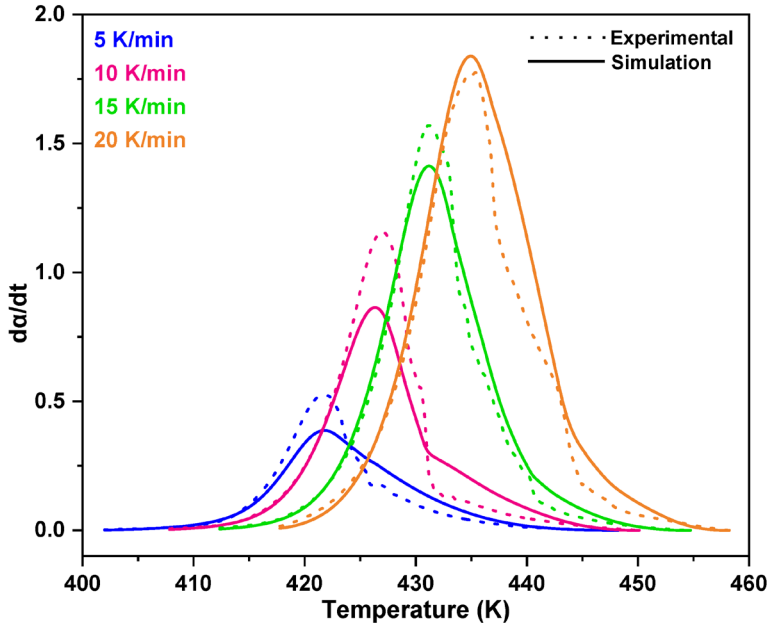

Figure 5.5 Plot for reaction rate (dα/dt) as a function of temperature for the experimental and simulation results for NPF/HMTA resin at different heating rates (autocatalytic model m+n=2).

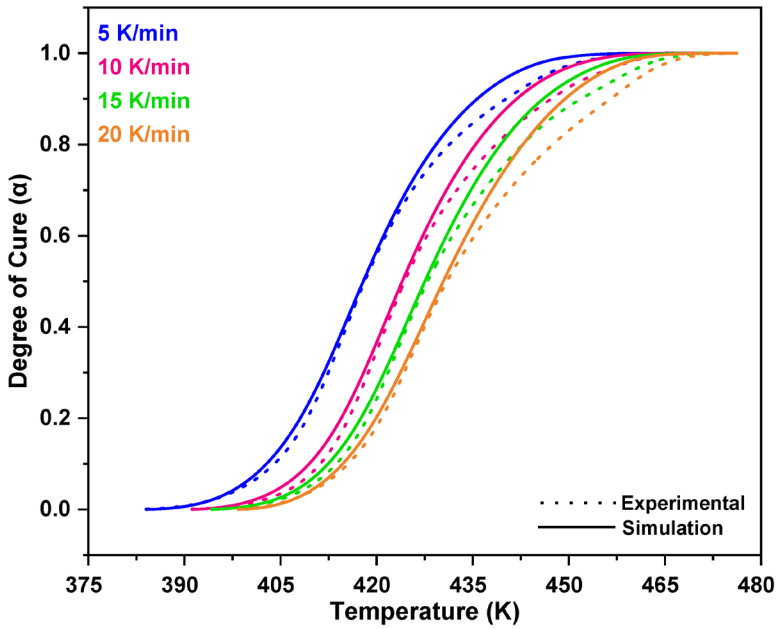

Figure 5.6 Plot for conversion (α) as a function of temperature for the experimental and simulation results for BNPF/HMTA resin at different heating rates (Kamal model E1=E2 m+n=2).

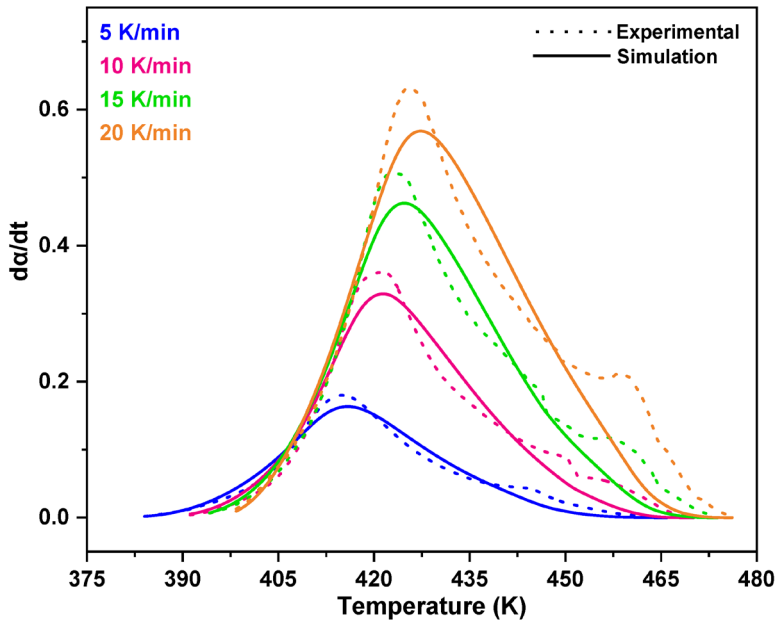

Figure 5.7 Plot for reaction rate (dα/dt) as a function of temperature for the experimental and simulation results for BNPF/HMTA resin at different heating rates (Kamal model E1=E2 m+n=2).

5.4 Conclusions

The kinetics of the curing reaction of novolac type PF resin system, i.e., NPF/HMTA and BNPF/HMTA resins, was investigated in this study with non-isothermal DSC measurements. The simulation data are verified against the experimental data for both NPF and BNPF resins. The results showed that an autocatalytic simulation model for curing NPF/HMTA resin was adapted to fit the experimental data and agreed well with the model. At the same time, a Kamal model is employed and proved a best-fitting model in describing the curing behavior of the BNPF/HMTA resin. The curing process of BNPF/HMTA resin follows the autocatalytic mecha-nism at the earlier curing stage, while the nth-order kinetic mechanism controls the later part of

curing. We hope this research will provide valuable and significant kinetic information for BNPF resin application in 3D printing.

5.5 References

(1) Zhang, Y.; Wang, F.; Duvigneau, J.; Wang, Y.; Wang, B.; Feng, X.; Mao, Z.; Vancso, G. J.; Sui, X. Highly Stable and Nonflammable Hydrated Salt-Paraffin Shape-Memory Gels for Sustainable Building Technology. *ACS Sustain. Chem. Eng.* **2021**, *9* (46), 15442–15450. https://doi.org/10.1021/acssuschemeng.1c04586.

(2) Ertelt, M. J.; Hilbig, H.; Grosse, C. U.; Lieleg, O. Small Pores, Big Impact - Controlling the Porosity Allows for Developing More Sustainable Construction Materials. *ACS Sustain. Chem. Eng.* **2021**. https://doi.org/10.1021/acssuschemeng.1c03625.

(3) Yan, N.; Zhang, B.; Zhao, Y.; Farnood, R. R.; Shi, J. Application of Biobased Phenol Formaldehyde Novolac Resin Derived from Beetle Infested Lodgepole Pine Barks for Thermal Molding of Wood Composites. *Ind. Eng. Chem. Res.* **2017**, *56* (22), 6369–6377. https://doi.org/10.1021/acs.iecr.7b00353.

(4) Milazzo, M.; Amoresano, A.; Pasquino, R.; Grizzuti, N.; Auriemma, F.; De Stefano, F.; Sin Xicola, A.; Iodice, V.; De Rosa, C. Curing Efficiency of Novolac-Type Phenol–Formaldehyde Resins from Viscoelastic Properties. *Macromolecules* **2021**, *54* (24), 11372–11383. https://doi.org/10.1021/acs.macromol.1c01598.

(5) Zhang, X.; Solomon, D. H. Chemistry of Novolac/Furfuryl Alcohol Resins Cured with Hexamethylenetetramine: A Solid-State NMR Study. *Chem. Mater.* **1998**, *10* (7), 1833–1840. https://doi.org/10.1021/cm9800175.

(6) De Medeiros, E. S.; Agnelli, J. A. M.; Joseph, K.; De Carvalho, L. H.; Mattoso, L. H. C.

Curing Behavior of a Novolac-Type Phenolic Resin Analyzed by Differential Scanning Calorimetry. *J. Appl. Polym. Sci.* **2003**, *90* (6), 1678–1682. https://doi.org/10.1002/app.12838.

(7) Mahajan, J. S.; O'Dea, R. M.; Norris, J. B.; Korley, L. S. T. J.; Epps, T. H. Aromatics from Lignocellulosic Biomass: A Platform for High-Performance Thermosets. *ACS Sustain. Chem. Eng.* **2020**, *8* (40), 15072–15096. https://doi.org/10.1021/acssuschemeng.0c04817.

(8) Nolan Wilson, A.; Price, M. J.; Mukarakate, C.; Katahira, R.; Griffin, M. B.; Dorgan, J. R.; Olstad, J.; Magrini, K. A.; Nimlos, M. R. Integrated Biorefining: Coproduction of Renewable Resol Biopolymer for Aqueous Stream Valorization. *ACS Sustain. Chem. Eng.* **2017**, *5* (8), 6615–6625. https://doi.org/10.1021/acssuschemeng.7b00864.

(9) Bansode, A.; Barde, M.; Asafu-adjaye, O.; Patil, V.; Hinkle, J.; Via, B. K.; Adhikari, S.; Adamczyk, A. J.; Farag, R.; Elder, T.; Labb, N.; Auad, M. L. Synthesis of Biobased Novolac Phenol − Formaldehyde Wood Adhesives from Biore Fi Nery-Derived Lignocellulosic Biomass. *ACS Sustain. Chem. Eng.* **2021**. https://doi.org/10.1021/acssuschemeng.1c01916.

(10) Hager, I.; Golonka, A.; Putanowicz, R. 3D Printing of Buildings and Building Components as the Future of Sustainable Construction? *Procedia Eng.* **2016**, *151*, 292–299. https://doi.org/10.1016/j.proeng.2016.07.357.

(11) Trifol, J.; Jayaprakash, S.; Baniasadi, H.; Ajdary, R.; Kretzschmar, N.; Rojas, O. J.; Partanen, J.; Seppälä, J. V. 3D-Printed Thermoset Biocomposites Based on Forest Residues by Delayed Extrusion of Cold Masterbatch (DECMA). *ACS Sustain. Chem. Eng.* **2021**, *9* (41), 13979–13987. https://doi.org/10.1021/acssuschemeng.1c05587.

(12) Shahzad, A.; Lazoglu, I. Direct Ink Writing (DIW) of Structural and Functional Ceramics: Recent Achievements and Future Challenges. *Compos. Part B Eng.* **2021**, *225* (August). https://doi.org/10.1016/j.compositesb.2021.109249.

(13) Shen, L.; Wang, T. P.; Lee, T. H.; Forrester, M.; Becker, A.; Torres, S.; Pearson, C.; Cochran, E. W. 3D Printable All-Polymer Epoxy Composites. *ACS Appl. Polym. Mater.* **2021**, *3* (11), 5559–5567. https://doi.org/10.1021/acsapm.1c00889.

(14) Wang, B.; Arias, K. F.; Zhang, Z.; Liu, Y.; Jiang, Z.; Sue, H. J.; Currie-Gregg, N.; Bouslog, S.; Pei, Z. (Z J.).; Wang, S. 3D Printing of In-Situ Curing Thermally Insulated Thermosets. *Manuf. Lett.* **2019**, *21*, 1–6. https://doi.org/10.1016/j.mfglet.2019.06.001.

(15) Ziaee, M.; Johnson, J. W.; Yourdkhani, M. 3D Printing of Short-Carbon-Fiber-Reinforced Thermoset Polymer Composites via Frontal Polymerization. *ACS Appl. Mater. Interfaces* **2022**. https://doi.org/10.1021/acsami.2c02076.

(16) Mariani, A.; Fiori, S.; Chekanov, Y.; Pojman, J. A. Frontal Ring-Opening Metathesis Polymerization of Dicyclopentadiene [5]. *Macromolecules* **2001**, *34* (19), 6539–6541. https://doi.org/10.1021/ma0106999.

(17) Pojman, J. A. *Frontal Polymerization*; Elsevier B.V., 2012; Vol. 4. https://doi.org/10.1016/B978-0-444-53349-4.00124-2.

(18) Goli, E.; Parikh, N. A.; Yourdkhani, M.; Hibbard, N. G.; Moore, J. S.; Sottos, N. R.; Geubelle, P. H. Frontal Polymerization of Unidirectional Carbon-Fiber-Reinforced Composites. *Compos. Part A Appl. Sci. Manuf.* **2020**, *130* (November 2019), 105689. https://doi.org/10.1016/j.compositesa.2019.105689.

(19) Zheng, T.; Xi, H.; Wang, Z.; Zhang, X.; Wang, Y.; Qiao, Y.; Wang, P.; Li, Q.; Li, Z.; Ji, C.; Wang, X. The Curing Kinetics and Mechanical Properties of Epoxy Resin Composites

Reinforced by PEEK Microparticles. *Polym. Test.* **2020**, *91* (August), 106781. https://doi.org/10.1016/j.polymertesting.2020.106781.

(20) El-Thaher, N.; Mekonnen, T.; Mussone, P.; Bressler, D.; Choi, P. Nonisothermal DSC Study of Epoxy Resins Cured with Hydrolyzed Specified Risk Material. *Ind. Eng. Chem. Res.* **2013**, *52* (24), 8189–8199. https://doi.org/10.1021/ie400803d.

(21) Chaiwan, P.; Kaewkittinarong, A.; Pumchusak, J. Nonisothermal Curing Kinetics of Solid Resole by Differential Scanning Calorimetry. *Thermochim. Acta* **2019**, *675* (October 2018), 119–126. https://doi.org/10.1016/j.tca.2019.03.023.

(22) Um, M. K.; Daniel, I. M.; Hwang, B. S. A Study of Cure Kinetics by the Use of Dynamic Differential Scanning Calorimetry. *Compos. Sci. Technol.* **2002**, *62* (1), 29–40. https://doi.org/10.1016/S0266-3538(01)00188-9.

(23) Heinze, S.; Echtermeyer, A. T. A Practical Approach for Data Gathering for Polymer Cure Simulations. *Appl. Sci.* **2018**, *8* (11), 1–31. https://doi.org/10.3390/app8112227.

(24) Chandran, M. S.; Krishna, M.; Rai, S.; Krupashankara, M. S.; Salini, K. Cure Kinetics and Activation Energy Studies of Modified Bismaleimide Resins. *ISRN Polym. Sci.* **2012**, *2012* (i), 1–8. https://doi.org/10.5402/2012/309861.

(25) Ma, H.; Zhang, X.; Ju, F.; Tsai, S. B. A Study on Curing Kinetics of Nano-Phase Modified Epoxy Resin. *Sci. Rep.* **2018**, *8* (1), 1–15. https://doi.org/10.1038/s41598-018-21208-0.

(26) Yang, G.; Lee, J. K. Curing Kinetics and Mechanical Properties of Endo - Dicyclopentadiene Synthesized Using Different Grubbs' Catalysts. *Ind. Eng. Chem. Res.* **2014**, *53* (8), 3001–3011. https://doi.org/10.1021/ie403285q.

(27) Kim, P.; Weaver, S.; Noh, K.; Labbé, N. Characteristics of Bio-Oils Produced by an

Intermediate Semipilot Scale Pyrolysis Auger Reactor Equipped with Multistage Condensers. *Energy and Fuels* **2014**, *28* (11), 6966–6973. https://doi.org/10.1021/ef5016186.

(28) Thomas, R.; Sinturel, C.; Pionteck, J.; Puliyalil, H.; Thomas, S. In-Situ Cure and Cure Kinetic Analysis of a Liquid Rubber Modified Epoxy Resin. *Ind. Eng. Chem. Res.* **2012**, *51* (38), 12178–12191. https://doi.org/10.1021/ie2029927.

(29) Patel, A.; Maiorana, A.; Yue, L.; Gross, R. A.; Manas-Zloczower, I. Curing Kinetics of Biobased Epoxies for Tailored Applications. *Macromolecules* **2016**, *49* (15), 5315–5324. https://doi.org/10.1021/acs.macromol.6b01261.

(30) Perejón, A.; Sánchez-Jiménez, P. E.; Criado, J. M.; Pérez-Maqueda, L. A. Kinetic Analysis of Complex Solid-State Reactions. A New Deconvolution Procedure. *J. Phys. Chem. B* **2011**, *115* (8), 1780–1791. https://doi.org/10.1021/jp110895z.

(31) Yang, G.; Yuan, Z.; Yang, Z.; Zhang, M. Nonisothermal Curing Kinetics of a Novel Polymer Containing Phenylsilylene and Propargyl-Hexafluorobisphenol a Units. *J. Appl. Polym. Sci.* **2013**, *127* (4), 3178–3185. https://doi.org/10.1002/app.37717.

(32) Wan, J.; Li, C.; Fan, H.; Li, B. G. Branched 1,6-Diaminohexane-Derived Aliphatic Polyamine as Curing Agent for Epoxy: Isothermal Cure, Network Structure, and Mechanical Properties. *Ind. Eng. Chem. Res.* **2017**, *56* (17), 4938–4948. https://doi.org/10.1021/acs.iecr.7b00610.

(33) Mashouf Roudsari, G.; Mohanty, A. K.; Misra, M. Study of the Curing Kinetics of Epoxy Resins with Biobased Hardener and Epoxidized Soybean Oil. *ACS Sustain. Chem. Eng.* **2014**, *2* (9), 2111–2116. https://doi.org/10.1021/sc500176z.

(34) Li, J.; Qiao, Y.; Zong, P.; Wang, C.; Tian, Y.; Qin, S. Thermogravimetric Analysis and

Isoconversional Kinetic Study of Biomass Pyrolysis Derived from Land, Coastal Zone, and Marine. *Energy and Fuels* **2019**, *33* (4), 3299–3310. https://doi.org/10.1021/acs.energyfuels.9b00331.

(35) Friedman, H. L. Kinetics of Thermal Degradation of Char-Forming Plastics from Thermogravimetry. Application to a Phenolic Plastic. *J. Polym. Sci. Part C Polym. Symp.* **2007**, *6* (1), 183–195. https://doi.org/10.1002/polc.5070060121.

(36) Hao, H.; Chang, T.; Cui, L.; Sun, R.; Gao, R. Theoretical Study on the Mechanism of Hydrogen Donation and Transfer for Hydrogen-Donor Solvents during Direct Coal Liquefaction. *Catalysts* **2018**, *8* (12). https://doi.org/10.3390/catal8120648.

(37) Langtry, B. N. Identity And Spatio-Temporal Continuity. *Australas. J. Philos.* **1972**, *50* (2), 184–189. https://doi.org/10.1080/00048407212341221.

(38) Blaine, R. L.; Kissinger, H. E. Homer Kissinger and the Kissinger Equation. *Thermochim. Acta* **2012**, *540*, 1–6. https://doi.org/10.1016/j.tca.2012.04.008.

(39) Vyazovkin, S. Evaluation of Activation Energy of Thermally Stimulated Solid-State Reactions under Arbitrary Variation of Temperature. *J. Comput. Chem.* **1997**, *18* (3), 393–402. https://doi.org/10.1002/(SICI)1096-987X(199702)18:3<393::AID-JCC9>3.0.CO;2-P.

(40) Hosseinpour, A.; Nazockdast, H.; Behzad, T.; Salimijazi, H. R. Investigation of the Cure Kinetics of an Epoxy Resin by Advanced Isoconversional and Model-Fitting Methods. *AIP Conference Proceedings*. 2016. https://doi.org/10.1063/1.4942315.

(41) Zhang, C.; Binienda, W. K.; Zeng, L.; Ye, X.; Chen, S. Kinetic Study of the Novolac Resin Curing Process Using Model Fitting and Model-Free Methods. *Thermochim. Acta* **2011**, *523* (1–2), 63–69. https://doi.org/10.1016/j.tca.2011.04.033.

(42) Li, S.; Järvelä, P. Application of a Model-Free Isoconversional Method to the Cure of

Phenolic Systems. *J. Polym. Sci. Part B Polym. Phys.* **2001**, *39* (13), 1525–1528. https://doi.org/10.1002/polb.1125.

(43) Ma, S.; Fan, H.; Zhang, N.; Li, W.; Li, Y.; Li, Y.; Huang, D.; Zeng, L.; Shi, X.; Ran, X.; Xu, H. Investigation of a Low-Toxicity Energetic Binder for a Solid Propellant: Curing, Microstructures, and Performance. *ACS Omega*. 2020, pp 30538–30548. https://doi.org/10.1021/acsomega.0c04439.

(44) Zhan, X.; Liu, H.; Zhang, J. Two Branched Silicone Resins with Different Reactive Groups: A Comparative Evaluation. *Ind. Eng. Chem. Res.* **2018**, *57* (16), 5606–5615. https://doi.org/10.1021/acs.iecr.7b05172.

(45) Zhou, Z.; Si, Q.; Wan, L.; Kuo, S. W.; Zhou, C.; Xin, Z. Curing Kinetics of Main-Chain Benzoxazine Polymers Synthesized in Continuous Flow. *Ind. Eng. Chem. Res.* **2022**, *61* (7), 2947–2954. https://doi.org/10.1021/acs.iecr.1c04771.

(46) Horadam, W.; Venkat, N.; Tran, T.; Bai, L.; Josyula, K.; Mehta, V. Leaching Studies on Novolac Resin-Coated Proppants-Performance, Stability, Product Safety, and Environmental Health Considerations. *J. Appl. Polym. Sci.* **2018**, *135* (8). https://doi.org/10.1002/app.45845.

(47) Domínguez, J. C.; Alonso, M. V.; Oliet, M.; Rojo, E.; Rodríguez, F. Kinetic Study of a Phenolic-Novolac Resin Curing Process by Rheological and DSC Analysis. *Thermochim. Acta* **2010**, *498* (1–2), 39–44. https://doi.org/10.1016/j.tca.2009.09.010.

Chapter 6

Biobased Polyurethane Derived from Lignin as a Coating Material for Urea Fertilizer to achieve Controlled Release of Nutrients

This chapter is being prepared for submission[5]

6.1 Introduction

Fertilizers are crucial agrochemicals that provide ~70% of the nutrients to satisfy plant growth and help to increase agricultural productivity.[1] Nitrogen (N), phosphorus (P), and potassium (K) are three indispensable macronutrients that fulfill nutritional needs, which are supplemented through fertilizer applications.[2] Among these three macronutrients (N, P, K), nitrogen plays a significant role in maintaining crop quality and yield because N deficiency can restrain the biosynthesis of chlorophyll and other proteins.[3,4] Urea is the most widely used nitrogenous fertilizer (N-fertilizer) because of its high nitrogen content (46%), comparatively low cost, and commercial availability.[5,6] However, to ensure the plants get enough nitrogen elements, overuse of urea fertilizer is practiced, which results in an undesirable loss of nitrogen into the environment through volatilization, runoff, and leaching due to its high affinity for water and thermal instability.[7] This inefficient nitrogen absorption causes economic losses and severe environmental problems, including water eutrophication, acid rain, groundwater pollution, and excessive greenhouse gas emissions.[8]

[5] Bansode, A.; Guertal E.; Hinkle J.; Cuesta N.M.; Alizadeh N.; Farag R.; Auad, M. L.; Biobased polyurethane Derived from Lignin as a Coating Material for Urea Fertilizer to achieve Controlled Release of Nutrients, In Preparation, 2022

Controlled-release fertilizers (CRFs) have been designed and developed as an effective approach by increasing fertilizer utilization efficiency while being economical and eco-friendly to achieve sustainable agriculture further.[9–11] The CRFs are generally referred to as advanced fertilizers that release nutrient ingredients into the growing media over a longer time in a controlled way throughout the plant's growing cycle. For example, the nutrient release performance of CRFs in the first 28 days of application should not exceed 75% in total.[12] The nutrient use efficiency of CRFs is higher than traditional fertilizers. Two types of CRFs have been widely chosen and studied to achieve controlled release function, such as using low solubility compounds and coating or encapsulating water-soluble granular fertilizer (e.g., urea). The coating fertilizer is a well-controlled strategy that can provide a tunable barrier through the effective nutrient-release process as follows: (1) The external water vapors permeate through the coating membrane of the CRFs into the core and dissolves the part of the fertilizer, which allows the formation of saturated nutrient solution in the core. This creates the vapor pressure gradient inside the membrane. (2) If the membrane layer is damaged with the generated pressure, the nutrient will be released quickly through the rapture mechanism. In another case, the membrane withstands the internal pressure, and nutrients are released via diffusion.[13] (3) As the release continues, the concentration of the solution in the core decreases, which affects the release rate accordingly.[14]

It is thus demonstrated that the coating material is the critical component of the coated CRFs that effectively hold nutrients and regulate nutrient release through diffusion mechanisms.[15] The coating materials are classified into two main categories: polymer-based and mineral-based coating materials.[16,17] Polymer-coating materials have shown several merits over mineral-coating materials (e. g., sulfur), as these materials are strong mechanical properties and good film-forming behavior with impermeable or semi-permeable membranes.[18,19] The polymers are a potential candi-

date for developing coating formulation. At present several polymers have been used to produce CRFs, including polyethylene, polyurethane, epoxy resin poly(vinyl alcohol), poly(vinyl chloride), polyacrylamide, polyacrylonitrile, and polysulfone.[20–23]

Polyurethane (PU) is one of the broadest potential candidates for preparing coating formulation for fertilizers due to its wide range of versatile and attainable properties, such as good water resistance, film-forming properties, high adhesion strength, and elasticity.[24] PU is typically synthesized through a polyaddition reaction between polyol polyether or polyol polyester ($HO{-}R^1{-}OH$) and polyisocyanate ($O{=}C{=}N{-}R^2{-}N{=}C{=}O$) to form urethane linkages ($O{-}R^1{-}O{-}CO{-}NH{-}\ R^2{-}NH{-}CO{-}$).[25,26] Conventionally, both polyols and isocyanates are derived from petroleum-based feedstocks, which increase both the environmental impact and cost of the resulting polyurethanes. Moreover, applying petroleum-derived PU-coated CRFs could lead to the undesirable accumulation of microplastic residues.[22] Meanwhile, in early 2018, the European Commission launched a circular economy action plan, and as an integrated part of the deal, biopolymers were employed in fertilizing products.

In this context, significant efforts have been made in both academia and industry in the development of biobased polymeric materials for the application of controlled delivery systems.[27,28] Owing to their chemistry and characteristics, many types of renewable natural resources, such as cellulose, lignin, vegetable oil, castor oil, chitosan, pectin, starch, tannin, and alginate, have been explored to design biobased polymers for CRFs, which can naturally degrade in the soil environment. Among these sustainable substitutes, lignin has attracted enormous attention because of its chemical structure, composed of hydroxyl groups and a rigid aromatic backbone that provides mechanical strength, rigidity, and other favorable attributes to the resultant resins.[29,30] Lignin is the second most organic biopolymer in nature, surpassed by cellulose, and is highly variable

across different plant species.[31] It is formed through radical polymerization of p-hydroxyphenyl (H), guaiacyl (G), and syringyl (S), which are collectively known as monolignols. Each of these units is linked through various linkages such as β-O-4, 4-O-5, α-O-4, β-β, β-5, β-1, and 5-5, which result in versatile functional biomacromolecules.[32] Lignin has been produced as an industrial residue (black liquor) in pulping and biorefinery industries. At the same time, they are underutilized and subjected to burning to supplement their energy requirements. Therefore, several commercial lignin recovery systems have been isolating technical lignin from black liquor (for instance, INDULIN® lignin is isolated from black liquor by Ingevity). Considering the functionalization and availability, we expect that introducing lignin in the polyurethane system could provide a sustainable coating material for CRFs.

In this work, kraft lignin, polytetramethylene ether glycol (DIOL), 2-Ethyl-2-(hydroxymethyl)-1,3-propanediol (TRIOL), and polymeric methylene diphenyl diisocyanate (p-MDI) were used as the ingredients for the preparation of biobased polyurethane (BPU) formulations. Wherein lignin with a high concentration of hydroxyl functionalities (both aliphatic and phenolic) serves as a bio-polyol and provide good reacting sites towards p-MDI. Additionally, DIOL and TRIOL were applied as co-polyols to improve the performance of BPU formulation. The mixture design DOE tool was employed to find the optimum composition of polyols to formulate biobased polyurethane. Therefore, this study aims to develop BPUs by introducing natural materials such as lignin and investigate the effectiveness of the synthesized BPU-coated fertilizer by release behavior in water and soil environments.

Biobased polyurethane formulations were synthesized with [NCO]/[OH] equivalent ratio of 1:1 to coat urea fertilizer prills to achieve this objective. The structure of the resultant BPU film was identified by the Fourier transform infrared spectroscopy (FTIR). The surface morphology of fer-

tilizing granules was examined by scanning electron microscopy (SEM). The crushing strength analysis determined the mechanical properties of the BPU-coated fertilizers. The release kinetics of the developed controlled-release urea was studied.

6.2 Experimental Section

6.2.1 Materials

The urea prills having 46% N were sieved through 2 mm and 4 mm opening sieves (USA standard testing sieves, ASTM E−11 specifications). Indulin AT lignin (IN_KL) used in this study obtained by the kraft pulping process was kindly supplied by Ingevity Corporation, South Carolina. 2-Ethyl-2-(hydroxymethyl)-1,3-propanediol (TRIOL; 134.18 g/mol) was received from VWR International, USA. Polytetramethylene ether glycol (PTMEG 1400, DIOL; 1400 g/mol) was acquired from The Lycra Company LLC, USA. Polymeric MDI (Rubinate M; Amine equivalent weight 135 eq/g) was supplied by Huntsman, USA. Duration CR® from Allied Nutrients, USA, and Polyon® from Harrell's, USA, were received as a commercial controlled release fertilizer. Deuterated chloroform (with 0.03 v/v% TMS, 99.8+ atom% D), chromium (III) acetylacetonate (relaxation agent, 98.0%), endo-N-hydroxy-5-norbornene-2,3-dicarboximide (NHND, internal standard, 99.0%) and pyridine were purchased from VWR International, USA. 2-Chloro-4,4,5,5-tetramethyl-1,3,2-dioxaphospholane (TMDP, phosphitylation reagent, 95%) was procured from Sigma-Aldrich, USA.

6.2.2 Characterization of Lignin

6.2.2.1 Phosphorus-31 Nuclear Magnetic Resonance (^{31}P-NMR) Spectroscopy

The hydroxyl groups in the kraft lignin (KL) have been measured by quantitative ^{31}P-NMR analysis. Approximately 15 mg of the sample was dissolved in 550 µL of the stock solution, which

was prepared by mixing 3 ml pyridine and 2 ml deuterated chloroform in 20 mg of NHND and 20 mg of chromium (III) acetylacetonate according to a published method.[33] The deuterium signal for locking NMR experiment was provided by deuterated chloroform, which also helps to dissolve the derivatized phenolic prepolymers and averts the precipitation of pyridine-HCl salts.[34] After complete dissolution of the sample in the stock solution, 150 µL of phosphitylating reagent, 2-chloro-4, 4, 5, 5-tetramethyl-1, 3, 2-dioxaphospholane (TMDP) was added. TMDP reacts with hydroxyl groups in the sample, liberating hydrogen chloride which is captured by pyridine. The phosphatized sample (650 µL) was transferred into the 5 mm NMR tube for subsequent determination. The NMR was performed using a Bruker Ultrashield Plus 500 MHz spectrometer with broadband nitrogen-cooled prodigy probe using a 90° pulse angle and an inverse gated proton decoupling pulse to eliminate the nuclear overhauser effects for quantitative purposes, a delay time of 25 seconds, and 128 scans. The spectra analysis was carried out using Mestrelab Research (MestReNova 7.1.1) software.

6.2.3 Biobased Polyurethane Coating Formulations through Mixture Design Approach

The polyurethane (PU) was prepared through a polyaddition reaction between a polyol and isocyanate. In this study, KL, DIOL, and TRIOL were used as the polyol segment, whereas the pMDI was used as isocyanate for the synthesis of biobased polyurethanes by using an overall [NCO]/[OH] equivalent ratio of 1:1.

The Design of experiments (DOE) is a statistical technique utilized for planning and analysis of experiments. In this study, a user-defined mixture design approach of DOE has been employed to find the optimal mixture of polyols to formulate biobased polyurethane to coat urea fertilizer. In the mixture design, the sum of all the proportions must be equal to the unity and non-negative.[35]

The equivalent ratio of lignin, DIOL, and TRIOL in the coating material and the coating film percentage were selected as the design variables. Based on the preliminary tests, the equivalent ratio of the lignin to the total equivalent ratio of polyol was set at 0 − 1, the equivalent ratio of the DIOL to the total equivalent ratio of polyol was selected as 0 – 1, the equivalent ratio of the TRIOL to the total equivalent ratio of polyol was taken as 0 – 0.50, and the percentage of the coating film was set at 3−9%. These four design variables generated a total of 27 experimental runs with the different compositions of each polyol component, as detailed in Table 6.1. Experimental designs and subsequent analysis were carried out using the Design-Expert® (Version 12, Stat-Ease, Inc. Minneapolis) software. Urea release in water, N release in soil, plant growth and turfgrass color response were set as a response value.

Table 6.1 Polyols mixture formulation using Design-Expert® Version 12 software

Run	Component 1 A: Lignin	Component 2 B: DIOL	Component 3 C: TRIOL	Factor 4 D: Coating Percentage
1	0.5	0	0.5	6
2	0	0.75	0.25	3
3	0.375	0.375	0.25	3
4	0	1	0	9
5	0	0.75	0.25	6
6	0.75	0	0.25	9
7	0.25	0.25	0.5	3
8	0.375	0.375	0.25	9
9	0	0.75	0.25	9
10	0.375	0.375	0.25	6
11	0.5	0.5	0	9
12	0.75	0	0.25	6
13	0.5	0.5	0	3
14	1	0	0	3
15	0.5	0.5	0	6
16	0	1	0	3
17	0	0.5	0.5	6
18	0.25	0.25	0.5	9
19	0	0.5	0.5	9
20	0.25	0.25	0.5	6
21	1	0	0	6
22	0	0.5	0.5	3
23	1	0	0	9
24	0	1	0	6
25	0.5	0	0.5	9
26	0.5	0	0.5	3
27	0.75	0	0.25	3

6.2.4 Preparation of BPU Coated Urea Fertilizers (BPU)

The biobased polyurethane formulations were synthesized by the reaction between isocyanate and the obtained 27 polyol mixture through DOE design as detailed in Table 6.1 with NCO/OH

equivalent ratio of 1:1. First, the DIOL and TRIOL were melted in an oven at 70 °C. Afterward, the KL, DIOL and TRIOL polyols were weighted according to the calculation based on equation 1 and added slowly into the plastic beaker. The polyol mixture was thoroughly dispersed and mixed using a glass stirring rod for 5 min. The polyol mixture was allowed to cool down and then desired amount of pMDI (weighted as per equation 6.1) was added to the mixture of polyol and homogenized.

$$\frac{NCO}{OH} = \frac{W_{P-MDI}[NCO]_{P-MDI}}{W_{KL}[OH]_{KL}+W_{DIOL}[OH]_{DIOL}+W_{TRIOL}[OH]_{TRIOL}} \quad [6.1]$$

The weight of the total coating material for each biobased PU formulation has been calculated based on the amount of urea prills and the coating percentages (3, 6, 9 %), as shown in equation 6.2.

$$\text{Weight of Coating Material (g)} = \text{Weight of Urea Prills (g)} \times \text{Coating percentage} \quad [6.2]$$

The layer-by-layer (LBL) technique formed the biobased polyurethane coating by dividing the coating formulation into two parts to help coat the urea surface more evenly. Subsequently, the required amount of urea granules (2.0 − 5.0 mm in diameter) were fed into the first part of coating formulations, where a layer BPU polymer coated it. Afterward, the coated granules were removed from the plastic beaker and dried overnight at room air temperature. The second part of the BPU coating was achieved by immersing the single-coated dried urea fertilizer into the prepared coating formulation (the procedure repeated as per the first BPU coating formulation). The mechanism of the urea granules coating is illustrated in Figure 6.1.

Finally, 27 BPU-coated urea fertilizer samples were obtained having various compositions of the selected polyols with three different coating percentages.

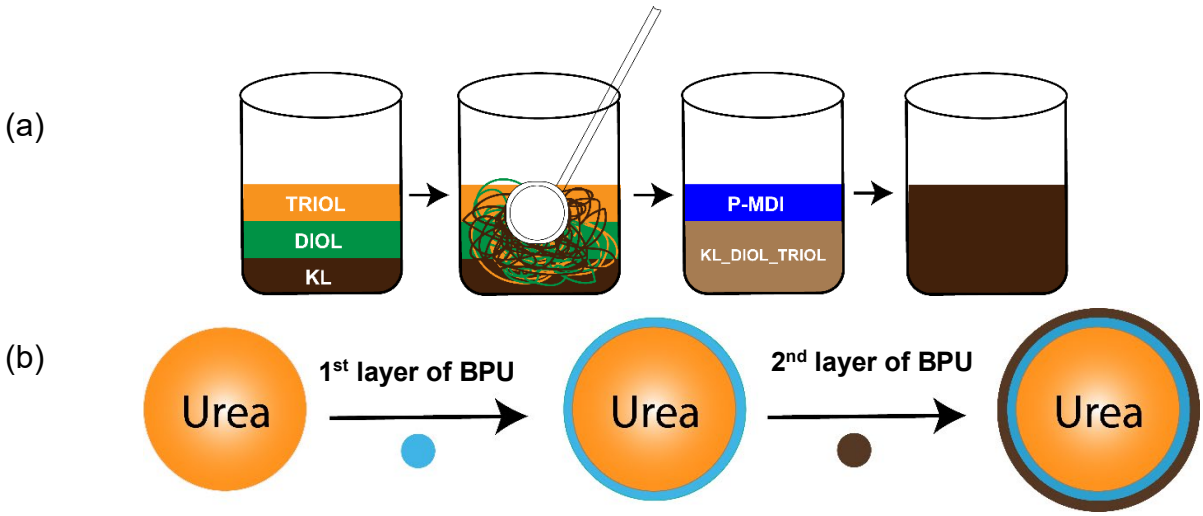

Figure 6.1 Mechanism of Biobased polyurethane (a) formulation preparation and (b) Coating of Urea Fertilizer.

6.2.5 Preparation of Biobased Polyurethane films by Solution Casting Method

The solid films of 27 different BPU formulations were fabricated by the solution casting method by pouring the formulation onto disposable aluminum smooth-wall weighing dishes (diameter around 5.0 cm). The dishes were then placed into an incubator drying oven at room temperature for 24 h. After leaving it for a natural drying and allowing it to be crosslinked, the dried films were then peeled off from the aluminum dish to obtain the required casting films. The casted films were then characterized by FTIR analysis to investigate their crosslinking during the solidifying process.

6.2.5.1 Fourier Transform Infrared (FTIR) Spectroscopy

The prepared biobased polyurethane films were scanned over a wavenumber range of 4000 cm^{-1} – 400 cm^{-1} at a resolution of 4 cm^{-1} with 64 scans by Nicolet 6700 FTIR spectrophotometer (Thermo Fisher Scientific Instrument., USA) using an attenuated total reflectance (ATR) mode. Before every sampling, background scanning was performed for correction. The FTIR spectra

were obtained using OMNIC Version 7.3 software. The FTIR measurements were used to observe the nature of functional groups that are formed during the curing of polyurethanes.

6.2.6 Surface Morphology by Scanning Electron Microscopy (SEM)

The particle surface and cross-section of the biobased polyurethanes (BPU) coated, and uncoated urea granules were examined with Zeiss EVO50 (Carl Zeiss Microscopy, NY, USA). The coated and uncoated urea granules were cut in the middle to acquire the cross-section. For analysis, the samples were mounted on the aluminum stubs using double-sided carbon tape and then sputtered with gold using an EMR Q150R sputter coating device before observation.

6.2.6.1 Determination of Average Crushing Strength Analysis of BPU-coated Fertilizer

The mechanical strength of fertilizer granules was determined by the measurements of the crushing strength. In measuring the crushing strength, the pressure was applied in a radial direction by a flat end rod to individual fertilizer granules placed on the mounted flat surface using an Instron 5565 Universal Testing Machine (Bluehill, Instron, MA, USA) equipped with a 10 kN load cell. A crosshead speed was 10.00 mm/min. Twenty-one granules of a diameter ranging from 2.0 to 5.0 mm were randomly selected for each formulation of the BPU-coated fertilizers.

The crushing strength is calculated according to equation 6.3.

$$\text{Crushing Strength} = \frac{F_{max}}{\pi D^2} \qquad [6.3]$$

where, F_{max} (N) is the load at which the fertilizer granule was crushed, and D (mm) is the diameter of the fertilizer granule. The final crushing strength value is expressed in units of MPa.

6.2.7 Urea Release from the BPU Coated Fertilizer in Distilled Water as a Function of Time

Briefly, 10 g of each BPU coated urea fertilizer were placed in conditioned glass bottles, and 200 mL of deionized water was added. The amount of urea released from each coated fertilizer at 1, 3, 5, 7, 14, and 28 days was measured to analyze the release profile of urea in distilled water. The urea concentration values were measured using Digital Pocket Refractometer Atago PAL-Urea (Tokyo, Japan). Aliquots of 0.5 mL were taken out from each bottle at a predetermined time and placed on the prism surface, and the urea percentage was recorded in approximately 3 sec. The system volume was kept constant by adding the measured aliquot on the prism back to the release medium. The urea refractometer was calibrated throughout the experiment before each measurement by recording a 0 % urea value for the distilled water. The urea release experiments for each BPU coated fertilizer were performed in triplicate, and the average value was reported. For comparison analysis, urea release in water from uncoated urea fertilizer was also determined.

6.2.8 Experimental Field Studies

To study the controlled-release behavior, the BPU/PU-coated urea fertilizers were applied to the field studies. The experimental field studies were conducted at the Auburn University Turfgrass Research Unit (TGRU) in Auburn, Alabama. The studies were carried out on a Marvyn Loamy Sand soil type. Perennial Ryegrass (cultivar 'Express II' DLF seed company) was used as planting material for all the experiments. Overall, two research experiments were performed as follows.

6.2.8.1 Percent Nitrogen Release Experiment

Based on the previous urea release study results, thirteen BPU/PU-coated urea fertilizers (as depicted in Table 6.1) were selected to investigate the nitrogen release rate in the soil environment by the buried bag method, according to the literature.[36,37] The known weight of coated urea prills was placed into the 5 cm × 4 cm polypropylene bag with a mesh size of 1.2 mm^2. The bags were sealed to avoid prills loss. Each coated fertilizer sample bag was then buried approximately 6 cm below the soil surface, ensuring soil/prill contact. The bag with coated CRF granules per replicate was taken out at selected time points (weeks 1, 2, 3, 5, 8, 11, 14) and then, rinsed with distilled water to remove the soil attached to the coating material. The bags were then dried at room temperature and weighed to measure the total N loss by weight. Throughout the experiment, mesh bags and the prills samples are weighted to track the nutrient loss over time. All of the above experiments were carried out in triplicate.

The nitrogen release (% NR) was calculated out of the percentage of weight loss using the following equation 6.4.[37]

$$\%NR_w = \left[1 - \left(\frac{F_s - F_c}{F_i - F_c}\right)\right] * 100 \qquad [6.4]$$

Where Fs is the weight of the polymer-coated coated urea (PCU) on the sampling date, Fc is the weight of the polymer coating in grams, Fi is the initial amount of polymer-coated urea in the sample, and % NRw is the percentage of N release by weight.

6.2.8.2 Greenhouse Pot Experiment

This greenhouse experiment was conducted to assess the performance of BPU/PU-coated urea fertilizers on plant growth and to validate the results of the previous N-release study. Four BPU/PU-coated fertilizers were selected based on the previous study. The dry marvyn loamy soil was first placed into each pot (6.0 inches in diameter) with drainage holes to improve the aeration and promote more oxygen supply to the root system. Each pot was sown evenly over the soil surface with ryegrass seeds at a rate of 30 pounds/Acre on November 8th, 2021. All the pots were fertilized at a rate of 60 pounds/Acre, and ryegrasses were allowed to germinate. The plant growth was measured in terms of the plants' dry weight and was evaluated at a specified interval (Days 7, 11, 21, 38, 45, 63, 70, 80) a week after germination. The total aboveground growth of the ryegrass was clipped by leaving 2 inches for the remaining growth, and clipping was harvested from each pot. The dry weights of the clippings were measured after drying in an oven for plant growth analysis. Five pots were used for each BPU/PU-coated urea fertilizer (Run 11, Run 18, Run 19, Run 25), along with uncoated urea and commercial PU fertilizer (Duration 90).

6.3 Results and Discussion

6.3.1 Lignin Structural Analysis by ^{31}P NMR

^{31}P NMR analysis is the most recognized method used for the quantitative analysis of the various hydroxyl groups (aliphatic, phenolic, and acidic) within the lignin macromolecule.[38] The OH content was determined after phosphitylation of hydroxyl moieties present in the lignin with ^{31}P reagent (TMDP) followed by peak integration using NHND (152.80−151.0 ppm) as an internal standard.[39] Herein, kraft lignin (Indulin AT) was characterized by ^{31}P NMR to gain a detailed analysis of hydroxyl functionalities which is used as input material (polyol) in the next step,

where BPU is synthesized. The resultant ^{31}P NMR spectra are presented in Figure 6.2. The spectra showed distinct signals in the region between 150.0−145.0 ppm (Figure 6.2), which originated from the aliphatic hydroxyl groups mainly located in the side chains of lignin. For phenolic hydroxyl groups, the signals appeared between 144.70−137.30 ppm (Figure 6.2) with different units of C5−OH, G−OH, p−OH, and C−OH at 144.70−140.20, 140.20−139.0, 139.0−138.20, 138.20−137.30 ppm, respectively. A close examination of ^{31}P NMR data reveals that total phenolic −OH (2.20 mmol/g) is significantly higher than the aliphatic −OH (1.78 mmol/g), likely associated with the botanical origin (softwood) and lignin extraction (kraft biorefinery) process. Additionally, the signals of the acidic −OH groups were located in the range of 136.60−133.60 ppm (Figure 6.2) with −OH groups of 1.12 mmol/g. These results agree with the documented observation for similar lignin types.[40–42]

Overall, the total hydroxyl groups of 4.68 mmol/g were observed. Hence, we believe it will be promising to explore the functionality of lignin as a polyol for the development of biobased polyurethane.

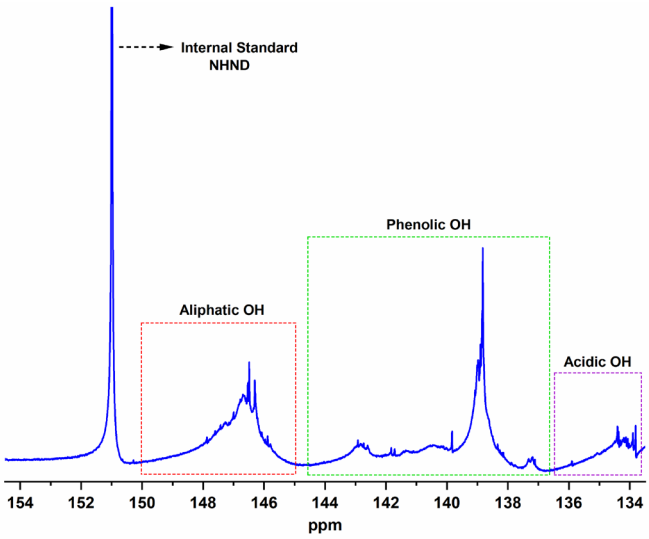

Figure 6.2 ^{31}P NMR spectra and signal assignments of lignin

6.3.2 BPU/PU Resin Synthesis and Characterization by FTIR

The results obtained from the quantification of −OH groups (total OH content: 4.68 mmol/g) were used to determine the mass content of lignin for all the obtained equivalent molar ratios presented in Table 6.1. The commercial polyols such as DIOL and TRIOL used in this study have hydroxyl functionalities of 2 and 3, respectively. Stoichiometric calculations were performed. Further, the BPU/PU films were prepared by reacting polyols (−OH of lignin, DIOL, and TRIOL) with the isocyanates (N=C=O of polymeric MDI) at an equivalent molar ratio of [NCO]/[OH] of 1:1 as described in the Experimental Section. During experimentation, each formulated film was undergone a curing process under ambient conditions. To investigate the chemical changes in the structure, the FTIR analysis was performed before and after curing. The FTIR spectra (Figure 6.3a) show a strong absorption band at 2250 − 2270 $cm^{-1,}$ which corresponds to the stretching vibration of the N=C=O bond in the p-MDI. However, this signal (2250 − 2270 cm^{-1}) becomes less intense or almost disappears in Figure 6.3b, indicating the consumption of the isocyanate group during the formation of the urethane bond in the reaction with the hydroxyl group of polyols to yield crosslinked BPU/PU material. The formation of urethane linkages can be confirmed via the appearance of a shoulder peak at 3305 cm^{-1} attributed to N−H and others related to the C=O stretching vibration of amide linkage(−CO−NH−) at 1600 cm^{-1}. Whereas while curing, the signals attributed to the Indulin AT basic lignin structure, which was reported in previous publications,[43] remain practically unvaried, indicating the stability of the macromolecular system of lignin.

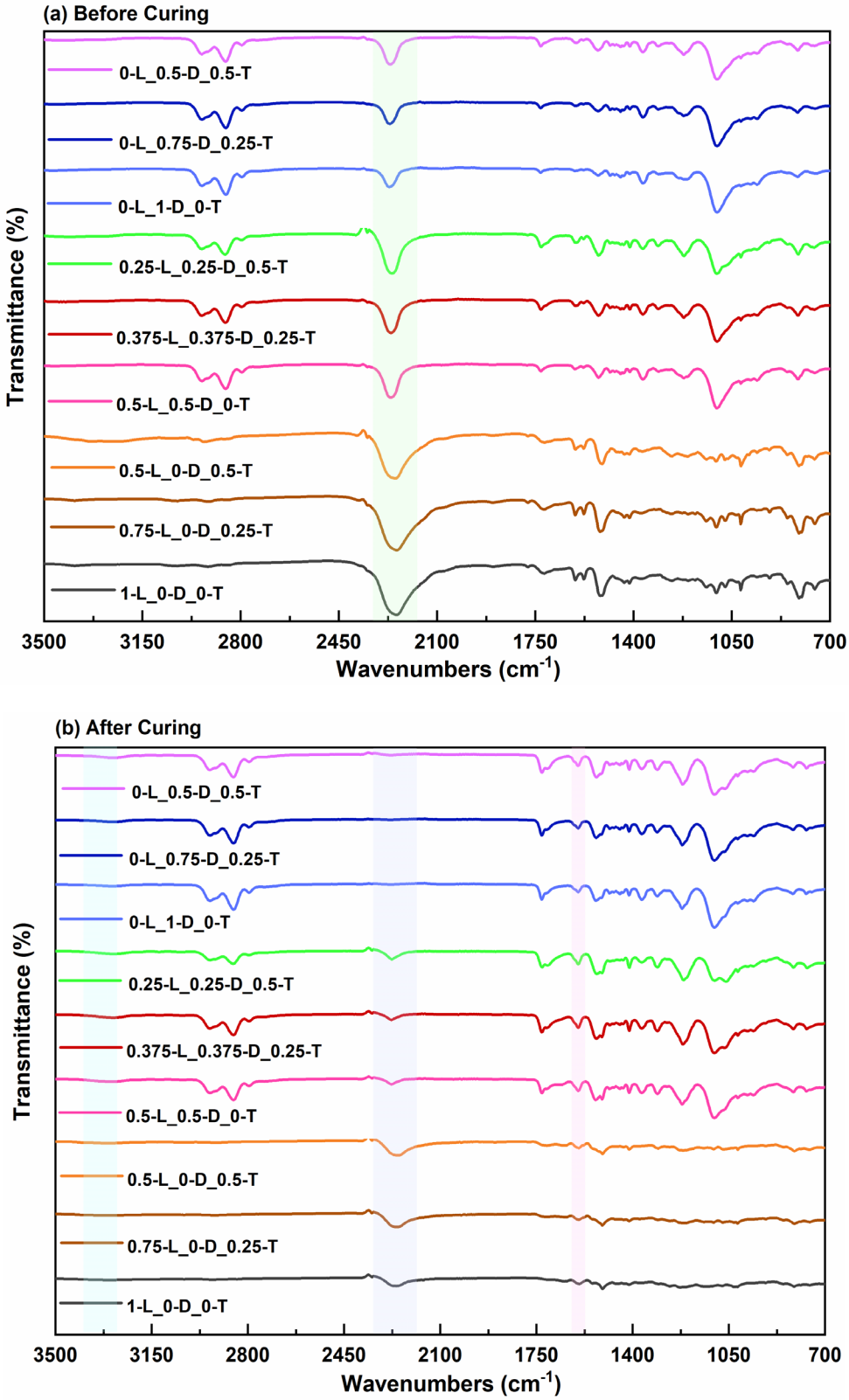

Figure 6.3 FTIR spectra of the BPU/PU films (a) before curing (b) after curing

6.3.3 Morphologies of BPU/PU Coated Urea Fertilizer

The surface morphologies of the BPU/PU coated urea granules were obtained using the SEM method, as shown in Figure 6.4A−J, which presents cross-sections of coated granules and cross-sections of the coated shells, and the whole surface of coated granules. The cross-sectional SEM images of BPU-coated urea granules (Figure 6.4A) clearly showed a formation of a homogenous, cohesive polymer film adhered around the surface of the fertilizer core. Similarly, the SEM analysis of commercial PU-coated urea (Figure 6.4B) was performed to compare the surface morphology. Additionally, the inner surface of the coating shells (Figure 6.4C−D) which is recovered after the nutrient release study showed a regular, dense, and compact structure, suggesting that the coating layer served as an effective barrier through the controlled diffusion rate of water into the core and nitrogen outside the core with no mechanical damage.

Furthermore, the outer surface of whole coating shells (Figure 6.4E, G, and I) was examined to analyze the coating material, which showed a roughed surface with different-sized protrusions. While the magnified SEM images of the respective coating shells (Figure 6.4F, H, J, respectively) appeared to be smooth with uncracked pine holes. The smooth surface can help to decrease the contact area between the fertilizer surface and coating material and improves the coating membrane structure.

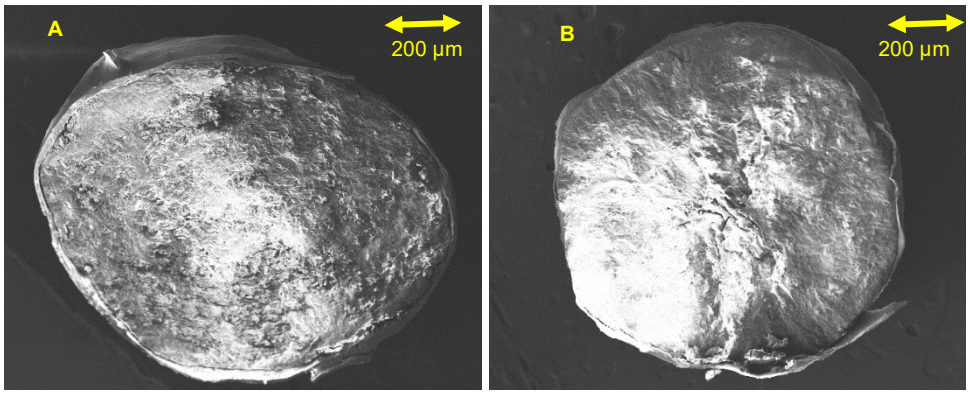

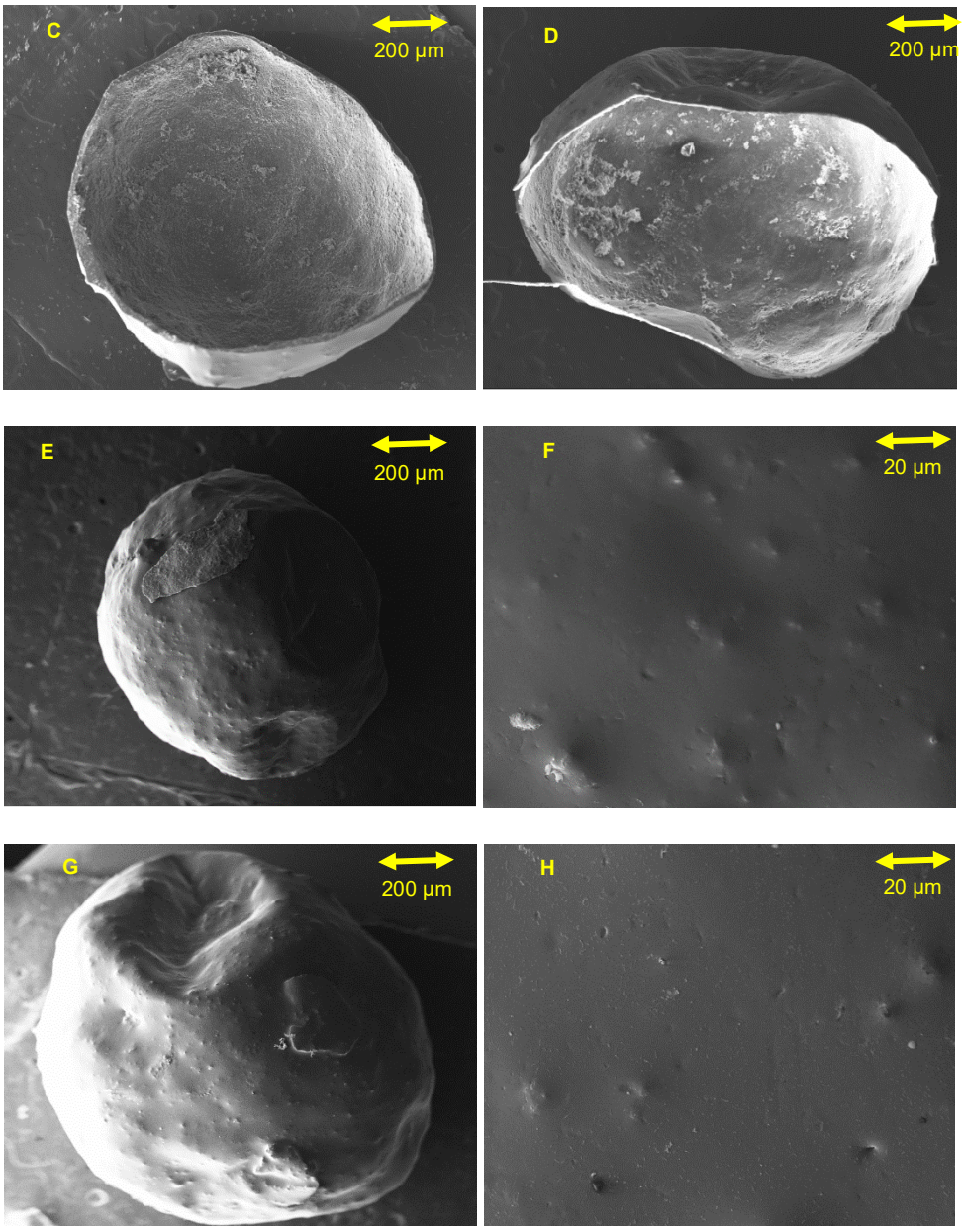
C
200 µm
D
200 µm
E
200 µm
F
20 µm
G
200 µm
H
20 µm

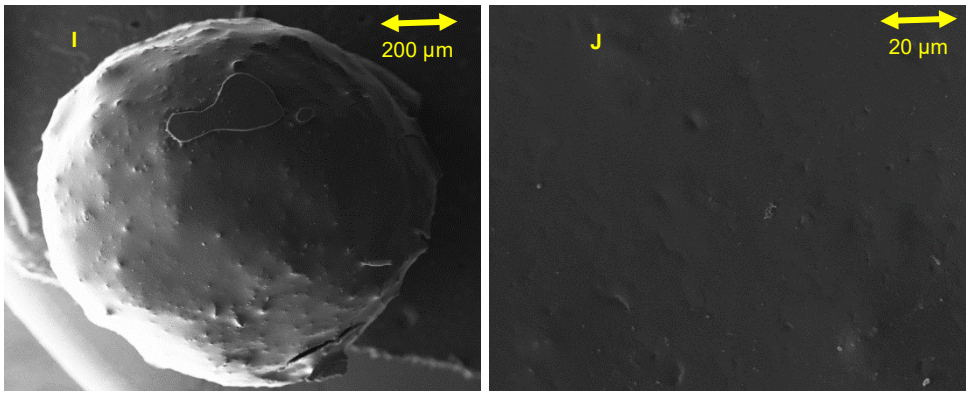

Figure 6.4 SEM images of BPU/PU-coated urea granules: (A) cross section of 3%_0.25-L_0.25-D_0.5-T (Run 18) (B) cross-section of Duration CR (commercial PU coated urea granule) (C) the inner surface of 3%_0.25-L_0.25-D_0.5-T (Run 18) coating shell (D) the inner surface of Duration CR coating shell (E) and (F) whole surface of 3%_0.25-L_0.25-D_0.5-T (Run 18) (G) and (H) whole surface of 6%_0.25-L_0.25-D_0.5-T (Run 18) (I) and (J) whole surface of 9%_0.25-L_0.25-D_0.5-T (Run 18).

6.3.4 Mechanical Strength of the BPU/PU coated urea

The fertilizer granules are required to have mechanical strength to ensure that it is capable of withstanding physical handling during storage and transportation throughout the supply chain without fracture.[44] As in the agriculture field, the usage of powdered urea is inevitable. The mechanical strength can be characterized by measuring the crushing strength by applying pressure to individually coated granules. The magnitude of maximum force where the granule disintegrated was recorded for calculating crushing strength as per equation 6.3. The crushing strength results of developed BPU/PU-coated fertilizers are presented in Figure 6.5. In our experiments, the uncoated urea prills (control) and commercial PU-coated urea (Duration CR) were crushed at 1.31 ± 0.184 and 1.79 ± 0.290 MPa strength, respectively. Compared with the control, all the BPU/PU-coated urea fertilizers showed higher resistance toward the crushing force (Figure 6.5).

This observation corresponds to the ability of the coating material to penetrate the particle. It facilitates the adhesion of material inside the fertilizer particle, which helps in improved resistance to deformed under pressure. Another reason for the improved particle strength could be the coating formulation's increased flexibility and ductile properties.

It can be observed that the presence of all three polyols (lignin, DIOL, and TRIOL) in the coating material was found to improve the crushing strength, and this increase showed a linear coating thickness dependence, owing to their important roles in structural characteristics of coated urea. For example, the crushing force reached 2.39 ± 0.596 MPa in fertilizer coated with an equivalent ratio of 0.25-L_0.25-D_0.5-T (Run 18) polyol formulation. This behavior could be attributed to the high concentration of TRIOL that enhanced crosslinking, and the equal amount of lignin and DIOL in the structure improved the integrity of the PU film.

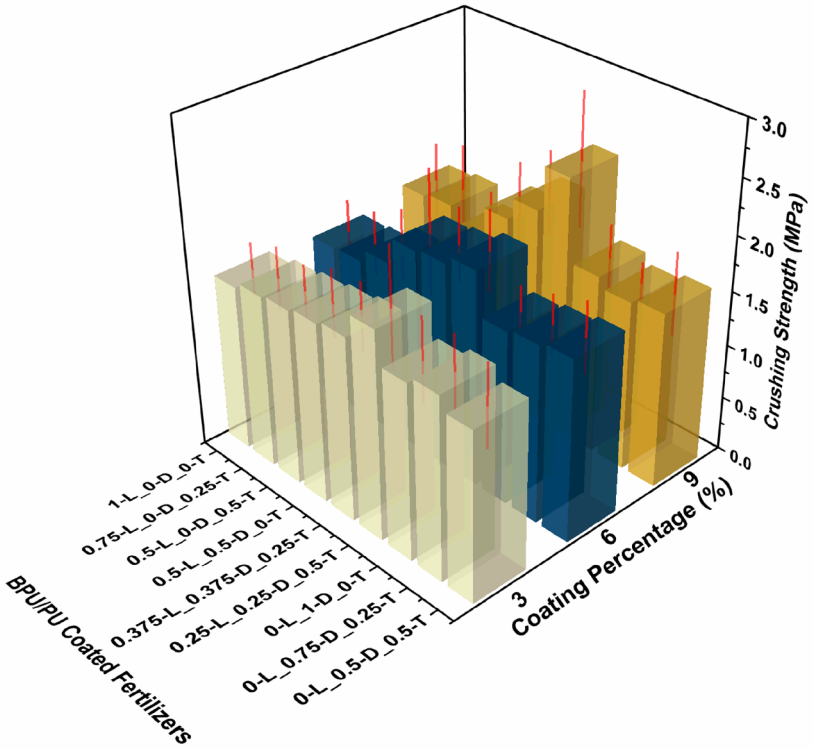

Figure 6.5 Crushing strength of developed BPU/PU coated urea fertilizers. The bar heights represent means, and error bars represent ±SE.

6.3.5 Urea Release Behavior of BPU/PU-coated Fertilizer in Water

The principal property of the coated controlled-release fertilizers (CRFs) is the sustained nutrient release performance. So, to understand the urea release profile in deionized water, the percentage of released urea against time (Days) was determined and presented in Figure 6.6a−k for BPU/PU coated urea, uncoated urea, and commercial CRFs. The rapid release of urea was observed in the case of uncoated urea fertilizer, as it dissolves immediately after exposure to water (Figure 6.6i). On the other hand, the release of urea showed a typical sustained release plateau curve for the developed BPU/PU coated and commercial CRFs (Figure 6.6a−I and Figure 6.6k). It could be seen that the coating material protected fertilizer release against rapid urea release, with an initial burst of less than 20% after day 1.

Further, the developed coated fertilizers (27 coated fertilizers) were grouped as shown in Figure 6.6 (Figure 6.6a−c, Figure 6.6d−f, and Figure 6.6g−i) based on the different polyol formulations and coating percentages (Table 6.1) to evaluate and compare the release performance. In the case of Figure 6.6c, the urea release raised with the increasing proportion of DIOL, a decreasing proportion of TRIOL, and no lignin content for the granules covered by 3% coating material, whereas granules coated with 3% and 6% material (Figure 6.6a and 6.6b) showed inverse trend after the day one release. The analysis reason might be that when the proportion of DIOL increases, the swelling of the coating material occurs, which affects the integrity of polyurethane coating and, ultimately, release performance. All the coated fertilizers developed from the polyol formulation of 0.25-L_0.25-D_0.5-T and 0.375-L_0.375-D_0.25-T slowed down the urea release compared to that of other coated urea, as seen in (Figure 6.6d−f), which is related to the presence of significant proportion of various hydroxyl (−OH) groups to react with the p-MDI leading to a large number of hydrogen bonding in polyurethane formation, resulted in an increase in release performance. Also, in Figure 6.6d−f when the proportion of lignin and DIOL increases with lowering TRIOL it lowers the urea release. It is noted that the cumulative urea release appears higher in the case of fertilizers coated with polyurethane with no content of DIOL as shown in Figure 6.6g−i. Throughout the experiment, the release characteristic of coated urea is in line with the increasing coating percentage. Overall, it was found that the 0.25-L_0.25-D_0.5-T (Run 18) polyol formulation is a good candidate for fertilizer coating. The urea release of all the coated fertilizers was over 90% and reached the equilibrium stage when the incubation time reached 28 days.

The nutrient release in water and nutrient release in the soil are quite different since the release rate depends on the medium used.[12] Also, the agricultural field application of the urea would not

generally involve their complete immersion in water; hence the field experiments are studied and discussed in the following sections.

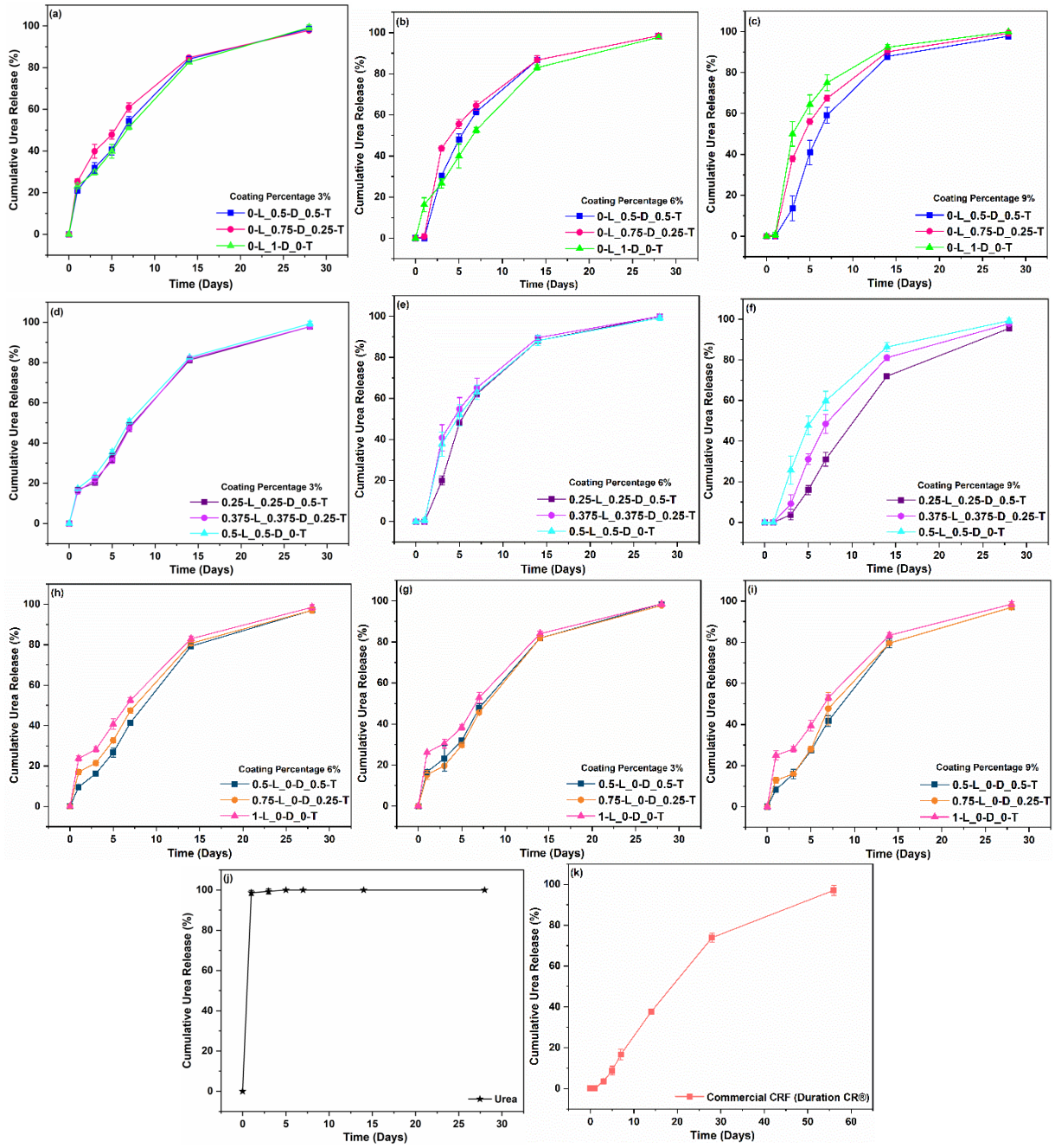

Figure 6.6 Cumulative urea release of all developed BPU/PU coated fertilizers, urea, and commercial CRF (Duration CR®) in water. The data points on the release curves are the means of three measurements, and error bars represent ±SE.

6.3.6 Nitrogen Release Behavior of BPU/PU-coated Fertilizer in Soil

The practical usage of controlled-release fertilizers (CRFs) in agriculture involves their burial application in the natural soil.[2] Nitrogen release behaviors of the developed BPU/PU-coated, uncoated urea, and commercial fertilizers were studied, and the plots of the amount of nitrogen release (Percent N Release) against time (Week after Start) are illustrated in Figure 6.7a−f. The nitrogen release profile for urea was not presented here because observation from our experiment (Figure 6.7i) showed that uncoated urea would readily dissolve in water after being added to the soil (soil solution). Therefore, developed BPU/PU coating materials were used as a physical barrier to decrease the dissolution of urea. From the experimental results (Figure 6.7a−f), it is clear that the nutrient release reduces in coated urea, this is mainly due to the coating layer that would slowly absorb the water in the soil and get swollen after being added into soil, and then N nutrient would release slowly into the soil through diffusion. The results for fertilizer coated with 0.25-L_0.25-D_0.5-T formulations (Figure 6.7a) indicate that the increasing film percentage (from 3% to 9%) could reduce the release of N nutrients, it is because the thicker layer is formed with high coating percentage on the fertilizer surface, which lock the hydrophilic urea inside and preventing the quicker release of nutrients through the coating. According to the results, the release behavior of the fertilizer coated with 0.375-L_0.375-D_0.25-T formulations (Figure 6.7b) is similar to Figure 6.7a. The reason may be that those formulations prepared with various functional polyols (Lignin, DIOL, and TRIOL) provide functionality (as discussed in Figure 6.6) and helps in making flexible and mechanically strong coating, as observed in Figure 6.5, and hence contribute to increasing release performance. The blending of lignin with TRIOL (equal proportions) in the absence of DIOL (0.5-L_0-D_0.5-T) might have reduced the release rate initially (Figure 6.7c). Still, it is not consistent over the period linked with the film percentage increase.

Similarly, 0.75-L_0-D_0.25-T formulation coated fertilizers (Figure 6.7d) showed rapid release of nitrogen within week one for all coating percentages (3, 6, and 9%), and N released remained the same throughout 14 weeks. This is most likely due to the absence of the DIOL, which occupies the intramolecular space between polymer chains, increases the free volume, and hence induces the swelling of coating material. The observed phenomena are in accordance with the literature work.[45] therefore, Figure 6.7c and Figure 6.7d show the importance of DIOL in controlled-release coating formulations. The N-release performance of the fertilizers coated with the formulations (0-L_0.5-D_0.5-T) could be affected by the absence of lignin, as shown in Figure 6.7e.

In summary, the results of N nutrient suggested that the fertilizers coated with 0.25-L_0.25-D_0.5-T and 0.375-L_0.375-D_0.25-T with 9% coating percentage and the commercial CRF have good release profile and reached to the requirement of controlled-release fertilizer.[46] Considering the total amount of N released in the tested timeframe, we anticipated that the remaining percentage of the total N in the coated fertilizer would eventually be released in the soil.

In the next step, a greenhouse pot experiment was conducted to investigate the efficiency of the developed coated fertilizers on plant growth in the soil.

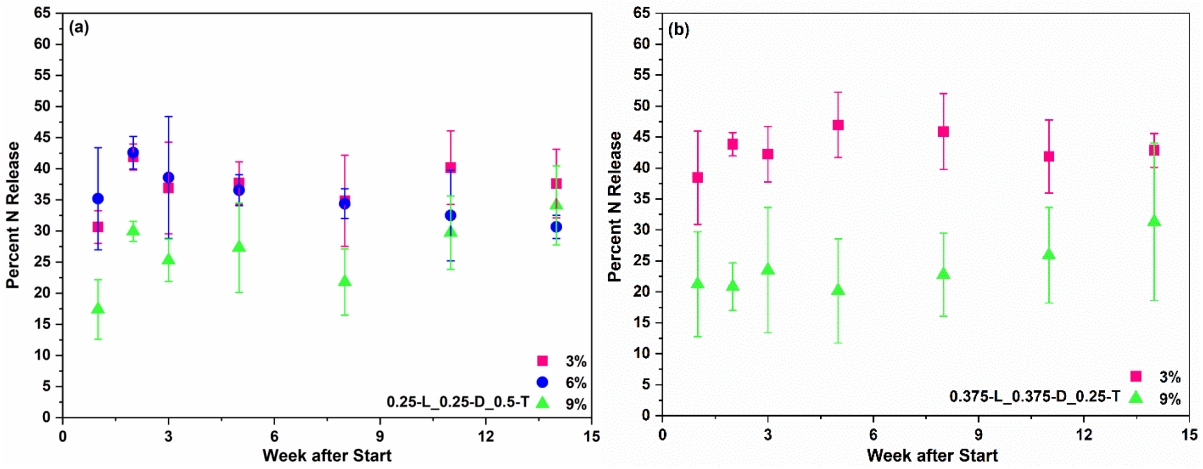

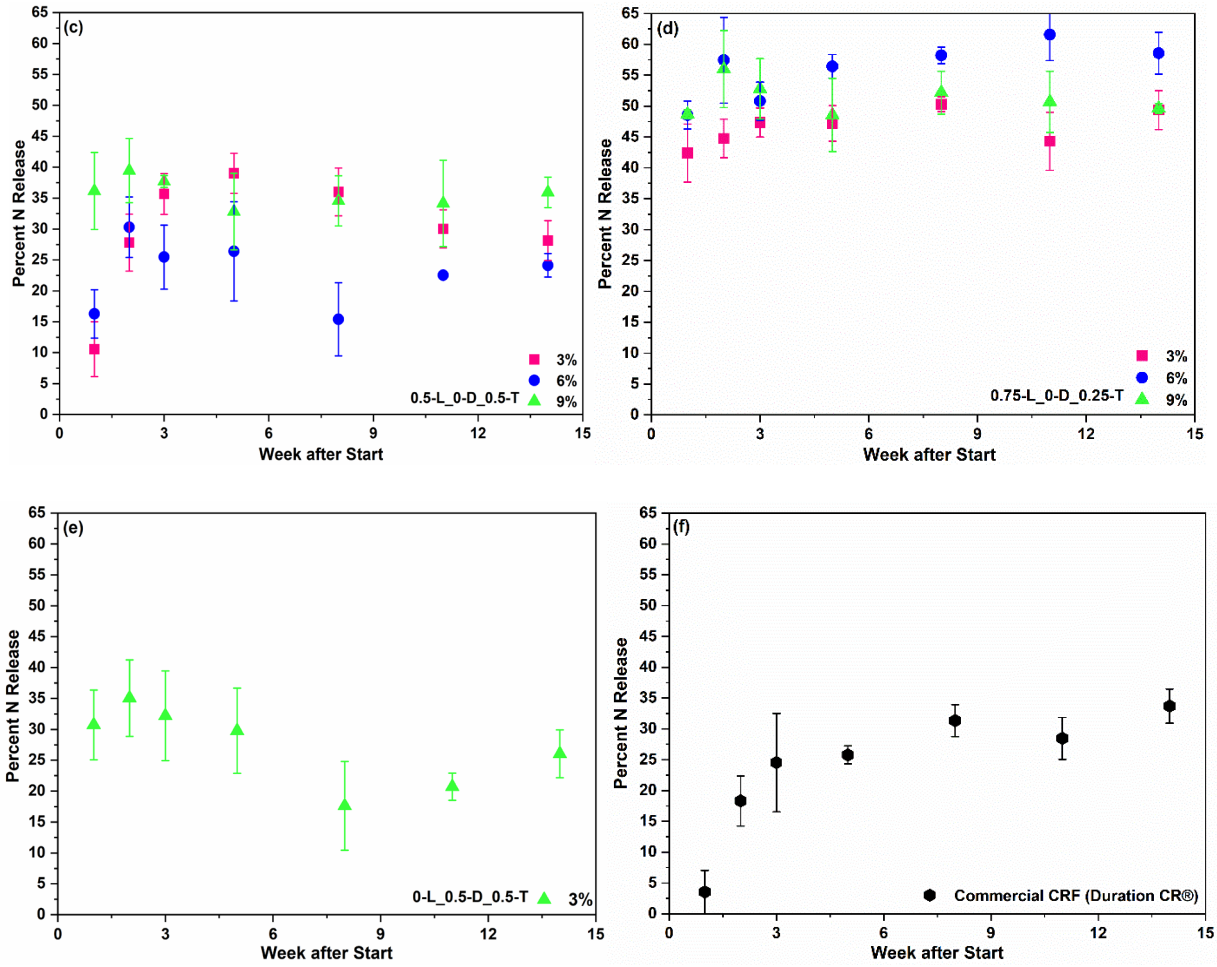

Figure 6.7 Percent nitrogen release from developed BPU/PU formulations of (a) 0.25-L_0.25-D_0.5-T (b) 0.375-L_0.375-D_0.25-T (c) 0.5-L_0-D_0.5-T (d) 0.75-L_0-D_0.25-T with 3%, 6% and 9% coating percentage, (e) 0-L_0.5-D_0.5-T at 3% coating percentage and (f) commercial CRF (Duration CR®) in soil. The data points on the release curves are the means of three measurements, and error bars represent ±SE.

6.3.7 Plant Growth Response of BPU/PU-coated Fertilizers

The greenhouse pot experiment was conducted for ryegrass to examine the effectiveness of the coated urea on plant growth. The investigation employed developed BPU/PU-coated urea, uncoated urea, and commercial CRFs as described in Experimental Section. The plant growth re-

sponse was collected by clipping aboveground biomass and was expressed in cumulative plant growth (Dry weight or matter: g/plant), as shown in Figure 6.8. The dry matter yield is associated with the nitrogen supply from fertilizers. In plants' growing stages, the demand for N nutrients is stable and continuous.[21] Our results show that the fertilizer coated with 0.5-L_0-D_0.5-T (Run 25) formulation had significantly greater clipping weight than the other coated and noncoated fertilizers in the first 11 days of growth. In the early growing stage, plants absorb more available N, and coated fertilizer of 0.5-L_0-D_0.5-T (Run 25) formulation released 36−39% of nitrogen, as reported in Figure 6.6c, which fulfills the plant needs. From then on, the weight decreased relative to the other coated and noncoated fertilizers. The urea granules coated with developed 0.5-L_0.5-D_0-T (Run 11), 0.25-L_0.25-D_0.5-T (Run 18), 0-L_0.5-D_0.5-T (Run 19) formulations provided enough nitrogen nutrient throughout the growing period of ryegrass to improve the plant growth, which could be attributed to the effectiveness of coating material, that provided sustained release of N as shown in Figure 6.5a. However, the noncoated urea-treated pots showed less growth in the early stage due to the rapid hydrolysis of urea in soil. Later, the high availability of N nutrients in the soil provided enough nutrients over the growing cycle. That's another reason for noncoated urea showing high growth in the later stage (21 days after planting) since the content of inorganic N in the soil for coated fertilizer was lower than noncoated urea as coated fertilizer releases their nutrients at a slower rate. The exact mechanism was observed previously for urea and coated fertilizers.[47,48]

The N nutrient uptake reflected in plant growth over the entire growing season tended more for coated fertilizer than uncoated fertilizer. Compared to our developed CRFs, the commercial coated fertilizer applied pot showed superior results in aboveground growths.

Overall, our results provide a positive step for the preparation and development of BPU/PU formulations based on controlled release fertilizers that can promote nutrients while reducing microplastic accumulation in the soil system.

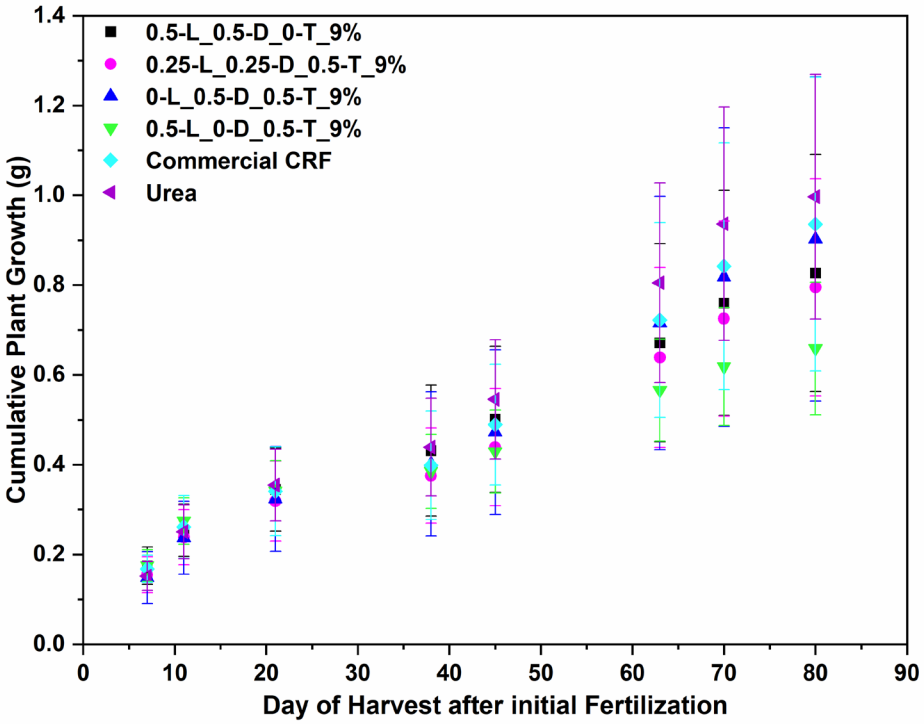

Figure 6.8 Plant growth response of developed BPU/PU formulations coated fertilizers of 0.5-L_0.5-D_0-T (Run 11), 0.25-L_0.25-D_0.5-T (Run 18), 0-L_0.5-D_0.5-T (Run 19), 0-L_0.5-D_0.5-T (Run 25), Commercial CRF (Duration CR®) and noncoated urea fertilizers in the soil. The data points on the release curves are the means of three measurements, and error bars represent ±SE.

6.4 Conclusions

This study shows the great interest in developing biobased controlled-release fertilizers based on lignin to promote the efficient use of fertilizers for sustainable agriculture. A series of BPU/PU-

coated fertilizers with three different coating percentages (3, 6, and 9%) were successfully fabricated using the formulation derived from the DOE. The chemical structure of the synthesized BPU/PU resin was confirmed by the FTIR, which recorded the presence of urethane linkages and consumption of isocyanate groups. SEM revealed the coated fertilizers' morphology, which showed good adhesion between the surface of fertilizer particles and coating materials. Moreover, the developed BPU/PU coated fertilizers demonstrated relatively high crushing strength, ensuring that coated particles would maintain their integrity during practical use and transportation. Coated fertilizers' nutrient release behavior was tested in water and soil media. The results demonstrated that the developed BPU/PU-coated fertilizers have a controlled release profile. Using the output from the release profile experimental data, it can be concluded that 0.25-L_0.25-D_0.5-T and 0.375-L_0.375-D_0.25-T proportions would be desirable for fertilizer coating formulations. In addition, the pot experimental results showed that the developed coated fertilizers could provide nutrients to plants at different growing stages. The developed BPU/PU coated fertilizers' release behavior was significantly affected by the different coating formulations, percentage of the coating material, and release medium. It was experimentally confirmed that the developed fertilizers have many advantages over commercial CRFs used in this study, including being environmentally friendly, similarly nutrient release performance, and renewable. This study offers a sustainable approach to using lignin biomacromolecule to design and develop controlled-release fertilizer with desired nutrient-release properties.

6.5 References

(1) Li, T.; Lü, S.; Yan, J.; Bai, X.; Gao, C.; Liu, M. An Environment-Friendly Fertilizer Prepared by Layer-by-Layer Self-Assembly for PH-Responsive Nutrient Release. *ACS*

Appl. Mater. Interfaces **2019**, *11* (11), 10941–10950. https://doi.org/10.1021/acsami.9b01425.

(2) Tang, Y.; Wang, X.; Yang, Y.; Gao, B.; Wan, Y.; Li, Y. C.; Cheng, D. Activated-Lignite-Based Super Large Granular Slow-Release Fertilizers Improve Apple Tree Growth: Synthesis, Characterizations, and Laboratory and Field Evaluations. *J. Agric. Food Chem.* **2017**, *65* (29), 5879–5889. https://doi.org/10.1021/acs.jafc.7b01699.

(3) De Matos, M.; Mattos, B. D.; Tardy, B. L.; Rojas, O. J.; Magalhães, W. L. E. Use of Biogenic Silica in Porous Alginate Matrices for Sustainable Fertilization with Tailored Nutrient Delivery. *ACS Sustain. Chem. Eng.* **2018**, *6* (2), 2716–2723. https://doi.org/10.1021/acssuschemeng.7b04331.

(4) Liu, X.; Tao, Y.; Wen, G.; Kong, F.; Zhang, X.; Hu, Z. Influence of Soil and Irrigation Water Ph on the Availability of Phosphorus in Struvite Derived from Urine through a Greenhouse Pot Experiment. *J. Agric. Food Chem.* **2016**, *64* (17), 3324–3329. https://doi.org/10.1021/acs.jafc.6b00021.

(5) Nursalam, 2016, metode penelitian; Fallis, A. . *Green Urea For Future Sustainability*; 2013; Vol. 53.

(6) Costa, M. M. E.; Cabral-Albuquerque, E. C. M.; Alves, T. L. M.; Pinto, J. C.; Fialho, R. L. Use of Polyhydroxybutyrate and Ethyl Cellulose for Coating of Urea Granules. *J. Agric. Food Chem.* **2013**, *61* (42), 9984–9991. https://doi.org/10.1021/jf401185y.

(7) Nitrogen Release Rates from Slow-and Controlled-Release Fertilizers Influenced by Placement and Temperature.

(8) Heuchan, S. M.; Fan, B.; Kowalski, J. J.; Gillies, E. R.; Henry, H. A. L. Development of Fertilizer Coatings from Polyglyoxylate-Polyester Blends Responsive to Root-Driven PH

Change. *J. Agric. Food Chem.* **2019**, *67* (46), 12720–12729. https://doi.org/10.1021/acs.jafc.9b04717.

(9) Davidson, D.; Gu, F. X. Materials for Sustained and Controlled Release of Nutrients and Molecules to Support Plant Growth. *J. Agric. Food Chem.* **2012**, *60* (4), 870–876. https://doi.org/10.1021/jf204092h.

(10) Zhang, S.; Zhang, S.; Zhang, S.; Yang, Y.; Yang, Y.; Tong, Z.; Gao, B.; Gao, N.; Shen, T.; Wan, Y.; Yu, Z.; Liu, L.; Ma, X.; Guo, Y.; Fugice, J.; Li, Y. C. Self-Assembly of Hydrophobic and Self-Healing Bionanocomposite-Coated Controlled-Release Fertilizers. *ACS Appl. Mater. Interfaces* **2020**, *12* (24), 27598–27606. https://doi.org/10.1021/acsami.0c06530.

(11) Guo, Y.; Liu, Z.; Zhang, M.; Tian, X.; Chen, J.; Sun, L. Synthesis and Application of Urea-Formaldehyde for Manufacturing a Controlled-Release Potassium Fertilizer. *Ind. Eng. Chem. Res.* **2018**, *57* (5), 1593–1606. https://doi.org/10.1021/acs.iecr.7b04629.

(12) Lubkowski, K.; Smorowska, A.; Grzmil, B.; Kozłowska, A. Controlled-Release Fertilizer Prepared Using a Biodegradable Aliphatic Copolyester of Poly(Butylene Succinate) and Dimerized Fatty Acid. *J. Agric. Food Chem.* **2015**, *63* (10), 2597–2605. https://doi.org/10.1021/acs.jafc.5b00518.

(13) Kabiri, S.; Degryse, F.; Tran, D. N. H.; Da Silva, R. C.; McLaughlin, M. J.; Losic, D. Graphene Oxide: A New Carrier for Slow Release of Plant Micronutrients. *ACS Appl. Mater. Interfaces* **2017**, *9* (49), 43325–43335. https://doi.org/10.1021/acsami.7b07890.

(14) Liang, R.; Liu, M. Preparation and Properties of a Double-Coated Slow-Release and Water-Retention Urea Fertilizer. *J. Agric. Food Chem.* **2006**, *54* (4), 1392–1398. https://doi.org/10.1021/jf052582f.

(15) Zhang, L.; Tian, H.; Zhang, M.; Wu, L.; Guo, W.; Fang, F.; Sun, X.; Zhong, Z.; Du, L.; Liu, Z. Preparation and Properties of Bio-Based Polyurethane Controlled Release Urea Coating with Photosensitivity. *ACS Omega* **2022**, *7* (10), 8558–8569. https://doi.org/10.1021/acsomega.1c06432.

(16) Fu, J.; Wang, C.; Chen, X.; Huang, Z.; Chen, D. Classification Research and Types of Slow Controlled Release Fertilizers (SRFs) Used - a Review. *Commun. Soil Sci. Plant Anal.* **2018**, *49* (17), 2219–2230. https://doi.org/10.1080/00103624.2018.1499757.

(17) Eghbali Babadi, F.; Yunus, R.; Masoudi Soltani, S.; Shotipruk, A. Release Mechanisms and Kinetic Models of Gypsum-Sulfur-Zeolite-Coated Urea Sealed with Microcrystalline Wax for Regulated Dissolution. *ACS Omega* **2021**, *6* (17), 11144–11154. https://doi.org/10.1021/acsomega.0c04353.

(18) Ni, B.; Liu, M.; Lü, S.; Xie, L.; Wang, Y. Environmentally Friendly Slow-Release Nitrogen Fertilizer. *J. Agric. Food Chem.* **2011**, *59* (18), 10169–10175. https://doi.org/10.1021/jf202131z.

(19) Ibrahim, K. A.; Naz, M. Y.; Shukrullah, S.; Sulaiman, S. A.; Ghaffar, A.; AbdEl-Salam, N. M. Nitrogen Pollution Impact and Remediation through Low Cost Starch Based Biodegradable Polymers. *Scientific Reports*. 2020. https://doi.org/10.1038/s41598-020-62793-3.

(20) Legras-Lecarpentier, D.; Stadler, K.; Weiss, R.; Guebitz, G. M.; Nyanhongo, G. S. Enzymatic Synthesis of 100% Lignin Biobased Granules as Fertilizer Storage and Controlled Slow Release Systems. *ACS Sustain. Chem. Eng.* **2019**, *7* (14), 12621–12628. https://doi.org/10.1021/acssuschemeng.9b02689.

(21) Zhao, X.; Qi, X.; Chen, Q.; Ao, X.; Guo, Y. Sulfur-Modified Coated Slow-Release

Fertilizer Based on Castor Oil: Synthesis and a Controlled-Release Model. *ACS Sustain. Chem. Eng.* **2020**, *8* (49), 18044–18053. https://doi.org/10.1021/acssuschemeng.0c06056.

(22) Fertahi, S.; Bertrand, I.; Amjoud, M.; Oukarroum, A.; Arji, M.; Barakat, A. Properties of Coated Slow-Release Triple Superphosphate (TSP) Fertilizers Based on Lignin and Carrageenan Formulations. *ACS Sustain. Chem. Eng.* **2019**, *7* (12), 10371–10382. https://doi.org/10.1021/acssuschemeng.9b00433.

(23) Silviana, S.; Janitra, A. A.; Sa'Adah, A. N.; Dalanta, F. Synthesis of Aminopropyl-Functionalized Mesoporous Silica Derived from Geothermal Silica for an Effective Slow-Release Urea Carrier. *Ind. Eng. Chem. Res.* **2022**, *61* (26), 9283–9299. https://doi.org/10.1021/acs.iecr.2c00424.

(24) Li, L.; Wang, M.; Wu, X.; Yi, W.; Xiao, Q. Bio-Based Polyurethane Nanocomposite Thin Coatings from Two Comparable POSS with Eight Same Vertex Groups for Controlled Release Urea. *Sci. Rep.* **2021**, *11* (1), 1–12. https://doi.org/10.1038/s41598-021-89254-9.

(25) Bote, S. D.; Narayan, R. Synthesis of Biobased Polyols from Soybean Meal for Application in Rigid Polyurethane Foams. *Ind. Eng. Chem. Res.* **2021**, *60* (16), 5733–5743. https://doi.org/10.1021/acs.iecr.0c06306.

(26) Yang, Z.; Feng, Y.; Liang, H.; Yang, Z.; Yuan, T.; Luo, Y.; Li, P.; Zhang, C. A Solvent-Free and Scalable Method to Prepare Soybean-Oil-Based Polyols by Thiol-Ene Photo-Click Reaction and Biobased Polyurethanes Therefrom. *ACS Sustain. Chem. Eng.* **2017**, *5* (8), 7365–7373. https://doi.org/10.1021/acssuschemeng.7b01672.

(27) Tian, H.; Liu, Z.; Zhang, M.; Guo, Y.; Zheng, L.; Li, Y. C. Biobased Polyurethane, Epoxy Resin, and Polyolefin Wax Composite Coating for Controlled-Release Fertilizer. *ACS Appl. Mater. Interfaces* **2019**, *11* (5), 5380–5392. https://doi.org/10.1021/acsami.8b16030.

(28) Liu, L.; Ni, Y.; Zhi, Y.; Zhao, W.; Pudukudy, M.; Jia, Q.; Shan, S.; Zhang, K.; Li, X. Sustainable and Biodegradable Copolymers from SO2 and Renewable Eugenol: A Novel Urea Fertilizer Coating Material with Superio Slow Release Performance. *Macromolecules* **2020**, *53* (3), 936–945. https://doi.org/10.1021/acs.macromol.9b02202.

(29) Wang, Y. Y.; Wyman, C. E.; Cai, C. M.; Ragauskas, A. J. Lignin-Based Polyurethanes from Unmodified Kraft Lignin Fractionated by Sequential Precipitation. *ACS Appl. Polym. Mater.* **2019**, *1* (7), 1672–1679. https://doi.org/10.1021/acsapm.9b00228.

(30) Wang, S.; Liu, W.; Yang, D.; Qiu, X. Highly Resilient Lignin-Containing Polyurethane Foam. *Ind. Eng. Chem. Res.* **2019**, *58* (1), 496–504. https://doi.org/10.1021/acs.iecr.8b05072.

(31) Holt, C. A.; Cottyn, B.; Baumberger, S.; Kovacs-Schreiner, K.; Blacker, A. J. High-Throughput Analysis of Lignin by Agarose Gel Electrophoresis. *J. Agric. Food Chem.* **2020**, *68* (48), 14297–14306. https://doi.org/10.1021/acs.jafc.0c06308.

(32) Jampa, S.; Puente-Urbina, A.; Ma, Z.; Wongkasemjit, S.; Luterbacher, J. S.; Van Bokhoven, J. A. Optimization of Lignin Extraction from Pine Wood for Fast Pyrolysis by Using a γ-Valerolactone-Based Binary Solvent System. *ACS Sustain. Chem. Eng.* **2019**, *7* (4), 4058–4068. https://doi.org/10.1021/acssuschemeng.8b05498.

(33) Barde, M.; Celikbag, Y.; Via, B.; Adhikari, S.; Auad, M. L. Semi-Interpenetrating Novolac-Epoxy Thermoset Polymer Networks Derived from Plant Biomass. *J. Renew. Mater.* **2018**, *6* (7), 724–736. https://doi.org/10.32604/JRM.2018.00116.

(34) Ben, H.; Ragauskas, A. J. NMR Characterization of Pyrolysis Oils from Kraft Lignin. *Energy and Fuels* **2011**, *25* (5), 2322–2332. https://doi.org/10.1021/ef2001162.

(35) Barbi, S.; Barbieri, F.; Andreola, F.; Lancellotti, I.; Barbieri, L.; Montorsi, M. Preliminary

Study on Sustainable NPK Slow-Release Fertilizers Based on Byproducts and Leftovers: A Design-of-Experiment Approach. *ACS Omega* **2020**, *5* (42), 27154–27163. https://doi.org/10.1021/acsomega.0c03082.

(36) Cheng Qian. Effect of Real and Simulated Traffic on Coated Fertilizer Prill Integrity and Nitrogen Release, Auburn University, 2017.

(37) Wilson, M. L.; Rosen, C. J.; Moncrief, J. F. A Comparison of Techniques for Determining Nitrogen Release from Polymer-Coated Urea in the Field. *HortScience* **2009**, *44* (2), 492–494. https://doi.org/10.21273/hortsci.44.2.492.

(38) Serrano, L.; Esakkimuthu, E. S.; Marlin, N.; Brochier-Salon, M. C.; Mortha, G.; Bertaud, F. Fast, Easy, and Economical Quantification of Lignin Phenolic Hydroxyl Groups: Comparison with Classical Techniques. *Energy and Fuels* **2018**, *32* (5), 5969–5977. https://doi.org/10.1021/acs.energyfuels.8b00383.

(39) Meng, X.; Crestini, C.; Ben, H.; Hao, N.; Pu, Y.; Ragauskas, A. J.; Argyropoulos, D. S. Determination of Hydroxyl Groups in Biorefinery Resources via Quantitative 31P NMR Spectroscopy. *Nat. Protoc.* **2019**, *14* (9), 2627–2647. https://doi.org/10.1038/s41596-019-0191-1.

(40) Argyropoulos, D. S.; Sadeghifar, H.; Cui, C.; Sen, S. Synthesis and Characterization of Poly(Arylene Ether Sulfone) Kraft Lignin Heat Stable Copolymers. *ACS Sustain. Chem. Eng.* **2014**, *2* (2), 264–271. https://doi.org/10.1021/sc4002998.

(41) Ahvazi, B.; Cloutier, É.; Wojciechowicz, O.; Ngo, T. D. Lignin Profiling: A Guide for Selecting Appropriate Lignins as Precursors in Biomaterials Development. *ACS Sustain. Chem. Eng.* **2016**, *4* (10), 5090–5105. https://doi.org/10.1021/acssuschemeng.6b00873.

(42) Constant, S.; Wienk, H. L. J.; Frissen, A. E.; Peinder, P. De; Boelens, R.; Van Es, D. S.;

Grisel, R. J. H.; Weckhuysen, B. M.; Huijgen, W. J. J.; Gosselink, R. J. A.; Bruijnincx, P. C. A. New Insights into the Structure and Composition of Technical Lignins: A Comparative Characterisation Study. *Green Chem.* **2016**, *18* (9), 2651–2665. https://doi.org/10.1039/c5gc03043a.

(43) Bansode, A.; Barde, M.; Asafu-Adjaye, O.; Patil, V.; Hinkle, J.; Via, B. K.; Adhikari, S.; Adamczyk, A. J.; Farag, R.; Elder, T.; Labbé, N.; Auad, M. L. Synthesis of Biobased Novolac Phenol-Formaldehyde Wood Adhesives from Biorefinery-Derived Lignocellulosic Biomass. *ACS Sustain. Chem. Eng.* **2021**, *9* (33), 10990–11002. https://doi.org/10.1021/acssuschemeng.1c01916.

(44) Ibrahim, K. R. M.; Babadi, F. E.; Yunus, R. Comparative Performance of Different Urea Coating Materials for Slow Release. *Particuology* **2014**, *17* (April 2021), 165–172. https://doi.org/10.1016/j.partic.2014.03.009.

(45) Fertahi, S.; Bertrand, I.; Ilsouk, M.; Oukarroum, A.; Amjoud, M.; Zeroual, Y.; Barakat, A. Impact of Plasticizers on Lignin-Carrageenan Formulation Properties and on Phosphorus Release from a Coated Triple Superphosphate Fertilizer. *Ind. Eng. Chem. Res.* **2020**, *59* (31), 14172–14179. https://doi.org/10.1021/acs.iecr.0c03143.

(46) Jin, S.; Yue, G.; Feng, L.; Han, Y.; Yu, X.; Zhang, Z. Preparation and Properties of a Coated Slow-Release and Water-Retention Biuret Phosphoramide Fertilizer with Superabsorbent. *J. Agric. Food Chem.* **2011**, *59* (1), 322–327. https://doi.org/10.1021/jf1032137.

(47) Geng, J.; Ma, Q.; Zhang, M.; Li, C.; Liu, Z.; Lyu, X.; Zheng, W. Synchronized Relationships between Nitrogen Release of Controlled Release Nitrogen Fertilizers and Nitrogen Requirements of Cotton. *F. Crop. Res.* **2015**, *184*, 9–16.

https://doi.org/10.1016/j.fcr.2015.09.001.

(48) Geng, J.; Yang, X.; Huo, X.; Chen, J.; Lei, S.; Li, H.; Lang, Y.; Liu, Q. Effects of Controlled-Release Urea Combined with Fulvic Acid on Soil Inorganic Nitrogen, Leaf Senescence and Yield of Cotton. *Sci. Rep.* **2020**, *10* (1), 1–11. https://doi.org/10.1038/s41598-020-74218-2.

Chapter 7
General Conclusions

The primary stimulus of this dissertation is the growing interest in utilizing potentially sustainable and less hazardous building blocks for synthesizing polymeric resins. The biorefinery approach permits the production of value-added biobased materials and chemicals through the conversion of biomass feedstock. Inspired by structural chemistry, lignocellulosic biomass (both woody and waste biomass) consists of polysaccharides, and lignin is a prime candidate for biorefinery. Four types of biorefinery-derived biomass were chosen as monomers to synthesize biobased polymeric resins, which include lignin recovered from kraft biorefinery (L-KB), bio-oil prepared from laboratory-scale solvent liquefaction of lignin (BO-SL/L), bio-oil produced from fast pyrolysis of pinewood (BO-FP/PW) and bio-oil synthesized from hydrothermal liquefaction (HTL) of municipal sewage sludge (MSS-Bio-oil). The molecular characterization of L-KB, BO-SL/L, BO-FP/PW, and MSS-Bio-oil showed that they contain various reactive groups (hydroxyl groups) whose relative chemistry is applicable in synthesizing biobased polymeric resins. The resulting polymeric resins have potential practical applications as wood adhesive, resin for 3D printing of structural materials, and functional coating material for controlled-release fertilizers.

In chapter 2, the biobased novolac phenol-formaldehyde (NPF) resin adhesives were successfully developed by substituting 50% (w/w) of petroleum-based phenol with lignin derived from kraft biorefinery (L-KB), bio-oils prepared from laboratory-scale solvent liquefaction of lignin (BO-SL/L) and fast pyrolysis of pinewood (BO-FP/PW), respectively. For comparison purposes, the commercially available NPF resin was duplicated in the lab. The dry adhesion performance of the lignin-derived NPF resin was higher than the lab-made commercially available NPF resin.

The highest adhesion strength corresponds to the polyphenolic structure of lignin, which improves reactivity. Therefore, lignin derived from kraft biorefinery can be effectively used to replace phenol in NPF resin for adhesive applications in the wood industry, reducing the detrimental effect of phenol.

In chapter 3, the simultaneous partial replacement of both petroleum-based phenol and formaldehyde with unmodified kraft biorefinery lignin and modified kraft biorefinery lignin, respectively, have been performed for producing sustainable adhesives with less toxicity. The periodate oxidation process has obtained the modified lignin structure, which utilizes sodium periodate ($NaIO_4$) as an oxidizing agent. The $NaIO_4$ oxidized the hydroxyl groups present in the interunit linkages of the lignin structure to aldehyde groups and converted lignin partly to a quinone. The oxidized structure was validated by FTIR, elemental analysis, solid-state $^{1}H–^{13}C$ 2D HETCOR NMR, and aldehyde content analysis. The partial replacement of formaldehyde by oxidized lignin demonstrated adhesion strength (2.42 MPa) comparable to the lab-made commercially available NPF resin. This work opened up a new way to use lignin biomass to synthesize biobased adhesives.

Chapter 4 uses bio-oils derived from hydrothermal liquefaction (HTL) of municipal sewage sludge (MSS-Bio-oil) as a functional reactive filler for pMDI wood adhesive formulation. The addition of MSS-Bio-oil in pMDI wood adhesives showed a great potential to reduce the usage of the petroleum-derived pMDI while lowering the cost of maintaining good bonding performance. The bio-oil prepared under the nitrogen atmosphere with no catalyst (MSS-Bio-oil_N) was found to be an excellent filling material to enhance the adhesion performance of pMDI by forming robust interphase between the wood substrates which improves the mechanical strength

of wood joints. The MSS-Bio-oil has shown the key component for pMDI adhesives and expanded their application in the wood industry.

In chapter 5, the curing behavior of bio-based novolacs phenol-formaldehyde (BNPF) resin cued with hexamethylenetetramine (HMTA) curing agent has been studied using the non-isothermal differential scanning calorimetry (DSC) scan method. The thermal curing kinetics were studied through model-fitting approaches. According to the model-fitting analysis, the BNPF resin systems were found to undergo different curing reaction mechanisms, that is, nth-other and autocatalytic model, combined known as the Kamal model, which showed a good agreement with the experimental curves. The obtained curing kinetic information of BNPF resin could guide the curing process and make the actual operation of the 3D printing process more convenient and flexible.

In chapter 6, this study provides a sustainable approach to utilizing kraft biorefinery lignin in preparation of coating material for controlled and prolonged release of nutrients. At a fixed NCO/OH ratio (1:1), a series of biobased polyurethanes were prepared for coating urea prills from the polyaddition reaction between three polyols (lignin, DIOL, and TRIOL) and isocyanate (p-MDI). The mechanical property (crushing strength) of fertilizers granules coated with biobased polyurethane is significantly better than the uncoated fertilizer. The coated and uncoated fertilizers' nutrient release behavior was tested in water and soil media, which reveals that the developed BPU/PU-coated fertilizers have a controlled release profile. This study offers a reference for developing sustainable controlled-release fertilizers using lignin biomacromolecules.

Overall, the fundamental knowledge gained from this study allows us to understand better the crucial role of biorefinery-derived biomass in the preparation of biobased polymeric resins for application in wood adhesives, resin for 3D printing of structural materials, and functional coating material for controlled-release fertilizers.